

**Starbon<sup>®</sup> Materials**  
**for a Circular Economy**

**Jennifer Attard**

**PhD**

**University of York**

**Chemistry**

**December 2018**



# Abstract

Starbons are a patented group of sustainably-produced bio-based mesoporous materials derived from polysaccharides, namely; starch (from potato peel waste), alginic acid (from brown algae) and pectin (from orange peel waste). Starbons exhibit exceptional surface areas and mesopore volumes as well as tuneable surface functionalities, making them ideal candidates for numerous applications, mainly heterogenous catalysis, chromatography and metal recovery.

This thesis reports studies on Starbon materials, as well as the first report on novel nitrogen-doped Starbon materials (*N*-Starbons). Both classes of materials were characterised by elemental analysis, nitrogen adsorption / desorption porosimetry, scanning electron microscopy and thermogravimetry. Being newly discovered materials, *N*-Starbons were further characterised by x-ray photoelectron spectroscopy, both solid-phase and gas-phase diffuse-reflectance infrared spectroscopy in Fourier Transform mode and attenuated total reflection Fourier Transform infrared spectroscopy.

Crucially, *N*-Starbons retained the typical high and stable surface areas (up to 563 m<sup>2</sup> g<sup>-1</sup>) and pore volumes (up to 0.75 cm<sup>3</sup> g<sup>-1</sup>) of Starbon materials. Apart from having remarkably high nitrogen content of up to 11.5%, *N*-Starbons were interestingly found to contain nitrile functionalities on their surface. Nitriles are highly valuable functionalities for porous materials due to their ease of reactivity and substitution, thus allowing for ease of further functionalisation. Furthermore, nitriles have a high dielectric constant and can therefore improve the electrical properties of a material.

Herein, a number of original applications for both Starbon and *N*-Starbon materials were demonstrated. Starbons proved to be successful in simple and 100% gold recovery from e-waste. Furthermore, in natural product purification, Starbon was found to be highly effective in isolating valuable usujirene from a complex seaweed extract for use as a natural and biodegradable sunscreen. In CO<sub>2</sub> sequestration, *N*-Starbons showed improved adsorption capacities (2.4 mmol g<sup>-1</sup>) compared to Starbons, as well as significant and stable capacitance behaviour (> 100 F g<sup>-1</sup>).



# Contents

Abstract .....	iii
Contents.....	v
List of Figures .....	ix
List of Tables.....	xvii
Acknowledgements .....	xxi
Declaration .....	xxiii
Introduction .....	1
1.1    Circular Economy .....	3
1.2    Green Chemistry .....	5
1.3    Mesoporous materials.....	6
1.3.1    Carbonaceous mesoporous materials .....	7
1.3.2    Starbon .....	8
1.4    Thesis outline.....	20
Starbons® .....	21
Starbon® Characterisation .....	23
2.1    Introduction .....	25
2.2    Elemental analysis .....	26
2.3    Porosimetry.....	28
2.4    Scanning Electron Microscopy.....	35
2.5    Thermogravimetric Analysis .....	37
WEEE Recycling .....	39
3.1    Introduction .....	41
3.2    WEEE Metal Leaching.....	43
3.3    Gold .....	46
3.3.1    Gold Adsorption.....	48
3.3.2    Gold-Starbon characterisation.....	50
3.3.3    Gold desorption .....	55
3.4    Indium.....	62
3.4.1    Adsorption from LCDs.....	65

3.4.2	Adsorption from standard solutions.....	66
3.4.3	Indium-Starbon characterisation.....	69
3.4.4	Desorption and re-use .....	74
3.4.5	Selectivity for tin(IV) over indium(III) .....	76
	Adsorption of MAAs.....	79
4.1	Introduction .....	81
4.2	HPLC characterisation of MAAs.....	84
4.3	Comparison of extraction techniques.....	86
4.4	Solvent mixture screening.....	89
4.5	Isolation of usujirene using Starbons .....	90
4.5.1	Starbon screening.....	90
4.5.2	Scale-up .....	93
4.5.3	Flow simulation .....	94
4.5.4	Further purification.....	96
	<i>N</i> -Starbons.....	97
	<i>N</i> -Starbon Characterisation .....	99
5.1	Introduction .....	101
5.1.1	Seafood waste valorisation .....	102
5.2	Porosimetry .....	105
5.2.1	Pore stability over time.....	110
5.3	Scanning electron microscopy .....	112
5.4	Elemental analysis.....	114
5.5	Thermogravimetric analysis.....	116
5.6	Infrared spectroscopy .....	117
5.6.1	Gas-phase DRIFT spectroscopy .....	117
5.6.2	ATR - FTIR .....	120
5.6.3	DRIFT spectroscopy.....	123
5.7	X-ray Photoelectron Spectroscopy.....	125
	Capacitance .....	131
6.1	Introduction .....	133
6.1.1	Electrochemical testing.....	136
6.2	Results.....	138
6.2.1	Galvanostatic charge-discharge .....	138
6.2.2	Cyclic voltammetry .....	145
	CO <sub>2</sub> Capture .....	151

7.1	Introduction .....	153
7.2	Results .....	155
7.2.1	Adsorption at atmosphere pressure .....	156
7.2.2	Adsorption at high pressure.....	161
Conclusions & Further Work .....		163
8.1	Starbons .....	165
8.1.1	Pecbon development .....	165
8.2	WEEE recycling .....	166
8.2.1	Indium recovery .....	166
8.2.2	Starbon supported gold for catalysis .....	167
8.3	Separation of MAAs.....	167
8.4	<i>N</i> -Starbon characterisation .....	168
8.4.1	Proteins as precursors.....	168
8.5	Capacitance.....	168
8.6	CO <sub>2</sub> capture.....	169
8.7	Acetylene hydrochlorination .....	170
Experimental .....		171
9.1	Materials and chemicals .....	173
9.2	Starbon <sup>®</sup> production.....	174
9.2.1	Starch.....	174
9.2.2	Alginic acid .....	175
9.2.3	Pectin.....	175
9.2.4	Alginic acid / Chitosan hybrid ( <i>N</i> -Starbon) .....	176
9.3	Starbon & <i>N</i> -Starbon characterisation.....	178
9.3.1	Porosimetry .....	178
9.3.2	Scanning electron microscopy .....	178
9.3.3	Elemental analysis.....	178
9.3.4	Thermogravimetric analysis.....	178
9.3.5	Thermogravimetric analysis – Diffuse reflectance infrared spectroscopy in Fourier transform mode.....	179
9.3.6	X-ray Photoelectron Spectroscopy.....	179
9.3.7	Attenuated Total Reflection - Fourier Transform Infrared Spectroscopy.....	179
9.3.8	Diffuse Reflectance Infrared Fourier Transform .....	179
9.4	Metal solution qualitative and quantitative analysis.....	180
9.4.1	Inductively Coupled Plasma – Mass Spectrometry.....	180
9.5	Real e-waste metal leaching & adsorption .....	180

9.5.1	Waste from an industrial waste stream.....	180
9.5.2	Waste from a laptop.....	180
9.6	Indium (III) studies .....	182
9.6.1	Adsorption .....	182
9.6.2	Desorption.....	182
9.6.3	Re-use .....	183
9.7	Tin (IV) studies .....	183
9.8	Indium (III) vs. Tin (IV) studies .....	183
9.9	Starbon-metal characterisation.....	184
9.9.1	Transmission electron microscopy .....	184
9.9.2	X-ray photoelectron and auger electron spectroscopy.....	184
9.9.3	Simultaneous thermal analysis .....	184
9.10	Separation of MAAs .....	185
9.10.1	High-Performance Liquid Chromatography .....	185
9.10.2	Repeated solvent wash extraction .....	185
9.10.3	Soxhlet extraction.....	186
9.10.4	Counter-current chromatography simulation .....	187
9.10.5	Automated Starbon screening .....	187
9.10.6	Scale-up.....	188
9.10.7	Flow simulation.....	188
9.10.8	Further purification.....	188
9.11	Electrode preparations.....	189
9.11.1	Carbon cloth coating .....	189
9.11.2	Monolith preparation.....	189
9.12	Electrochemical testing.....	191
9.12.1	Galvanostatic charge/discharge.....	192
9.12.2	Cyclic voltammetry.....	193
9.13	CO <sub>2</sub> capture .....	194
9.13.1	Atmospheric pressure .....	194
9.13.2	Elevated pressure.....	194
Appendix A.....		195
Appendix B.....		201
Abbreviations.....		205
Bibliography.....		211

# List of Figures

Figure 1.1: Comparison of linear and circular economies. ....	3
Figure 1.2: The 12 Principles of Green Chemistry. <sup>7</sup> .....	5
Figure 1.3: Diagrammatic representation of micro-, meso- and macropores in a) 3D and b) 2D. Reproduced from ref 12 with permission from the Royal Society of Chemistry. <sup>12</sup> .....	6
Figure 1.4: The monomers that make up the starting materials for the various Starbons. .....	9
Figure 1.5: General Starbon preparation phases. ....	11
Figure 1.6: The proposed structure of StarCat. Reproduced from ref 31 with permission from the Royal Society of Chemistry. <sup>31</sup> .....	12
Figure 1.7: Effects of carbonisation temperature on the stability and surface functionality of Starbon materials. Reproduced from ref 23 with permission from the John Wiley and Sons. <sup>23</sup> .....	14
Figure 1.8: Schematic representation of the use of Starbons in adsorption of phenols from wastewater. Reproduced from ref 47 with permission from the American Chemical Society. <sup>47</sup> .....	18
Figure 1.9: Bright field STEM of Starbon + 20% graphite showing a) graphite flakes in amorphous carbon and b) the stacking of graphite layers from the dashed box in (c). Reproduced from ref 52 with permission from the Royal Society of Chemistry. <sup>52</sup> .....	19
Figure 2.1: a) Nitrogen, b) carbon, c) hydrogen and d) oxygen contents of Starbons, Algibons and Pecbons. ....	26
Figure 2.2: Classification of physisorption isotherms. <sup>8</sup> .....	28

Figure 2.3: Classification of hysteresis loops. <sup>8</sup> .....	30
Figure 2.4 Surface areas of Starbons, Algibons and Pecbons carbonised to various temperatures. ....	32
Figure 2.5: Micro- (t-plot), meso- (BJH) and total (t-plot + BJH) pore volumes of Starbons, Algibons and Pecbons carbonised to various temperatures. ....	32
Figure 2.6: a) Langmuir isotherms and b) pore size distribution plots for various 1) Starbons, 2) Algibons and 3) Pecbons. ....	34
Figure 2.7: SEM images of 1) A300, 2) A800 and 3) P300 at a) 30x and b) 25,000x magnification.....	36
Figure 2.8: Differential thermal analysis of Starbon, Algibon and Pecbon up to 800 °C. ....	37
Figure 3.1: The amount of each metal leached (%) into aqua regia from PCB with respect to time (h).....	45
Figure 3.2: The amount of each metal leached (%) into aqua regia from LCD with respect to time (h).....	45
Figure 3.3: Adsorption of Au <sup>3+</sup> from PCB waste solution (5 mL) by various Starbons, Algibons and some Pecbons (20 mg) after stirring for 24 h at 35 °C (*P800 not tested). ....	48
Figure 3.4: Adsorption of Au <sup>3+</sup> from PCB waste solution by various Starbons, Algibons and Pecbons (20 mg) after shaking for 2.5 h at room temperature. ....	49
Figure 3.5: TEM images at 135000x magnification 1) before gold adsorption and 2) after gold adsorption of a) A300 and b) A800. Scale bar = 100 nm. ....	51
Figure 3.6: The high-resolution XPS spectra of the gold region for gold on a) A300 and b) A800.....	52
Figure 3.7: Cyclic voltammetry of Au on a) A800 and b) P800 at 100 mV s <sup>-1</sup> . ....	57
Figure 3.8: Chronoamperometry of Au on A800 and P800 at 2 V. ....	57

Figure 3.9: a) High resolution XPS spectra of i) gold, ii) tin and iii) carbon for A800 before and after metal removal. b) TEM images of A800 before and after metal desorption at a magnification of 98000x.....	60
Figure 3.10: a) High resolution XPS spectra of i) gold, ii) tin and iii) carbon for P800 before and after metal removal. b) TEM images of P800 before and after metal desorption at a magnification of 98000x.....	61
Figure 3.11: The components of an LCD.....	62
Figure 3.12 Adsorption of $\text{In}^{3+}$ (0.35 mg) onto 10 mg A800 after stirring for 5 h at 35 °C in solutions of various pH values.....	65
Figure 3.13: Adsorption of $\text{In}^{3+}$ (0.35 mg) onto various Starbons, Algibons, Pecbons and activated carbon (10 mg) after shaking for 3 h at room temperature.....	66
Figure 3.14: Adsorption of $\text{In}^{3+}$ onto A800 at several time intervals at room temperature and at 50 °C.....	67
Figure 3.15: TEM images 1) at 135000x magnification before indium adsorption and 2) at 220000x magnification after indium adsorption of a) A300 and b) A800.....	70
Figure 3.16: XPS peaks for In on a) A300 and b) A800.....	72
Figure 3.17: AES peaks for In on a) A300 and b) A800.....	72
Figure 3.18: The heat flow of A300/In obtained by STA when heated up to 625 °C.	73
Figure 3.19: Showing the percentage desorption of indium after washing with aqueous solutions of different pH values. ....	74
Figure 3.20: The reusability of Pecbons for indium(III) adsorption.....	75
Figure 3.21: Adsorption of Sn (0.055 mg) and In (0.22mg) onto a range of Starbons (10 mg). ....	76
Figure 3.22: Complete removal of $\text{Sn}^{4+}$ by a) S300 and b) S450 from a standard aqueous solution of $\text{In}^{3+}$ and $\text{Sn}^{4+}$ after 3 repeats. ....	78

Figure 4.1: Chemical structure of a few MAAs found in Dulse. ....	83
Figure 4.2: HPLC chromatograms for extracted samples of a) usujirene and palythene, b) palythine, c) shinorine and d) porphyra .....	84
Figure 4.3: Labelled Dulse extract HPLC chromatogram (provided by Unilever).....	85
Figure 4.4: HPLC chromatograms of Dulse crude extracts in water, obtained by extraction using 1) Unilever's method, 2) methanol Soxhlet and 3) ethanol Soxhlet, at a) 310 nm, 320 nm, 330 nm and 360 nm, and b) zoomed in at 360 nm.....	87
Figure 4.5: HPLC chromatogram of Nori crude extract in water, obtained by extraction using 1) Unilever's method and 2) methanol Soxhlet, at a) 310 nm, 320 nm, 330 nm and 360 nm, and b) zoomed at 360 nm. ....	88
Figure 4.6: Dulse extract dissolved in 6 different solvent mixtures as described in Table 10.2.....	89
Figure 4.7: HPLC chromatogram for the butanol:water solvent system containing Dulse extract, a) butanol phase and b) water phase.....	90
Figure 4.8: HPLC chromatograms of 1) Dulse crude extract in water, 2) Dulse extract after adsorption through S450 and 3) Dulse extract desorbed off S450 with methanol, at a) 310 nm, 320 nm, 330 nm and 360 nm, and b) zoomed in at 360 nm. .....	92
Figure 4.9: HPLC chromatogram of the extract used for large scale adsorption.....	93
Figure 4.10: HPLC chromatograms of solutions after the 4th a) adsorption and b) desorption.....	93
Figure 4.11: The in-flow a) adsorption and b) desorption of 1 sample of Nori solution repeatedly (1 - 6) passed through S450 to simulate a flow type system. ....	95
Figure 4.12: HPLC chromatograms of the desorbed phase a) after one run through the Starbon and b) after a second run through the Starbon.....	96
Figure 5.1: Chemical structure of D-glucosamine, the monomer of which chitosan is composed.....	103

Figure 5.2: Surface areas of <i>N</i> -Starbon materials carbonised to various temperatures. .....	107
Figure 5.3: Micro- (t-plot), meso- (BJH) and total (t-plot + BJH) pore volumes of <i>N</i> - Starbon materials carbonised to various temperatures.....	107
Figure 5.4: Langmuir isotherms for <i>N</i> -Starbons a) 3AA:1C, b) 2AA:1C, c) 1AA:1C, d) 1AA:1CpTSA, e) 1AA:1CpCSA and f) expanded chitosan.....	108
Figure 5.5: Pore distribution plots for <i>N</i> -Starbons a) 3AA:1C, b) 2AA:1C, c) 1AA:1C, d) 1AA:1CpTSA, e) 1AA:1CpCSA and f) expanded chitosan.....	109
Figure 5.6: a) BET surface area and b) t-plot and BJH pore volumes of expanded alginic acid, chitosan and <i>N</i> -Starbons all carbonised to 600 °C, when fresh and after some amount of time. ....	110
Figure 5.7: a) Langmuir isotherm and b) pore size distribution of expanded i) alginic acid, ii) chitosan, iii) <i>N</i> -Starbon made with pTSA and iv) <i>N</i> -Starbon made with pCSA when fresh and after some amount of time. ....	111
Figure 5.8: The SEM images of 2AA:1C at a) high magnification and b) low magnification carbonised to 300 °C.....	112
Figure 5.9: The SEM images of 2AA:1C at a) high magnification and b) low magnification carbonised to 450 °C.....	113
Figure 5.10: The SEM images of 2AA:1C at a) high magnification and b) low magnification carbonised to 600 °C.....	113
Figure 5.11: Showing the nitrogen content in the range of <i>N</i> -Starbon materials.....	115
Figure 5.12: Showing the carbon content in the range of <i>N</i> -Starbon materials. ....	115
Figure 5.13: Showing the assumed oxygen content in the range of <i>N</i> -Starbon materials. .....	115
Figure 5.14: Showing the DTG plot for chitosan and <i>N</i> -Starbon 2:1 as they are carbonised from room temperature to 600 °C at 10 °C min <sup>-1</sup> . ....	116

Figure 5.15: Showing the gas-phase 3D DRIFT spectrum recorded during the thermal decomposition of chitosan up to 800 °C at 10 °C min <sup>-1</sup> .....	118
Figure 5.16: Showing the gas-phase 3D DRIFT spectrum recorded during the thermal decomposition of <i>N</i> -Starbon 2:1 up to 600 °C at 10 °C min <sup>-1</sup> . ....	118
Figure 5.17: Showing the gas-phase DRIFT spectra at the major decomposition temperatures for chitosan and <i>N</i> -Starbon.....	119
Figure 5.18: Showing the gas-phase DRIFT spectra at 100 °C for chitosan and <i>N</i> -Starbon. ....	119
Figure 5.19: Showing the IR spectra of the <i>N</i> -Starbon starting materials: alginic acid and chitosan.....	120
Figure 5.20: Showing the IR spectra of the <i>N</i> -Starbon materials pre-carbonisation with different ratios of alginic acid : chitosan (3:1, 2:1).....	121
Figure 5.21: Showing the IR spectra of the <i>N</i> -Starbons (alginic acid : chitosan; 3:1 and 2:1 carbonised to 300 °C and 600 °C.....	122
Figure 5.22: Showing the DRIFT spectrum for <i>N</i> -Starbon (alginic acid : chitosan; 2:1) materials carbonised to 300 °C, 450 °C and 600 °C with and without indium adsorbed to the surface.....	124
Figure 5.23: C1s region of the XPS spectra of 3:1 <i>N</i> -Starbons carbonised as follows: a) pre-carbonisation, b) 300 °C and c) 600 °C.....	126
Figure 5.24: N1s region of the XPS spectra of 3:1 <i>N</i> -Starbon carbonised as follows: a) pre-carbonisation, b) 300 °C and c) 600 °C. ....	127
Figure 5.25: C1s region of the XPS spectra for 2:1 <i>N</i> -Starbon carbonised as follows: a) pre-carbonisation, b) 300 °C, c) 450 °C and d) 600 °C. ....	128
Figure 5.26: N1s region of the XPS spectra for 2:1 <i>N</i> -Starbon carbonised as follows: a) pre-carbonisation, b) 300 °C, c) 450 °C and d) 600 °C. ....	129

Figure 6.1: Examples of how a gradient can be taken from GCD plots of <i>N</i> -Starbons (600 °C) coated on carbon cloth analysed at a) 2 mA and b) 10 mA. ....	138
Figure 6.2: Galvanostatic charge/discharge of an <i>N</i> -Starbon (600 °C) 1) coated carbon cloth and 2) monolith at a) 2 mA, b) 10 mA, c) 25 mA and d) 50 mA.....	141
Figure 6.3: Galvanostatic charge/discharge of an <i>N</i> -Starbon (800 °C) 1) coated carbon cloth and 2) monolith at a) 2 mA, b) 10 mA, c) 25 mA and d) 50 mA.....	141
Figure 6.4: Galvanostatic charge/discharge of an <i>N</i> -Starbon (ScCO <sub>2</sub> dried, 800 °C) monolith having undergone 1) standard carbonisation and 2) carbonisation with a prolonged (2 h) hold at 800 °C, a) 2 mA, b) 10 mA, c) 25 mA and d) 50 mA..	142
Figure 6.5: Galvanostatic charge/discharge of a blank 2x1cm section of carbon cloth at 2 mA over 5 cycles.....	143
Figure 6.6: Galvanostatic charge/discharge of an <i>N</i> -Starbon (ScCO <sub>2</sub> dried, 800 °C + 2 h hold) monolith at 2 mA over 5 cycles.....	144
Figure 6.7: Capacitance stability of an <i>N</i> -Starbon (ScCO <sub>2</sub> dried, 800 °C + 2 h hold) monolith at 25 mA over 320 cycles, as measured by galvanostatic charge/discharge.....	144
Figure 6.8: The cyclic voltammogram of an <i>N</i> -Starbon (600 °C) a) coated carbon cloth and b) monolith. ....	147
Figure 6.9: The cyclic voltammogram of an <i>N</i> -Starbon (800 °C) a) coated carbon cloth and b) monolith. ....	147
Figure 6.10: The cyclic voltammograms of scCO <sub>2</sub> dried <i>N</i> -Starbon (800 °C) monoliths prepared a) normally, with post-drying pTSA doping and b) post-drying pTSA doping + 2 h hold at 800 °C. ....	147
Figure 6.11: The cyclic voltammograms of carbon cloths coated with various materials carbonised to 800 °C: a) regular Starbons and b) <i>N</i> -Starbon containing 25% chitosan. ....	147

Figure 6.12: CV of N-Starbon 800 °C monolith at 2 mA, 10 mA, 25 mA and 50 mA. .....	149
Figure 6.13: CV of N-Starbon 800 °C coated carbon cloth at 2 mA, 10 mA, 25 mA and 50 mA.....	149
Figure 7.1: The 1) heat flow data and 2) weight change over time for A300 (a), N300 (b) and C300 (c) for 5 cycles of CO <sub>2</sub> adsorption and desorption.....	158
Figure 7.2: The 1) heat flow data and 2) weight change over time for A800 (a), N800 (b) and C600 (c) for 5 cycles of CO <sub>2</sub> adsorption and desorption.....	159
Figure 7.3: The a) heat flow data and b) weight change over time for activated carbon for 5 cycles of CO <sub>2</sub> adsorption and desorption. ....	159
Figure 9.1: Soxhlet extraction set-up .....	186
Figure 9.2: The appearance of the N-Starbon throughout monolith formation.....	190
Figure 9.3: Showing the set-up used for electrochemical experiments. ....	191
Figure A.1: HPLC chromatogram for the Dulse extract in solvent systems 1) 9, 2) 13, 3) 17, 4) 21 and 5) 28 as described in Table 10.10, a) upper (less polar) phase and b) lower (more polar) phase.....	197
Figure A.2: HPLC chromatograms of the fourth repeat of Starbon screening for isolation of usujirene from Dulse extracts using 1) S300 and 2) S800, showing a) adsorption in water and b) desorption in methanol at 310 nm, 320 nm, 330 nm and 360 nm on the left, and zoomed in at 360 nm on the right.....	198
Figure A.3: HPLC chromatograms of the fourth repeat of Starbon screening for isolation of usujirene from Dulse extracts using 1) A300, 2) A450 and 3) A800, showing a) adsorption in water and b) desorption in methanol at 310 nm, 320 nm, 330 nm and 360 nm on the left, and zoomed in at 360 nm on the right.....	199
Figure A.4: HPLC chromatograms of first three repeats (1, 2, 3) for purification of usujirene from Nori extract using S450, showing a) adsorption in water and b) desorption in methanol at 310 nm, 320 nm, 330 nm and 360 nm.....	200

# List of Tables

Table 2.1: Comparing C:O ratios calculated from CHN bulk elemental analysis of Starbons, Algibons and Pecbons carbonised to a range of temperatures, prepared in this work and published in the literature. <sup>26, 27, 53</sup> .....	27
Table 3.1: Concentrations (ppb) of various metals present in PCB and LCD leachate. ....	44
Table 3.2: A summary of the binding energies (eV) for the XPS peaks for gold on A300 and A800. ....	52
Table 3.3: The percentage composition of total gold after adsorption onto both A300 and A800, calculated from XPS spectra and ICP-MS. ....	54
Table 3.4: The percentage metal composition in A800 and P800 before gold removal as analysed by ICP-MS and XPS. ....	59
Table 3.5: The percentage gold composition and subsequent percentage of removed gold in A800 and P800 after gold removal as analysed by ICP-MS and XPS. ...	59
Table 3.6: The percentage tin composition and subsequent percentage of removed tin in A800 and P800 after gold removal as analysed by ICP-MS and XPS. ....	59
Table 3.7: The adsorption capacities of all Pecbons for indium(III). ....	68
Table 3.8: A comparison of indium(III) adsorption capacities of various adsorbents in the literature. ....	69
Table 3.9: The binding energies (eV) for the XPS peaks of In on A300 and A800. ...	72
Table 3.10: The kinetic energies (eV) for the AES peaks of In on A300 and A800. ..	72
Table 3.11: Showing the percentage composition of total indium after adsorption of each metal onto both A300 and A800, calculated from XPS spectra. ....	73

Table 4.1: Comparison of HPLC peak times for various MAAs obtained in this work and by Unilever.....	85
Table 4.2: Summary of the yields obtained from each extraction attempt. ....	86
Table 5.1: Showing the nitrile peaks ( $\text{cm}^{-1}$ ) along with their peak shifts ( $\text{cm}^{-1}$ ) caused by the presence of indium on the surface of the <i>N</i> -Starbon (alginic acid : chitosan; 2:1) materials carbonised to 300 °C, 450 °C and 600 °C.....	124
Table 5.2: A summary of the N1s peaks obtained by XPS of <i>N</i> -Starbons 3:1 and 2:1. ....	130
Table 5.3: A summary of the relative concentrations (%) of nitrogen present in each functional group according to XPS data. ....	130
Table 6.1: The capacitance ( $\text{F g}^{-1}$ ) measurements calculated from galvanostatic charge/discharge plots where materials were dried by either freeze-drying, vacuum oven drying or $\text{scCO}_2$ drying.....	142
Table 6.2: The capacitance measurements calculated from CV plots. †.....	148
Table 6.3: A comparison of the capacitance of <i>N</i> -Starbons to other porous carbons in the literature. ....	150
Table 7.1: Calculated $\text{CO}_2$ adsorption data for a range of Starbons and activated carbon at atmospheric pressure, including their pore properties and nitrogen content..	160
Table 7.2: Calculated $\text{CO}_2$ adsorption data for a range of Starbons and activated carbon at 10 bar, including their pore properties and nitrogen content. ....	162
Table 9.1: Showing the furnace carbonisation steps.....	175
Table 9.2: The solvent mixtures selected for simulating CCC of MAAs from Dulse extract.....	187
Table 9.3: The parameters entered into the EC-Lab® software for galvanostatic charge/discharge experiments of carbon cloth samples. ....	192

Table 9.4: The parameters entered into the EC-Lab® software for galvanostatic charge/discharge experiments of monoliths samples. ....	192
Table 9.5: The parameters entered into the EC-Lab® software for cyclic voltammetry of carbon cloth samples.....	193
Table 9.6: The parameters entered into the EC-Lab® software for cyclic voltammetry of monolith samples. ....	193
Table B.1: Elemental analysis determined by XPS of <i>N</i> -Starbons (alginic acid : chitosan; 2:1) prepared at different carbonisation temperatures. ....	203



# Acknowledgements

My first and most important thank you goes to Prof. James Clark for giving me the freedom to explore my own ideas and solve my own problems, whilst also providing much-needed valuable advice. You have always encouraged me to be an independent researcher and for that I am forever grateful. It has been a privilege to be your student and to learn from you.

I would like to thank Dr Avtar Matharu for always supporting me, supervising my progress and being there to answer my questions whenever I needed. Thank you also for the endless supply of laptops to break apart! This was good stress relief.

A huge thank you also goes to Tom and Rob for patiently being my go-to people whenever I needed help i.e. was completely lost. I am so grateful for the endless guidance, entertainment, encouragement and the numerous opportunities that you both trusted me with.

A special thanks goes to Vitaliy and Paul. Your extensive knowledge never ceases to amaze me! And no matter how busy you both were, you were always happy to find the time to help me. Thank you, Alison, for sorting out all things always. Thank you Duncan, Mina, Andrea, Maria, Amanda and Hannah for your help and advice over the years. I am also grateful to the Endeavour Scholarship for funding my PhD.

My PhD would have been a lot less fun if I did not make such good friends along the way: Tom, Dina, Jonny, Marc, Rob, Yann, Javier, Roxana, James S and Anna. It's been so much fun to work with you all. You have made York feel like home to me. You have made me laugh on the most boring of lab days and the most (un)forgettable nights out. Thank you also to my new friend Briannah for all the random adventures.

Finally, I would like to thank my whole family, especially my parents, for their immense love and support throughout not only my PhD, but my whole education. You have been there to encourage me at all times, no matter my mood. I am so happy to be where I am today, and you have both made this so easy for me to achieve.



# Declaration

I declare that this thesis is a presentation of original work and I am the sole author. This work has not previously been presented for an award at this, or any other, University. All sources are acknowledged as references. Some of the results presented in this thesis were obtained in collaboration with other workers who are fully acknowledged in the text. All other results are the work of the author. Part of the work presented in this thesis was published in the following publication:

J. Attard, R. Milesco, V. Budarin, A. S. Matharu and J. H. Clark, *Chem. Commun.*, 2018, 54, 686.



Jennifer Attard

2018

<b>Collaborator</b>	<b>Work conducted</b>
Unilever	Nori extraction (Chapter 4)
Prof. Ying Li	Acetylene hydrochlorination (Chapter 8)



# Chapter 1

## Introduction



## 1.1 Circular Economy

“Modern economics lacks what we call an *existence theorem*: a guarantee that any economic optimum is associated with a stable ecological equilibrium.” - Pearce and Turner.<sup>1</sup>

A raw material may be defined as a feedstock of unprocessed material that is utilised to generate a host of different goods or energy.<sup>2</sup> Raw materials are continuously extracted from the earth and undergo a vast array of manufacturing processes to create all the products that people use throughout their lives. Their production and retailing builds industries that the economy has grown to depend on. Once a product has been used to its supposed full extent, it gets disposed of. From this point on, all the material used to make up the product is viewed as waste. Apart from the constituent material being lost forever, it also likely pollutes the area in which it is disposed of. This model is known as a linear economy *i.e.* a ‘take-make-consume-throw away’ approach to resources.<sup>1</sup>

There are alternatives to this model. Once a product has been used, it does not necessarily need to be disposed of. If products are designed well, they may, for example, be reused several times. They could also be designed to biodegrade at their end-of-life so that they do not cause pollution once discarded. Alternatively, the materials that make up the products may be recovered and re-entered into the manufacturing process, for use in the fabrication of new products. This is known as recycling.<sup>1</sup> These methods all prevent the need to extract new materials and dispose of ‘used’ materials, keeping everything in a continuous cycle of use and thus creating what is known as a circular economy; “a closed loop material flow in the whole economic system”.<sup>1</sup> A diagrammatic representation of linear and circular economies is shown in Figure 1.1.

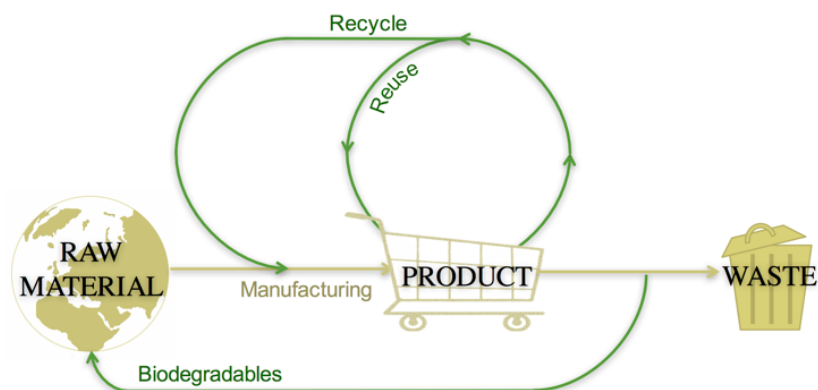


Figure 1.1: Comparison of linear and circular economies.

The need to establish and sustain a symbiotic relationship between industry and the environment has only been realised in recent decades.<sup>3</sup> Circularity is not the responsibility of any one entity. Having said that, there are some entities that bear more responsibility than others simply because of the amplified potential impact of their behaviour. An individual can change their lifestyle to one that is environmentally benign for example, by living a zero-waste lifestyle. As positive as this is, it does not compare to the volumes of waste (and other environmental damage) that a manufacturing company can prevent.

Encouraging people, especially those in high economic positions, to change their ways is possible through either education or law, or a mixture of the two. Education is key to ensure that future generations truly appreciate the fundamental necessity of a circular economy for our existence. If change is to be brought about sooner, however, it is important that governments and global organisations design and enforce more laws that immediately prevent any waste of resources. The time-frame available for us to effectively stop environmental destruction and leave hope to reverse the effects of humankind's behaviour is closing.<sup>4</sup>

Apart from the ever-increasing pollution prevention regulations that industry must follow, resource scarcity means that costs will increase. This is, of course, while the resources are still available in the first place. These unavoidable challenges mean that the performance of an industry will ultimately depend on its ability to change. It is possible that the wait for real and meaningful change will be long, which may only come into effect on a global scale once the damage is too disturbing to ignore. At some point, people's daily lives will be unbearably inconvenienced.<sup>4</sup>

It is at moments like these that humanity tends to pull up its socks and focus on solving a problem. By this point, investment will undoubtedly be abundant for technological development and thus allow for a complete shift in our economic system; away from a linear economy and towards a circular economy.

## 1.2 Green Chemistry

Green chemistry is a relatively new way of doing chemistry, where the aim is to design means by which chemistry can be carried out in a more sustainable way than what is currently the norm.<sup>5,6</sup> The 12 Principles of Green Chemistry have been established as a guide to the general aims of green chemistry and how they can be achieved.<sup>7</sup> They are as follows;

1. Waste prevention
2. Atom economy
3. Less hazardous chemical syntheses
4. Designing safer chemicals and products
5. Use of safer solvents and reaction conditions
6. Increase in energy efficiency
7. Use of renewable feedstocks
8. Avoiding chemical derivatives
9. Use of catalysts, not stoichiometric reagents
10. Designing degradable chemicals and products
11. Analysis in real time for pollution prevention
12. Minimise the potential for accidents

Figure 1.2: The 12 Principles of Green Chemistry.<sup>7</sup>

Circular economy encompasses the majority of these principles. The work in this thesis has been designed so as to apply the Principles of Green Chemistry wherever possible. Part I of this project exhibits ways in which renewable mesoporous materials, Starbons, can contribute towards a circular economy. With regards to WEEE (Chapter 3), recovering and recycling indium and gold will prevent waste (Principle 1) as these elements will be redirected from landfills to new products and applications, turning them into a renewable feedstock (Principle 7). Chapter 4 discusses using Starbons to isolate a mycosporine-like amino acid from seaweed for use as a potential natural sunscreen. This could replace the current products in the market today, thus avoiding production of synthetic compounds and derivatives (Principles 3 and 8), using natural and safe products (Principle 4) and using biodegradable products (Principle 10).

Part II of this project exhibits ways in which modified Starbon materials, nitrogen-doped Starbon materials (*N*-Starbons), put several of the 12 Principles of Green Chemistry into practice. Chapter 5 discusses how chitosan from shrimp shell waste can be used as the nitrogen dopant for *N*-Starbons, thus obtaining value from waste (Principle 1). In Chapter 6, capacitance of *N*-Starbons was tested, to determine whether it can be used as a bio-based capacitor made from two renewable resources; algae and shrimp shell waste (Principle 7). Being metal-free, it is also safer than most energy storage materials that currently exist (Principle 4).

### 1.3 Mesoporous materials

Porosity provides materials with a high surface area, a property that allows for their use as catalyst supports and adsorbents, amongst other applications. IUPAC divides porous materials into three classes based on their pore diameters; microporous (< 2 nm), mesoporous (2-50 nm) and macroporous (> 50 nm).<sup>8</sup> A diagrammatic representation of the organisation of different pore sizes is shown in Figure 1.3. Microporous materials, having the smallest pores, have limited applications, such as the catalysis of only smaller molecules.<sup>9</sup> Additionally due to the pores being so small, surface interactions with adsorbed species is high, meaning that desorption is often unlikely and therefore selective adsorption is near impossible. Macroporous materials on the other hand tend to be too large for most applications, resulting in them not being very specific. Moreover, the surface area of macroporous materials will be inherently low. Macroporous materials have, however, found uses in biotechnological and biomedical areas and as capacitors.<sup>10, 11</sup>

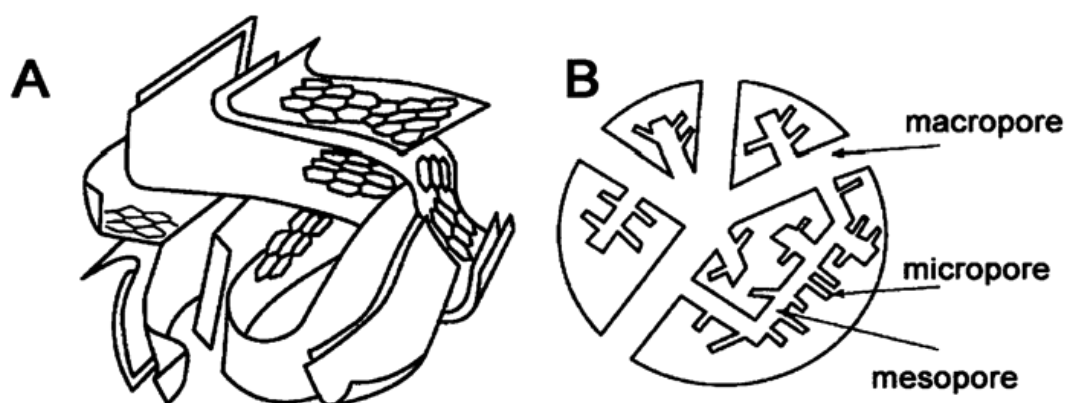


Figure 1.3: Diagrammatic representation of micro-, meso- and macropores in a) 3D and b) 2D. Reproduced from ref 12 with permission from the Royal Society of Chemistry.<sup>12</sup>

Mesoporous materials have the right balance between having pores which are small enough for selectivity and large enough to be used for numerous applications. One of the earliest mesoporous materials to become widely studied was MCM-41 (Mobil Composition of Matter No. 41), due to its easily controlled narrow pore-size distribution and hexagonally ordered pore arrangement.<sup>13</sup> These materials are aluminosilicates prepared through calcination of their liquid-crystal templated gels.<sup>14</sup> Another class of materials comparable to MCM-41 are the SBA (Santa Barbara Amorphous) class, which achieved 3D hexagonal order and were the first to be characterised in 3D.<sup>9</sup> One such example, is SBA-15, a material found to have micropores connecting the mesopores. This enables it to be used as a template for some of the most easily modifiable carbon-based mesoporous materials, where the carbon fills previously surfactant-filled space.<sup>9</sup>

### 1.3.1 Carbonaceous mesoporous materials

Carbons are used today for a vast number of applications. This is not only due to their ample availability. Carbons are highly stable and have exhibited electrical and thermal conductivity, amongst other properties. Catalytic supports, sorbents for separation, batteries, fuel cells and supercapacitors are only a few of their uses.<sup>15</sup> Structure and functionality modifications continuously create opportunities for improved properties and new applications. Activated carbon is a well-known porous carbon, synthesised through pyrolysis and activation of organic matter such as fruit shells or coal.<sup>16</sup> The simple and large-scale production of activated carbon has often made it the obvious choice for adsorption and supported catalysis.<sup>17</sup> Having said this, activated carbons tend to have a generally undesirable broad range of pores, from micro- to mesopores. Often, a particular pore size is favourable for a particular application. This can make activated carbons inefficient and unspecific. Hard and soft templating methods have been developed to overcome these limitations and produce materials with a controlled pore size in the mesopore range.<sup>18, 19</sup> Hard templating uses nanostructured templates, or moulds, into which the carbon is simply impregnated. Carbonisation then allows for the removal of the template. Soft templating on the other hand occurs by means of the self-assembly of organic molecules, followed by carbonisation. A key difference between the two templating methods is that the soft template interacts chemically with the precursor and this impacts the final pore structure. Conversely there are no such interactions with hard templating.<sup>18, 19</sup>

## 1.3.2 Starbon

Starbons are a patented group of novel nanostructured mesoporous carbonaceous materials derived from biomass, developed at the Green Chemistry Centre of Excellence (GCCE) at the University of York.<sup>20</sup> They are prepared by processing various polysaccharides, namely starch, alginic acid and pectin. Starbons have the benefit of being tuneable, allowing for the formation of materials with pore diameters between 2 - 50 nm, as well as ranging between being hydrophobic and hydrophilic. The diverse properties are attained through the use of different starting materials as well as by carbonising their aerogel forms to different temperatures. The ability to tune Starbons has led to a vast range of applications which continues to grow, including heterogenous catalysis, chromatography, purification and metal recovery.<sup>12, 21-23</sup> Part I of this thesis focuses on a further two applications of Starbons: e-waste recycling and separation of mycosporine-like amino acids.

### 1.3.2.1 Development of Starbon materials

Polysaccharides were found to be suitable starting materials due to their ability to form gels in water. The gelation process involves adding the polysaccharide granules to water, causing them to swell and subsequently open up and dissolve. Following this, the polysaccharide chains are allowed to reorganise themselves into a 3D network in a process known as retrogradation. This 3D network is what eventually yields porosity in the final product.

Starch, alginic acid and pectin are polysaccharides and are therefore all composed of monosaccharide units. Starch is made up of two glucose polymers, amylose and amylopectin. Amylose is a straight chain polymer composed of  $\alpha$ -D-glucose units linked by  $\alpha$ -(1 $\rightarrow$ 4) glycosidic bonds. Amylopectin is a highly branched glucose polymer formed by the introduction of  $\alpha$ -(1 $\rightarrow$ 6) glycosidic bonds between the amylose chains. Sources of starch include corn, potato and wheat.<sup>24</sup> Alginic acid can be obtained from brown algae, a type of seaweed.<sup>25</sup> It is made up of  $\beta$ -D-mannuronate and  $\alpha$ -L-guluronate connected through  $\alpha$ -(1 $\rightarrow$ 4) glycosidic linkages. The sub-units in pectin are also linked by  $\alpha$ -(1 $\rightarrow$ 4) glycosidic bonds. The monomers that make it up are mainly D-galaturonic acid units, although other sugars are also present. Pectin can be extracted from waste citrus peel.<sup>24</sup> Structures of the monosaccharides are shown in Figure 1.4.

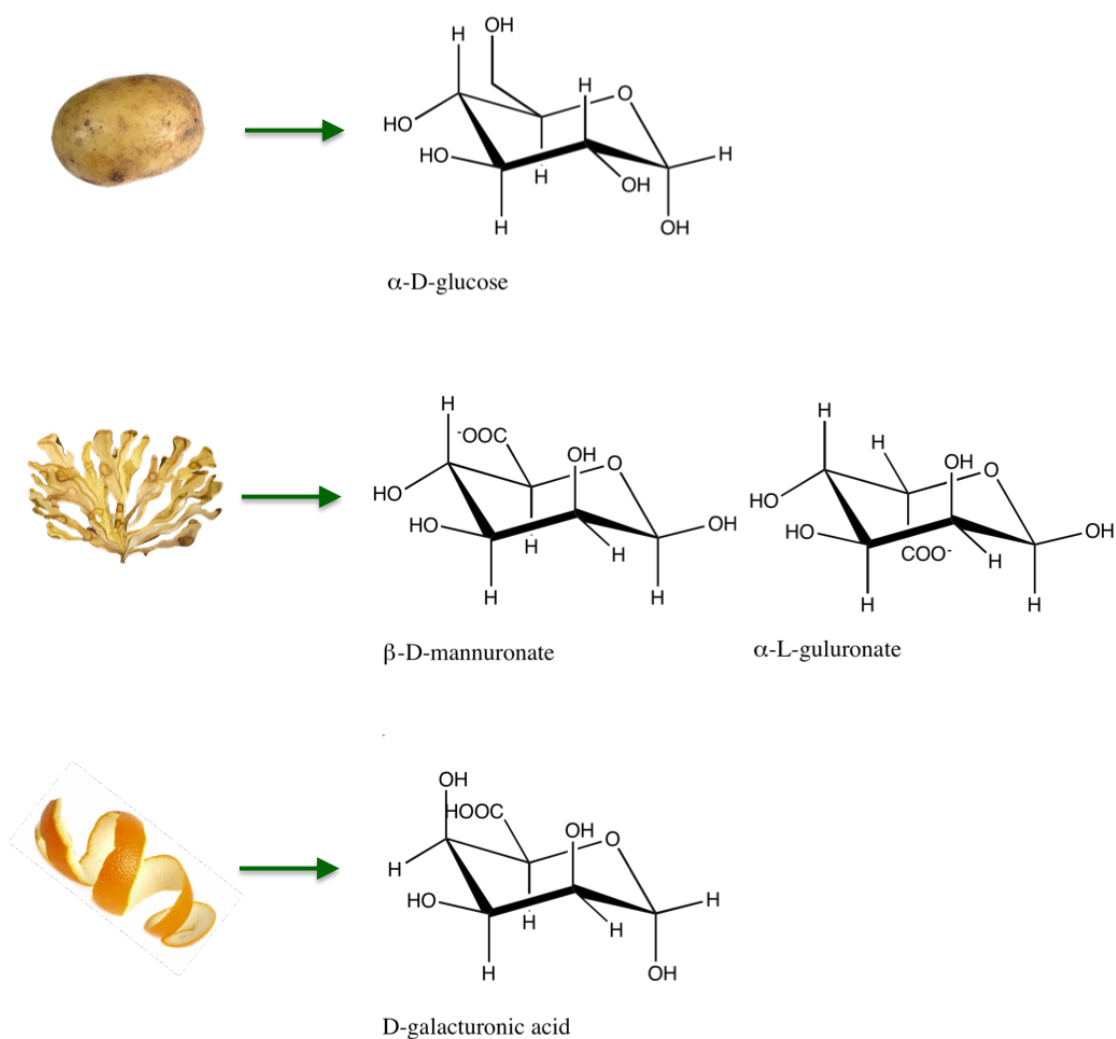


Figure 1.4: The monomers that make up the starting materials for the various Starbons. For starch, the pore dimensions are similar to those of amylose (poly- $\alpha$ (1-4)-D-glucopyranose) helices, which suggests that it is the helical structure that brings about the desired pore structure. This may also be the case for alginic acid and pectin as they too have helical forms.<sup>26</sup> This corroborates with the fact that larger dimensions of the helices formed by poly- $\beta$ -D-mannuronic acid give higher mesoporosity in Albigons compared to Starbons, which show some microporosity.<sup>27</sup>

Once the structures have set, the gel can be dried. In order to retain the delicate structure that has developed in the gel, it is imperative that harsh drying methods are avoided in this crucial step. When Starbons were first invented, the drying method chosen was vacuum oven drying. The high surface tension at the water-gel interface however made it impossible to retain the pore structure on evaporation. Thus, a pre-drying solvent-

exchange step was employed. Water was first exchanged to ethanol and then to acetone, which could then be dried off without collapsing the pores.<sup>22</sup>

Vacuum oven drying however is not the gentlest of drying techniques, and although it was suitable for starch, the pore quality of Algibons was insufficient, thus supercritical CO<sub>2</sub> was later used to slowly extract and displace the solvent inside the gel.<sup>27</sup>

With regards to sustainability, or “greenness” of the process, this technique was already an improvement on common methods used to achieve mesoporosity, such as templating, however there was still room for improvement. Solvent exchange requires a large volume of both ethanol and acetone. The most recent and most sustainable method of drying Starbons is the freeze-drying technique. As water has a high surface tension, 25 wt% tert-butanol (TBA) is added to aid the sublimation of water and thus, the solvent exchange step is eliminated. Freeze-drying successfully gave impressive mesoporosity with all three polysaccharides.<sup>28</sup>

The product obtained from drying is a mesoporous aerogel, which only shows surface areas of around 100 m<sup>2</sup> g<sup>-1</sup>, is thermally unstable above 200 °C and also chemically unstable. Carbonisation not only improves surface area and stability (and thus also reusability), but also alters the surface functionality of the material, allowing for the Starbon surface to be highly tuneable. Carbonisation commonly ranges between 300 °C, where a highly oxidised surface is still present, to 800 °C where a much more chemically reduced and graphitic-like surface is achieved.<sup>26</sup> The overall process is summarised diagrammatically in Figure 1.5.

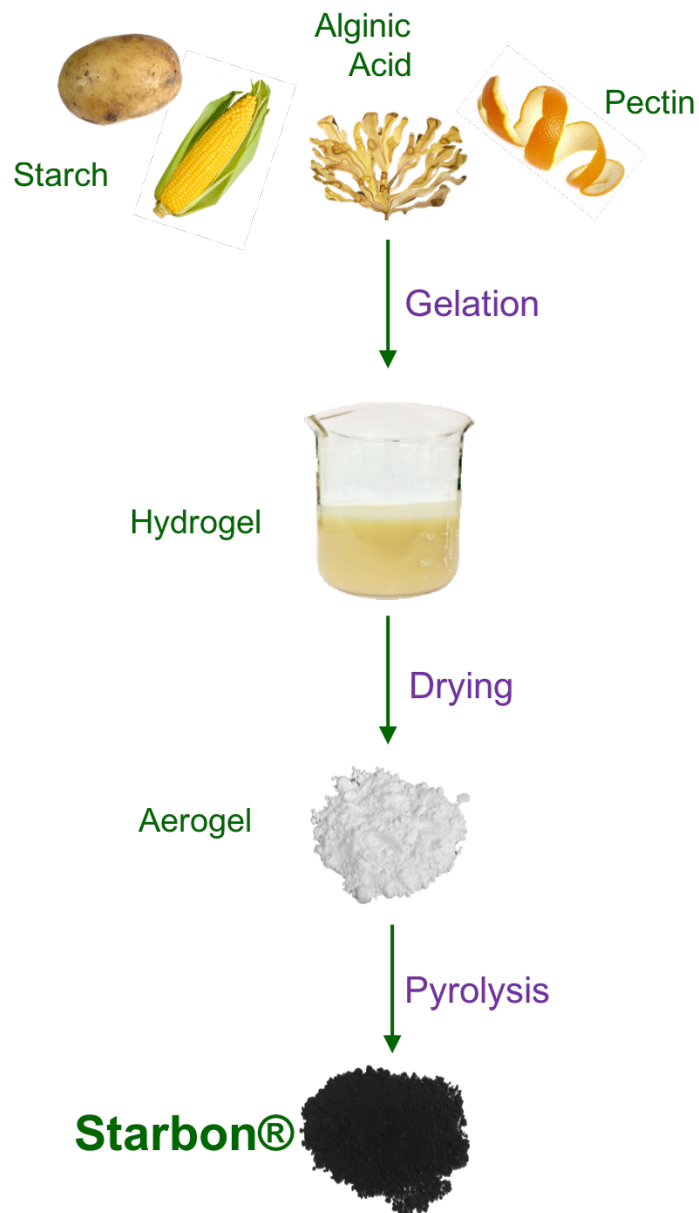


Figure 1.5: General Starbon preparation phases.

### 1.3.2.2 Applications of Starbon materials

In the development leading up to the final Starbon product, an intermediate material, expanded corn starch (ECS), was first studied. ECS is the aerogel obtained before carbonisation and was produced with surface areas of over  $150 \text{ m}^2 \text{ g}^{-1}$  and pore volumes of over  $0.5 \text{ cm}^3 \text{ g}^{-1}$ .<sup>29</sup> A number of applications were found for this material as it was the first time that starch, the second-most abundant polysaccharide, was made to have a large surface-area and pore volume.<sup>29</sup>

### 1.3.2.2.1 Pre-carbonisation

In 2002, Doi *et al.* published the first paper on ECS.<sup>29</sup> The high functionality of ECS makes surface modification possible. ECS could therefore be derivatised to both solid acids and bases for heterogenous catalysis. Sulfonic acid modified ESC showed to be an active catalyst in the reaction between 2-methylfuran and acetone to form the corresponding bisfurylalkane. The material also showed good chemical stability in a number of different environments as well as thermal stability up to 200 °C. Basic ECS was prepared through the introduction of primary aminoalkyl, tertiary amino alkyl or quaternary ammonium hydroxide functions and showed to be active catalysts in the Knoevenagel and Michael reactions.<sup>29</sup>

Research on ECS was continued by Milkowski *et al.* through chemical modification at the solvent exchange stage of ECS production with glycidyl methacrylate and epichlorohydrin, and subsequent monomer grafting with styrene,  $\alpha$ -methyl styrene, indene and methyl acrylate. The composites showed good thermal stability and porosity and thus a more environmentally friendly alternative to similar synthetic materials.<sup>30</sup>

Heterogenous catalysis using ECS was next attempted by Gronnow *et al.*<sup>31</sup> C – C bond formation reactions: Suzuki, Heck and Sonogashira, were all successful using palladium supported onto ECS as a heterogenous catalyst. Palladium was chelated onto the surface of ECS using Schiff bases (Figure 1.6). The resultant palladium catalyst on ECS, termed StarCat, was used to replace phosphine ligands in C – C bond formation reactions due to the number of drawbacks of using phosphine ligands. These include them being air and moisture sensitive (resulting in irreversible oxidation), difficult to make and toxic. ECS, being a biomaterial, is renewable, cheap, biodegradable and shows low toxicity. Furthermore, the catalyst was stable, performing well under microwave irradiation, and palladium was found to be easily recovered from the spent catalyst.<sup>31</sup>

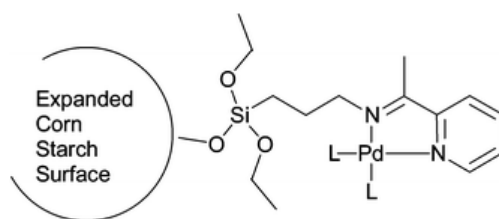


Figure 1.6: The proposed structure of StarCat. Reproduced from ref 31 with permission from the Royal Society of Chemistry.<sup>31</sup>

Budarin *et al.* followed up this work replacing the chelated palladium with simpler palladium nanoparticles.<sup>32</sup> Major drawbacks of forming nanoparticles usually include the use of harsh reagents such as NaBH<sub>4</sub>, which is not very 'green' and is difficult to control. This is avoided when using ECS however as the palladium is simply reduced by the solvent or by the material. Additionally, it was shown that nanoparticle size can easily be controlled in the ECS material by selecting the right solvent. A good dispersion of nanoparticles was achieved, and high conversions were again shown for three C – C bond formation reactions as before: Suzuki, Heck and Sonogashira, with the material maintaining high catalytic activity even after four uses.<sup>32</sup>

A different application of nanoparticles supported on ECS was tested by White *et al.*<sup>33</sup> This time, silver nanoparticles in the size range of 5 – 25 nm were prepared within ECS mesoporous for their antimicrobial properties. Prior to this work, native cellulose, starch and chitosan were used, however, without expanding the material's structure, the high functionality of the material remained unexploited. Thus, the nanoparticle loading was significantly reduced and there was no control over nanoparticle size through pore size control. With ECS, testing against two model bacteria, outstanding antimicrobial properties were achieved.<sup>33</sup>

As described earlier, porous materials are highly suitable for separating mixtures. In 2005, Budarin *et al.* therefore studied using the ECS as a bio-replacement for silica in column chromatography.<sup>34</sup> Although silica has a much greater surface area than ECS, it was found that silica has a larger proportion of its pores in the micropore range. Micropores are detrimental to chromatography because of the irreversible binding of species resulting from the large surface energy incurred in such small pores. Additionally, the pores may be too small to separate larger compounds. ECS as the stationary phase of column chromatography was tested in the separation of a mixture of ferrocene, acetylferrocene and diacetyl-ferrocene. Comparisons were made with native starch and silica, where both showed little to no separation. ECS was successful in achieving a well-defined separation of all three compounds, additionally showing high reusability. Separation was also successful for other mixtures of compounds including lipids, functionalised aromatics, natural pigments and pharmaceuticals, demonstrating the versatility of the material. Finally, a lower mass of material is required due to its expanded structure and therefore low density.<sup>34</sup>

### 1.3.2.2.2 Post-carbonisation

Given the promising results described in the previous section, research on ECS continued, and ECS was eventually carbonised under vacuum to make Starbon materials in 2006.<sup>23</sup> This was novel in that it was a template-free approach to producing mesoporous carbons. At the time, other mesoporous activated carbons could only be produced at high temperatures and using caustic substances and would result in a graphitic structure. The process required to make Starbons however avoids such steps and therefore Starbons can be prepared at any temperature (usually up to 800 °C). This means that the materials can be tuned depending on the whether an amorphous or graphitic carbon is needed (or anything in between), whilst simultaneously tuning the surface of the materials depending on the degree of hydrophobicity and stability desired. This is depicted in Figure 1.7. Surface areas also increased with temperature, going from  $< 200 \text{ m}^2 \text{ g}^{-1}$  in ECS to  $> 500 \text{ m}^2 \text{ g}^{-1}$  with Starbon when carbonised to 700 °C.<sup>23</sup>

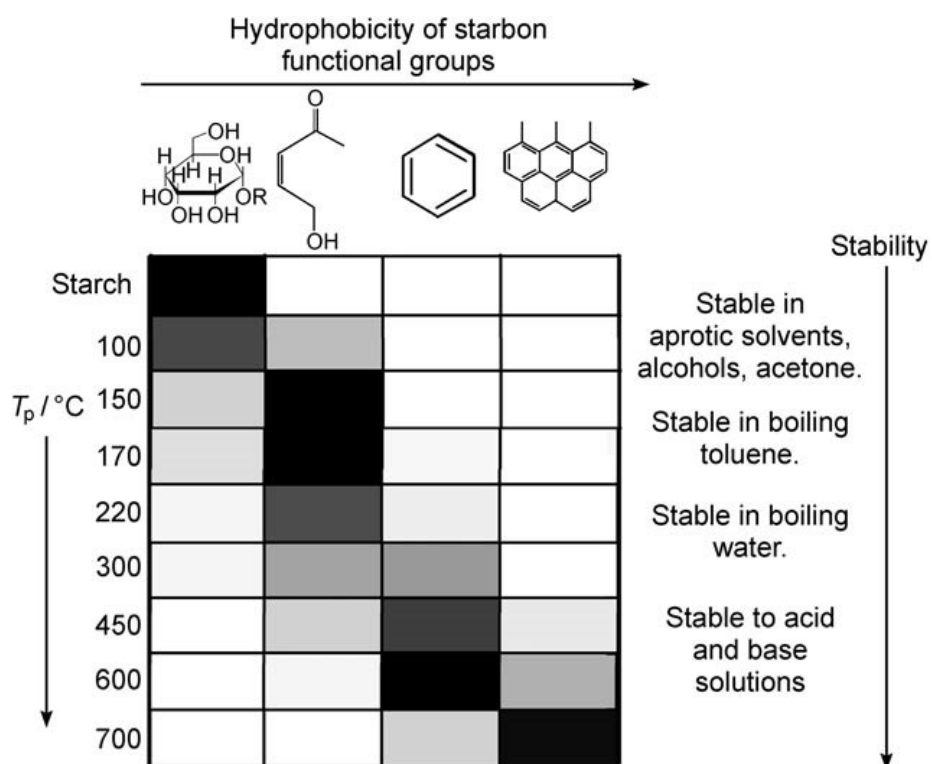


Figure 1.7: Effects of carbonisation temperature on the stability and surface functionality of Starbon materials. Reproduced from ref 23 with permission from the John Wiley and Sons.<sup>23</sup>

### 1.3.2.2.2.1 Catalysis

As was shown with ECS, the surface of Starbon materials was also modified for catalysis. Budarin *et al.* functionalised the surface with sulfonic acid groups to test the resulting solid acids in the esterification of diacids and found that Starbon performed between 5 and 10 times better than other commercial heterogenous catalysts.<sup>35</sup> The Starbon showed both improved conversion and also improved selectivity for the diester. Acylation of aromatic alcohols showed the same impressive performance, superior to zeolites, acidic Montmorillonite clay and mesoporous Al-MCM-41.<sup>35, 36</sup>

Budarin *et al.* later showed the applicability of the sulfonated Starbon acid catalyst in the aqueous esterification of succinic acid, a platform molecule.<sup>37</sup> The high activity was attributed to several factors; (i) the mesoporosity allows for good molecular diffusion, (ii) hydrophobicity boosts formation of hydrophobic esters and (iii) surface energy allows for strong attachments to the active sites.<sup>37</sup> This example shows the strong ability of Starbon materials to aid the shift from petroleum-based to biorefinery chemical production.<sup>37, 38</sup> Sulfonated Starbon also showed to be a highly active catalyst in the selective esterification of glycerol with acetic acid under microwave conditions.<sup>39</sup> The selectivity achieved by Luque *et al.* proved to be considerably higher than other catalysts reported in the literature. Similarly, Sulfonated Starbon exhibited unprecedented selectivity for the monoether in the etherification of glycerol with *tert*-butyl alcohol, again superior to other reported catalysts.<sup>39</sup>

With amides being such important functionalities in the pharmaceutical industry (and also several other industries), the sulfonated Starbons were tested for their catalytic activity in amide formation.<sup>40</sup> The formation of amides commercially involves stoichiometric quantities of toxic reagents and results in low atom economy. Low atom economies result in large amounts of waste. From an environmental perspective, the room for improvement in this field was great. Thus, the achievement in using sulfonated Starbons to catalyse several *N*-acylations with excellent yields and selectivities was significant.<sup>40</sup>

Furthermore, the sulfonated Starbon catalyst is an effective and environmentally friendly replacement for Lewis acid catalysts such as AlCl<sub>3</sub>, FeCl<sub>3</sub>, BF<sub>3</sub>, ZnCl<sub>2</sub>.<sup>41</sup> The catalyst performed better than other commercially available solid acids and supports in

both the acetylation of 5-acetyl methyl salicylate with acetic anhydride and the alkylation of phenol with cyclohexene.<sup>41</sup>

The successful palladium nanoparticles supported on ECS for C – C coupling reactions were later also supported on Starbon for oxidation of glycerol with hydrogen peroxide under microwave conditions.<sup>39</sup> This was the first report of such a reaction giving glycolic and oxalic acids as major products, retaining the same selectivity up to three reuses.<sup>39</sup>

Luque *et al.* prepared other nanoparticles on carbons: platinum, rhodium, ruthenium, and these, along with palladium were tested in the hydrogenation of succinic acid.<sup>42</sup> All supported nanoparticles were successfully prepared with a 5% loading retaining over 95% of their activity after 5 uses. Reactions were carried out in aqueous ethanol under mild reactions conditions, avoiding the harsh reaction conditions usually associated with hydrogenation reactions. High selectivity for 1,4-butanediol was observed with palladium, platinum and rhodium. 1,4-butanediol is a valuable chemical commonly used as a solvent and in the production of plastics. Additionally, with palladium and ruthenium, the reaction conditions could be optimised to improve selectivity for  $\gamma$ -butyrolactone, used as a solvent, herbicide, rubber additive and feedstock for pharmaceuticals.<sup>42</sup> The ruthenium supported Starbon was further shown to catalyse hydrogenations of fumaric, itaconic, levulinic and pyruvic acids.<sup>43</sup>

#### 1.3.2.2.2.2 Adsorption and separation

Adsorption is the concentration of ions or compounds on the surface of a solid.<sup>44</sup> The reverse of this process is desorption. Adsorption can be affected by several factors including, but not limited to; surface area, pore volume, pore size, temperature, concentration and also solvent, if the sorbate is dissolved. The adsorbate will be adsorbed onto the adsorbent by attractive intermolecular forces that occur between the two once the adsorbate has diffused or been pressurised towards the adsorbent surface. These intermolecular forces can be weak, for example van der Waals forces between an alkane and a carbon surface, or they can be strong, for example charge-charge forces between metal ions and an acidic surface.<sup>45</sup> Adsorption can be split into two main types; physisorption and chemisorption, although these two often occur consecutively.<sup>45</sup> In physisorption, no chemical bonds are formed, only weak electrostatic intermolecular forces. Physisorption may also occur due to simply having such a small pore size that

the adsorbate becomes trapped in the pores because of the high energy of the micropores. On the other hand, chemisorption involves electron transfer to form chemical bonds between the adsorbent and the adsorbate. Chemisorption is therefore very specific and a lot less common than physisorption.<sup>45</sup>

Starbon materials, similar to ECS, were also tested as stationary phases in chromatographic separation, this time with tuneable surface polarities and pore properties.<sup>27</sup> Alginic acid-based Starbon materials overcome the irreversible adsorption associated with materials of higher microporosity and also have significantly improved surface areas compared to ECS, making them more suitable for liquid chromatography columns. The publication by White *et al.* showed how such a column could be used to separate polar sugar analytes.<sup>27</sup>

Adsorption of other specific compounds was later studied too.<sup>46, 47</sup> Adsorption of methylene blue and acid blue 92 dyes was tested with both low temperature (300 °C) and high temperature (800 °C) carbonised alginic- and starch-based Starbon materials and compared to that of commercial activated carbon (Norit).<sup>46</sup> Alginic acid-based Starbons were found to be the most superior materials with both dyes. Being the most mesoporous of the three types of materials tested, it was concluded that mesoporosity is a key factor in dye adsorption. Furthermore, when carbonised to 300 °C it was found to be the most superior material for adsorption of methylene blue with an adsorption capacity of 186 mg g<sup>-1</sup> compared to activated carbon's 83 mg g<sup>-1</sup>. With regards to acid blue 92, a higher carbonisation temperature was beneficial to avoid electrostatic repulsion between the material surface and the dye. Thus, tuning the material's surface proved highly beneficial in achieving high adsorption capacities of dyes for application in wastewater cleaning.<sup>46</sup>

Phenols can be toxic to human health and the environment but unfortunately, are also found in wastewater from herbicide, steel and petroleum industries, thus, Starbons have been tested for their adsorption of phenols.<sup>47</sup> Adsorption was tested with high temperature starch- and alginic acid-based Starbons, as well as several commercial activated carbons. Alginic acid-based Starbon showed different adsorption capacities depending on the phenol, however this was not the case with starch-based Starbon as it is less functionalised and therefore there is less possibility for electrostatic repulsion. In all cases, desorption and thus, recovery was achieved to some extent (up to 40%) with

solution  $\text{pH} > 11$ . A diagrammatic representation of the phenol adsorption and desorption process is shown in Figure 1.8.<sup>47</sup>

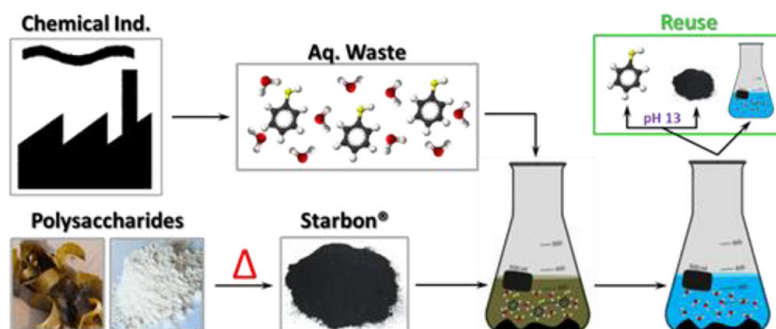


Figure 1.8: Schematic representation of the use of Starbons in adsorption of phenols from wastewater. Reproduced from ref 47 with permission from the American Chemical Society.<sup>47</sup>

Starbon materials and Fenton's reagents were used together to clean up real laundrette wastewater.<sup>48</sup> Laundrette wastewater, or grey water, is highly concentrated with detergents and can thus cause damage when released into the environment. Of all the techniques that have attempted to clean wastewater, adsorption tends to be the simplest of methods. Fenton's reagent (hydrogen peroxide and a ferrous salt) is also ideal because it is able to both oxidise and coagulate contaminants at room temperature and atmospheric pressure. Combining Starbon (carbonised to 300 °C) adsorption and Fenton's reagents, 93% chemical oxygen demand (COD) was removed, with a significant reduction in the quantity of Fenton's reagents required and therefore a reduction in the amount of sludge produced and the overall cost.<sup>48</sup> It was later found that use of Fenton's reagent can be eliminated altogether by using alginic acid-based Starbon carbonised to 800 °C to achieve 91% COD removal.<sup>49</sup>

Later on, adsorption and separation of phenolic compounds onto several different Starbons was studied in depth by Zuin *et al.*<sup>50</sup> A solid phase extraction (SPE) set up was employed and statistical analysis applied to determine which materials were most suitable for adsorption of which phenolics. Materials carbonised to low temperatures showed to be the most superior in recovery of all the compounds tested. Materials carbonised to high temperatures bound to the phenols more tightly, making them more suitable for purification purposes. Carbonisation to intermediate temperatures proved beneficial for selective adsorption due to a balance of textural and chemical properties.<sup>50</sup>

Adsorption of metals was investigated by Muñoz García *et al.* where from a complex mixture of metals, Starbons were found to selectively adsorb the precious elements (gold, platinum and palladium).<sup>21</sup> The metals predominately remaining in solution were nickel, copper and zinc. The mechanism responsible for selective adsorption was found to be a redox mechanism where the metal is reduced from solution to nanoparticles, while the Starbon surface is simultaneously oxidised from a more graphitic carbon, to carbon with hydroxyl and carbonyl functionalities.<sup>21</sup>

Current research on CO<sub>2</sub> adsorption shows that microporous materials are highly effective.<sup>51</sup> Thus, Starbon materials were tested for this application, and it was found that apart from high surface area, mesoporosity in Starbons benefited adsorption too. In fact, the materials performed better than activated carbon. The study showed that the presence of a degree of mesoporosity improves movement of CO<sub>2</sub> within the material, making the micropores more available and thus increasing the effective surface area.<sup>51</sup>

#### 1.3.2.2.2.3 Energy storage

Starbon possesses several of the properties necessary to make a good energy storage material: chemical and thermal stability, high surface area and mesoporosity.<sup>52</sup> Unfortunately, however, Starbons do not contain any heteroatoms or other polarizable functionalities. This makes Starbon materials not conductive enough to act as good capacitors on their own. A study by Muñoz García *et al.*, however, showed that the introduction of only 20% graphite, significantly improves the conductivity of material, producing a monolith with a capacitance of 175 F g<sup>-1</sup>.<sup>52</sup>

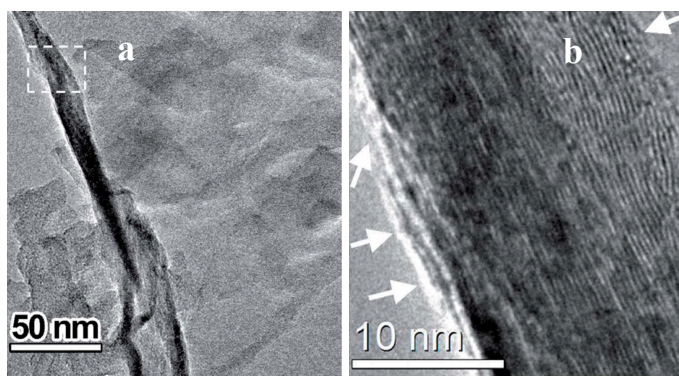


Figure 1.9: Bright field STEM of Starbon + 20% graphite showing a) graphite flakes in amorphous carbon and b) the stacking of graphite layers from the dashed box in (c). Reproduced from ref 52 with permission from the Royal Society of Chemistry.<sup>52</sup>

## 1.4 Thesis outline

The aim of this thesis is to continue to discover applications for Starbon materials that help to work towards a circular economy, applying the Principles of Green Chemistry in all aspects along the way. The work in this thesis will extend the list of Starbon applications to include e-waste recycling, isolation and purification of small organic compounds from natural complex mixtures, completely bio-based energy storage and a new path to improved CO<sub>2</sub> adsorption.

Starbons have been synthesised from various sources of biomass, namely starch obtained from waste potato peel, alginic acid from seaweed (brown algae) and pectin from orange peel waste. The characterisation of Starbons and the applications found and tested are described in Part I of this thesis (Chapters 2 – 4). To allow for further broadening of the potential applications of Starbons, for the first time, nitrogen-doped Starbons were developed. The new materials, termed *N*-Starbons, were prepared using chitosan obtained from shrimp shell waste as the nitrogen source. Part II (Chapters 5 – 9) contains development, full characterisation and preliminary experiments of potential applications for these new materials. Obtaining the starting materials from food waste gives added benefits in that they are low cost, completely renewable and in themselves, reducing waste. Thus, this thesis is divided into two parts:

Part I – Starbons

Part II – *N*-Starbon

Part I:

Starbons<sup>®</sup>



## Chapter 2

# Starbon<sup>®</sup> Characterisation



## 2.1 Introduction

Starbons are now well-established materials with over 30 articles published in high impact journals on their characterisation or application. Full characterisation has therefore already been performed on batches prepared by other researchers. It is therefore unnecessary to fully characterise the materials prepared in this work, however some characterisation is necessary to ensure the quality of the materials is the same as that in previously published work. A single batch of each material in the whole range of Starbons (from starch), Algibons (from alginic acid) and Pecbons (from pectin) was prepared and carbonised to 300 °C, 450 °C, 600 °C and 800 °C. This was to ensure that no differences between batches affect the results of any experiments performed in this project, such as for the applications tested in the following two chapters. The materials will be referred to by their code, where the first letter represents the polysaccharide used and the following three digits represent the carbonisation temperature; for example, A300 represents Algibon carbonised to 300 °C.

Elemental analysis is essential to ensure carbonisation has taken place as per usual, causing a decrease in oxygen content and the corresponding increase in carbon content. Additionally, it is important to check for any heteroatoms such as nitrogen, which could significantly alter the properties of the materials and the way it interacts with other species, thus having a significant effect on applications such as the adsorption of metals. Thus, for each material, the percentage carbon, hydrogen and nitrogen were determined.

As the materials' principal property is their mesoporosity, nitrogen adsorption / desorption porosimetry was used to ensure that all materials contained significant mesopore volumes as well as high surface areas. It is important that all materials are tested to ensure that they retain their mesoporosity and the pores do not collapse on carbonisation to high temperatures. Thermogravimetric analysis (TGA) was performed on each material in its aerogel form, pre-carbonisation (i.e. expanded starch, alginic acid and pectin), thus allowing for an understanding of the temperatures at which major chemical changes take place in the materials. Literature could then be used to determine the reactions taking place within the materials as they carbonise. The surfaces of a few of the materials were additionally viewed under a scanning electron microscope (SEM) to determine particle size and further understand the textural properties of the materials.

## 2.2 Elemental analysis

Elemental (CHN) analysis of all Starbons was performed. The oxygen content was assumed to be the remaining material after subtracting carbon, hydrogen and nitrogen. The results are shown in Figure 2.1. The carbon content for each material increases with increasing carbonisation temperature, while the hydrogen and oxygen contents decreased. This means that Starbon degradation is occurring through loss of molecules containing significantly more hydrogen and oxygen than carbon. The increase in carbon is consistent until 600 °C but drops at 800 °C.

When comparing the different types of materials, Pecbons contain the most oxygen, followed by Algibon and then Starbon. It is expected that Starbon contains the least oxygen as it does not contain a carboxylate group, which both Algibon and Pecbon contain. It is unclear however, why Pecbons contain higher oxygen contents than Algibons. This is more likely to be impurities in pectin, as opposed to oxygen itself. Unexpectedly, Pecbons (and also A800) contained a small amount of nitrogen. This is also from impurities within the pectin.

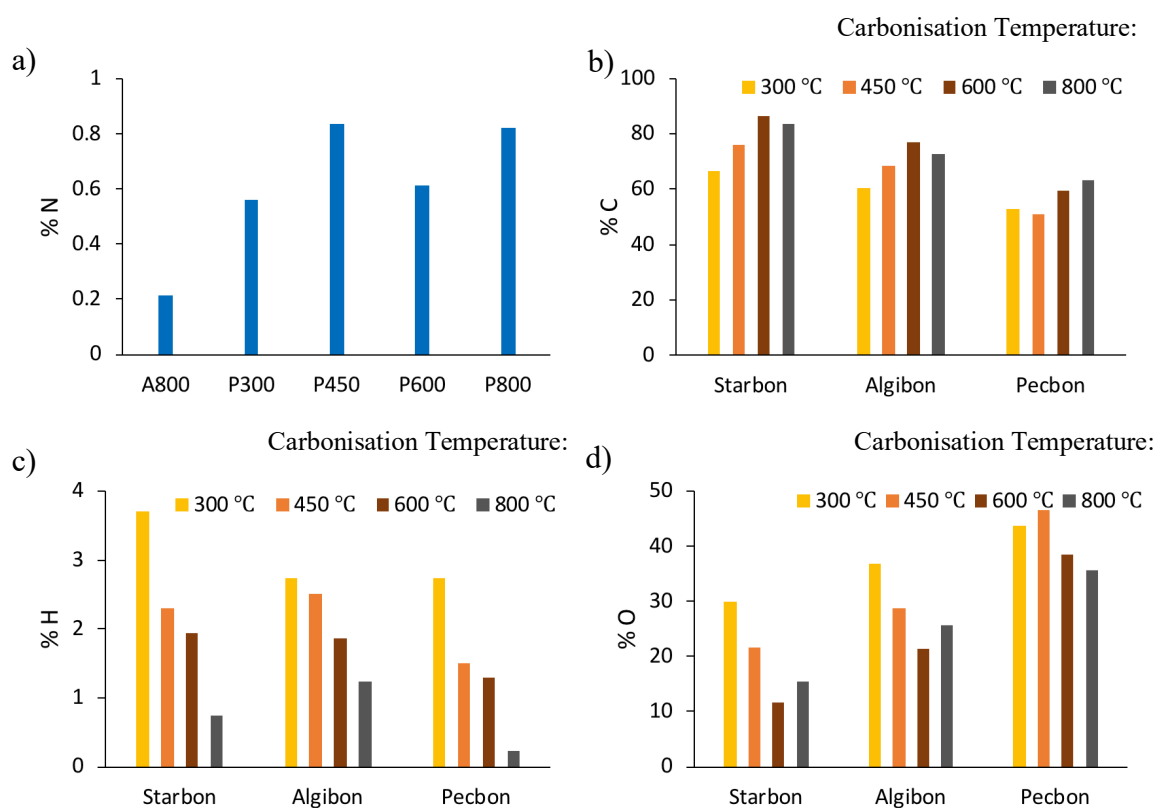


Figure 2.1: a) Nitrogen, b) carbon, c) hydrogen and d) oxygen contents of Starbons, Algibons and Pecbons.

When comparing these materials to Starbons prepared in the past, literature shows significantly higher C:O ratio for the majority of the materials, especially for Algibons and Pecbons. The data is summarised in Table 2.1. The most notable difference between these materials and those previously prepared is the use of *p*-toluenesulfonic acid (pTSA) which was previously avoided to make the process more sustainable by preventing the use of synthetic chemicals, as well as reducing the number of steps involved in the material preparation. This also eliminated the presence of sulfur in the materials, which may allow for applications such as heterogenous catalysis.<sup>27, 53</sup> Additional acid however, was found to be beneficial to the overall porosity of the material and was thus used here, potentially increasing the amount of stable oxygen as well as sulfur, both contributing to a higher apparent oxygen content.

Table 2.1: Comparing C:O ratios calculated from CHN bulk elemental analysis of Starbons, Algibons and Pecbons carbonised to a range of temperatures, prepared in this work and published in the literature.<sup>26, 27, 53</sup>

Material	C:O ratio	
	This work	Literature
<b>S300</b>	2.22	3.43
<b>S450</b>	3.51	6.01
<b>S600</b>	7.40	7.53
<b>S800</b>	5.38	8.60
<b>A300</b>	1.64	3.86
<b>A450</b>	2.38	~ 6
<b>A600</b>	3.60	7.98
<b>A800</b>	2.83	8.59
<b>P300</b>	1.21	4.99
<b>P450</b>	1.10	7.99
<b>P600</b>	1.54	8.65
<b>P800</b>	1.77	> 9

## 2.3 Porosimetry

Adsorption of gases such as nitrogen or carbon dioxide are often used to analyse and measure the porosity of a material. This includes measurements of Brunauer–Emmett–Teller (BET) surface area and Barrett-Joyner-Halenda (BJH) pore volume and pore size distribution.

The processes involved in adsorption can be studied by plotting adsorption isotherms.<sup>8</sup> These are plots of the amount of materials adsorbed against the relative vapour pressure under constant temperature. Brunauer, Deming, Deming and Teller classed these isotherms into six types as shown in Figure 2.2.

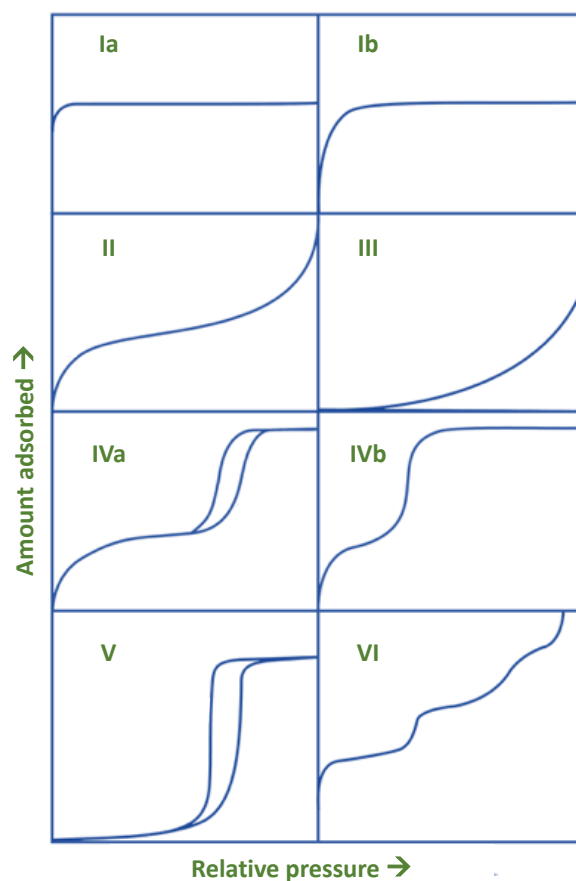


Figure 2.2: Classification of physisorption isotherms.<sup>8</sup>

Type I(a) isotherms show a sharp increase in adsorption at low pressure. This means that the accessible pores are filled very quickly, indicating that full capacity is reached and therefore the pore size is very small. The plateau is reached due to the openings of the micropores being so narrow that it is no longer possible for adsorbate to fit through. Type I(b) differs in that the plateau is reached after a higher pressure is reached, indicating that pore accessibility is less limiting and therefore the pores are on the larger side of the micropore region.

Type II is characterised by the initial monolayer coverage, followed by multilayer coverage which continues up to infinity, indicating that the material keeps adsorbing and is therefore non-porous. Type III differs in that the monolayer is not complete. This implies that adsorbate – adsorbate interactions are stronger than adsorbate – adsorbent interactions.

Type IV(a) is similar to Type II but differs in that it plateaus at high pressure, showing that the adsorption capacity has been reached. The second difference is that a hysteresis loop is present due to adsorption and desorption following different mechanisms. At high pressure, capillary condensation of the adsorbate occurs which restricts desorption. This is typical of mesopores. Type IV(b), although very similar, characterises smaller mesopores where there is not enough room for capillary condensation to occur and thus adsorption is reversible.

Just as Type IV is similar to Type II, Type V is similar to Type III in that the adsorbate – adsorbate interactions are stronger than the adsorbate – adsorbent interactions. The difference here is that the graph both plateaus due to limited multilayer coverage in the mesopores and forms a hysteresis loop due to capillary condensation in the mesopores. Finally, Type VI is a lot less common than the previous types of materials. This indicates a material that is completely homogeneous and non-porous, allowing for complete formation of each individual layer, represented by each step increase in the isotherm.

Hysteresis loops can be further classified depending on their shape. IUPAC identifies six characteristic types; H1, H2(a), H2(b), H3, H4 and H5, as shown in Figure 2.3.<sup>8</sup>

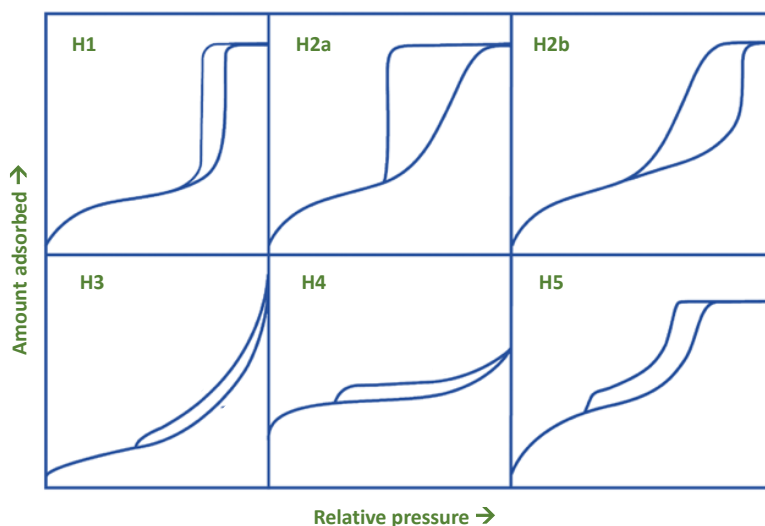


Figure 2.3: Classification of hysteresis loops.<sup>8</sup>

Type H1 shows steep and narrow adsorption branches, and is given by materials having simple, uniform mesopores of a narrow size range. The network connecting the pores has a negligible effect on the hysteresis, which is solely dependent on condensation of the adsorbate and its surface tension within the pores. The steepness of the loop therefore indicates delayed condensation. Conversely, Type H2 hysteresis loops are affected by the network connecting the pores, implying that the pore structure is more complex. The adsorption branch here is a gradual increase. Type H2 is split up into H2(a) and H2(b), where the main difference can be seen in the desorption branch. Type H2(a) shows a very steep desorption branch caused by pore-blocking in the narrow necks of the pores or due to evaporation induced by cavitation. Type H2(b) desorption also results from pore-blocking but as the pore necks vary over a wider range, a more gradual decrease is shown.

Type H3 hysteresis loops are characterised by two distinct features. The first is that adsorption resembles Type II isotherms in that no plateau is reached, and the second is that the desorption branch meets the adsorption branch at a pressure corresponding to the cavitation point of the adsorbate. Type H3 loops are typical of plate-like particle aggregates. Similarly, Type H4 also does not reach a plateau and the cavitation pressure is given by the point that the loop is closed. The difference here is the high initial adsorption due to micropore filling. Type H4 hysteresis loops are typical of composites of Type I and II. Finally, Type H5 hysteresis loops occur when a combination of both open and partially blocked mesopores occurs, leading to the unusual pattern that can be seen in Figure 1.3.

The results obtained from porosimetry of Starbons, Algibons and Pecbons are shown in the following three figures (2.4 – 2.6). Figure 2.4 shows a clear trend in increasing surface area on going from lower to higher carbonisation temperatures, with A800 having the highest surface area at  $610 \text{ m}^2 \text{ g}^{-1}$ . This is consistent with the literature.<sup>26, 27, 53</sup> As the material condenses, a small percentage of the pores collapse. This has an insignificant effect on the mesoporosity, but a highly significant effect on the microporosity, which is what gives such an increase in surface area.

When comparing to values in literature however, the surface areas obtained here are significantly improved for Algibons and Pecbons, but fairly consistent for Starbons. For example, S600, A600 and P600 have been reported to have surface areas of 528, 360 and  $233 \text{ m}^2 \text{ g}^{-1}$ , respectively. This is likely because of the use of pTSA, which further catalysed carbonisation, as opposed to the published results where acid-catalysis was dependent on acid groups within the polysaccharides themselves.

Total pore volumes on the other hand appear to depend solely on the type of starting material and do not appear to be changing on carbonisation, as has been shown in the literature.<sup>26, 27, 53</sup> Total pore volumes were calculated by adding BJH desorption (mesopore) volumes and t-plot (micropore) volumes. The results are shown in Figure 2.5. This trend is consistent with all the materials except for P800, which showed a remarkably high pore volume at  $1.21 \text{ cm}^3 \text{ g}^{-1}$ . All Pecbon materials were made from the same batch of pectin with the exception of P800, indicating that the pectin used for the lower temperature materials may have been of inferior quality. Other possible reasons are that the freeze-dryer may have not been working at optimum conditions or variations in gel layer thickness in the freeze-drier caused the effectiveness of drying to vary between samples.

When distinguishing between the mesopore and micropore volumes, a trend can again be observed with carbonisation temperature. Micropore volumes increase with increasing temperature. This correlates well with the discussed corresponding increase in BET surface area. Mesopore volume remains relatively constant, only slightly fluctuating. Both these observations are in agreement with published data.<sup>26, 27, 53</sup>

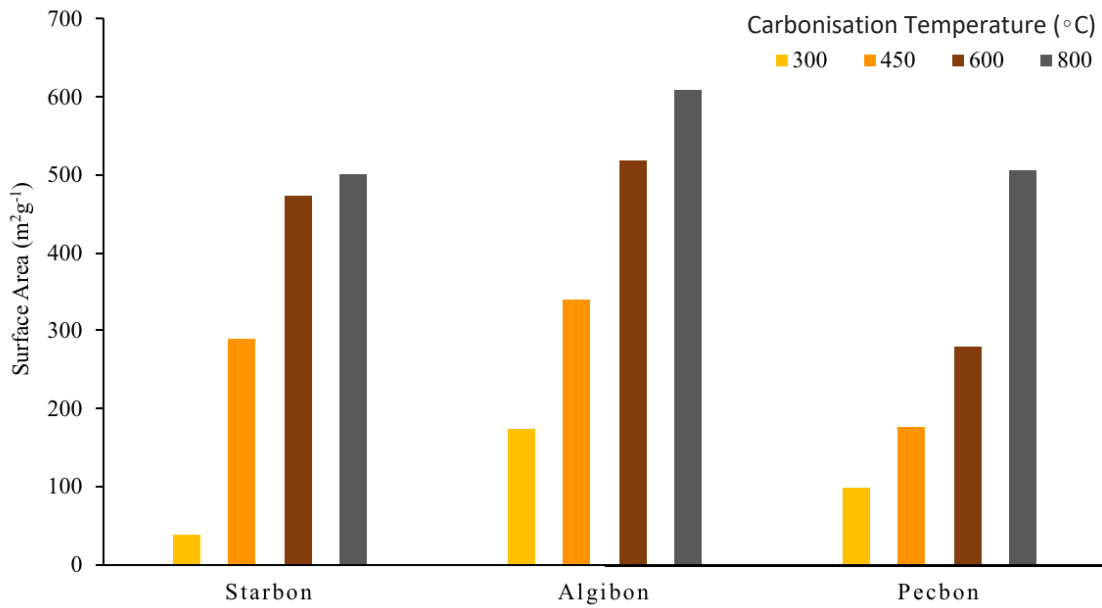


Figure 2.4 Surface areas of Starbons, Algibons and Pecbons carbonised to various temperatures.

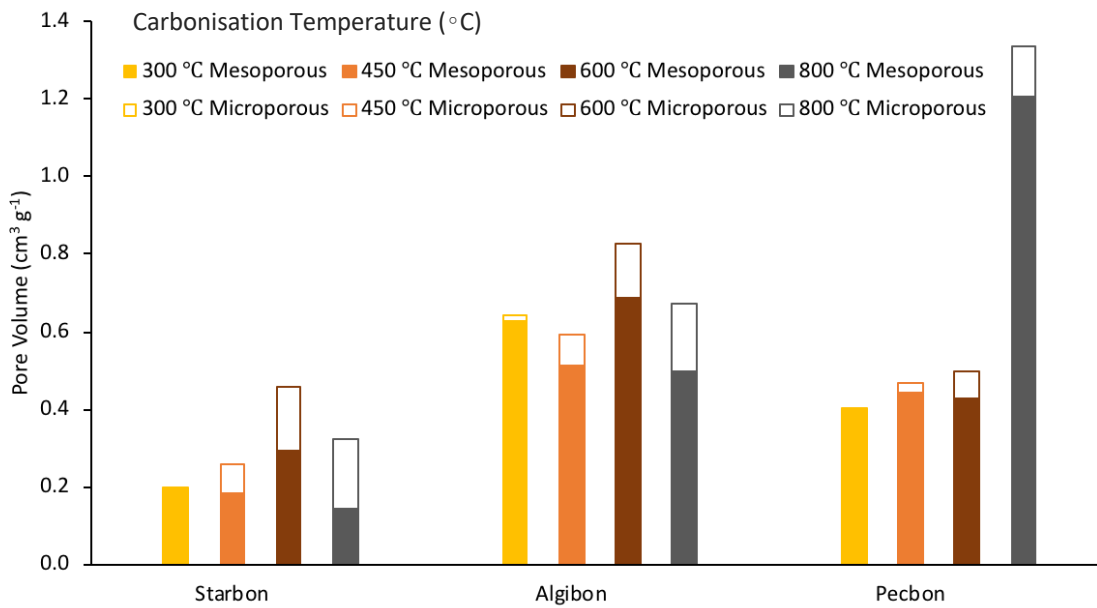


Figure 2.5: Micro- (t-plot), meso- (BJH) and total (t-plot + BJH) pore volumes of Starbons, Algibons and Pecbons carbonised to various temperatures.

The hysteresis loops shown in Figure 2.6a are type IV or V Langmuir isotherms.<sup>54</sup> This indicates that the materials are all predominantly mesoporous with multilayer adsorption taking place followed by capillary condensation. Due to unsuitable analysis conditions, the hysteresis loops of a few of the materials did not close which makes it difficult to correctly interpret the results or obtain more meaningful data for these samples. Having said this, the primary purpose of this type of characterisation is to confirm mesoporosity, which is evident in the results. The hysteresis loops can be classified as Type H3 at lower carbonisation temperatures, moving towards Type H4 at higher carbonisation temperatures, as shown by the steep initial adsorption caused by micropore filling. As described in Chapter 1, these hysteresis loops are typical of aggregated plat-like particles.<sup>8</sup> These form pores that are slit shaped.<sup>26</sup> Although some hysteresis loops did not close, this characterisation of Starbons was also shown in the literature, further confirming the likelihood of these conclusions to be correct.<sup>27, 55</sup>

The pore size distributions plots shown in Figure 2.6b further confirm mesoporosity. As these results are based on the BJH model, as is the mesopore volume, the same trend can be observed, with mesoporosity decreasing at 800 °C for Starbons and Algibons. The corresponding increase in microporosity can be observed and again confirmed for all materials. Pecbons were unaffected up until 600 °C, after which mesoporosity improved with a more defined pore size distribution, again due to the material being of superior quality. Of all the materials, Algibons have the narrowest pore size distribution, which may allow for them to be more specific in applications such as adsorption and catalysis.

It is important to note here that each material has only been made once and analysis of each material has only been performed once. This means that errors have not been accounted for.

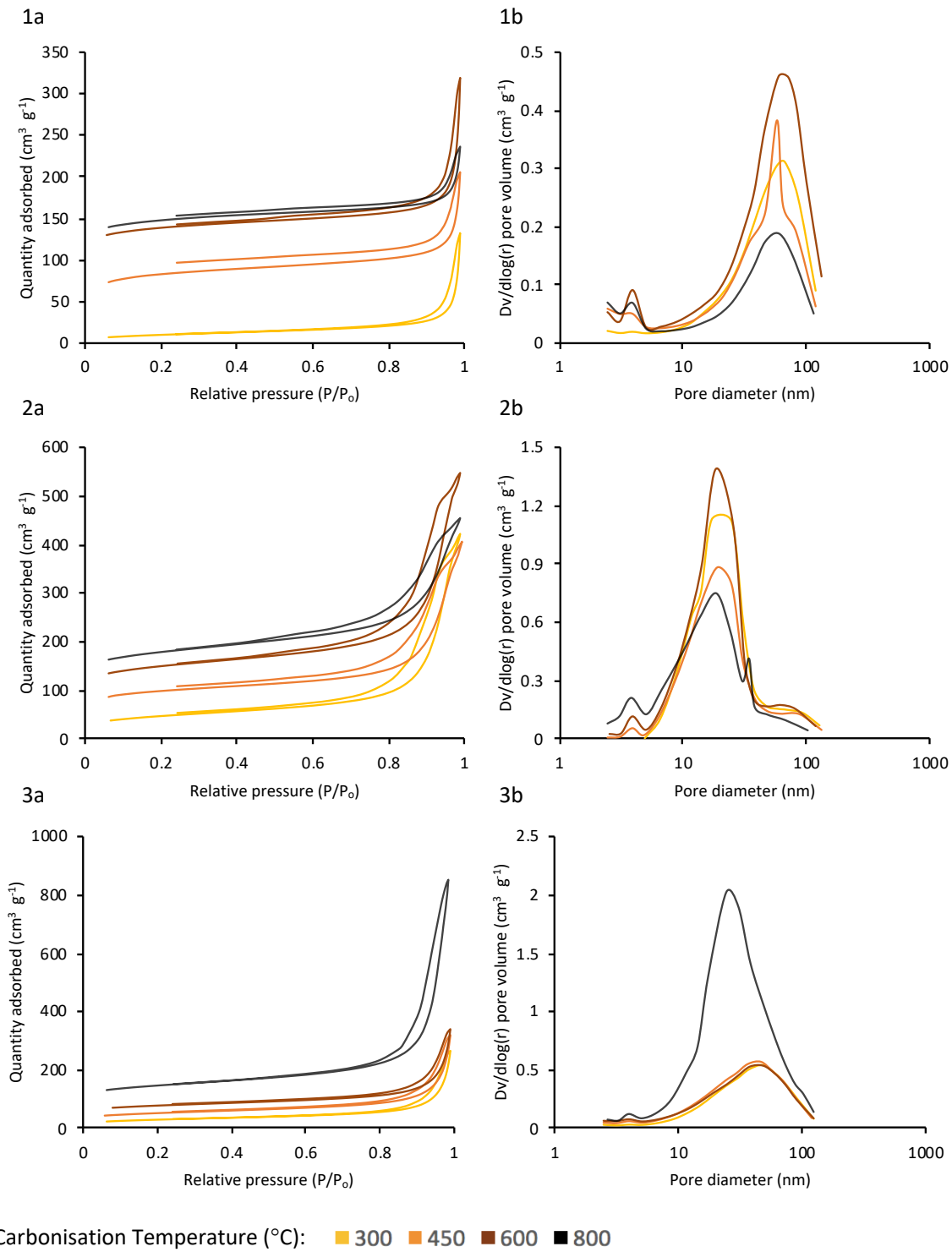


Figure 2.6: a) Langmuir isotherms and b) pore size distribution plots for various 1) Starbons, 2) Algibons and 3) Pecbons.

## 2.4 Scanning Electron Microscopy

A few of the materials were further analysed under a Scanning Electron Microscope. The SEM images for A300, A800 and P300 are shown in Figure 2.7 at low magnification (a) and high magnification (b). In all cases, the porosity of the materials was clearly demonstrated.

There were significant differences in the appearances of Algibons and Pecbons. At low magnification, the images show that the particle sizes for the Pecbon samples (~ 1 mm in diameter) are significantly larger than the Algibon samples (10 - 100  $\mu\text{m}$  in diameter) by a magnitude of 10 or more. At high magnification, the alginic acid samples appear to have a rough texture, whilst the pectin samples appear to have a highly ordered microporous structure. These observations are identical to those described in the literature.<sup>27, 53</sup>

The effect that these structural properties have on the materials' applications will be studied and analysed in the following chapters. For example, a more ordered structure allows for easy transport within the material, making it suitable for electrochemical applications. Order may also provide improved flexibility within the material due to the availability of equal amounts of room for stretching in particular directions throughout the whole of the material. On the other hand, the small particle sizes observed with the Algibons are highly sought after as they can be beneficial for applications that involve printing.

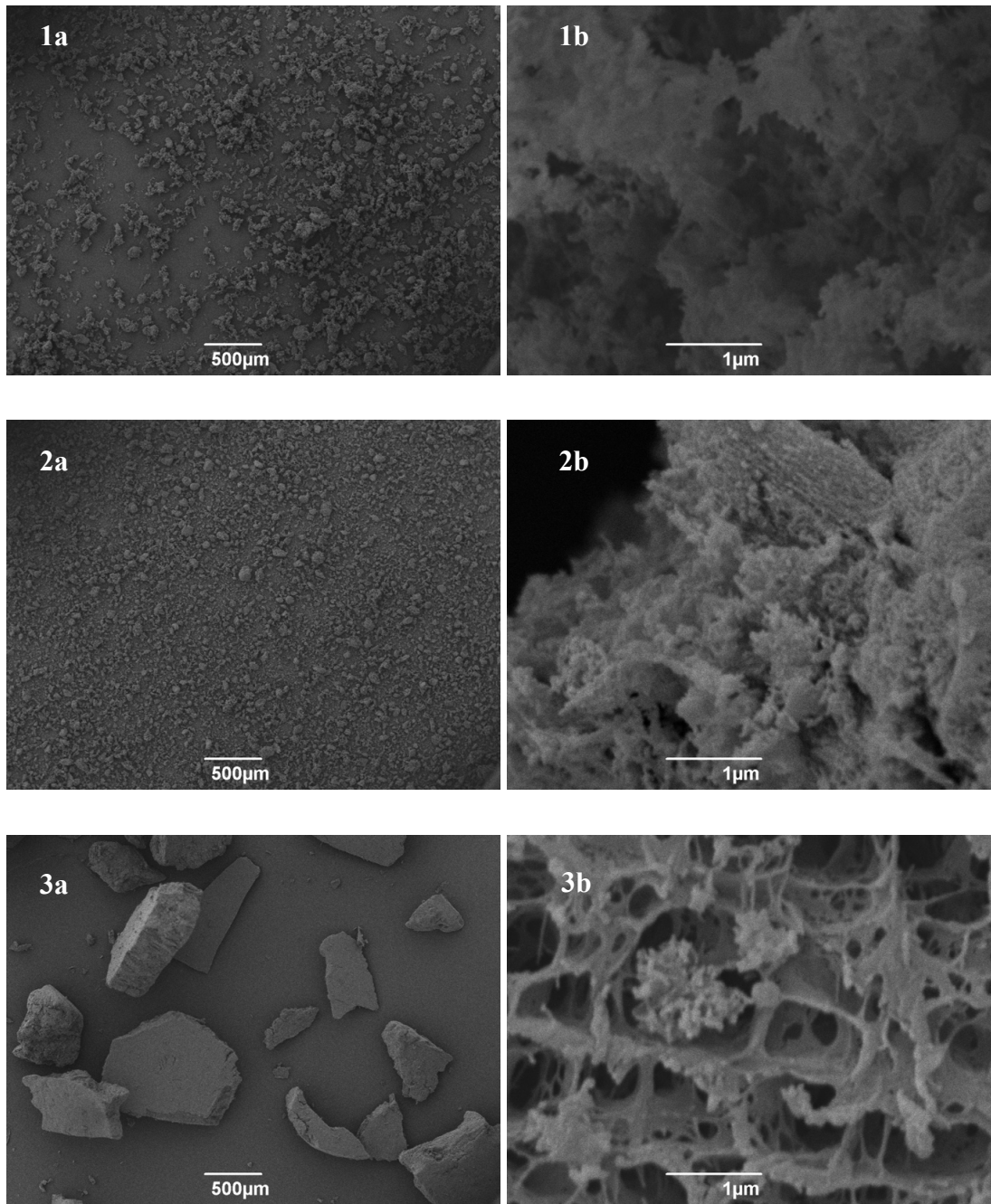


Figure 2.7: SEM images of 1) A300, 2) A800 and 3) P300 at a) 30x and b) 25,000x magnification.

## 2.5 Thermogravimetric Analysis

The results from thermogravimetric analysis of expanded starch, alginic acid and pectin are shown in Figure 2.8. Mass shown at or below 100 °C can be attributed to loss of water adsorbed onto the surface of the materials. All materials were consistent in showing a significant loss in mass starting at around 150 °C, which indicates where hydroxyl groups reduce down to ether groups, releasing molecules of water. This is followed by the conversion of the remaining hydroxyl groups to carbonyl groups conjugated with alkenes above 200 °C.<sup>22</sup> This is consistent with results found in literature where Diffuse Reflectance Infrared spectroscopy in Fourier Transform mode (DRIFT) indicated the formation of ether moieties and carbonyl groups through intermolecular cross-linking and dehydration.<sup>26</sup> Surface decarboxylation occurs at around 250 °C in alginic acid and pectin, and overlaps with the peak above 300 °C in all materials, caused by aliphatic groups which continue to be converted to aromatic systems all the way up to 800 °C.<sup>22, 27</sup>

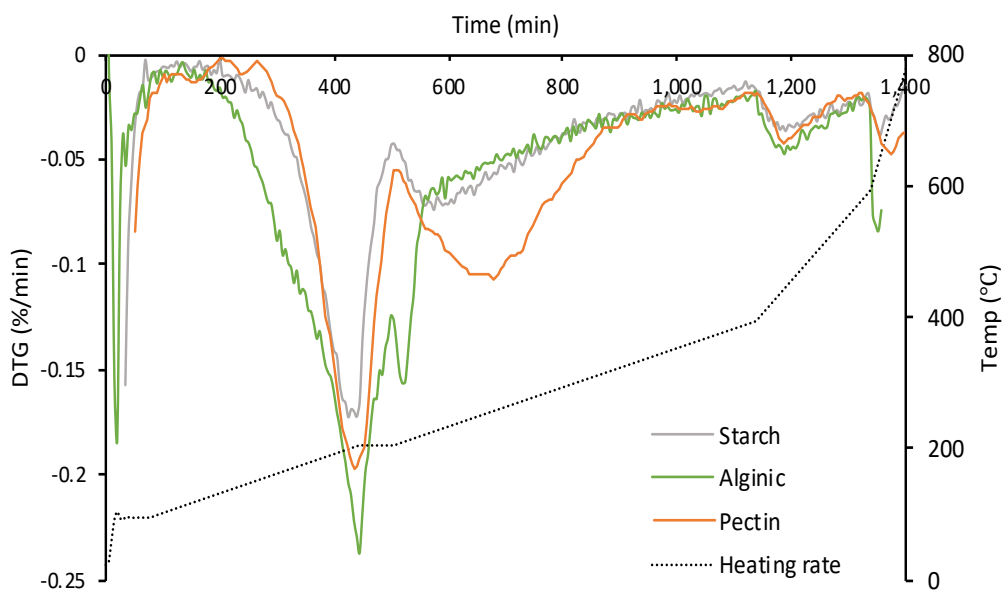


Figure 2.8: Differential thermal analysis of Starbon, Algibon and Pecbon up to 800 °C.



## Chapter 3

# WEEE Recycling



## 3.1 Introduction

In today's culture, the desire to constantly improve efficiency has shaped the way technology advances. We often feel as though we need to know everything as soon as it happens, or when possible, even before that. Making such rapid communication possible requires developers to push technology to its limits, to compete and create new devices that tempt consumers to own the best of the best. Many of these technologies are heavily dependent on elements that the world simply does not have enough of. There are two obvious solutions to this, where the first would be to change the direction that technologies are heading, and the second would be to find a way to allow technology to advance with its current direction by somehow creating a way to make these materials available. Both options pose a potentially insurmountable number of challenges. The former would require a great deal of research to investigate alternative resources that work as well as, or better than, what is currently available. However, there is a lot of risk involved in developing alternative technologies, both from an economical as well as a performance perspective and it is for this reason that an extensive amount of research has been carried out on trying to make the latter solution a reality.<sup>56</sup>

A third approach, which can be simultaneously applied with either of the previous two, is to put the responsibility onto those who profit: the manufacturers. Consumers do not have the power to make any significant difference as they can only control what they personally purchase and how long they use their own personal devices before throwing them out. If, manufacturers were only permitted to loan out products, and not sell them, they would ensure that the products would last as long as possible. This is the opposite of the current situation where products are often created with a predetermined life-span, ensuring product breakdown and therefore guaranteeing future sales. They would also ensure that their products are returned to them at their end-of-life, and any valuable elements recovered and recycled. In this way, profit-makers will push for sustainability.

A fourth, slightly more out-of-the-box solution, would be to simply educate ourselves to understand and accept how unnecessary or rather, detrimental, consumer-based technological advances are to both the environment and our own physical and mental health. Nevertheless, as this is a chemistry project, one of the first two solutions will be tackled here; WEEE recycling.

The required elements can be obtained from two different kinds of sources. The first is from ores in the earth, many of which are known to be limited and soon to be completely depleted.<sup>57</sup> Alternatively, these elements can be obtained from waste through recycling. Waste electrical and electronic equipment (WEEE) is one of the fastest growing waste streams today due to the continual disposal of EEE, for the reasons discussed above. Most of it ends up in landfills creating a toxic environment of wasted resources.<sup>56</sup> Elements of high supply risk and economic importance are termed critical elements.<sup>58</sup> In 2017, the European Commission released a report defining which materials are critical based on these two factors. The list includes antimony, beryllium, bismuth, cobalt, gallium, germanium, hafnium, helium, indium, magnesium, natural graphite, niobium, phosphorus, platinum group metals, rare earths (heavy), rare earths (light), scandium, tungsten, vanadium.<sup>59</sup> Hunt *et al.* also include manganese, zinc, arsenic, silver, cadmium, tin, gold, thallium and uranium, and reported that these elements, together with a few from the previous list, will run out within the next 50 years.<sup>58</sup>

A sustainable approach to dealing with WEEE would be to realise its value as an “urban mine”. Instead of regarding it as waste and disposing of it, its constituent elements may be extracted back out and reused. In this way, a circular economy may be achieved.<sup>1, 3, 60</sup> Waste is generally recycled by either dismantling, metallurgical processes or partial dismantling followed by processing.<sup>56</sup> Metallurgical processes can be pyrometallurgical, hydrometallurgical or biometallurgical. Pyrometallurgy includes incineration, smelting, sintering and pyrolysis. Waste is burned to remove plastics, leaving behind metal oxides. This kind of process is efficient in recovering copper, lead and precious metals such as gold but is energy intensive, incurs high costs and leads to the production of hazardous gases.<sup>61</sup> Hydrometallurgy is a more predictable and controlled method which has been successful in recovering metals including gold.<sup>61</sup> In this case, the gold (or other metal) is selectively leached out by acid or other caustic substances, followed by isolation from the rest of the materials by techniques such as adsorption, solvent extraction or ion-exchange and electro-refined, or other metal recovery treatments. Leaching agents often include cyanides, halides, thiosulfates and thiourea.<sup>61</sup> Biometallurgy is split up into bioleaching and biosorption. Bioleaching is used when metals are present as sulfides in their ores and microorganisms are used to increase metal leaching rates. Biosorption makes use of charged groups on the surfaces of microorganisms that are capable of interacting with heavy and precious metals.<sup>62</sup>

## 3.2 WEEE Metal Leaching

Leaching of metals from an end-of-life PCB and LCD was performed using aqua regia as a leachate in a ratio of 1:7 solid (g) : liquid (mL). See Experimental section 9.5.2 for more details. Table 3.1 shows the concentrations, as determined by ICP-MS, of the metals found in the aqua regia leachate after 3 days. It is important to note that the metals analysed were selected based on literature examples of similar experiments.<sup>63-68</sup> Therefore, it is possible that there are other unknown metals present in the leachate solution.

As expected, PCB waste is significantly more concentrated with metals than LCD waste due to its complex nature, containing several different parts and serving the major functionalities of the laptop. The LCD screen on the other hand should technically only contain indium and tin from the ITO layer. However other metals are also found in its casings and connections. For example, copper is found throughout the laptop due to its high conductance, low weight and cheap price. Zinc is added to several metals to form alloys due to its resistance to corrosion, as well as being used for the majority of screws throughout the laptop as a black zinc coating.<sup>69</sup> The screws themselves are often made from steel, which accounts for the presence of iron in the waste. Care was taken to remove the majority of these additional parts however it is possible that some remained in the waste sample. In a real waste example, it is highly unlikely that it will be worth the effort to remove all the small parts that do not form part of the PCB itself, as many of these parts are difficult to reach or too small and can therefore be easily disregarded.

The remaining elements will only be present in high concentration in the PCB waste, and not the LCD waste. Chromium is another element used for its corrosion resistance. Several parts will be chrome-plated to protect them from detrimental oxidation. Cobalt is alloyed with aluminium and nickel to make powerful magnets and is likely to become a lot more popular in the future. Tin, apart from being used for the LCD display, is vastly used in the PCB as a solder, especially more recently as lead is used less due to its toxicity. Manganese is commonly alloyed into other metals to improve strength. Contaminations of manganese may be present from the battery or from steel used in manufacturing. Silver is highly resistant to corrosion as well as being an excellent electrical conductor and would substitute copper completely if it were more available.<sup>69</sup>

Table 3.1: Concentrations (ppb) of various metals present in PCB and LCD leachate.

<b>Element</b>	<b>PCB</b>	<b>LCD</b>
<b>Cr</b>	1,320	296
<b>Co</b>	931	19
<b>Zn</b>	26,400	3,530
<b>Sn</b>	1,610,000	7,900
<b>Mn</b>	590	9
<b>Ni</b>	926,000	643
<b>Ag</b>	19,800	18
<b>In</b>	3,770	44,700
<b>Fe</b>	27,300	2,000
<b>Cu</b>	46,800,000	14,400
<b>Pb</b>	424,000	20
<b>Au</b>	17,600	27

Apart from simply finding the final concentrations of leached metals, their rate of leaching was monitored at several intervals (0, 0.5, 1, 2, 24, 48, 72 and 96 h). This is important because adsorption and, therefore, recovery of any metals may be hindered by the presence of other metals by preferential adsorption. Thus, being able to reduce the presence of metals that are difficult to separate and also less critical metals in the leachate would be ideal. Additionally, a low leaching time makes for a faster overall process. The changes in metal concentration in the leachate solutions for the PCB and LCD are shown in Figures 3.1 and 3.2, respectively. As metals of low concentration are unlikely to affect adsorption, they were omitted from these plots.

As gold and indium are the main targets for recovery in this project, the results were favourable in that both elements reach their maximum concentration within the first hour. Thus, in future, repetitions of this experiment can be done in under 2 hours, allowing some extra time for differences between waste samples. For PCB, this will mean that the leachate solution will contain significantly less aluminium, zinc, copper and iron. This may allow for gold to be more stabilised in the leachate solution,

preventing it from precipitating out of solution after the first few hours. It has often been shown that gold adsorption capacities are highly dependent on concentration, therefore the more gold in solution, the less adsorbent required.<sup>21</sup>

With regards to LCD leachate, again, concentrations of zinc and copper will be reduced with a shorter leaching time. Unlike the PCB waste, concentrations of aluminium and iron will not be affected, likely because their concentrations are significantly lower in LCD waste and therefore do not require much time to leach out.

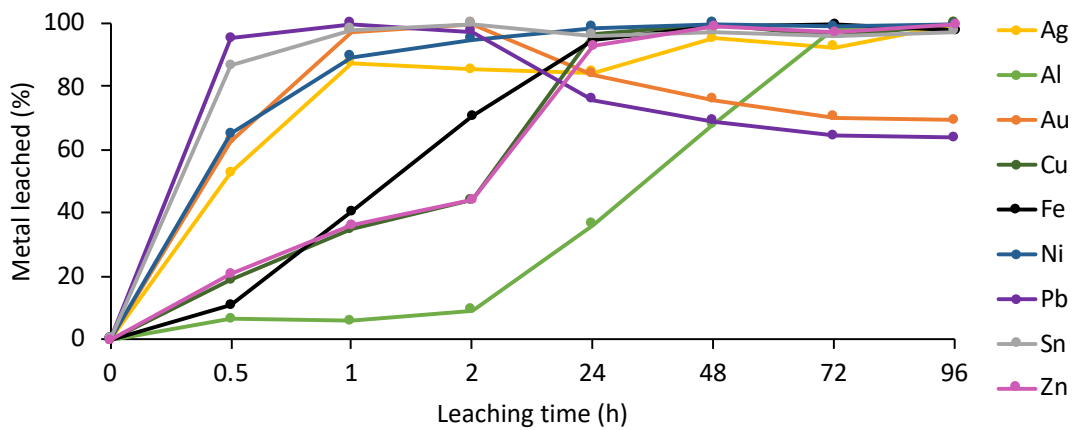


Figure 3.1: The amount of each metal leached (%) into aqua regia from PCB with respect to time (h).

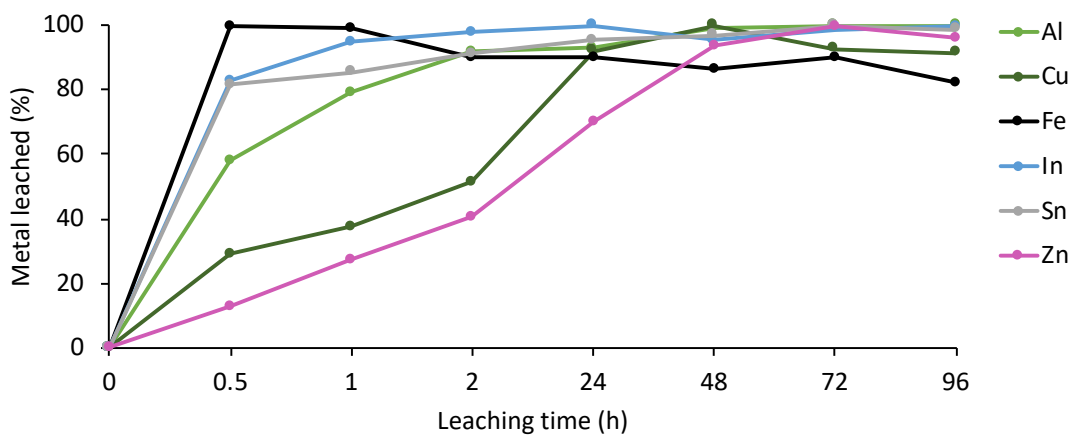


Figure 3.2: The amount of each metal leached (%) into aqua regia from LCD with respect to time (h).

### 3.3 Gold

Gold is of high economic value, which is why gold recycling has been studied so extensively.<sup>70, 71</sup> Over 50% of end-of-life gold is recycled, mainly due to the ease of recovery from jewellery.<sup>71</sup> Another 10% of gold however, is lost in WEEE. Gold's conductivity and corrosion resistance make it suitable for electrical connectors and contacts. It is present in relatively large amounts in printed circuit boards as exemplified in the previous section.<sup>62</sup> Unlike many of the other elements, gold can already be recovered in high yields and purities. Common methods are pyrometallurgical or hydrometallurgical. Unfortunately, these methods can be energy intensive and harmful to the environment, such as use of cyanide. The aim now is to develop a green, more environmentally benign process to achieve the same results. The difficulty arises due to the vast range of metals present with gold in PCBs. This makes selectivity a challenge, as well as making any leaching solutions incredibly hazardous.

In an attempt to move away from techniques that use polluting cyanidation, aqua regia and chlorination has been studied.<sup>68</sup> It has the advantage of achieving selectivity through redox potential control. He *et al.* showed that supercritical water could be used as a pre-treatment for the chlorination process to obtain over 99% leaching of gold, although the high incurred cost has to be taken into consideration.<sup>68</sup> H<sub>2</sub>O<sub>2</sub> has also been employed as a leachant for gold as it increases the efficiency of HCl and decreases the overall environmental impact.<sup>72</sup> A slightly different, yet significantly more efficient approach is to first remove the less noble metals by a much weaker (and reusable) oxidiser; Fe<sup>3+</sup>, as opposed to strong acids. The remaining precious metals can then be leached with a significantly lower volume of acidic medium, in this case; acidic thiourea. The pre-treatment step here involved separation of the magnetic and non-magnetic fractions so that the rare earth elements (REE) could also be recovered. A major drawback of this process however is the inability to regenerate the oxidants.<sup>65</sup> Regeneration of leaching solutions is made facile through electrochemical reduction, or electrowinning, where gold can be electrodeposited out of solution by applying a voltage. This is a popular choice over chemical precipitation not only because of the leachate regeneration but also because of its low energy consumption.<sup>72</sup>

Iodine has also been employed as a gold recovery agent. In their three-step process, Serpe *et al.* recovered gold, copper and silver. In the first step, PCB waste is added to

refluxing aqueous HCl (1:5, solid:liquid) in an argon atmosphere to remove non-noble metals. The residue is added to  $\text{NH}_3/(\text{NH}_4)_2\text{SO}_4$  in  $\text{H}_2\text{O}_2$  to dissolve copper and silver, and is etched with *N,N'*-dimethyl-perhydrodiazepine-2,3-dithione ( $\text{Me}_2\text{dazdt}$ ) or tetraalkylthiouramdisulphides in the presence of diiodine ( $\text{Et}_4\text{TDS}/\text{I}_2$ ) acetone mixtures to dissolve gold. In this way, an attempt has been made to avoid hazardous materials (e.g. aqua regia), although the “greenness” of the alternatives is questionable.<sup>63</sup> Further research by Serpe *et al.* investigated the “chameleonic” behaviour of iodine by testing its performance in aqueous media. This was done to avoid the costs incurred in their previous study that made the method less appealing for large-scale application. Although less effective than  $\text{Me}_2\text{dazdt}$ , the cost benefits make it considerably more suitable. It was also established that the first HCl leaching step could be replaced by a higher concentration of citric acid without the need for an inert atmosphere. Citric acid is preferred for its harmlessness, solid nature, natural availability and lower cost. In the second step, the  $\text{H}_2\text{O}_2$  was replaced by an  $\text{IO}_3^-/\text{I}^-$  solution, allowing for a higher atom economy.<sup>67</sup> A separate study comparing all the common leaching techniques (including cyanidation and aqua regia) found that iodine / iodine leaching is the most efficient gold leachant as it not only leaches out 100% of gold, but shows rapid leaching rates and has the lowest environmental impact. Compared to aqua regia and cyanidation, iodine/iodide shows the highest selectivity for precious metals.<sup>70</sup>

As described previously, it is also possible to leach metals through bioleaching. This is an attractive method due to it being environmentally friendly and low cost.<sup>73</sup> It has therefore been applied to the recovery of gold as a greener alternative method. *Aspergillus* strains, for example, are capable of leaching 87% of gold from PCBs.<sup>74</sup> This was also shown to work for copper although not nearly as efficiently. A more recently developed procedure is a two-step process whereby acidophiles are first used to obtain 98% Cu recovery followed by the addition of biogenic cyanide for a 44% recovery of Au.<sup>73</sup> These methods however were only proof-of-concept and it was only later that Sheel *et al.* developed a combined leaching-sorption method for gold recovery, achieving 84% gold recovery with a mixture of chemical (ammonium thiosulfate) and microbial (*Lactobacillus acidophilus*) approaches.<sup>75</sup>

A non-chemical approach was instead employed by Lahtinen *et al.*. In this example, aqua regia extracts were obtained and then passed through a 3D-printed “scavenger”. The adsorbent in this case is nylon, which shows excellent selectivity towards gold via

its amide group which binds to  $[\text{AuCl}_4]^-$  due to hydrogen bonding between the hydrogen of the protonated amide group and the chlorides of the gold complex.<sup>76</sup>

### 3.3.1 Gold Adsorption

Using the aqua regia e-waste solution described in the previous section, adsorption of metals from the PCB waste was tested at 35 °C for 24 hours. ICP-MS was used to analyse the samples before and after adsorption to monitor the change in concentration. The results showed that concentrations of only gold, and no other elements, were found to have decreased significantly. The percentage adsorption of gold for all Starbons, Algibon and some Pecbons are shown in Figure 3.3. This means that all materials were successful in showing complete selectivity for gold in one simple step. For these experiments, 100% adsorption implies 3 mg g<sup>-1</sup> loading. P800 was omitted for these experiments due to it not being available at the time.

The experiments show that higher carbonisation temperatures yield better adsorption capacities. Algibons and Pecbons perform better than Starbons and it is likely, given the trends, that P800 will be the most ideal material for selective gold adsorption. A800 achieved highest adsorption (92%). Adsorption percentages (%) were calculated as follows;

$$\% \text{ ads} = \frac{[\text{Au}^{3+}] \text{ in PCB solution} - [\text{Au}^{3+}] \text{ after adsorption}}{[\text{Au}^{3+}] \text{ in PCB solution}} \times 100$$

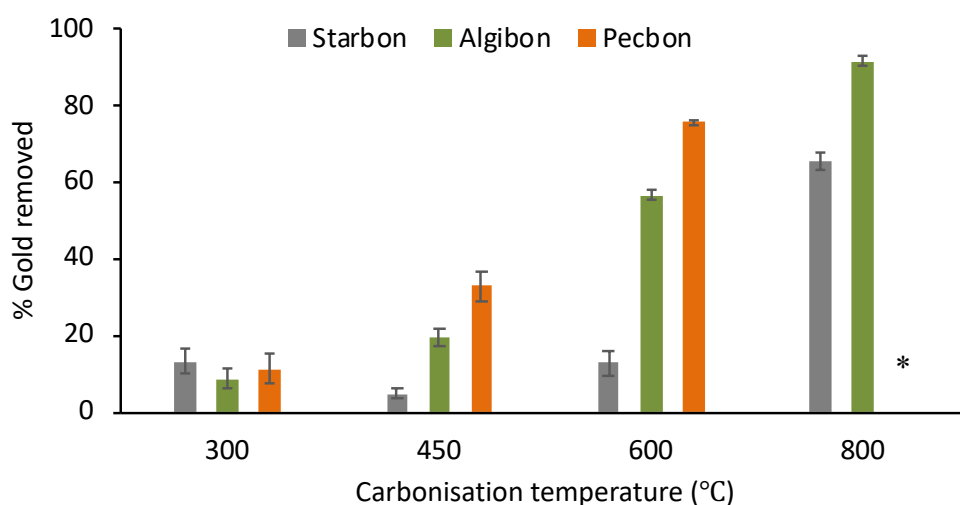


Figure 3.3: Adsorption of  $\text{Au}^{3+}$  from PCB waste solution (5 mL) by various Starbons, Algibons and some Pecbons (20 mg) after stirring for 24 h at 35 °C (\*P800 not tested).

The main differences between low temperature and high temperature materials are their surface areas and chemical functionality. As described in Chapter 2, materials prepared at higher temperatures have significantly higher surface areas and also different surface functionalities. This experiment therefore shows that one or both of these properties is leading to high adsorptions of gold. The gold-containing Starbons will be characterised in the coming sections for further investigation of this problem. When comparing the different starting materials at each temperature, surface areas are highest in Algibons, Starbons and then Pecbons, however the adsorption results favour Pecbons over both Starbons and Algibons. Additionally, Algibons also have higher pore volumes compared to Pecbons so the reason for the improved results must be due to pore structure or chemical functionality. Although both compounds share the same functionalities, pectin may carbonise differently due to structural differences, as well as impurities such as the ~ 0.8% nitrogen present in Pecbons.

The experiment was repeated with the four best performing materials in an attempt to optimise the process and compare the results to activated carbon. The time was shortened from 24 hours to 2.5 and 5 hours, and the temperature was lowered from 35 °C to room temperature (20 °C). As there were no differences between the results obtained at 2.5 and 5 hours, a shorter time is preferable and therefore the results from the 5 hours experiment are omitted. In this case, near complete selectivity for gold was achieved, with iron potentially also being adsorbed by the higher temperature materials. Up to 15% and 18% iron may have been adsorbed by A800 and activated carbon respectively. ICP-MS often gives varying results for complex solutions containing several metals, for this reason, large errors were obtained when testing for iron. The results for iron from this experiment are thus not necessarily reliable. The results for the percentage adsorption of gold by each material are shown in Figure 3.4. As before, P600 and A800 performed best, with A800 only slightly outperforming activated carbon.

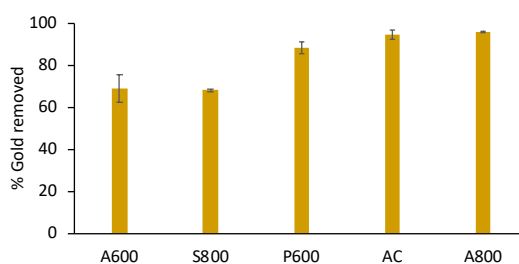


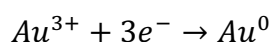
Figure 3.4: Adsorption of Au<sup>3+</sup> from PCB waste solution by various Starbons, Algibons and Pecbons (20 mg) after shaking for 2.5 h at room temperature.

### 3.3.2 Gold-Starbon characterisation

For the purposes of characterisation, a real e-waste leachate solution was obtained from and concentrated by Benito Roggio Ambiental SA. The leachate used here was also aqua regia and adsorption was tested at room temperature for 24 h (see Experimental section 9.5.1 for more details). Again, high temperature materials performed better than low temperature materials, with A800 adsorbing 98% of gold and A300 adsorbing 58% of gold. In this case, no tin was adsorbed in either case, however 4% tin was adsorbed by A800. No tin was adsorbed by A300. In this case, 100% adsorption of gold corresponds to 242 mg g<sup>-1</sup>. Transmission electron microscopy (TEM) and X-ray photoelectron spectroscopy (XPS) were used to characterise the gold on Starbons.

Figure 3.5 shows TEM images for fresh A300 and A800 materials, as well as after gold adsorption, where the gold nanoparticles are clearly visible in both materials. The nanoparticle sizes varied between the two samples; 5 nm in A300 and 20 nm in A800, however the sizes did not vary significantly within the materials.

It was expected that nanoparticle size might correlate with pore diameter, however in Chapter 3, porosimetry data clearly shows that A300 and A800 have similar pore diameters of between 10 and 30 nm. A800 actually shows a higher percentage of pores of smaller diameters (5 nm). This indicates that the reason for the nanoparticle sizes lies not in the material's pore structure but its surface functionality. The formation of the nanoparticles itself implies chemical adsorption and not physical adsorption, so this correlates well with the latter statement. The reduction of gold from solution to nanoparticles in the Starbons is as follows;



and has a reduction potential of +1.52 V. For this to occur, the Starbon must have groups that are capable of being oxidised, meaning that a more reduced surface is favourable. Since higher temperature materials have more reduced surfaces, this explains why higher temperature materials give higher adsorption capacities. This is further favoured by a higher surface area, which makes more of the reduced surface available for gold so that the redox reaction can occur.

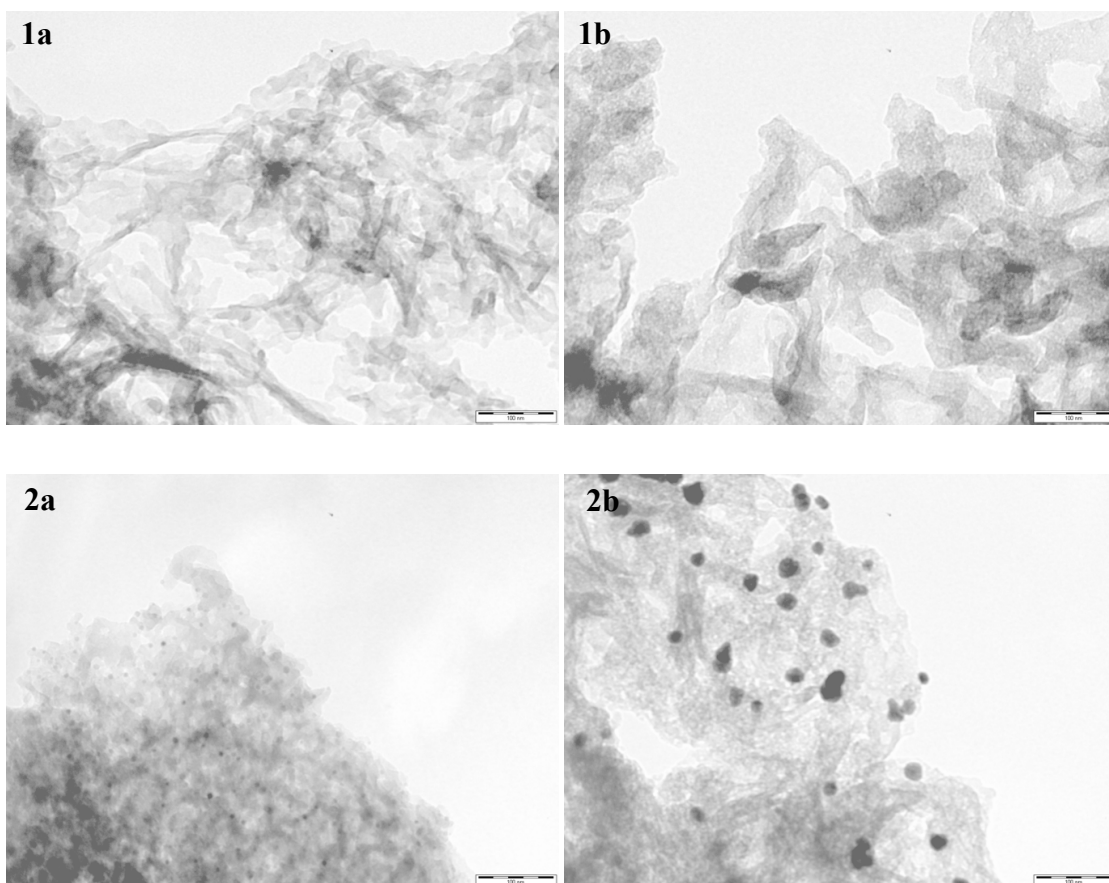


Figure 3.5: TEM images at 135000x magnification 1) before gold adsorption and 2) after gold adsorption of a) A300 and b) A800. Scale bar = 100 nm.

To confirm the presence of gold on the Starbon surface, XPS was carried out on both A300 and A800 after gold adsorption. XPS is also capable of showing oxidation states of gold and can therefore additionally confirm its reduction from  $\text{Au}^{3+}$  to  $\text{Au}^0$ . The high-resolution spectra for gold are shown in Figure 3.6 and the peak positions are summarised in Table 3.2.

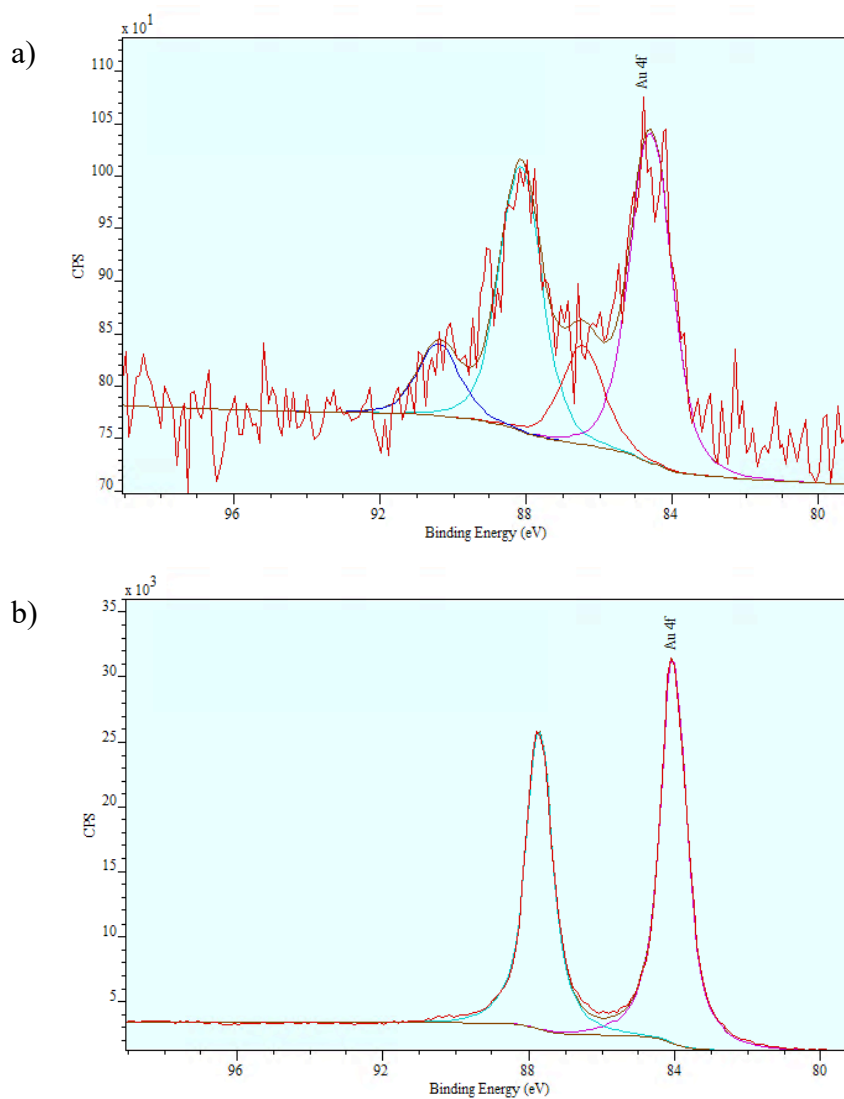


Figure 3.6: The high-resolution XPS spectra of the gold region for gold on a) A300 and b) A800.

Table 3.2: A summary of the binding energies (eV) for the XPS peaks for gold on A300 and A800.

Sample	Peak 1 4f 5/2	Peak 2 4f 7/2	Peak 3 4f 5/2	Peak 4 4f 7/2
<b>Au-A300</b>	84.60	86.46	88.16	90.40
<b>Au-A800</b>	84.04	-	87.72	-

From Table 6.3, Peaks 1 and 3 for gold in both A300 and A800 are characteristic of Au(0), confirming that the nanoparticles observed in the TEM images were indeed the reduced form of gold (Au<sup>0</sup>). The slight shift in binding energy for gold within the two samples will be due to different interactions between the gold and the Starbon surface due to the materials having different surface functionalities. Peaks 2 and 4 on the other hand are only present in A300 and are characteristic of Au<sup>3+</sup>.<sup>77, 78</sup>

Gold adsorbed onto A300 therefore occurred part by redox as in A800, and part by simple electrostatic interactions, leaving some gold (Au<sup>3+</sup>) unchanged. A300 has a much more oxidised surface than A800, which is most likely the main cause for this result. As described in Chapter 2, while A800 contains only ~ 20% oxygen, A300 still contains over 35% oxygen. These oxidised functionalities on the surface of A300 include carboxylate groups, which are negatively charged and will therefore form strong interactions with the positively charged Au<sup>3+</sup>. Several of the other oxidised functionalities on A300 may not be capable of pulling gold out of the aqua regia solution, along with the low surface area, this may further decrease the adsorption capacity.

Apart from the above qualitative data, XPS spectra also give quantitative data. By measuring the area under the peaks, it is possible to determine the percentage composition of each of the elements in the materials. To do this, the area ( $A_j$ ) first needs to be corrected ( $A_{corr}$ ) according to its relative sensitivity factor ( $RSF$ ), transmission factor ( $T$ ) and mean free path ( $MFP$ ) as follows;

$$A_{corr} = \frac{A_j}{RSF \times T \times MFP}$$

The values for the  $RSF$ ,  $T$  and  $MFP$  were obtained from NEXUS, who ran the XPS analysis.  $RSF$  values are specific to each elements and act as a corrective weighting for elements that give stronger peaks than others. The transmission factor and mean field path are instrumental properties. The percentage of gold ( $P_{at}$ ), and all other elements, in the two materials can then be calculated by dividing the corrected area by the total corrected areas of all elements in the sample as follows;

$$P_{at} = A_{corr} / \sum A_{corr} \times 100$$

XPS gives analysis by number of atoms, and therefore to compare these values to those obtained by ICP-MS after adsorption, they need to be converted from an atomic percentage ( $P_{at}$ ) to a weight percentage ( $P_{wt}$ ).

$$P_{wt} = P_{at} \times RMM / \sum P_{at} \times 100$$

The atomic and weight percentages for gold in A300 and A800 have been calculated and are shown in Table 3.3.

Table 3.3: The percentage composition of total gold after adsorption onto both A300 and A800, calculated from XPS spectra and ICP-MS.

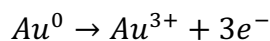
Starbon	XPS		ICP-MS
	Au at%	Au wt%	Au wt%
A300	0.03	0.45	13.9
A800	1.96	23.63	23.67

XPS and ICP-MS show excellent agreement for A800. With A300 on the other hand, there is a significant discrepancy. There are two possible reasons for this, the first is that although ICP-MS shows the total gold removed from solution, XPS analyses only a small sample of the whole and this may not be representative of the whole 10 mg used for adsorption. The gold may not be homogenously distributed within the material. This will especially affect the results if most of the gold is adsorbed further than 5 nm from the outmost surface of the sample as XPS is only a surface technique so it will not be detected.

In addition to this, unlike gold nanoparticles,  $Au^{3+}$  on the Starbon surface can be washed out. Before drying and sending the materials off for XPS analysis, they were centrifuged and rinsed several times so that any unabsorbed metals will not affect the results and be incorrectly assumed to be adsorbed. During this rinsing process, water will have diluted any remaining aqua regia, leaving the Starbon in a solution that is still strongly acidic but much less concentrated with metals. Therefore a large concentration gradient will have been present between the Starbon surface and the solution, potentially desorbing  $Au^{3+}$  back off the Starbon.

### 3.3.3 Gold desorption

Gold in the form of nanoparticles can be desorbed from carbons by applying a voltage to the material when in an oxidising solution such as a strong acid. This will re-oxidise the gold into solution as shown;



There are two ways a voltage can be applied to the materials; either by repeatedly sweeping through a voltage range (Cyclic Voltammetry or CV), or by holding the cell at a particular voltage for a length of time (Chronoamperometry or CA). This was done by creating a three-electrode set-up, using the Starbon pasted on carbon cloth as the working electrode (WE), a carbon rod as the counter electrode (CE) and Ag/AgCl as the reference electrode (RE). The acidic electrolytes tested were 1 mol dm<sup>-3</sup> sulfuric acid and 1 mol dm<sup>-3</sup> hydrochloric acid.

To test desorption, a third batch of PCB waste was obtained and leached into aqua regia for two hours. This was mixed with A800, the best performing material so far, and P800, which is expected to outperform A800. After adsorption for 2.5 hours, the materials were rinsed, dried, formed into a slurry and pasted onto carbon cloth.

After adsorption with both A800 and P800, ICP-MS was carried out twice at two separate facilities. Both showed no change in concentration for several elements including but not limited to; Ag, Co, Cr, Cu, Fe, In, Mn, Ni, Pb, and Zn. Slight changes in concentration were observed for tin in the results from only one facility, however these are uncertain as they are within error, which tends to be large and unreliable when dealing with complex mixtures of metals. The only definite change in concentration was of Au, with 70% (0.238 mg) and 71% (0.240 mg) of gold removed by 40 mg of A800 and P800, respectively. Although unexplained, the trend observed in Figure 4.3 indicated that P800 would perform significantly better than A800, however this was not shown to be the case here.

Cyclic voltammetry and chronoamperometry in 1 mol dm<sup>-3</sup> H<sub>2</sub>SO<sub>4</sub> showed no oxidation peaks for gold, meaning that the acid was not strong enough to oxidise the gold off of the Starbon. The CVs and CAs for A800 and P800 are shown in Figure 3.7 and 3.8, respectively. For both A800 and P800, CVs in Figure 3.7 show three reactions

occurring; one oxidation (I) and two reductions (II and III). In both A800 and P800, the current of each peak decreases in magnitude with every scan (in the directions indicated by the arrows in Figure 4.8) until it reaches a stable straight line, indicating the termination any faradaic processes that were occurring in the system.

The oxidation peak(s) for gold on the Starbon surface is expected to be induced at around 1.2 – 1.3 V, depending on whether oxidation of Au to Au<sup>+</sup> or Au<sup>3+</sup> is occurring.<sup>79</sup> In cyclic voltammetry, the currents are equal but opposite in sign for a redox reaction. As there is no such peak for the oxidation process, it is likely that it is being overshadowed by the evolution of oxygen from solution, which caused the peak I at 1.8 V. Although literature shows a similar decrease in current for the evolution of oxygen in such processes, the reason for the occurrence is unclear.<sup>80</sup> As there are two reduction peaks, there are two reduction reactions occurring in the system. It can therefore be inferred that a second species is present and is being reduced too. The second species (III) is typically the more reactive of the two as it requires a lower potential to be induced. Reduction peak II is due to Au<sup>3+</sup> (and potentially also Au<sup>+</sup>) from solution reducing to Au at the counter electrode.<sup>79, 81</sup> The second reduction peak (III) may either be the Au<sup>+</sup> reducing at the counter electrode, or it may be the reduction of any gold complexes on the Starbon surface that were not previously reduced during adsorption.<sup>79</sup> Before and after gold removal, both materials were characterised by XPS (Figures 3.9 and 3.10). In each case, the gold spectra show not only Au but also a much smaller amount of Au<sup>3+</sup>, confirming the possibility of peak III being the reduction of this other species.

The ICP results indicate that tin might be adsorbed onto the Starbon. This is confirmed to be true by the XPS results in Figures 3.9 and 3.10. Typical cyclic voltammograms of tin and its oxides give oxidation and reduction peaks at negative voltages in acidic media, therefore no such peaks can be observed in the voltage range used for this experiment. The only peak that may be present is not a faradaic reaction but a transition phase from Sn(OH)<sub>4</sub> to SnO<sub>2</sub> which occurs at around 1.2 V in acidic media.<sup>80</sup> Again however, oxygen evolution overshadows any other peaks in this region, so their presence or lack thereof is unknown. If Sn(OH)<sub>4</sub> were present, Sn<sup>4+</sup> XPS characteristic peaks would be in the region of 486 eV.<sup>82</sup> The peaks in Figures 4.10 and 4.11 however are all at 487 eV, indicating the presence of Sn<sup>2+</sup>, therefore discounting the possibility of any redox reactions occurring with tin during CV.<sup>83</sup>

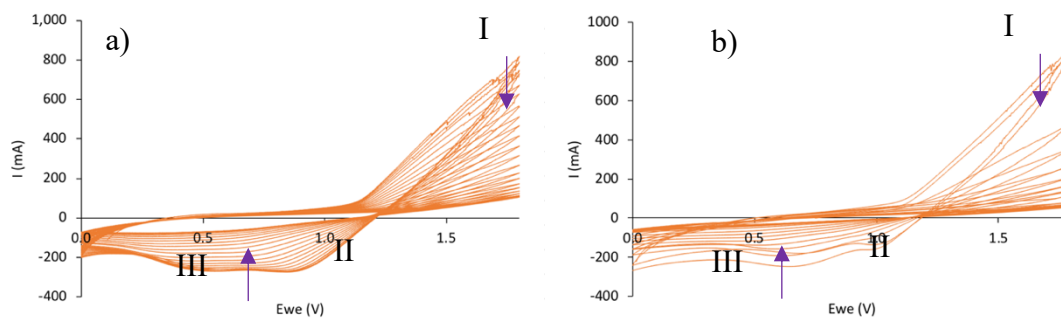


Figure 3.7: Cyclic voltammetry of Au on a) A800 and b) P800 at  $100 \text{ mV s}^{-1}$ .

CA plots in Figure 3.8 show an initial increase in charge as the reduction reaction of  $\text{Au}^{3+}$  to Au begins. This begins to decay exponentially with time due to diffusion limitations until the plot plateaus when the reduction rate and diffusion rate become equal, corresponding to the growth of electrodeposited gold films or crystals on the counter electrode.<sup>84</sup>

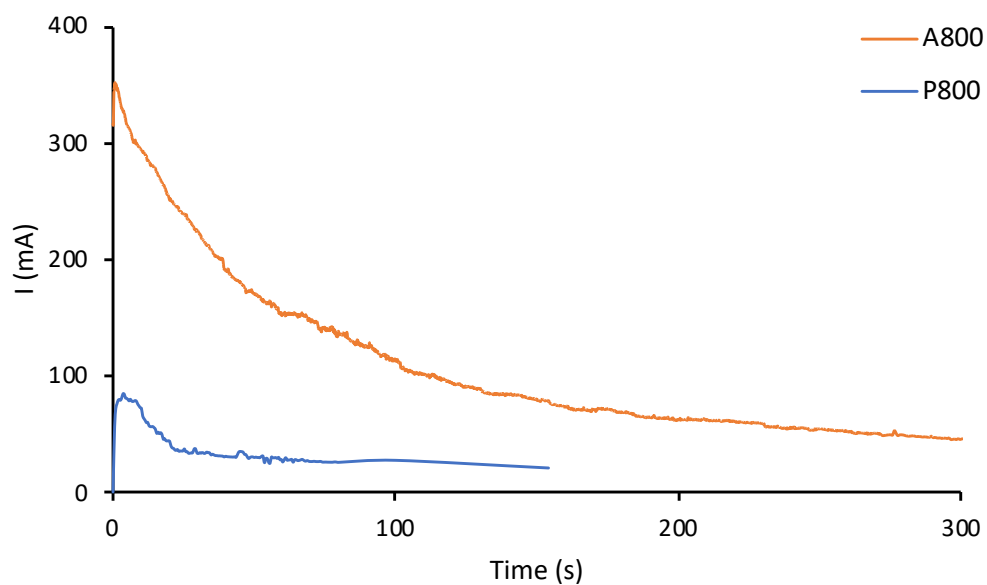


Figure 3.8: Chronoamperometry of Au on A800 and P800 at 2 V.

Cyclic voltammetry was repeated on both samples after chronoamperometry and in both cases, no change was seen. Since there was not enough material to test both methods separately, it is unknown whether CV or CA alone would have sufficed as a desorption method.

To further confirm the desorption of gold, XPS in Figure 4.10 and 4.11 shows peaks for gold going from strong clear peaks before desorption, to barely visible peaks after desorption for both A800 and P800, confirming that any gold in the samples has successfully been removed. This is again confirmed in both materials through TEM images by the presence of nanoparticles in the materials before desorption, and the lack of any particles after desorption.

XPS was also used to detect the presence of other metals in the sample and thus confirm adsorption data obtained by ICP-MS. As shown in Figure 3.9 and 3.10, tin was found in both A800 and P800. A summary of the concentrations is listed in Table 3.4. Atomic percentages were converted to weight percentages by the equations described in the previous section. The metal compositions correlate well between XPS and ICP-MS, indicating a good distribution of the metals throughout the sample. Compared to previous examples where close to 100% of the gold was adsorbed, in this case only around 70% of the gold was adsorbed, indicating that the materials have reached their adsorption capacity and therefore there should be homogenous metal distribution.

Two changes can be seen in the carbon XPS spectra before and after desorption. Firstly, a new peak at 290.3 – 290.4 eV characteristic of carbon bound to a fluorine atom.<sup>85</sup> The fluorine is present in the sample from the polyvinylidene fluoride (PVDF) binder used to attach the Starbons onto the carbon cloth. Residual fluorine in the sample indicated the need for a better rinsing procedure in future to ensure all PVDF is removed and the Starbon is returned to its original state so that it can be reused with the same efficiency for gold uptake. Secondly, an increase in sp<sup>3</sup> carbon, which is unlikely to have an effect on reduction of gold however further investigation is necessary to guarantee material reusability. If, the material is not found to be directly reusable, then it may require a simple regeneration step by heating up to 800 °C under vacuum.

With regards to desorption, the percentages obtained from XPS and ICP-MS for gold and tin have been calculated and are summarised in Table 3.5 and 3.6. Although complete gold desorption is shown through XPS, this was not the case with ICP-MS and this is because the desorbed gold did not remain in solution but was deposited onto the counter electrode, as was inferred through cyclic voltammetry in Figure 3.7. With regards to tin (Table 3.6), again some is present in solution as shown by ICP-MS but a large portion is shown to have desorbed according to XPS. The F content was found to

be 8at% and 15at% for A800 and P800, corresponding to 20wt% and 34wt% PVDF in the Starbons. If, PVDF were completely removed, then the weight percentages of tin in the samples would go up and therefore the desorption percentages would be significantly reduced. This means that deposited gold on the counter electrode is of a higher purity than indicated here. Additionally, tin can be desorbed separately by performing cyclic voltammetry at negative potential ranges to ensure 100% purity of gold at the working electrode during subsequent CVs at higher voltages.<sup>80</sup>

Table 3.4: The percentage metal composition in A800 and P800 before gold removal as

Starbon	XPS				ICP-MS	
	at%		wt%		wt%	
	Au	Sn	Au	Sn	Au	Sn
<b>A800</b>	0.04	0.21	0.59	1.87	0.60	1.64
<b>AP00</b>	0.06	0.63	0.85	5.39	0.60	5.36

analysed by ICP-MS and XPS.

Table 3.5: The percentage gold composition and subsequent percentage of removed

Starbon	XPS			ICP-MS	
	at%	wt%	Des (%)	wt%	Des (%)
<b>A800</b>	0	0	~ 100	0.05	7.99
<b>AP00</b>	0	0	~ 100	0.01	2.02

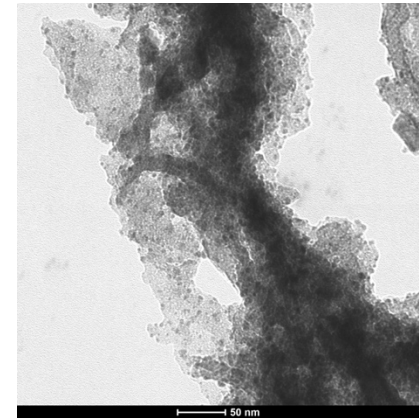
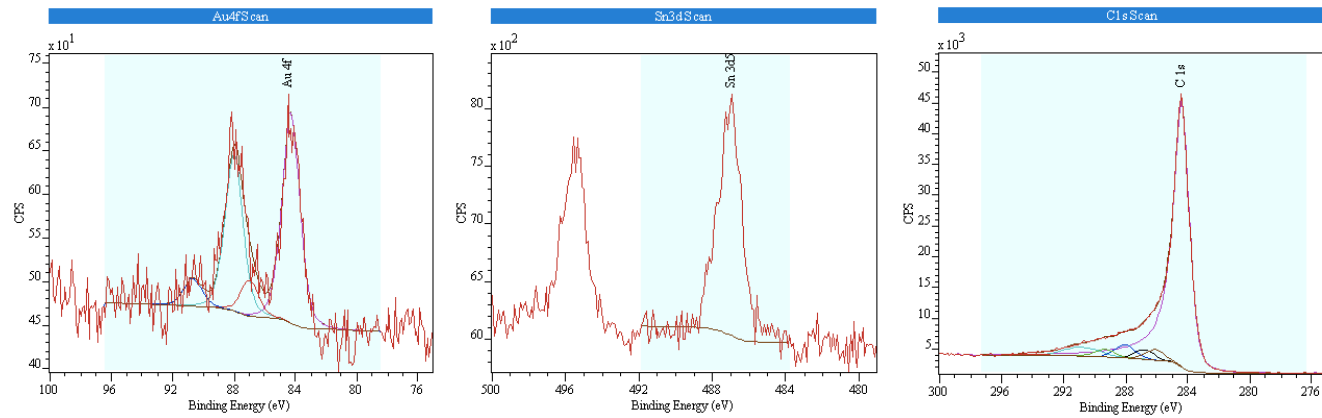
gold in A800 and P800 after gold removal as analysed by ICP-MS and XPS.

Table 3.6: The percentage tin composition and subsequent percentage of removed tin

Starbon	XPS			ICP-MS	
	at%	wt%	Des (%)	wt%	Des (%)
<b>A800</b>	0.11	1.10	41.2	0.17	10.3
<b>AP00</b>	0.02	0.22	95.9	0.13	2.38

in A800 and P800 after gold removal as analysed by ICP-MS and XPS.

Before desorption



After desorption

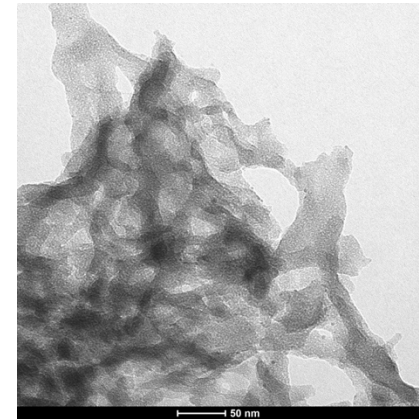
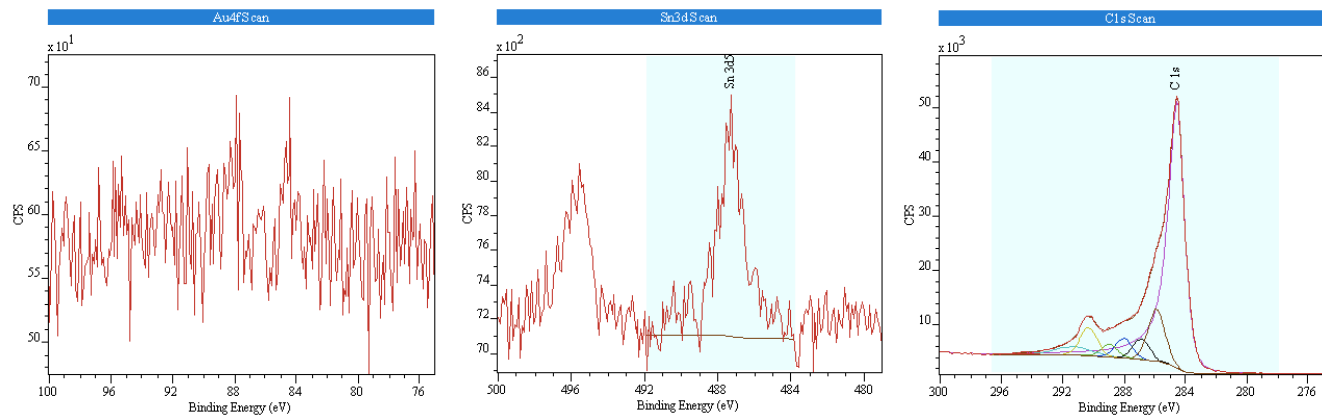
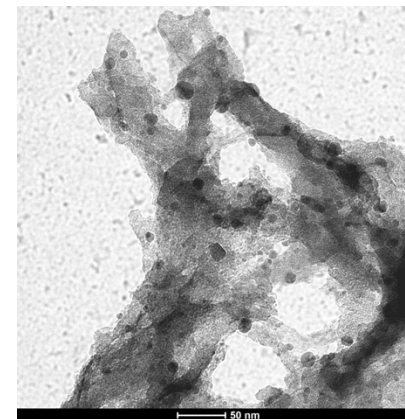
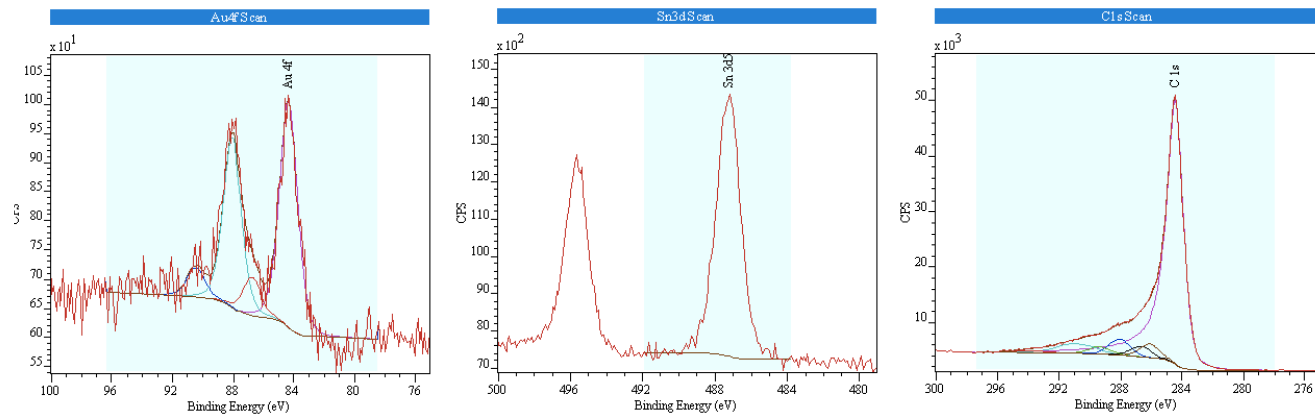


Figure 3.9: a) High resolution XPS spectra of i) gold, ii) tin and iii) carbon for A800 before and after metal removal. b) TEM images of A800 before and after metal desorption at a magnification of 98000x.

Before desorption



After desorption

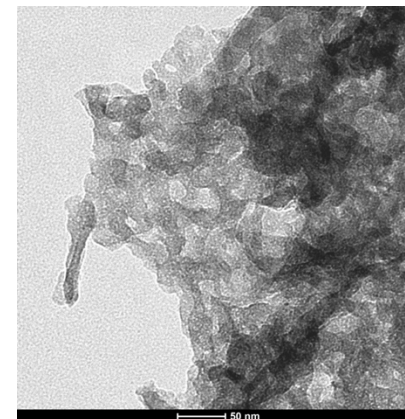
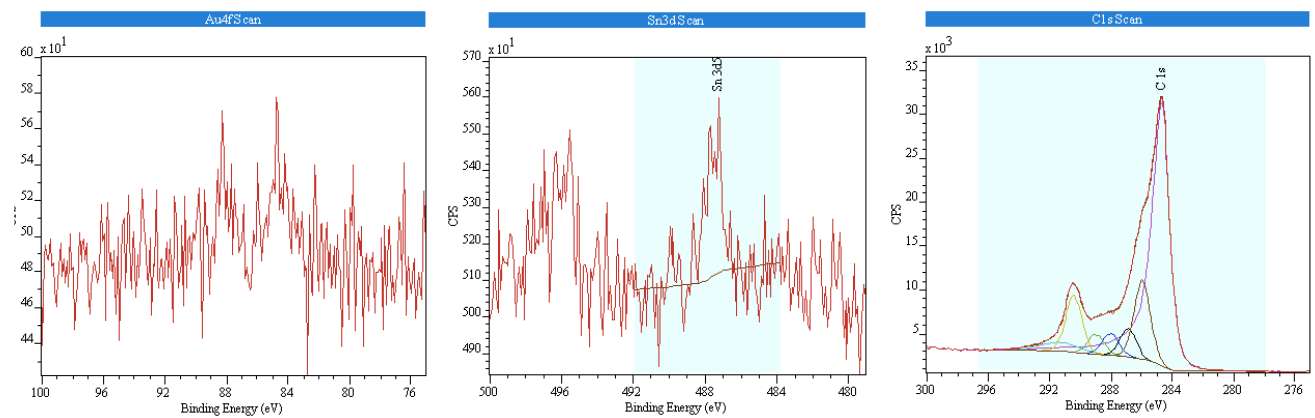


Figure 3.10: a) High resolution XPS spectra of i) gold, ii) tin and iii) carbon for P800 before and after metal removal. b) TEM images of P800 before and after metal desorption at a magnification of 98000x.

## 3.4 Indium

Indium is an element that has garnered considerable interest in terms of elemental recovery. Over 70% of indium is used in the manufacture of the alloy; indium tin oxide (ITO).<sup>86</sup> ITO is a transparent conductive coating that is sputtered on glass in liquid crystal displays (LCDs).<sup>56</sup> LCDs are flat-panel displays that have replaced cathode ray tubes (CRTs) because they are small, lightweight, emit less heat, have a lower power consumption, and do not emit harmful radiation.<sup>87</sup> The components that make up an LCD are shown in Figure 3.11. Component 1 provides the lighting of the screen, often comprising a light source on two opposite sides and a diffuser which ensures equal lighting throughout the whole screen. The polarising filters (component 2) dictate the brightness and contrast of the screen depending on their orientation respective to each other. The two glass panels (3) are each coated with the ITO electrode layer mentioned above, allowing voltage to pass through the screen. This voltage passes to the alignment layers (4), which themselves dictate the alignment of the liquid crystals held between the spacers (5). The amount of voltage passing through, determines the rotation of the liquid crystals in each pixel and thus how much light passes through that pixel. For example, if it were a blue pixel and blue was desired on the screen, then the other colour pixels would be switched off by their respective liquid crystal rotation.<sup>56</sup>

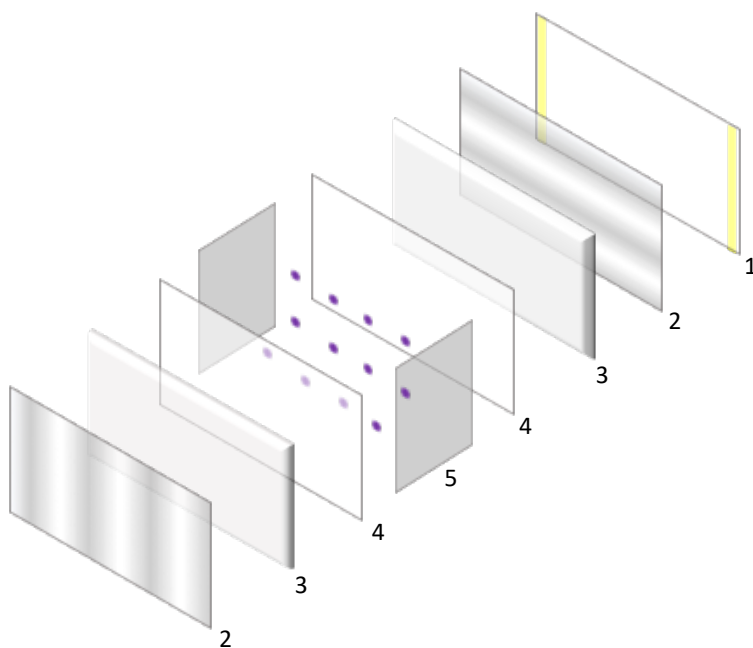


Figure 3.11: The components of an LCD.

ITO is composed of around 80 – 90%  $\text{In}_2\text{O}_3$  by weight and around 10 – 20%  $\text{SnO}_2$ . This means that over 65% of the ITO films can theoretically be recovered as pure indium.<sup>88</sup> Indium is not present in the earth in concentrated ores like many other metals, but rather is obtained as a by-product from zinc ores. Its weight content in these ores is less than what is present in LCDs, making end-of-life LCDs a highly valuable resource. The United Nations Environment Program reported that currently, the end of life recycling rate of indium is below 1%.<sup>71</sup> Indium is also used in other applications such as semiconductors, solar cells and solders. Waste indium is already commonly recycled from ITO sputtering targets. This is because during the sputtering process, only around 30% of the ITO ends up on the LCD screen itself. The remaining 70% ends up on the sputtering chambers. From here, it can be easily sand blasted and indium can be obtained at ~ 95% purity by size separation or acid dissolution followed by base precipitation.<sup>89-91</sup>

Recycling of indium from used LCD screens however has proven challenging. There are a few processes that have shown to work on a lab-scale but these use large volumes of solvents and corrosive acids which are hazardous and pose a great risk to the environment and are thus not green. Furthermore, there are only a handful of studies performed as a proof-of-principle showing the capability of certain materials to extract indium from prepared indium solutions, without any test for selectivity over other metals present in LCD waste such as tin. One study showed the possibility to adsorb indium onto chitosan-coated bentonite beads.<sup>92</sup> Another showed similar results on an amino methylene phosphoric acid resin and a third study used modified solvent impregnated resins containing *sec*-octylphenoxy acetic acid.<sup>93, 94</sup>

Many of these methods therefore rely on an efficient pre-treatment of the LCD modules before any indium can be recovered. Li *et al.* achieved 85% indium recovery using a thermal shock method to first remove the polarising film, followed by ultrasonic cleaning to remove the liquid crystals from the glass and finally acid dissolution to recover indium.<sup>95</sup> Wang *et al.* demonstrated a way to recover other valuable materials along with indium. This was done by initial dismantling and removal of the liquid crystal. The polarising film was separated from the glass with the ITO so that it could be pyrolysed to obtain compounds that could be used as gas fuels, gasoline, light and heavy fuels. The glass with ITO was immersed in acid for recovery of indium. The glass

could potentially then be used as construction material.<sup>96</sup> The idea of efficient liberation or size-reduction was also tested by Dodbiba *et al.* In their work, grinding methods were compared with electrical disintegration. A life cycle assessment (LCA) determined that the environmental burden of electrical disintegration is five times less than grinding, an interesting finding given the rarity of published research that utilised this method.<sup>88</sup>

Other studies, mainly those that involve solvent extraction, have focused on the comparison between various leaching solutions for the liberation of the ITO layer from the LCD panel. Large volumes of concentrated HCl, H<sub>2</sub>SO<sub>4</sub> and HNO<sub>3</sub> and aqua regia have shown to work well. Concentrations of acids and leaching times can be drastically reduced by ultrasonication.<sup>97, 98</sup> Shimofusa *et al.* patented one such procedure though the volume of HNO<sub>3</sub> required makes the process expensive.<sup>99</sup> HNO<sub>3</sub> shows the slowest dissolution rate of ITO.<sup>90</sup> Felix *et al.* included their solvent extraction method in a complete LCA. It was found that manual dismantling of the LCD screens avoids the largest amount of CO<sub>2</sub> production. Additionally, the optical components, being 25 wt% weight of the LCD monitor, were re-used to produce energy efficient LED fittings. With regards to the recovery of indium, various concentrations of H<sub>2</sub>SO<sub>4</sub> and HCl were compared as leaching solutions. Solvent extraction was performed with di-2-ethylhexylphosphoric acid (DEHPA) in kerosene. The extractant was unable to reach complete selectivity from either leachate. As a result of their differing selectivities however, it was suggested that leaching would be done in H<sub>2</sub>SO<sub>4</sub>, followed by solvent extraction to remove Al, Cu, Fe and Zn. Finally, a second solvent extraction with HCl is carried out to separate indium from tin.<sup>100</sup> The extraction mechanism here is through ion exchange. It is likely that a polymeric indium species is being formed in the process.<sup>101, 102</sup> Apart from using DEHPA alone, studies have shown that adding a modifier such as tributyl phosphate (TBP) improves selectivity of indium.<sup>103</sup>

The method developed by He *et al.* is different from those previously discussed. In this study, 90 wt% indium was recovered from LCD powder by vacuum carbon-reduction using coke powder at 1223 K and 1 Pa for 30 minutes. The by-product is CO, which is less hazardous than large volumes of acid. For this to work however, 30 wt% carbon is used. The weight percentage is calculated from that of the whole LCD, which includes the glass and SnO<sub>2</sub>. This leaves indium at only 0.2 g kg<sup>-1</sup> LCD scrap. Additionally, the SnO<sub>2</sub> is also reduced in small amounts to Sn, making the final indium product impure.<sup>86</sup>

### 3.4.1 Adsorption from LCDs

As was done for gold, adsorption of indium from LCD waste leached into aqua regia was tested. In this case, no adsorption was seen for indium, or any other element to any significant extent. This may be because no elements with high reduction potentials are present at a high enough concentration. Therefore, the metals are more likely to remain in the highly acidic and oxidising solution than be reduced by the Starbon surface. For this reason, adsorption of indium was tested from solutions of varying pH, to determine whether the acidity of aqua regia was preventing indium from being adsorbed. This was done by preparing solutions of indium(III) chloride at the same indium concentration as the LCD leachate ( $\sim 45 \text{ mg L}^{-1}$ , Table 3.1). The solution was found to have a pH of 3.7, acid and base were added until solutions of pH 1.5, 2.5, 4.5 and 5.5 were obtained. Adsorption was tested with A800 and the results are shown in Figure 3.12. Complete adsorption onto A800 was only reached at pH values at and above the natural pH of the indium(III) chloride solution as  $\text{H}^+$  reduces the number of binding sites available for adsorption of indium(III).<sup>92</sup>

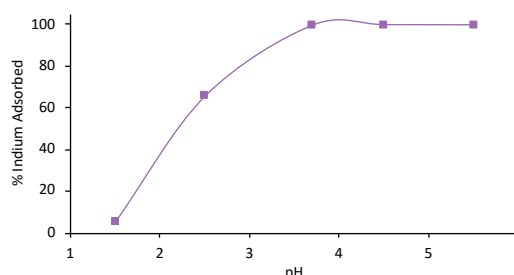


Figure 3.12 Adsorption of  $\text{In}^{3+}$  (0.35 mg) onto 10 mg A800 after stirring for 5 h at 35 °C in solutions of various pH values.

Due to the above results, sodium hydroxide was added to the leachate solution to obtain a pH of 3.7. Adsorption was again tested with Starbons, Algibons and Pecbons at 300 and 800 °C, as well as with activated carbon. Unfortunately, no drop in concentration was seen here either for indium. Additionally, from the 43 elements tested, the only change in concentration was for tin, as was sometimes observed with PCB waste. Adsorption ranged from 20% to 100% in the following order: S300, AC, P800, A800, P300, S800 and A300. No trend can be noted between material properties and adsorption due to the large errors that occur in rapid scan type analysis. Further investigation of tin adsorption is discussed later in this chapter.

### 3.4.2 Adsorption from standard solutions

In order to work towards recycling of indium from LCD screens using Starbon materials, adsorption of indium by Starbons needs to be better understood. For this reason, adsorption experiments using an indium(III) chloride solution were carried out. Standard solutions on indium(III) chloride solution were prepared at concentrations close to that found in the leachate. Starbons made from all three starting materials at both low (300 °C) and high (800 °C) preparation temperatures were tested. The results are shown in Figure 3.13.

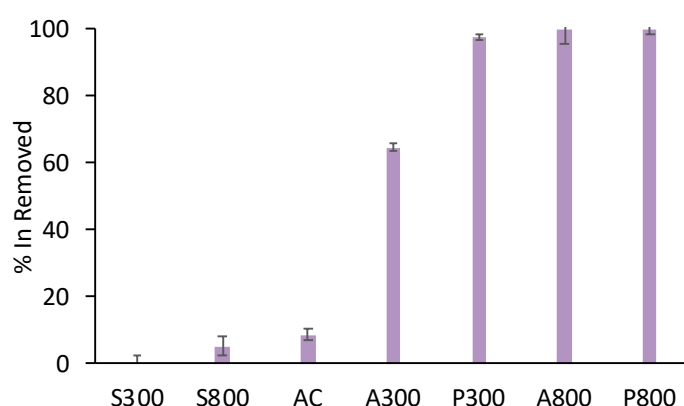


Figure 3.13: Adsorption of  $\text{In}^{3+}$  (0.35 mg) onto various Starbons, Algibons, Pecbons and activated carbon (10 mg) after shaking for 3 h at room temperature.

Adsorption is very clearly successful with Algibons and Pecbons, especially with materials prepared at higher temperatures, where complete adsorption was achieved. This implies a minimum adsorption capacity  $35 \text{ mg g}^{-1}$  for A800 and P800. Activated carbon performed poorly adsorbing less than 9% of the indium. Adsorption capacities (Q) were calculated by means of the following equation;

$$Q = \frac{(C_0 - C_e)V}{m}$$

where  $C_0$  ( $\text{mg L}^{-1}$ ) is the initial concentration,  $C_e$  ( $\text{mg L}^{-1}$ ) is the concentration after adsorption,  $V$  (mL) is the volume of solution and  $m$  (mg) is the mass of adsorbent.

The main difference between Algibons and Pecbons, and Starbons is that alginic acid and pectin both contain carboxylate groups while starch does not. Additionally, given the high temperature that activated carbons are produced at, it is unlikely that there are

any carboxylate groups on the surface, putting it in the same category as the Starbons, hence their similar performance in this experiment. Indium has a reduction potential of  $-0.34\text{ V}$ , meaning it is a lot less likely than gold to reduce down to nanoparticles within the Starbons. Literature shows that similar experiments onto similar carbons adsorb indium through interactions between  $\text{In}^{3+}$  and carboxylate groups.<sup>104, 105</sup> Having said this however, Starbons prepared to high temperature should contain no carboxylate groups and they will have chemically reduced on carbonisation.

Although Pecbons performed slightly better than Algibons, A800 was selected for further analysis as production is already scaled up to the kilogram stage. Investigation of the effects of pH were shown in the previous section (Figure 3.12), therefore all experiments were performed at the solution's natural pH of 3.7. Figure 3.14 shows the effect of temperature on adsorption over time. In this case, the samples were not agitated as to prevent adsorption from occurring too quickly to study. The results show that adsorption is quicker when heated to  $50\text{ }^{\circ}\text{C}$ . Although the adsorption did not reach 100% completion at  $20\text{ }^{\circ}\text{C}$ , previous experiment show that agitation does in fact give 100% adsorption in under 3 hours. Additionally, as explained in the introductory chapter, thermodynamics of physisorption state that heating actually favours desorption and not adsorption. This means that at a lower temperature, the materials are more likely to achieve higher adsorption capacities. Furthermore, it is clear that agitation is necessary to reach equilibrium in a more time-efficient manner.

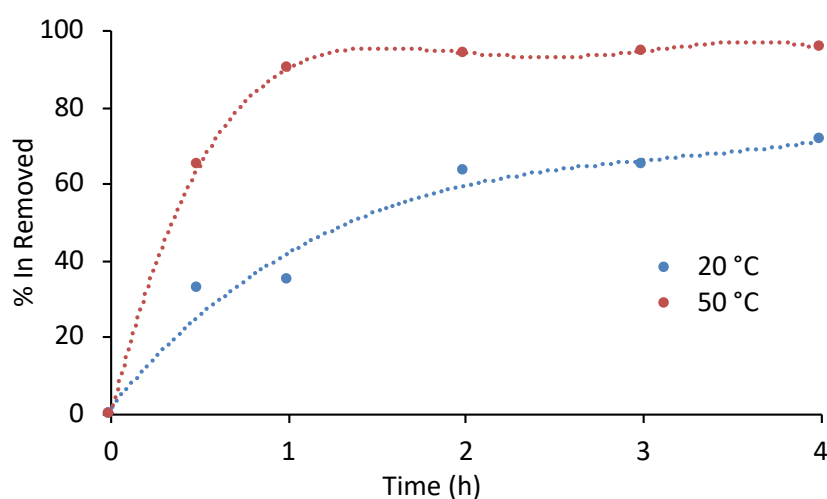


Figure 3.14: Adsorption of  $\text{In}^{3+}$  onto A800 at several time intervals at room temperature and at  $50\text{ }^{\circ}\text{C}$ .

As pectin-based materials exhibited the best results overall, further experiments were performed to determine the adsorption capacity (Q) of the materials at various carbonisation temperatures; 300 °C, 450 °C, 600 °C and 800 °C. This was done by increasing the volume of indium(III) solution, keeping the same indium(III) concentration (~ 70 mg L<sup>-1</sup>) and Pecbon mass. The adsorption capacities for each material are shown in Table 3.7.

Table 3.7: The adsorption capacities of all Pecbons for indium(III).

<b>Carbonisation temperature (°C)</b>	<b>In<sup>3+</sup> adsorption capacity (mg g<sup>-1</sup>)</b>
<b>300</b>	100.6
<b>450</b>	114.1
<b>600</b>	111.0
<b>800</b>	63.0

The main factors influencing the adsorption capacity are surface area, pore volume and surface functionality. Complexation requires electronegative groups on the surface of the materials to coordinate with In<sup>3+</sup>; such as –OH, -C=O, C-O-C and -COOH. On the other hand, high surface areas and pore volumes make room for several of these active sites to be available. The right balance between these properties seems to have been achieved at the lower three temperatures, which simultaneously allows for the process to be greener by avoiding excessively high temperatures for material preparations. These materials have largely different surface areas, which does not seem to have had a determining effect since P800 has the highest surface area but poorest adsorption. This also applies to pore volumes, where P800 has over three times the volume but the poorest adsorption again. The reason for P800’s poor performance is its loss of surface functionality on carbonising to such a high temperature. The right balance between the materials seems to have been achieved with P450 and P600.

Low carbonisation temperatures mean that less energy is required to produce the material, making the process more green and sustainable overall. Thus, P450 is considerably favoured over P600 in this case.

Finally, the results were compared to similar work in the literature (Table 3.9). The adsorption capacity of pecbons is exceedingly higher than any previous work. The reason for this is likely because the published systems involves use of resins or are simply coatings on other materials such as beads. This essentially dilutes the adsorbent materials, lowering their overall capacity.

Table 3.8: A comparison of indium(III) adsorption capacities of various adsorbents in the literature.

<b>Adsorbent</b>	<b>In<sup>3+</sup> adsorption capacity (mg g<sup>-1</sup>)</b>
<b>Pecbon-450</b>	114.1
<b>Chitosan-coated bentonite beads</b>	17.9 <sup>92</sup>
<b>Coated solvent impregnated resins</b>	23.8 <sup>106</sup>
<b>Modified solvent impregnated resins</b>	26.3 <sup>94</sup>

### 3.4.3 Indium-Starbon characterisation

To investigate the mechanism of adsorption of indium onto Starbons, TEM images were taken of A300 and A800 both before and after indium adsorption, as shown in Figures 3.15. Unexpectedly, spots are visible in the A300 sample after adsorption. These are lighter in colour than would be expected however. If, they were solid metal particles, then nothing would be able to pass through them, and therefore they should appear black. For this reason, it is unlikely that they are metal nanoparticles but instead are more likely artefacts potentially through damage caused by the electron beam. Moreover, none appeared in the A800 sample. Since A800 is more chemically reduced than A300, A800 would be the more likely sample to reduce indium down to In(0) nanoparticles, if it were possible at all.

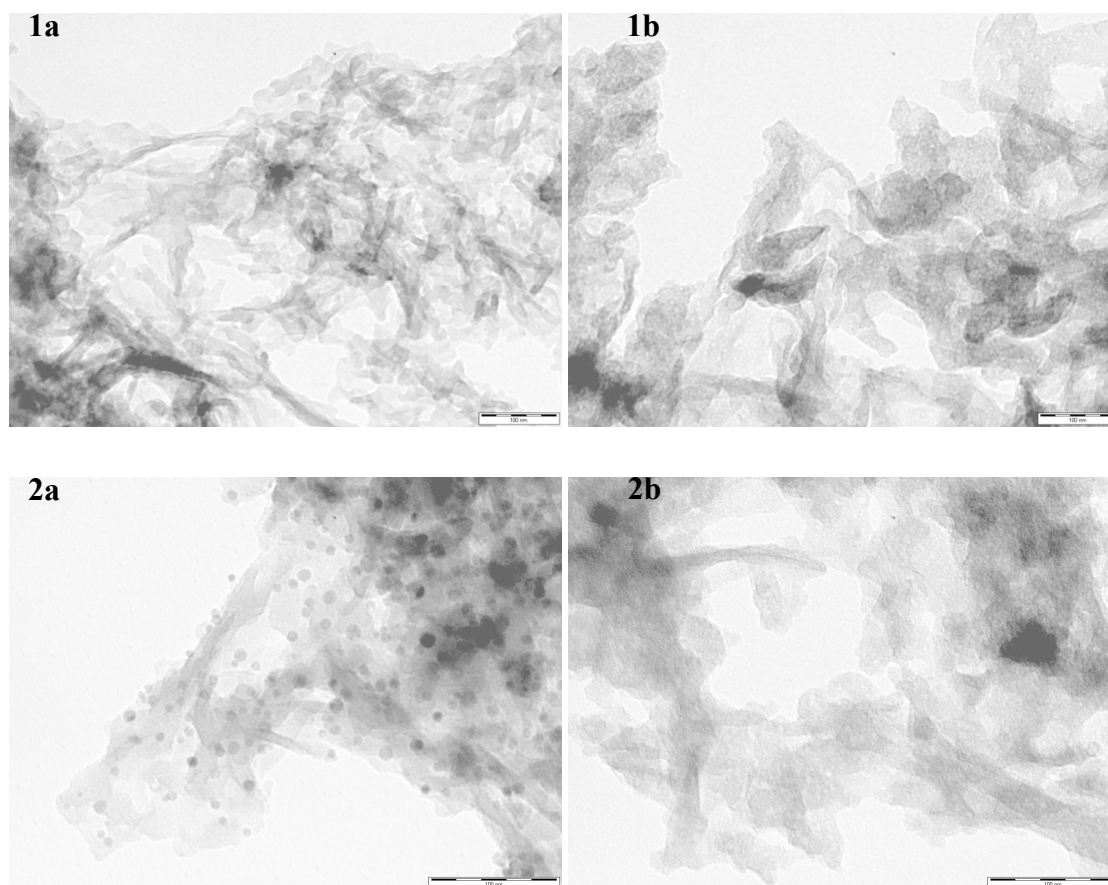


Figure 3.15: TEM images 1) at 135000x magnification before indium adsorption and 2) at 220000x magnification after indium adsorption of a) A300 and b) A800.

To compliment the images obtained by TEM, XPS was carried out on all Aligibons after adsorption with indium to confirm the metal's presence as well as determine its oxidation state(s). Low temperature (A300) and high temperature (A800) Aligibons are shown here (Figures 3.16 and 3.17, respectively) to illustrate any differences between the two extremes. No differences were noted between these two materials and A450 and A600 so they have been omitted from this discussion for simplicity.

Characteristic indium XPS peaks are clear in both A300 and A800, confirming the presence of indium in both samples. XPS of indium is however not straight forward in giving oxidation states because the peak shifts between the different states are too small. In these cases, Auger Electron Spectroscopy (AES) can be used in addition to XPS. AES gives information on the auger electron given off during X-ray irradiation. The peak shifts for the MNN electron of indium are clearly separated, allowing for easy determination of oxidation states. The disadvantage of using MNN peaks is that they

are a lot weaker in nature, and therefore low concentrations aren't always detected. The XPS and AES peak positions are tabulated in Tables 3.9 and 3.10, respectively.

For both materials, only one species (oxidation state) is present. When comparing A300 and A800, there were no differences in peak positions, indicating that the same species is adsorbed onto the surface of both. Literature data for AES In MNN peaks of different oxidation states is sparse, therefore exact comparisons of peak positions are unreliable. Having said this, it is still possible to deduce the oxidation state of indium in these spectra. With XPS, components with higher oxidation states have higher binding energies (XPS) and lower kinetic energies (AES) as shown;



conservation of energy requires that;

$$E(M) + hv = E(M^+) + E(e^-)$$

since the energy of an electron is the kinetic energy;

$$KE = hv - (E(M^+) - E(M))$$

and since difference in energies between the ionised and neutral atom is the binding energy;

$$KE = hv - BE$$

Indium(0) is known to have a kinetic energy of around 410 eV, therefore compounds such as indium(III) chloride or indium(III) hydroxide give appreciably lower kinetic energies of between 404 and 406 eV. As the kinetic energy of the In MNN peaks in Table 3.10 are considerably lower than 410 eV, it is probable that indium has formed an indium(III) complex bound to the carboxylate or other oxidised species on the Starbon surface, giving a peak of kinetic energy closer to those of indium(III) chloride and indium(III) hydroxide.<sup>83, 107, 108</sup>

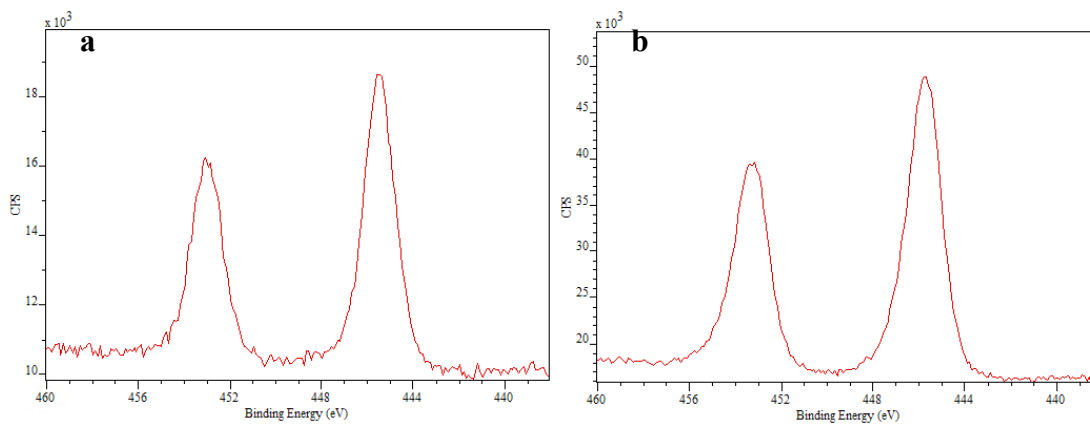


Figure 3.16: XPS peaks for In on a) A300 and b) A800.

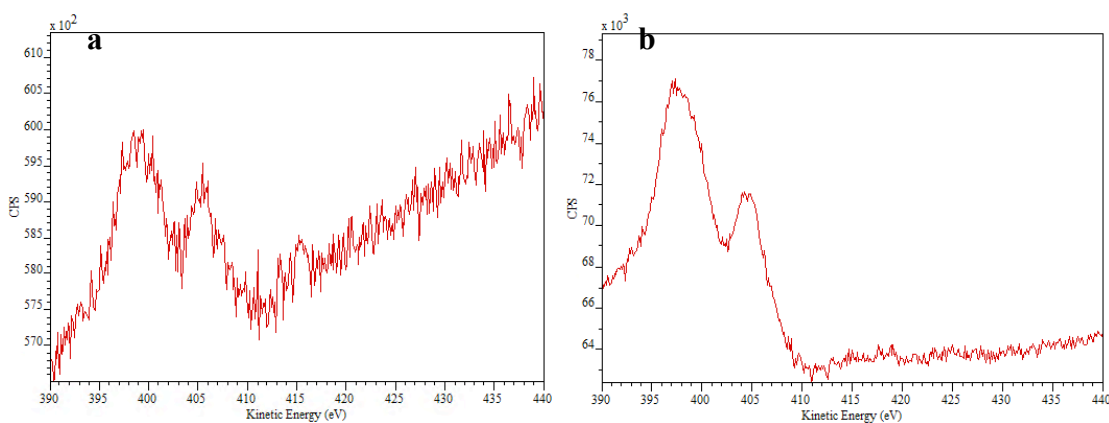


Figure 3.17: AES peaks for In on a) A300 and b) A800.

Table 3.9: The binding energies (eV) for the XPS peaks of In on A300 and A800.

Sample	Peak 1	$E_B$ (eV)	Peak 2	$E_B$ (eV)
In-A300	3d 3/2	453.00	3d 5/2	445.46
In-A800	3d 3/2	453.31	3d 5/2	445.72

Table 3.10: The kinetic energies (eV) for the AES peaks of In on A300 and A800.

Sample	Peak 1	$E_K$ (eV)	Peak 2	$E_K$ (eV)
In-A300	In MNN	404.89	In MNN	397.82
In-A800	In MNN	404.41	In MNN	397.50

From the XPS spectra, atomic and weight percentages were found as described in the previous section. The results are shown in Table 3.11, as a comparison with the data obtained from ICP-MS. Since XPS only analyses one portion of the sample, it may not be representative. This may account for the discrepancy between XPS and ICP-MS weight percentages in Table 4.10. In this case however, three portions of the sample were analysed, and in each case, similar results were obtained. This indicates that the majority of indium is adsorbed onto the outermost surface of the material, as XPS cannot analyse further than the first 5 nm on the material's surface. This reasoning is especially fitting in this case since 100% adsorption was reached in both cases, meaning there would be no  $\text{In}^{3+}$  left in solution to adsorb once the surface is completely bound.

Table 3.11: Showing the percentage composition of total indium after adsorption of each metal onto both A300 and A800, calculated from XPS spectra.

Starbon	XPS		ICP-MS
	at%	wt%	wt%
A300	0.50	4.18	1.86
A800	1.6	12.46	1.87

As the XPS and AES results are inconclusive, simultaneous thermal analysis was performed to check whether the above results were correct and reliable. A300 containing adsorbed indium was heated up to 625 °C. The melting point of indium is known to be 156.6 °C. Any indium(0) in the material would therefore melt at this temperature, and as it is an endothermic process, the heat flow should decrease and therefore show a strong trough. As this is not present in Figure 3.18, it is likely that there is no indium(0) in the material. This means that the adsorption mechanism of indium is not by reduction but is most probably by complexation.

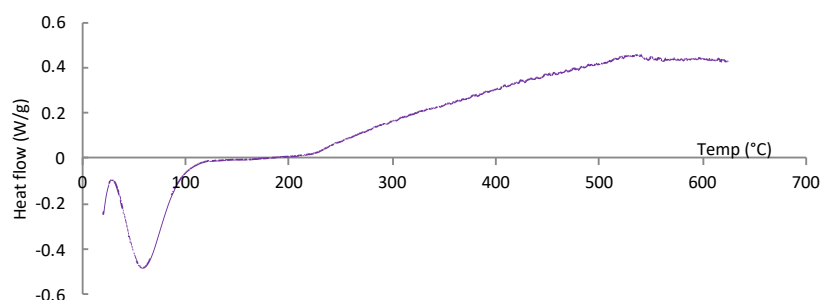


Figure 3.18: The heat flow of A300/In obtained by STA when heated up to 625 °C.

### 3.4.4 Desorption and re-use

Desorption was tested with three Starbons of low and high carbonisation temperatures and different starting materials so as to cover the whole range of materials that performed well in the adsorption of indium(III). The first desorption experiment involved a general test by washing with water, a pH 3.7 solution and acetone. Desorption was unsuccessful in each case, giving little to no desorption.

The second desorption experiment involved a longer wash with aqueous solutions of various pH values. The results for A800, P300 and P800 are shown in Figure 3.19. Desorption was negligible in all pH systems apart from the strongly acidic solution at pH 1, where desorption of above 90% was achieved with A800. P300 and P800 gave only slightly lower desorptions. Indium is sparingly soluble in basic solutions. It is soluble in neutral and acidic solutions.<sup>109</sup> Although a pH of 4 should be enough to solubilise indium, it is apparently not preferential when compared to the strength of complexation of indium(III) with the Starbon surface.

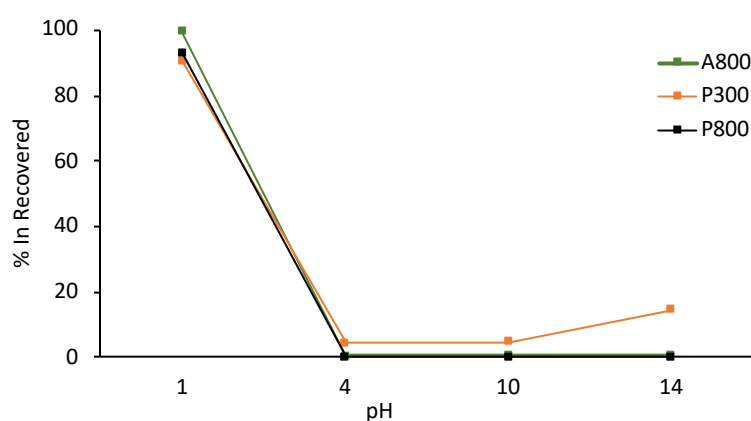


Figure 3.19: Showing the percentage desorption of indium after washing with aqueous solutions of different pH values.

With highly successful adsorption and desorption of indium(III), Starbons have the potential to be used in real applications. For the process to be both economically and environmentally sustainable, it is imperative that Starbons are reusable. With Pecbons performing best on adsorption, the whole range of Pecbons were therefore tested for their reusability.

The reusability experiment includes indium(III) adsorption and desorption in three repeats using the same material, each time calculating the percentage adsorbed and desorbed in order to test whether the materials retain their original adsorption capacity. Desorption percentages (%) were calculated as follows;

$$\% des = \frac{[In^{3+}] \text{ after desorption}}{[In^{3+}] \text{ adsorbed} + [In^{3+}] \text{ previously not desorbed}} \times 100$$

In each case, the maximum adsorption capacity for the materials was used to ensure that the materials are loaded to their full capacity and thus it will be certain that the entire effective surface via which adsorption is taking place, will be included and tested in each run. The results are shown in Figure 3.20. In all cases, complete desorption was repeatedly achieved. With regards to adsorption, it is clear from the results that materials carbonised to lower temperatures seem to be far more reusable than those carbonised to higher temperature. Adsorption remains well above 70% for both P300 and P450. P600 drops to around 50% and P800 down to 20%. Other reusability experiments were performed with A800, which also showed poor reusability. This indicates that all Starbon materials carbonised to lower temperatures are generally more reusable than those carbonised to higher temperatures. This may be due to the surface functionality of the materials post-desorption. The acid may be reacting almost irreversibly with the materials prepared at 800 °C, leaving them in an unusable form while the materials prepared at 300 °C are reacting with the acid in a close to irreversible way, allowing them to efficiently re-adsorb indium. P450 again gave the best results, making it the material with both the highest adsorption capacity and best reusability

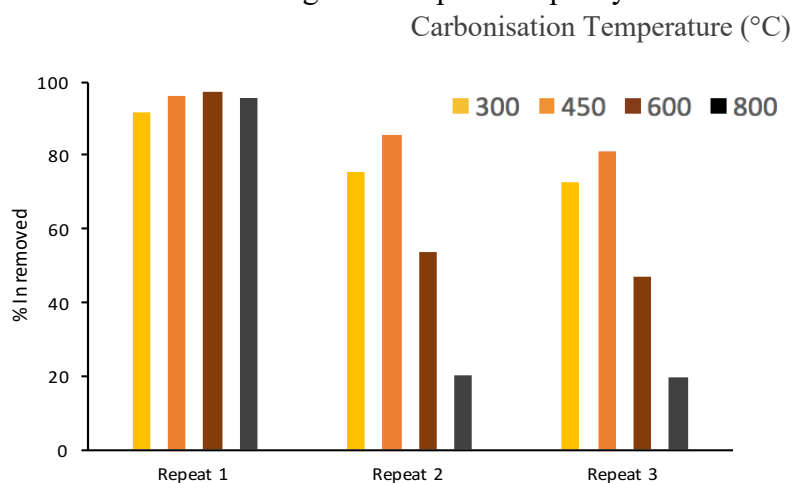


Figure 3.20: The reusability of Pecbons for indium(III) adsorption.

### 3.4.5 Selectivity for tin(IV) over indium(III)

From the first indium adsorption studies it was found that Algibons and Pecbons were capable of adsorbing indium, but the Starbons were not, and thus Starbons were excluded from all subsequent experiments. This fact however, makes Starbons the preferred candidates for selective adsorption of tin from the mixture. Tin adsorption by all four Starbons (S300, S450, S600 and S800) was tested and over 90% adsorption was achieved in each case.

Following successful tin adsorption, selectivity was tested for all four Starbons (S300, S450, S600 and S800) as well as low and high temperature Algibons (A300, A800) and Pecbons (P300, P800). Indium(III) and tin(IV) concentrations were chosen to imitate those in the leachate solution. The results are shown in Figure 3.21. With Starbons, in each case, adsorption of indium(III) remained below 22%. Adsorption of tin(IV) however was significantly higher (up to 94%), especially when using low temperature materials (300 °C and 450 °C). As with indium, since the more oxidised surfaces are more successful, adsorption is likely taking place via complexation and not reduction, this being due to the negative reduction potential of  $\text{Sn}^{2+}$  to  $\text{Sn}^0$  (-0.1375 V).<sup>110</sup> With regards to Algibons and Pecbons, very high adsorptions are obtained for both indium and tin with no preferential adsorption for either metal. Although complete selectivity is not achieved, the hypothesis of this experiment was proven as Starbons show a strong preference for tin adsorption over indium adsorption, a key step towards the metals' separation in ITO waste. The remaining solution after adsorption will be more highly concentrated in indium, and further adsorption steps could lead to even higher purity of indium in the final solution.

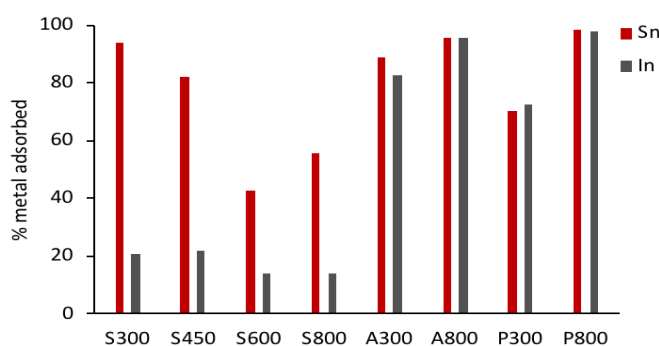


Figure 3.21: Adsorption of Sn (0.055 mg) and In (0.22mg) onto a range of Starbons (10 mg).

To ensure that a pure solution of  $\text{In}^{3+}$  is obtained, the solution can be passed through Starbon several times. By the end of the process, all the  $\text{Sn}^{4+}$  would have been removed. As Figure 3.21 showed that S300 and S450 were the best at selectively adsorbing  $\text{Sn}^{4+}$ , they were selected for further testing. The experiment involved passing an indium and tin solution through three batches of the Starbon and repeating this three times with fresh solution through the same Starbon samples. The results are shown in Figures 3.22a and 3.22b for S300 and S450, respectively.

In both cases, fresh Starbon adsorbed more  $\text{In}^{3+}$  than in the repeats. The main difference between using fresh material and used material is that fresh material will have empty micropores. Once these micropores fill up, it is difficult to remove anything from them unless placed under vacuum or heated up. This is due to the high interaction provided by the high surface area to volume ratio in such a small pore, which means that there is more material surface area available to bind to each metal ion. Thus, each metal ion is bound more tightly than it would be in a mesopore. Once the micropores fill up, adsorption and desorption should remain more or less constant in the mesopores unless the solutions react with the surface in a way that is detrimental to adsorption.

The fact that there is less selectivity in the first run implies that selectivity is affected by pore size. This falls in line with the fact that the materials carbonised to lower temperatures (300 °C and 450 °C) show better selectivity than the materials carbonised to higher temperatures (600 °C and 800 °C), since higher temperatures caused some of the mesopores to collapse, making the higher temperature materials more microporous than the lower temperature materials and therefore show less selectivity. This is again because material entering and binding to micropores will be irreversible and will occur on a first come first serve basis, since desorption will not occur and therefore there will be no opportunity to re-adsorb selectively and reach a more preferential energy state at equilibrium. The only factor influencing micropore adsorption is diffusion, and this is likely to favour adsorption of  $\text{Sn}^{4+}$  first since it has a higher charge and will be pulled towards the surface more strongly than  $\text{In}^{3+}$ . Thus, with a more oxidised surface and a lower degree of microporosity, S300 is the most successful selective adsorbent of  $\text{Sn}^{4+}$  over  $\text{In}^{3+}$ . For each repeat in Figure 3.22a, S300 showed 100% removal of  $\text{Sn}^{4+}$  from the first run. Subsequent runs may therefore not be imperative but may be useful in ensuring that the final solution is uncontaminated with tin.

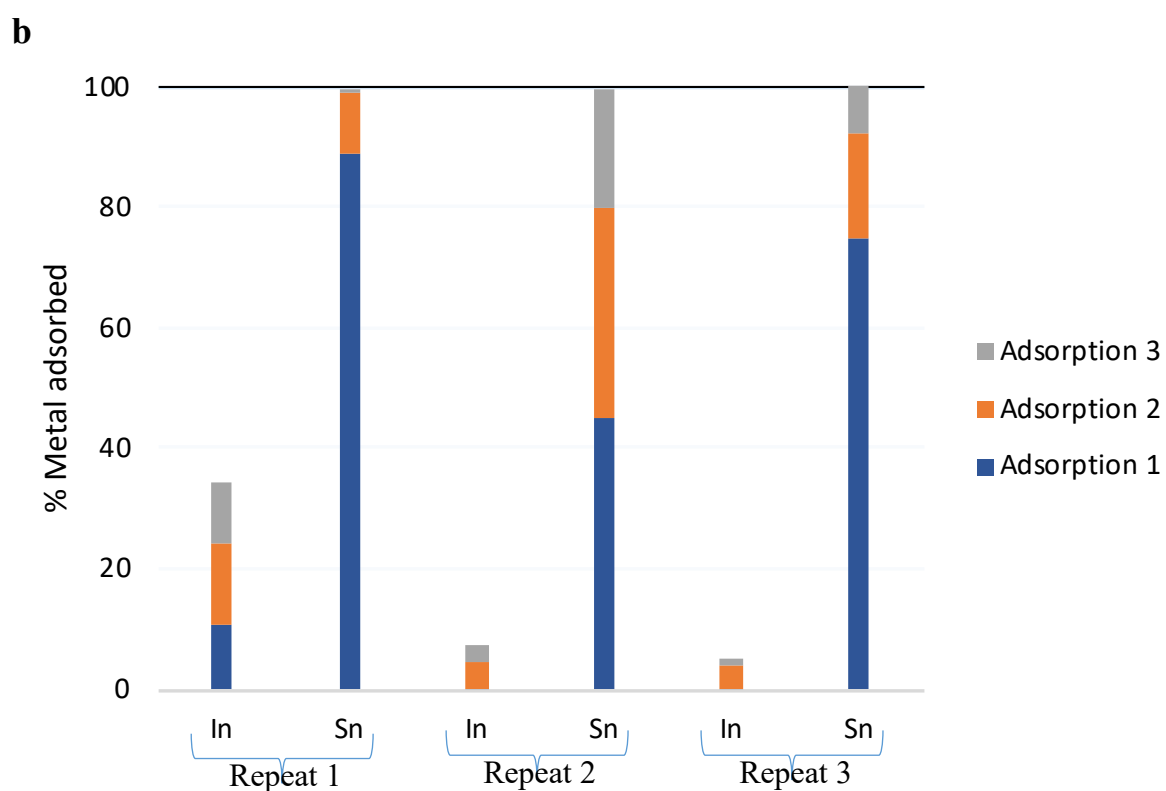
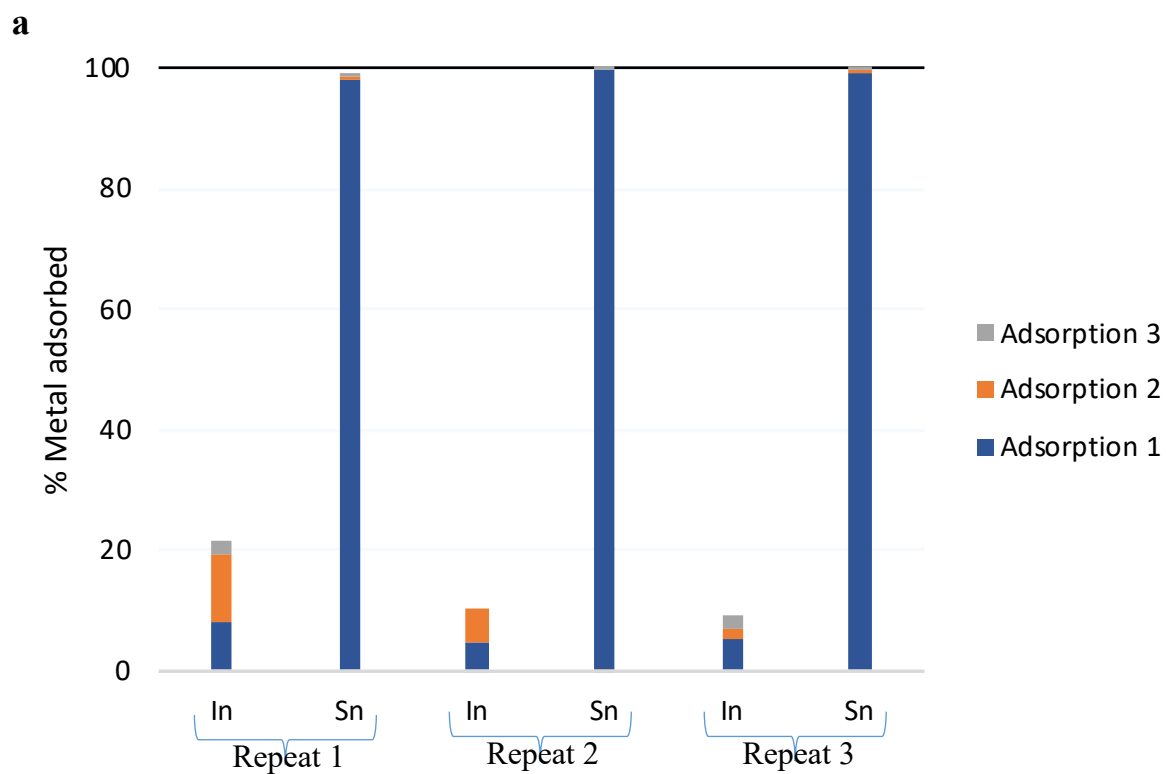


Figure 3.22: Complete removal of  $\text{Sn}^{4+}$  by a) S300 and b) S450 from a standard aqueous solution of  $\text{In}^{3+}$  and  $\text{Sn}^{4+}$  after 3 repeats.

## Chapter 4

# Adsorption of MAAs



## 4.1 Introduction

“Ultraviolet (UV) radiation in sunlight is the most prominent and ubiquitous physical carcinogen in our natural environment.” UV rays are capable of penetrating the skin but are unable to reach the rest of the human body. Human skin is therefore well adapted to UV radiation, especially in regions of the world that are exposed to stronger UV radiation from the sun. In fact, the people that inhabit these regions have well-pigmented skin while other people have paler skin, and when the latter chase sunshine and inhabit areas that they are not adapted to, skin cancer is a lot more prevalent. This is the case in the USA and Australia.<sup>111-113</sup>

UV light is divided into three ranges; UVA (400–315 nm), UVB (315–280 nm) and UVC (280–100 nm). Most of the UV radiation that reaches the earth’s surface is UVA. Although all are harmful, UVA is the least harmful of the three but is still associated with skin damage such as ageing, as well as genetic damage associated with skin cancer.<sup>111</sup> UVB is more harmful than UVA, but is mostly blocked by the ozone layer. However, any UVB that reaches the surface is more likely to cause health problems such as genetic damage, and subsequently skin cancer. UVC, the most harmful of the three, does not reach the surface of the earth as it is blocked by both O<sub>2</sub> and O<sub>3</sub>.<sup>113-115</sup>

The ozone layer has always been a form of protection from UV radiation reaching the Earth’s surface and offering protection for all living organisms. However, in the 1970s, it was discovered that nitrous oxides and chlorofluorocarbons were reacting with ozone in the stratosphere, and causing it to deplete.<sup>116, 117</sup> Throughout the 20<sup>th</sup> century, mankind increasingly expelled these compounds into the atmosphere, resulting in noticeable depletion of the ozone layer.<sup>118</sup> Finally, in 1987, productions of ozone-depleting compounds began to be controlled through a global agreements known as the Montreal Protocol.<sup>119</sup> However, the now thinned-out ozone layer is only just beginning to recover and thus its ability to absorb UV radiation is significantly diminished, causing increased exposure and consequently, increased occurrences of skin cancer.<sup>120,121</sup>

Mycosporine-like amino acids (MAAs) are small (<400 Da), highly polar, water soluble and largely colourless compounds characterised a by 6-membered carbon ring substituted with an amino side chain.<sup>122, 123</sup> They are natural compounds, synthesised as secondary metabolites by a wide range of marine, fresh water and some terrestrial

species.<sup>124, 125</sup> MAAs have received increased attention in recent years due to their ability to function as highly effective UV filters as they absorb light at wavelengths between 310 nm and 362 nm due to their characteristic conjugated systems.<sup>126</sup> This, along with their large molar extinction coefficients (28,000 - 50,000 mol<sup>-1</sup> dm<sup>-3</sup> cm<sup>-1</sup>) are ideal properties for sunscreen. Being natural, renewable and biodegradable compounds, the commercial success of MAAs is guaranteed. To date, over 30 MAAs have been identified.<sup>122-130</sup>

Isolation of MAAs however has so far been challenging. Pure MAAs are thus not yet commercially available. This work attempts to develop the first efficient method for usujirene isolation as well as its stereoisomer palythene. Usujirene was chosen as the target compound due to its high extinction coefficient (50,000 mol<sup>-1</sup> dm<sup>-3</sup> cm<sup>-1</sup>) and therefore its effectiveness as a UV absorber.<sup>131</sup> Porphyrin ( $\lambda$ -max of 334 nm) is a precursor to usujirene and palythene so its presence in the extract may also be beneficial.<sup>125</sup> Usujirene absorbs in the UVA and UVB range with a  $\lambda$ -max of 358 - 360 nm due to the lower energy of more extended conjugation system. Exposure of usujirene to UVA and/or UVB first causes a bond rotation, resulting in accumulation of palythene. Further exposure to UV light can reduce palythene to form palythine along with other non-UV absorbing compounds.<sup>125, 132</sup>

This project was carried out in collaboration with the British-Dutch consumer goods company; Unilever with support from a Business Interaction Voucher awarded by the High Value Chemicals from Plants Network, a BBSRC NIBB (grant number BB/LO13665/1). The work was started at Unilever, who identified the potential of MAAs for their application in sunscreen. They began working on extraction methodologies of MAAs from Dulse and Nori seaweed, two widely available types of algae. Although extraction was successful, there was still significant room for improvement in terms of sustainability as the method is complex and requires large volumes of solvent. The main extracted MAAs are shown in Figure 4.1. Following this, several attempts were made to isolate the target compounds from the crude extracts but were unfortunately unsuccessful. This led Unilever to collaborate with the GCCE to test Starbon materials as the potential solution to their problem. This chapter will therefore discuss the improvements made on the MAA extraction process as well as attempt different usujirene isolation methodologies including counter-current chromatography

and solid-phase extraction (SPE) using Starbon materials as the adsorbent. Successful experiments were repeated to show reusability in addition to being scaled-up to show applicability, both of which also emphasised novel, simple, efficient and sustainable procedure developed.

An additional difficulty encountered by Unilever was the presence of large quantities of floridoside. Floridoside is the major contaminant present in the seaweed extracts. It is a saccharide compound that is obtained in large quantities by the extraction method developed by Unilever. The saccharide proved difficult to remove from the extracts, causing several problems, such as clogging of systems, during any attempts made to separate MAAs. Unsuccessful methodologies employed included alumina chromatography, ion exchange chromatography and adsorption with activated carbon.

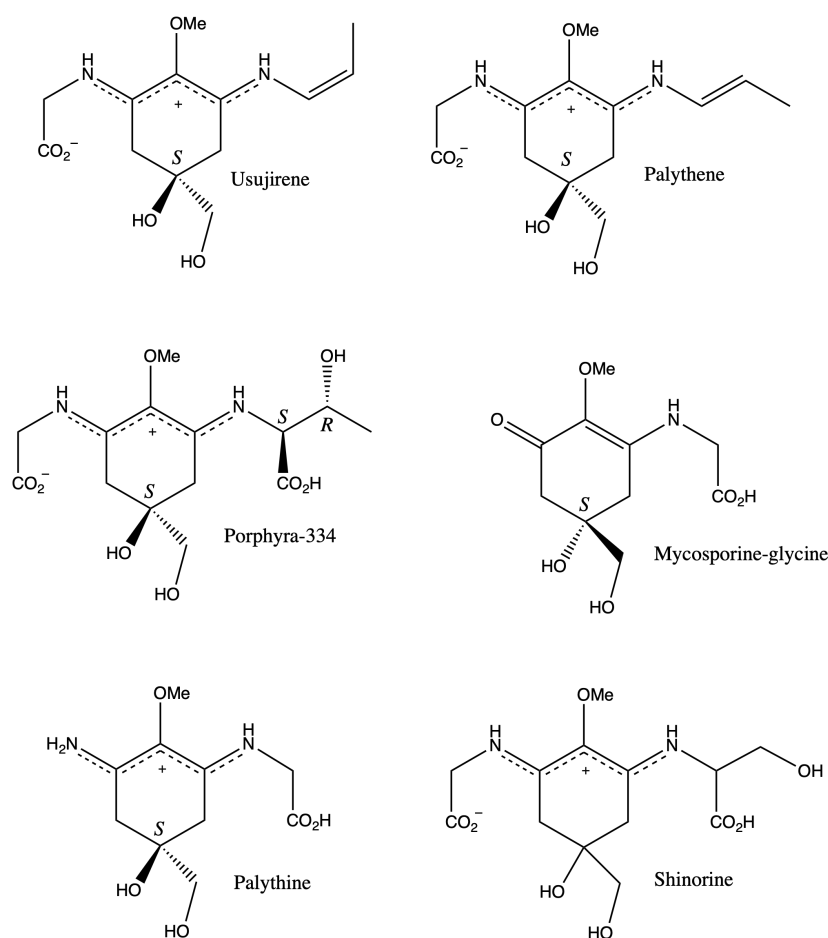


Figure 4.1: Chemical structure of a few MAAs found in Dulse.

## 4.2 HPLC characterisation of MAAs

A number of MAAs were provided by Unilever for uses as standards. Using a high-performance liquid chromatography (HPLC) method developed by Unilever (see experimental section), chromatograms for a number of MAAs in aqueous solution were obtained. As described above, decomposition of some compounds leads to formation of palythine, additionally palythine is heavily concentrated in the samples and is difficult to remove completely. For these reasons, many of the analysed standards were contaminated with palythine. The results of some of a few of the purer standards are shown in Figure 4.2. Unilever additionally sent over a standard labelled chromatogram obtained from their own in-house extraction of MAAs from Dulse (Figure 4.3). A summary of the peak positions from both characterisations is shown in Table 4.1.

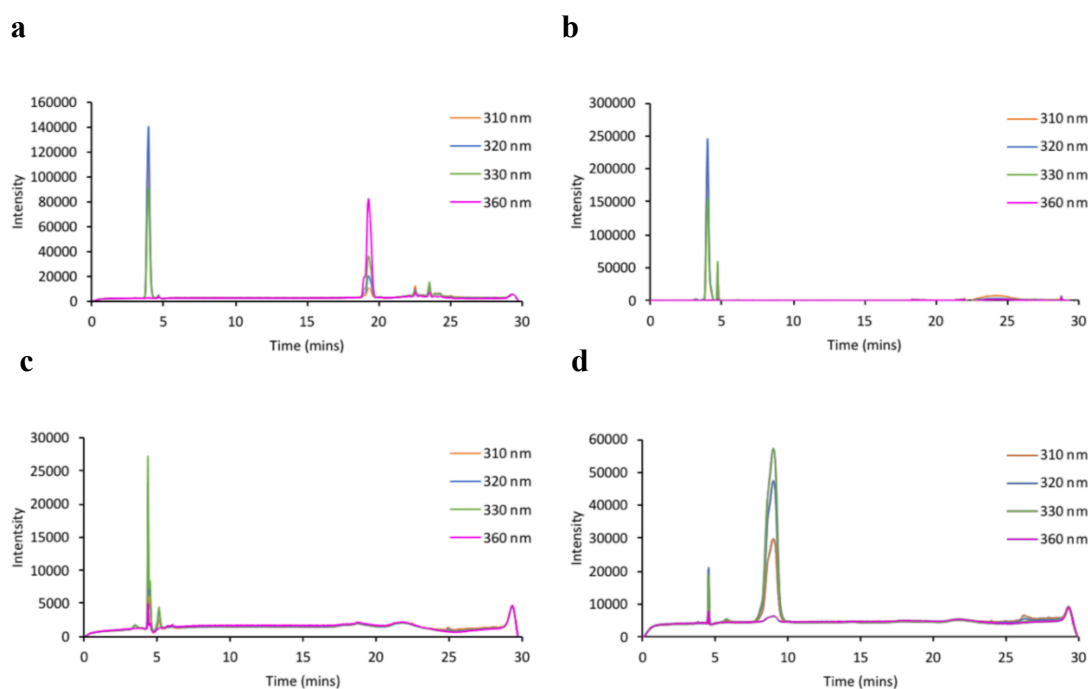


Figure 4.2: HPLC chromatograms for extracted samples of a) usujirene and palythene, b) palythine, c) shinorine and d) porphyra

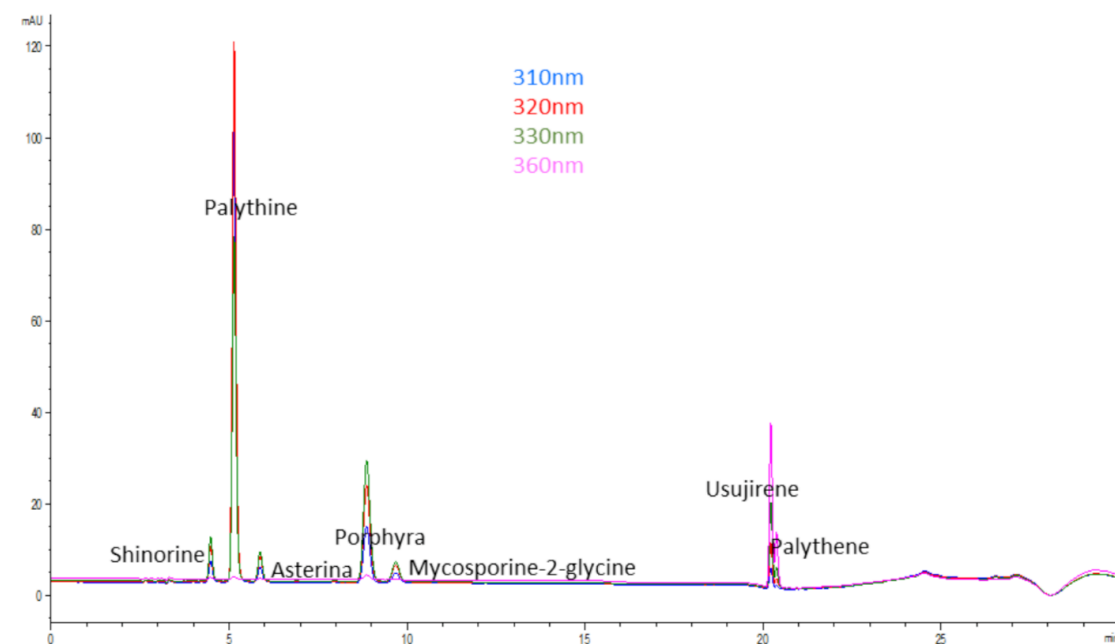


Figure 4.3: Labelled Dulse extract HPLC chromatogram (provided by Unilever).

Table 4.1: Comparison of HPLC peak times for various MAAs obtained in this work and by Unilever.

MAA	Peak time (mins)	
	This work	Unilever
Shinorine	(4.4)	4.5
Palythine	3.9	5.1
Asterina	-	5.9
Porphyra	9.1	8.8
Mycosporine-2-glycine	-	9.7
Usujirene/palythene	19.3	20.2

### 4.3 Comparison of extraction techniques

Unilever developed a solvent extraction method for Dulse seaweed. This involved three solvent washes with a mixture of water and methanol and a fourth wash with a mixture of water and ethanol. Centrifugation was carried out after each water/methanol extraction to combine the liquid fractions. Two rotary evaporation steps were also included; once to remove the water/methanol and once to remove the water/ethanol (see experimental section for details). The overall process takes between 1.5 – 2 days. In total, the amount of solvent required for this process is  $\sim 80 \text{ mL g}^{-1}$  dried Dulse. An HPLC chromatogram for the extract obtained by this method is shown in Figure 4.4.

The extraction procedure is successful in extracting MAAs from Dulse seaweed but is not sustainable due to the large amount of solvent required. A more solvent efficient method is Soxhlet extraction. This was tested using both ethanol and methanol with a solvent loading of  $10 \text{ mL g}^{-1}$  Dulse. The time taken to complete extraction was 4 hours (excluding rotary evaporation). This is a significant improvement in both time and solvent volume. Soxhlet extraction has the additional benefit of being a simple method involving only two steps; extraction and solvent evaporation. The percentage yields obtained from the different extraction methods are summarised in Table 4.2. Due to the low amount of usujirene in Dulse, extractions were also attempted using Nori, which is known to contain higher quantities of usujirene. HPLC chromatograms for Dulse and Nori extracts are shown in Figures 4.4 and 4.5, respectively.

Table 4.2: Summary of the yields obtained from each extraction attempt.

Extraction	Seaweed	Mass used (g)	Mass obtained (g)	% yield
Unilever's method	Dulse	1	0.341	34.1
	Nori	1	0.130	13.0
Methanol Soxhlet	Dulse	30.146	12.017	39.9
	Nori	10.000	0.469	4.7
Ethanol Soxhlet	Dulse	30.161	6.801	22.5

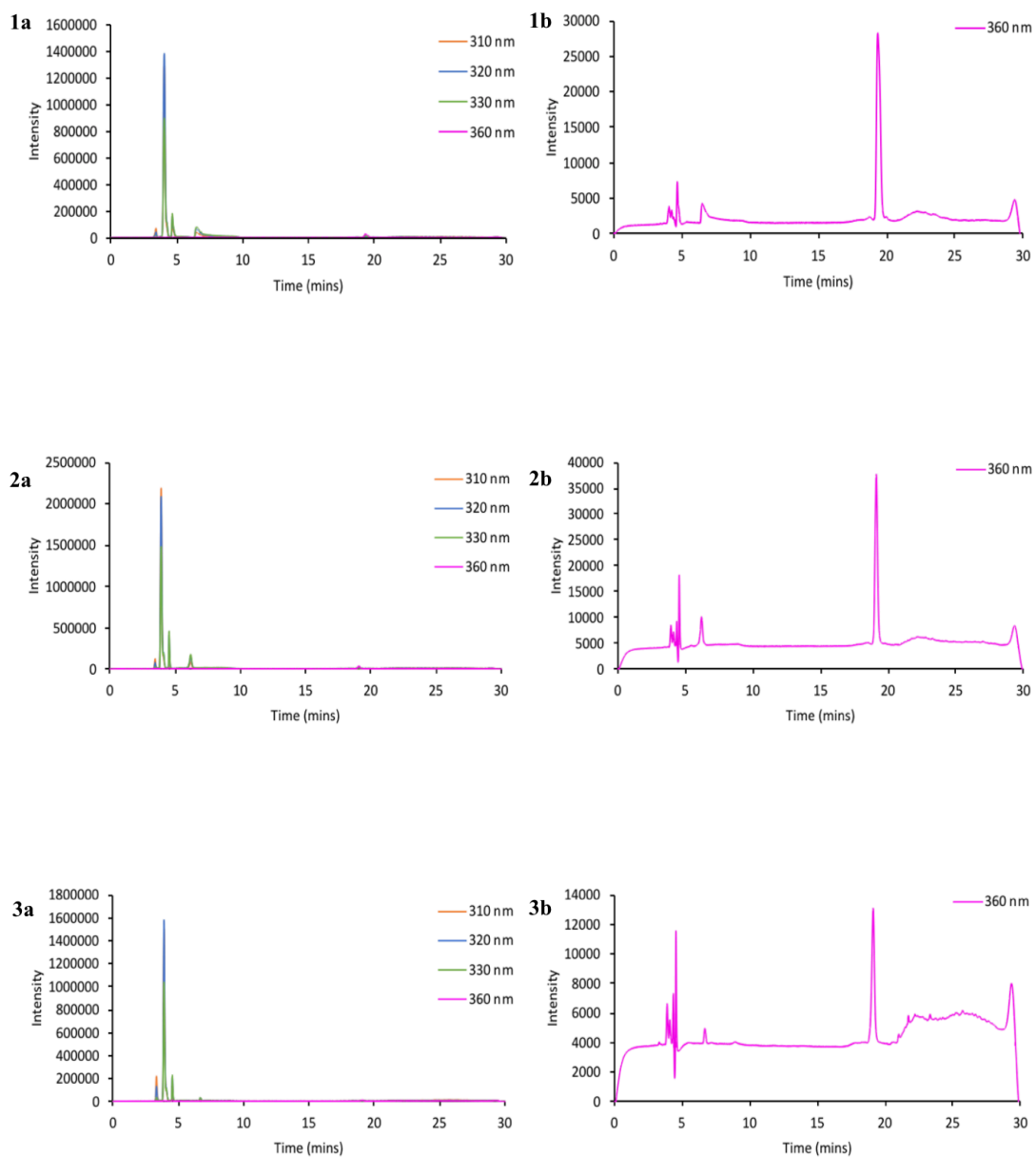


Figure 4.4: HPLC chromatograms of Dulse crude extracts in water, obtained by extraction using 1) Unilever's method, 2) methanol Soxhlet and 3) ethanol Soxhlet, at a) 310 nm, 320 nm, 330 nm and 360 nm, and b) zoomed in at 360 nm.

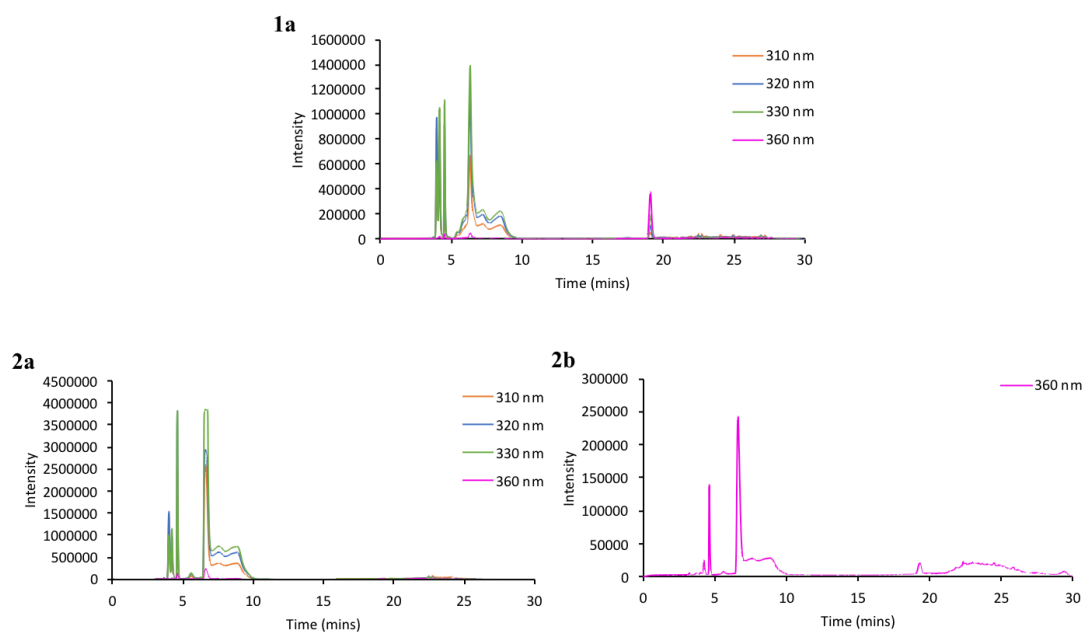


Figure 4.5: HPLC chromatogram of Nori crude extract in water, obtained by extraction using 1) Unilever’s method and 2) methanol Soxhlet, at a) 310 nm, 320 nm, 330 nm and 360 nm, and b) zoomed at 360 nm.

In all cases, sufficient usujirene (19 mins) was obtained, along with a mixture of other compounds. The Dulse sample used was around two years old and has therefore degraded. The porphyra has converted to palythene and usujirene, of which a significant quantity has subsequently decomposed into palythine, therefore a large amount of palythine is present in all Dulse extracts.

Soxhlet extraction with methanol showed to be slightly more effective in the extraction of MAAs from Dulse (Table 4.2), as compared to ethanol. This is to be expected as methanol is more polar than ethanol and the MAAs are highly polar molecules. The mass of crude extract obtained with Nori was significantly lower regardless of the extraction procedure. After extraction, in both cases it was noted that a large portion of the Nori seaweed remained relatively unchanged. Adding an initial rehydration step before extraction may therefore give improved results. The method developed by Unilever contains such a step, and may be the reason for the higher yield, but it is apparent from the results that the volume of water used was not sufficient for rehydration. As the Nori seaweed contained more usujirene, it was selected for all subsequent experiments.

## 4.4 Solvent mixture screening

Counter-current chromatography (CCC) is a type of chromatography where both phases are liquid, with the stationary phase being held in place by a centrifugal force. To determine if this method would be useful in isolating usujirene, a series of 6 biphasic solvent systems were prepared to offer a simple mimic of a CCC system with increasing polarity (Figure 4.6). The least polar mixture prepared was heptane:methanol (Vial 28) while the most polar was butanol:water (Vial 1).



Figure 4.6: Dulse extract dissolved in 6 different solvent mixtures as described in Table 10.2.

HPLC chromatograms of five of the systems (9, 13, 17, 21, 28) only showed extracts in the polar fraction and showed a mixture of all MAAs in each case, so none would have been suitable for isolation of usujirene (see appendix Figure A.1). The most polar system (Vial 1) showed MAAs in both fractions, but with low concentration in the less polar phase. Porphyra was the enriched in the aqueous phase as it is not soluble in butanol, (Figure 4.7). Thus, porphyra is the only compound with the potential to be isolated through CCC. However, with regards to the target compound, usujirene, these results conclude that CCC is not a suitable methodology for its isolation from Dulse seaweed.

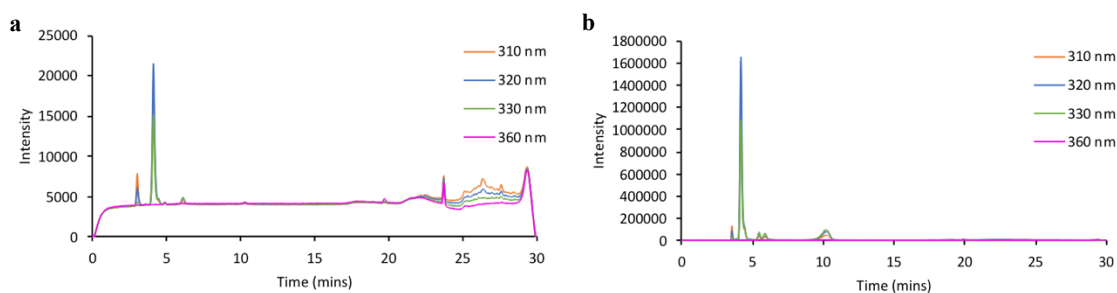


Figure 4.7: HPLC chromatogram for the butanol:water solvent system containing Dulse extract, a) butanol phase and b) water phase.

## 4.5 Isolation of usujirene using Starbons

### 4.5.1 Starbon screening

Solid-phase extraction was then tested using Starbon materials. To screen through the whole range of Starbons with great efficiency and minimal error, an autosampler was employed to perform the solid-phase extractions. For solid-phase extraction to work, the compound of interest must be soluble in the primary solvent but must then be preferentially adsorbed onto the solid adsorbent. Therefore the solubility of the compound of interest in the primary solvent must not be too great so as to prevent any adsorption. Conversely, the compound of interest must be highly soluble in the secondary solvent, so that it will preferentially desorb from the adsorbent to allow for recovery. For this reason, water was chosen as the primary solvent and methanol as the secondary solvent. White materials; expanded starch, alginic acid and pectin pre-carbonisation, were not tested as they absorb water and swell, making them unsuitable for packed solid-phase extractions with this system.

All Starbons showed adsorption and desorption of usujirene to differing extents. High temperature materials (A800 and S800) showed a small amount of usujirene in the desorbed phase with a large amount of other MAAs. Low temperature materials (A300 and S300) gave significantly higher concentrations of usujirene but still contain high amounts of other MAAs. A450 and S450 both concentrated the usujirene, with S450 giving the highest usujirene content (Figure 4.8). The HPLC chromatograms for the rest of the Starbons and Algibons have been included in Appendix A (Figure A.2 and A.3,

respectively). The experiments were performed in quadruplet and in all cases, repeatability was clearly demonstrated, indicating high reusability of Starbon materials.

The definite reason for the preferential adsorption of usujirene is not known, however a proposed explanation is to do the with the conformation of the compound. All the MAAs contain a certain degree of unsaturation, but usujirene contains the highest degree of conjugation, allowing for it to be partially planar. S300 and A300 show little to no conjugation in their chemical structures, meaning that there will be few planar components to the surface and therefore minimal preferential adsorption of usujirene over the rest of the MAAs. On the other hand, S800 and A800 contain a high degree of planarity in their graphite-like structures and therefore the non-planar component of usujirene will make adsorption unfavourable. With an intermediate carbonisation temperature such as 450 °C used to make S450 and A450, planarity is present to some extent in the adsorbent's surface structure, presumably allowing for the conformations of usujirene to be preferred over conformation of other MAAs.

Starbons carbonised to 300 °C and 800 °C still show adsorption of MAAs due to Van der Waals forces and electrostatic interactions between the functional groups of MAAs and the Starbon surfaces. Electrostatic interactions are especially the case in low temperature carbonisation materials due to their oxidised surfaces.

Apart from the excellent selectivity for usujirene, SPE using Starbons has the added benefit of overcoming any problems caused by floridoside. Floridoside often clogged any other attempted separation systems. However, given that water was chosen as the primary solvent in these experiments, floridoside has a higher affinity for the aqueous system and therefore is not adsorbed. This meant that clogging problems were avoided in the Starbon material and there was no hinderance in the liquid flow of SPE.

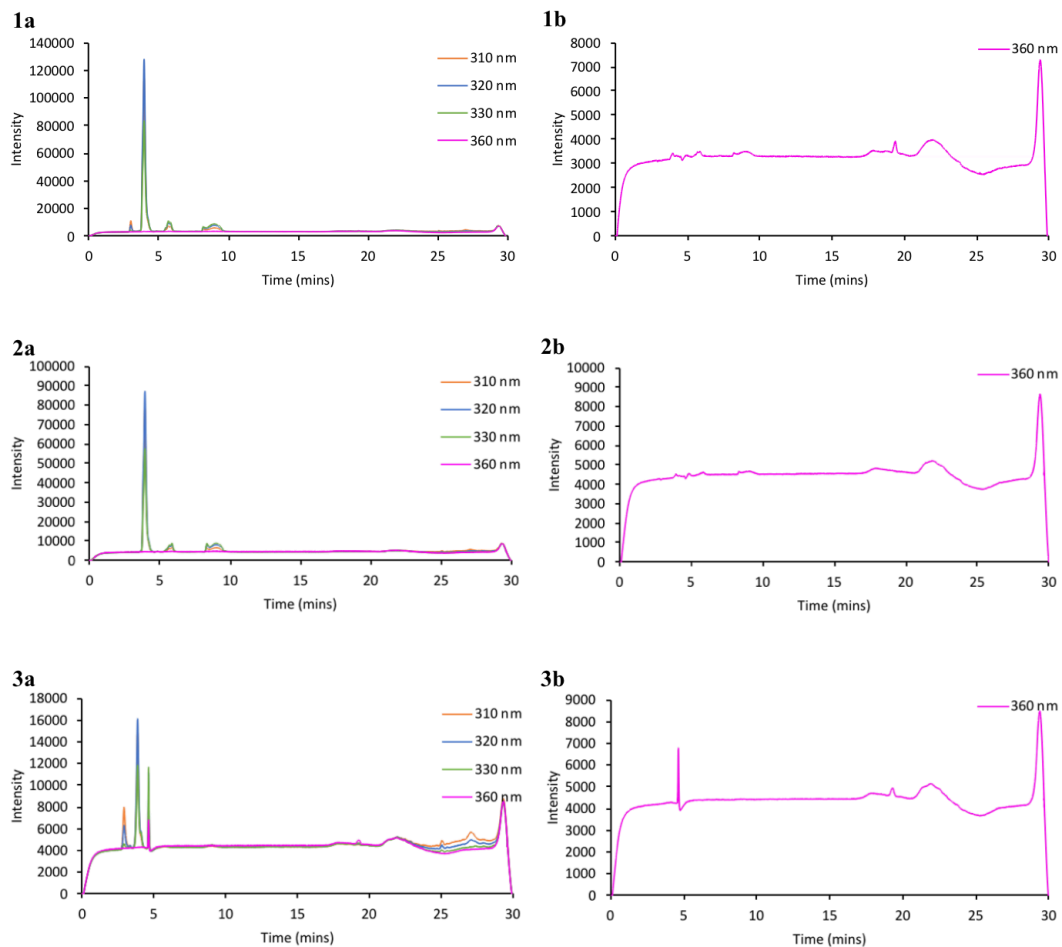


Figure 4.8: HPLC chromatograms of 1) Dulse crude extract in water, 2) Dulse extract after adsorption through S450 and 3) Dulse extract desorbed off S450 with methanol, at a) 310 nm, 320 nm, 330 nm and 360 nm, and b) zoomed in at 360 nm.

## 4.5.2 Scale-up

Once S450 was selected as the superior Starbon for adsorption, the experiment was scaled up from 0.018 g adsorbent to 1 g adsorbent. As the Dulse extracts used previously contained little usujirene, Nori extract was used for the rest of the work and the HPLC chromatogram of the solution used for adsorption is shown in Figure 4.9.

Again, four repeats were performed (see appendix Figure A.4), and the final repeat is shown in Figure 4.10. For each repeat, the same chromatogram was obtained, further confirming the reusability of the Starbon. The chromatogram clearly shows that S450 highly concentrates the usujirene, leaving only traces of other MAAs in the solution. Thus, scale-up to 1 g was undoubtedly successful.

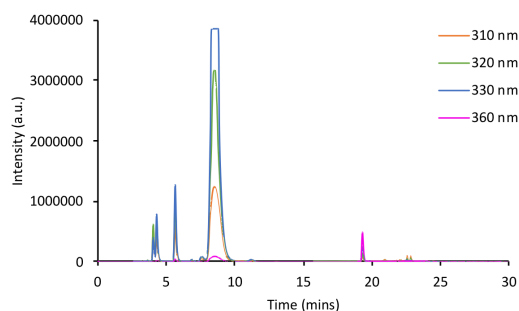


Figure 4.9: HPLC chromatogram of the extract used for large scale adsorption.

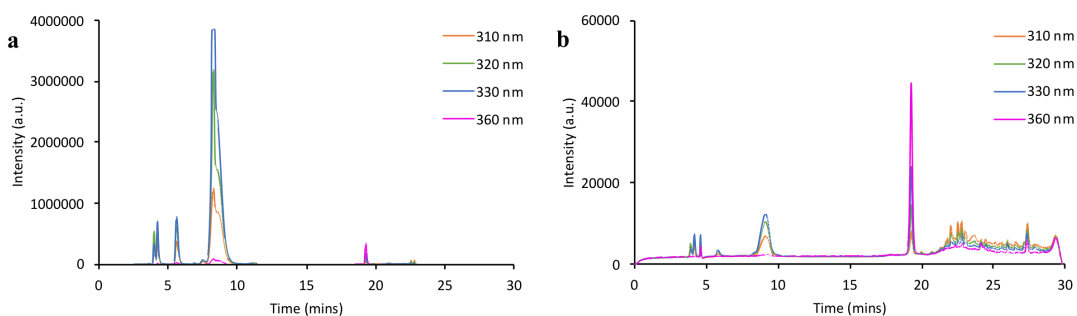


Figure 4.10: HPLC chromatograms of solutions after the 4th a) adsorption and b) desorption.

### 4.5.3 Flow simulation

On an industrial scale, such processes are more economically performed in flow, as opposed to batch processing. This is beneficial for two reasons; the first is that it will give an indication of the purity of usujirene that can be achieved from a single run, and the second is that it will show which compound(s) are selectively extracted after usujirene. Therefore, there is the potential that any secondary compounds of interest are also obtained once usujirene is removed.

The same extract solution was repeatedly passed through the same 1 g of S450, desorbing with methanol each time (Figure 4.11). Following each adsorption, usujirene content decreases until it is completely depleted in the final solution. Simultaneously, porphyra (~9 mins) content also begins to decrease slightly after the first repeat. Following the desorption, usujirene is continuously preferentially extracted until there is none left in the starting solution. As this occurs, concentration of porphyra in the desorbed phase increasingly dominates.

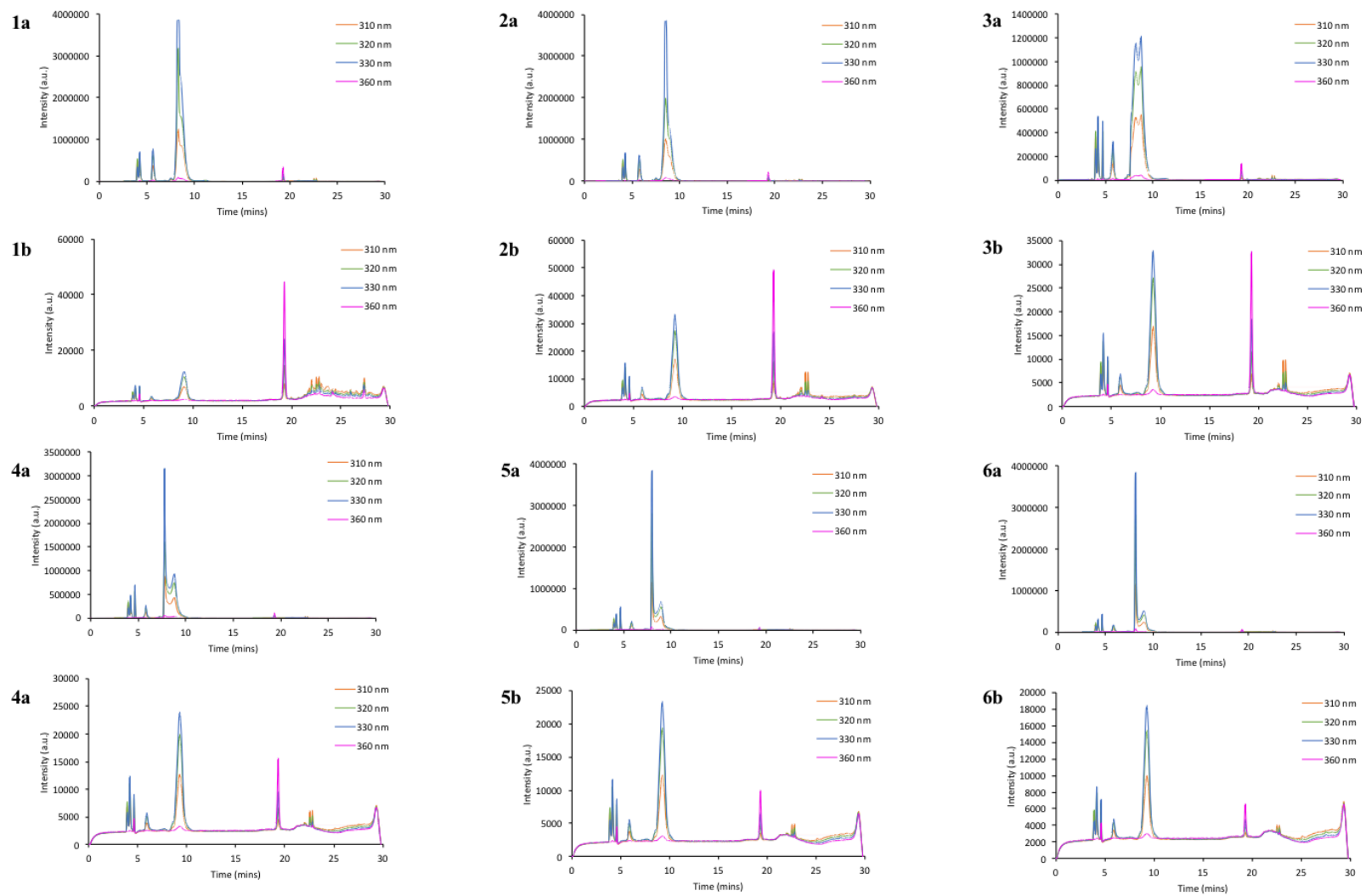


Figure 4.11: The in-flow a) adsorption and b) desorption of 1 sample of Nori solution repeatedly (1 - 6) passed through S450 to simulate a flow type system.

#### 4.5.4 Further purification

Although simple adsorption and desorption showed that one run of the extract through Starbon highly concentrates usujirene, small amounts of other MAAs are still present (Figure 4.12a). The next test was therefore to determine whether usujirene can be further purified. The methanol solvent from the desorbed solution from the scale-up experiment described previously was dried by rotary evaporation and the product re-dissolved in water so that it could be passed through the Starbon a second time for adsorption and desorption. The HPLC chromatograms of the first and second desorption runs are shown in Figure 4.12.

The second run worked extremely well in purifying usujirene. The most notable difference is the peak for porphyra at around 9 minutes, which is completely removed from the first to the second run. The other MAA peaks at around 4 minutes are significantly reduced and are only just about still visible. As MAAs are safe compounds, achieving 100 % purity for usujirene may not be essential, however it has clearly been shown that SPE using S450 is both a simple and sustainable method for isolating the usujirene target compound.

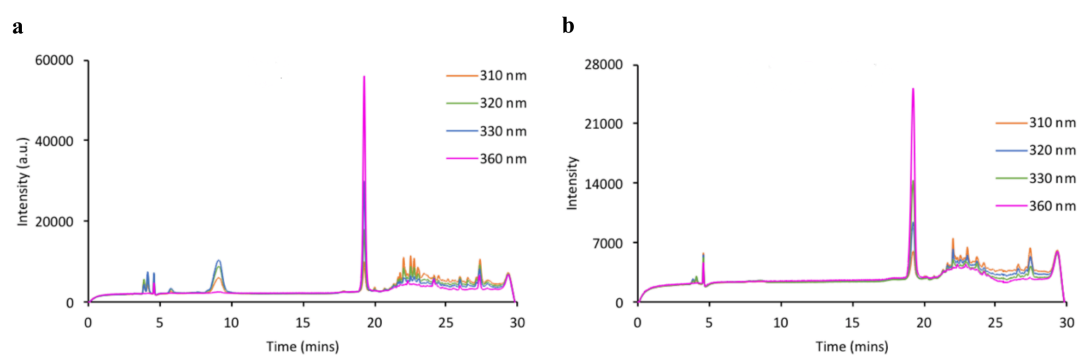


Figure 4.12: HPLC chromatograms of the desorbed phase a) after one run through the Starbon and b) after a second run through the Starbon.

Part II:

*N*-Starbons



# Chapter 5

## *N*-Starbon

# Characterisation



## 5.1 Introduction

*N*-Starbons are a new class of materials derived from Starbon materials by “doping” them with nitrogen. Altering surface functionality leads to a change in properties. The variation in functionality that can be achieved with the aforementioned three polysaccharides, carbonised to several temperatures, is indeed diverse. However, no further alterations have or can be made to achieve anything more functional without derivatising the surface, which may involve synthetic chemicals and energy-demanding reaction conditions. Development at this point may be accomplished with the introduction of other heteroatoms, such as nitrogen.

Examples of such materials in the literature include ordered mesoporous nitrogen doped carbons that have been synthesised by a chemical vapour deposition (CVD) method.<sup>133</sup> The scope here was to produce graphitic pore walls, as opposed to the amorphous pore walls that are usually obtained by hard templating. This was done with carbons alone, as well as with nitrogen-doped carbons. SBA-15 was chosen as the solid template, with styrene as the carbon source and acetonitrile as the nitrogen source. The carbonisation temperatures required here were above 950 °C, giving a nitrogen content of 8.5%. Nitrogen was found to be present in the form of quaternary nitrogen and pyridinic nitrogen.<sup>133, 134</sup>

Acetonitrile and other common nitrogen-doping sources are often toxic and non-renewable. A more sustainable attempt were the aerogels synthesised by White *et al.*, where the chosen precursors were D-glucose and ovalbumin.<sup>135</sup> This study showed a possible synthesis through hydrothermal conversion. The work was aimed at producing materials suitable for adsorption and energy applications. Previously, similar organic materials were carbonised to temperatures above 600 °C, which considerably reduces any functionality in the material. The resulting materials were, unfortunately, only weakly conductive. Aerogels (the uncarbonised precursors) would therefore be more suitable. Additionally, nitrogen doping increases the number of electron carriers, producing materials with higher conductivities, in addition to making them suitable catalysts for oxygen reduction reactions (ORR) in fuel cell electrodes.<sup>136-140</sup> The carbogels produced by White *et al.* contained pyrrolic-type nitrogen, primary and

secondary amine and pyridinic or quaternary nitrogen groups, with the potential for use in heterogeneous catalysis, separation, CO<sub>2</sub> adsorption and fuel cell catalyst supports.<sup>141</sup>

An alternative source of biomass is chitin; the second most abundant polysaccharide after cellulose, and therefore, the most abundant nitrogen-containing polysaccharide.<sup>142</sup> Gao *et al.* successfully produced chitin-derived mesoporous materials. Again, templating was avoided to reduce waste and cost, whilst also simplifying the process. The applications tested in this work included heavy-metal removal and styrene epoxidation. Heavy metal removal was achieved *via* low temperature carbonisation (400 – 600 °C) due to the resulting amines, amides and pyrrolic-nitrogen, while styrene epoxidation made use of the graphitic nitrogen which forms at higher temperatures (800 – 1000 °C).<sup>143</sup>

### 5.1.1 Seafood waste valorisation

Shrimp, crab and lobster shell waste is produced in large amounts globally, estimated at around 8 million tonnes a year.<sup>144</sup> This has the potential to be valorised due to its chemical composition. The shells are mainly composed of calcium carbonate, chitin and proteins. These components can already be separated, leading to a great deal of research on the design of a complete and efficient seafood waste biorefinery.<sup>145</sup> Once this becomes successful, the price of these materials and any resulting chemicals may be significantly reduced, making them more readily available. Seafood shells could therefore be diverted from landfill to factories and become a new renewable feedstock, further aiding in the attempt to create a circular economy.

The chemical structure of chitin is very similar to that of starch, alginic acid and pectin. Given its abundance, it is only logical to attempt to use it to produce a new Starbon-like product. The chemical structure of a starting material has a significant impact on its properties. For instance, starch-based and alginic acid-based Starbon materials are different in that alginic acid contains a carboxylic group, which starch does not. The resulting S800 and A800 materials performed differently in their adsorption and desorption of phenols, and this will also be seen in the adsorption of specific metals in Chapter 3 of this thesis.<sup>47</sup>

The exciting feature about chitin is that it contains nitrogen, which is not present in the Starbon materials produced so far contain. This could potentially give a whole range of novel mesoporous materials with new and interesting properties, including different metal selectivities and adsorption capacities. The major drawback of chitin is that it is not soluble in water and must first be converted to chitosan before it can be gelled; this can be done by a simple deacetylation of chitin using NaOH.<sup>142</sup>

Chitosan is made up of D-glucosamine, shown in Figure 1.6, linked by  $\beta$ -(1 $\rightarrow$ 4) glycosidic bonds. As discussed, the mesoporous structures obtained from Starbon materials result primarily from the ability of the starting materials to form helices. To prepare the same mesoporous materials from starting compounds that do not form such helices in their gel form, such as chitosan, requires other methods. Templating is a highly used method for such compounds where the chemical functionality is present, but the desired structure is absent. A simpler method involves dispersing it throughout a more structurally suitable polysaccharide. This may provide a route for the synthesis of a Starbon with its typical mesoporous structure and a newly introduced nitrogen content.

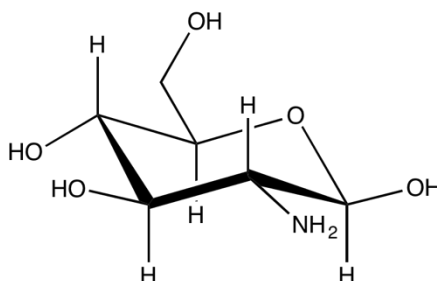


Figure 5.1: Chemical structure of D-glucosamine, the monomer of which chitosan is composed.

At the GCCE, alginic acid – chitosan hybrids have been attempted in ratios of 10:1, 5:1 and 3:1, using the previous production method; solvent exchange with ethanol and acetone, followed by vacuum oven drying. The work described in this thesis, in coordination with the current Starbon method (TBA addition and freeze-drying) attempts to take the production a step further, by carbonising such materials, something that has not been previously done.

In this chapter, as *N*-Starbons are new materials, they will be fully characterised in order to understand their properties and determine their potential as bio-based competitors in applications that nitrogen-doped mesoporous materials are known to be suitable for. *N*-Starbons were first made in a 3:1 alginic acid to chitosan ratio, and chitosan content was later increased to 2:1 and finally 1:1 to reach as high a nitrogen content as possible. Each material was carbonised to 300 °C, 450 °C and 600 °C in the same way as Starbon materials. Once a method was established and a suitable porosity with high nitrogen content was achieved, the material was further carbonised to 800 °C for applications such as electrodes for capacitors where high stability is a must.

Characterisation conducted includes nitrogen adsorption / desorption porosimetry to understand pore properties such as relative micropore and mesopore surface areas and pore volumes, and pore size distributions for each material. The pore properties were additionally tested after 1 year to ensure that the materials' pores are sufficiently stable, as Starbons have shown to be.

Scanning electron microscopy was performed to investigate particle size and textural properties. Elemental analysis was imperative primarily to determine nitrogen content and the stability of nitrogen functionalities during carbonisation. Thermogravimetric analysis helped give an indication of the temperatures at which major changes in functionality were taking place, which would then allow for characterisation of the gases given off at those temperatures. This was especially important for understanding the difference in stability of nitrogen in *N*-Starbon materials when compared with chitosan. Infrared spectroscopy, through both Attenuated Total Reflection - Fourier Transform Infrared (ATR-FTIR) and DRIFT, as well as XPS allowed for characterisation of the functional groups that are present on the surface of the final materials.

## 5.2 Porosimetry

The nitrogen adsorption / desorption porosimetry data for the *N*-Starbon materials is shown in Figures 5.2 – 5.5. Carbonisation has an overall positive effect on surface area (Figure 5.2) but specific differences between the samples appear to be random. All 1:1 (alginic acid : chitosan) materials seem fairly consistent but the 3:1 and 2:1 materials appear to reach a maximum surface area at lower temperatures. These two materials only vary between themselves in their 300 °C materials, and this may be due to an error during carbonisation. The 2:1 material was accidentally allowed to stand at 300 °C for several hours before beginning the cooling down process. This seems to have had a positive effect on the material's surface area.

Overall, despite these differences, surface areas are comparable to those of the original starch, alginic acid and pectin materials, thus chitosan addition has not been detrimental to surface area. Comparing these materials to chitosan alone, chitosan has slightly higher surface areas, especially at low temperatures. This is likely because the mesopores have collapsed to leave a highly microporous structure (Figure 5.5f).

On the other hand, pore volume is seen to decrease on increasing chitosan content. Similar to regular Starbons, carbonisation does not affect pore volume; only the starting material does. The choice of acid here seems to have a slight effect, with the pTSA materials giving better results than the pCSA materials, which showed pore volumes equal to those of chitosan alone. Again however, the pore volumes of the high chitosan content materials still show comparable pore volumes to the original Starbons. So, although the results are not impressive, the materials are still sufficiently mesoporous, which is a step forward for bio-based *N*-doped mesoporous materials.

It is important to note here that equipment problems may also have had an effect on material synthesis, with freeze-drying not reaching optimum conditions for the productions of 1:1 materials. Faults in production, such as the gel thickness on freeze-drying, add to the variables that can have a significant impact on the drying process. Furthermore, although porosimetry data is highly useful in determining the quality of the materials, the values tend to vary slightly between one analysis run and another, and it is therefore more useful to compare trends.

As in the pure Starbons, the hysteresis loops shown in Figure 5.4 are Type IV and V isotherms, indicating that the materials contain mesoporosity and adsorption occurs via monolayer adsorption followed by multilayer adsorption. The hysteresis loop is related to capillary condensation during desorption. Surprisingly, chitosan alone too gave a similar hysteresis loop (Figure 5.4f), even though pore distribution shows that it is highly microporous. With regards to the accuracy of the results, the hysteresis loops are not all closed and therefore the data cannot be interpreted correctly or fully.

Of all the porosity data obtained, pore distribution plots appear to show the only clear and explicable trend in data. The 3:1 and 2:1 materials showed high proportions of mesoporosity, which were stable even after carbonisation. When the chitosan content was further increased to a ratio of 1:1 however, the alginic acid content was no longer high enough to hold the material's pore structure. Thus, on heating to 450 °C and 600 °C, the pore structure collapsed, and the materials became predominantly microporous. The choice of acid is known to play a significant role here, which is why acetic acid (AcA) was replaced by pTSA, which succeeded in keeping a mesoporous structure at high temperatures. As pTSA is not considered a green chemical however, *p*-cymenesulfonic acid (pCSA) was attempted as its 'green equivalent'. As shown in Figures 6.4d and 6.4e, there is no difference in the mesoporosity of the pTSA and pCSA, showing that pCSA is a suitable substitute for acetic acid or pTSA. Comparing the *N*-Starbon to chitosan alone, it is clear that the pore quality has been significantly improved from highly microporous to highly mesoporous, similar to that of regular Starbons.

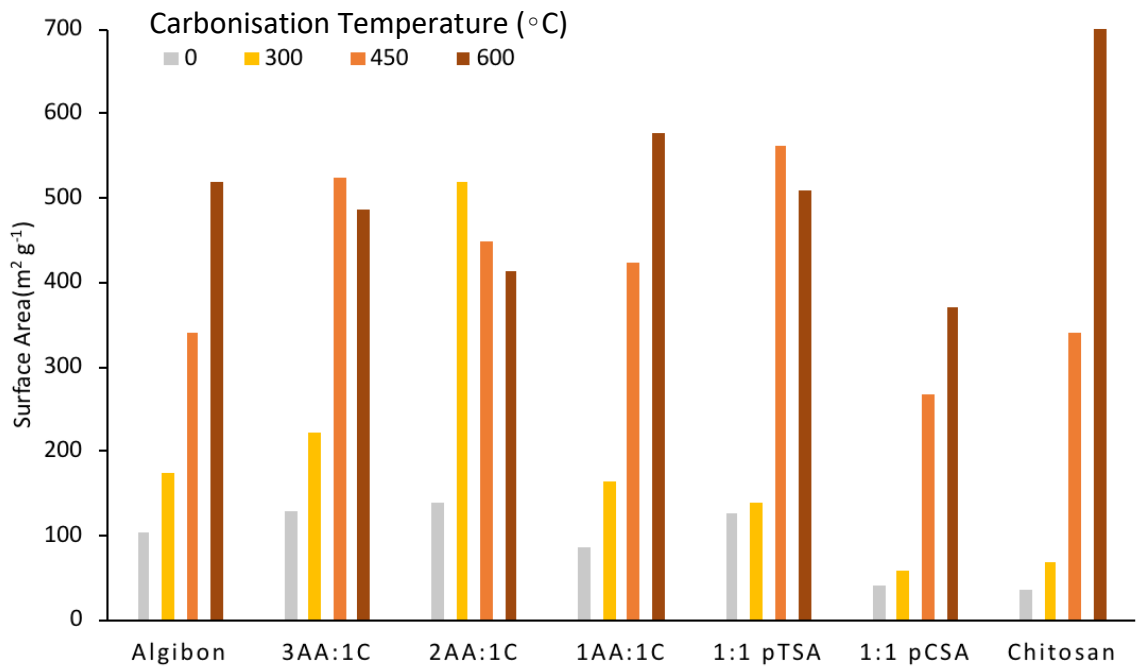


Figure 5.2: Surface areas of *N*-Starbon materials carbonised to various temperatures.

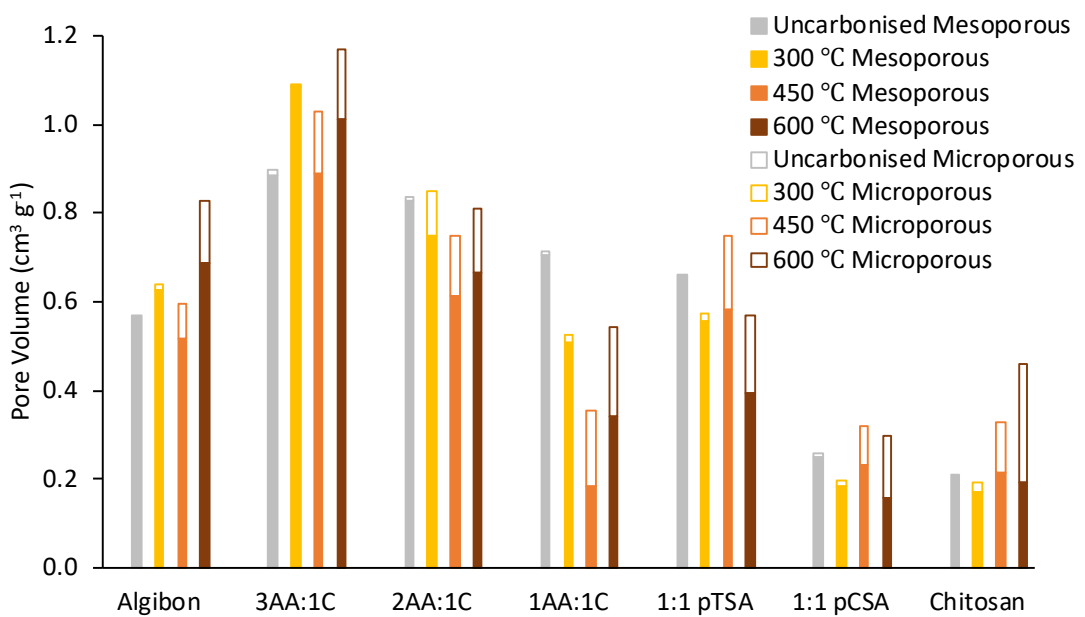


Figure 5.3: Micro- (t-plot), meso- (BJH) and total (t-plot + BJH) pore volumes of *N*-Starbon materials carbonised to various temperatures.

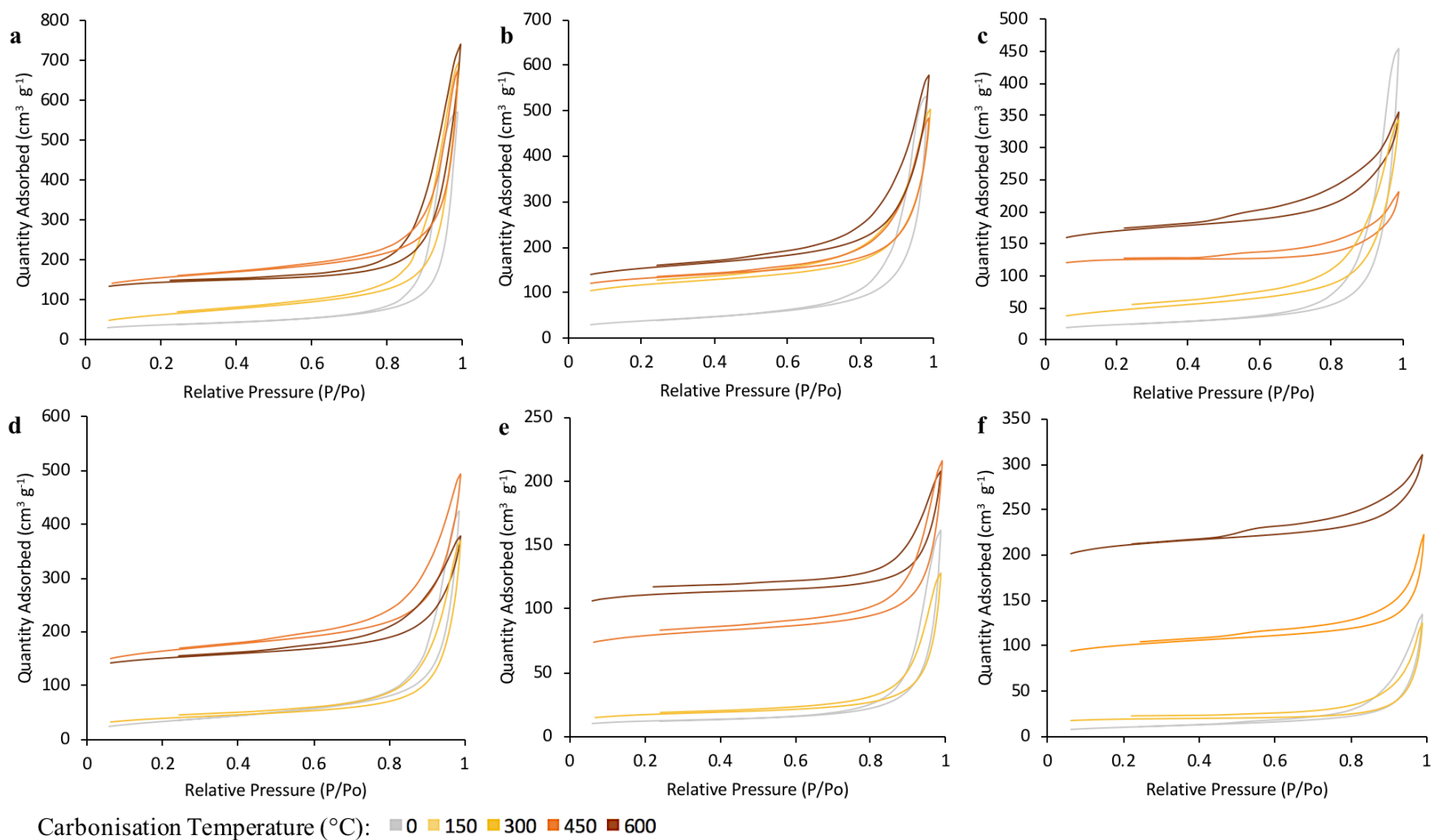


Figure 5.4: Langmuir isotherms for *N*-Starbons a) 3AA:1C, b) 2AA:1C, c) 1AA:1C, d) 1AA:1CpTSA, e) 1AA:1CpCSA and f) expanded chitosan.

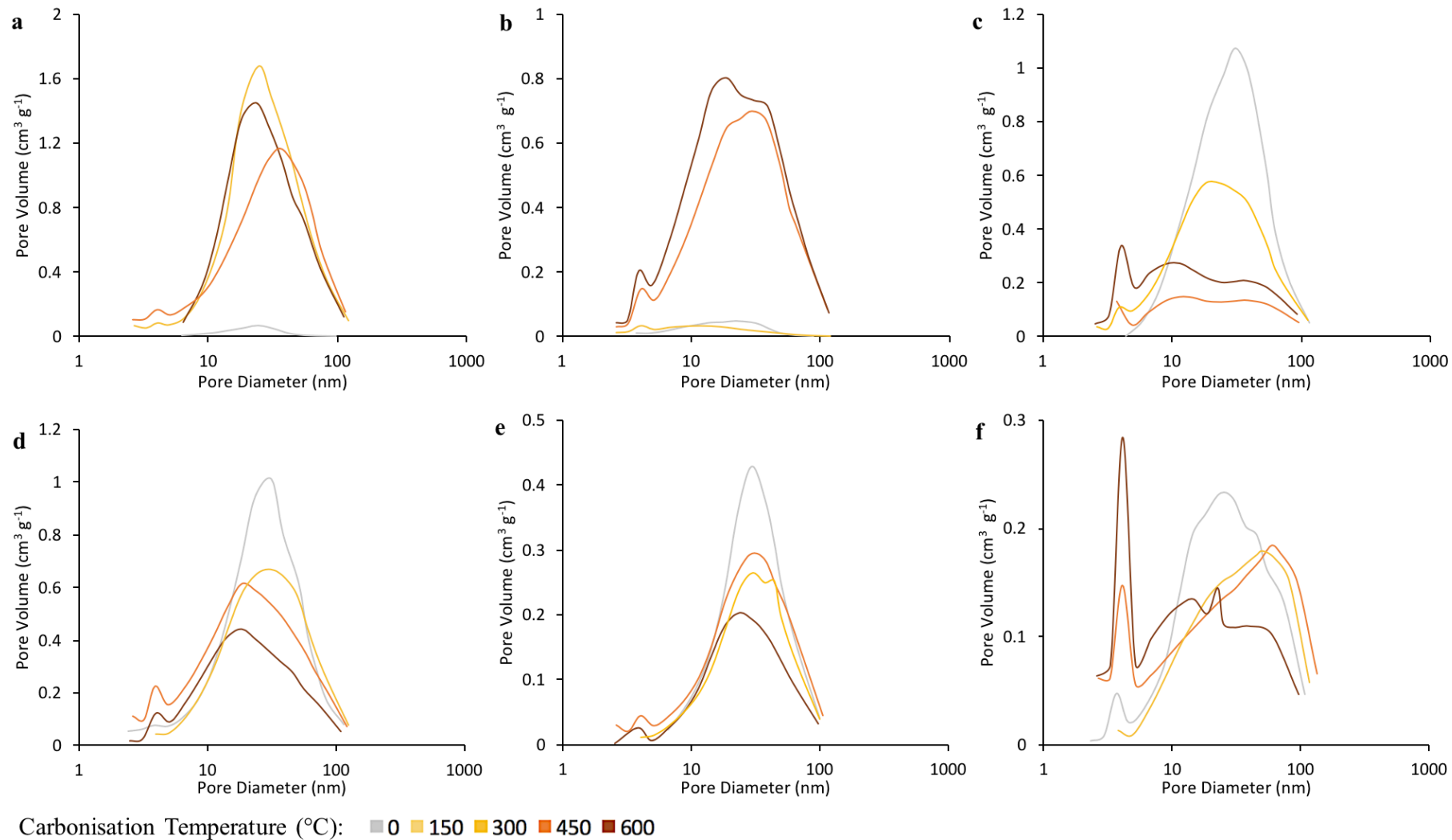


Figure 5.5: Pore distribution plots for *N*-Starbons a) 3AA:1C, b) 2AA:1C, c) 1AA:1C, d) 1AA:1CpTSA, e) 1AA:1CpCSA and f) expanded chitosan.

## 5.2.1 Pore stability over time

The stability of Algibon materials has been confirmed in previous work and therefore it is likely that the *N*-Starbons, since their structure is based around the alginic acid's pore structure, should be similarly stable.<sup>12</sup> However, materials made from chitosan alone are structurally different and therefore their stability must be tested. This will also indicate whether chitosan content is expected to have a detrimental effect on *N*-Starbons. The porosity was measured both when it was fresh and also when it was a year old and is shown in Figures 5.6 and 5.7. Surface area decreased by 16%, while pore volume decreased by 19%. The isotherm shows that N<sub>2</sub> adsorption has also decreased. Although this does mean that pore volume has diminished, it is still high enough to be considered highly porous and sufficiently stable. Furthermore, instrument calibration changes may also be affecting the results in some way, so some amount of change may be attributed to this. A600, as expected, showed no change in porosity after two years. Both pTSA and pCSA *N*-Starbons also performed exceedingly well, showing little to no signs or pore degradation after one year.

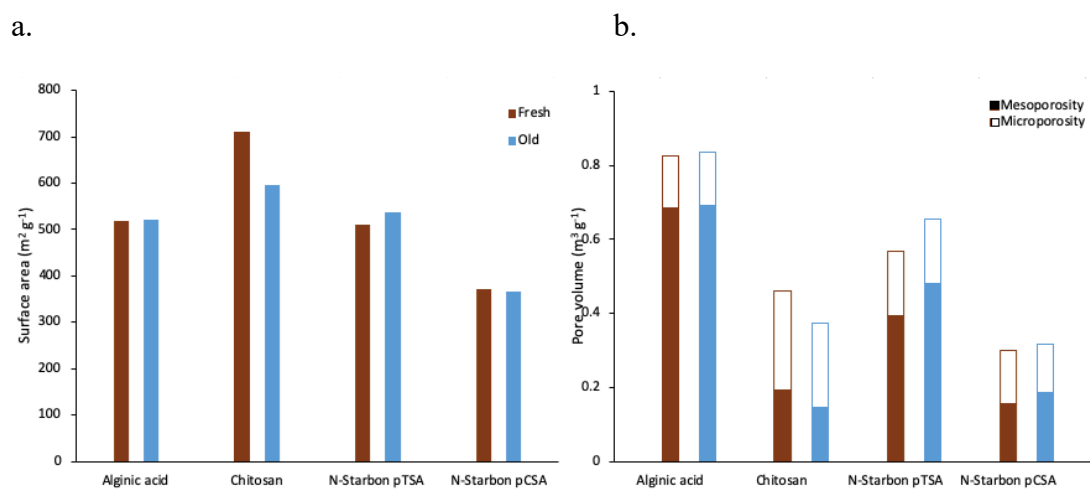


Figure 5.6: a) BET surface area and b) t-plot and BJH pore volumes of expanded alginic acid, chitosan and N-Starbons all carbonised to 600 °C, when fresh and after some amount of time.

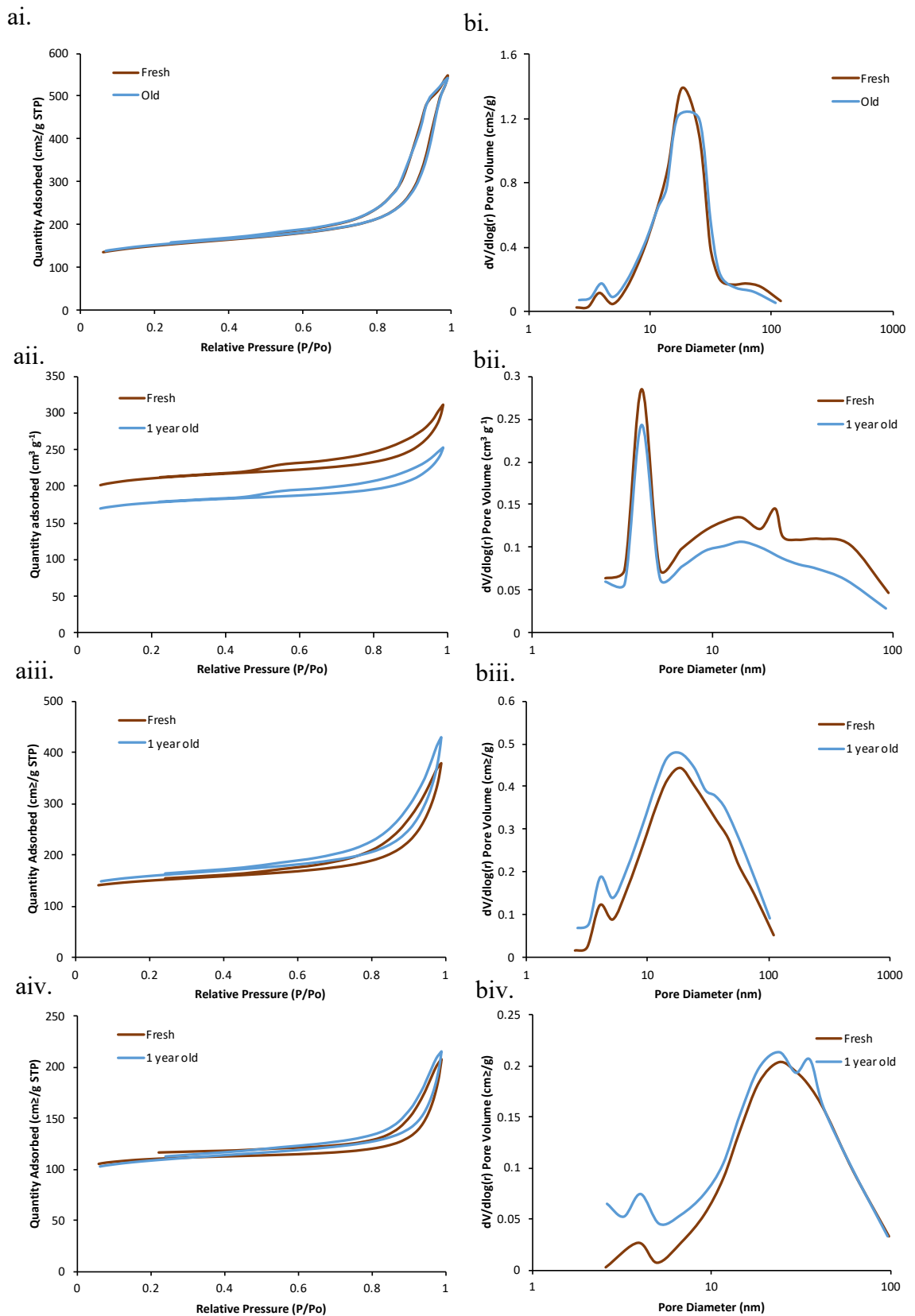


Figure 5.7: a) Langmuir isotherm and b) pore size distribution of expanded i) alginate, ii) chitosan, iii) *N*-Starbon made with pTSA and iv) *N*-Starbon made with pCSA when fresh and after some amount of time.

### 5.3 Scanning electron microscopy

SEM images at both low and high magnification were taken of 2:1 (alginic acid : chitosan) samples carbonised to 300 °C, 450 °C and 600 °C, and are shown in Figures 5.8, 5.9 and 5.10, respectively. At low magnification, all materials show a range of particle shapes and sizes, implying that the carbonisation temperature is not controlling particle size. There were significant differences in texture shown however at high magnification. At 300 °C, the surface appears mostly smooth with scattered porous areas. At 450 °C, the large porous regions are more dominant leaving few smoother regions. The material appears to be folding over itself. At 600 °C, the smooth regions are no longer visible and the surface shows the material's folds have developed into clearly visible pore channels. Few areas of large pore openings also appear but are now few relative to the material at 450 °C.

a.

b.

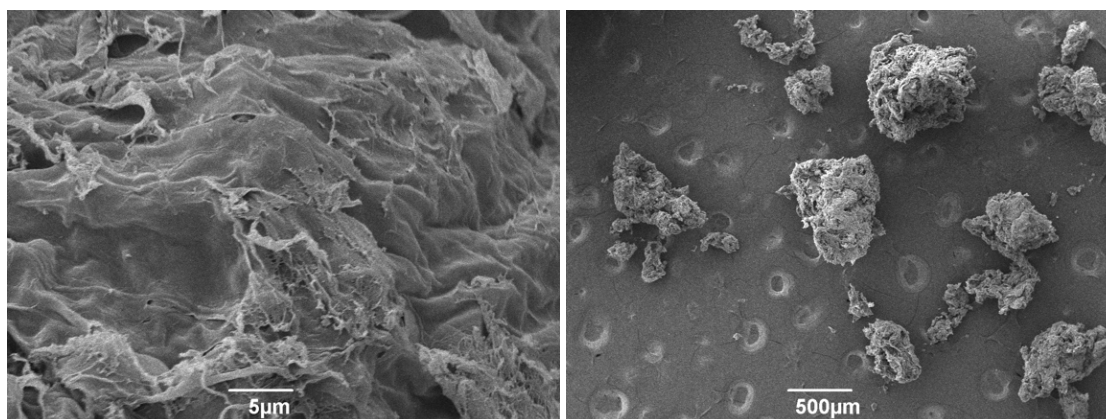
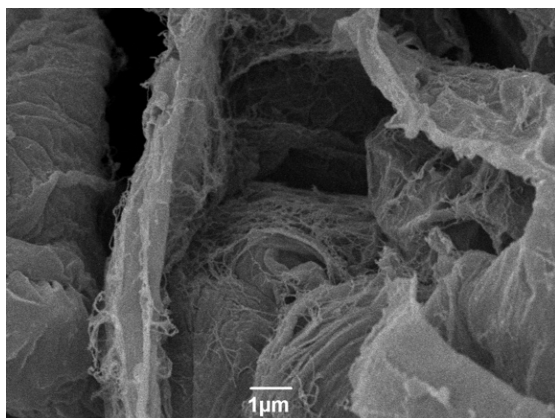


Figure 5.8: The SEM images of 2AA:1C at a) high magnification and b) low magnification carbonised to 300 °C.

a.



b.

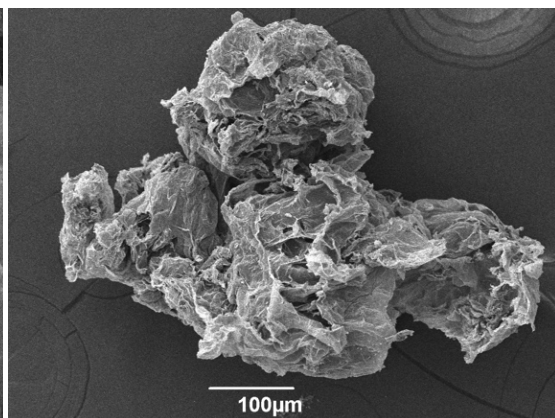
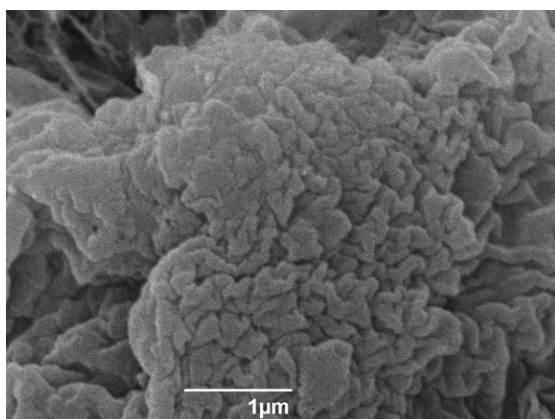


Figure 5.9: The SEM images of 2AA:1C at a) high magnification and b) low magnification carbonised to 450 °C.

a.



b.

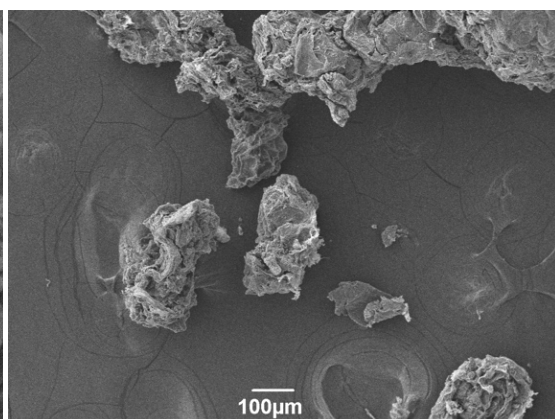


Figure 5.10: The SEM images of 2AA:1C at a) high magnification and b) low magnification carbonised to 600 °C.

## 5.4 Elemental analysis

As the aim of producing the new *N*-Starbon materials is to introduce nitrogen into the materials, elemental analysis of all materials was performed. The percentage content of nitrogen (w/w) (Figure 5.11), as well as that of carbon (Figure 5.12) and hydrogen (Figure 5.13) was determined and compared to that of chitosan alone as a reference.

Uncarbonised materials of different alginic acid : chitosan ratios showed similar nitrogen contents to their theoretical nitrogen contents; 2.0% (3:1), 2.7% (2:1) 4.1% (1:1) and 8.6% (0:1). On carbonisation, the majority of elemental loss occurs with oxygen and hydrogen, thus increasing the nitrogen content. This trend is consistent for *N*-Starbons made using pTSA and pCSA, as well as for chitosan alone. When acetic acid (AcA) was used however, this trend is followed only until 450 °C. At 600 °C, the nitrogen content is seen to either plateau or drop significantly instead of continuing to rise. Having said this, when comparing the use of different acids with the same chitosan content, the pTSA and pCSA materials still have lower nitrogen contents than the acetic acid material. Chitosan alone, containing double the nitrogen content as the 1:1 material, would relatively be expected to have between 20% and 26% nitrogen, but only contains 16%. Although the reasons for these changes have not yet been understood, there is the possibility that the carboxylic groups from alginic acid and acetic acid may be reacting and stabilising the nitrogen in some form.

The carbon and oxygen contents for all materials are shown in Figures 5.12 and 5.13, respectively. The oxygen content itself was not analysed but is assumed to be the remaining elemental composition after subtracting carbon, hydrogen and nitrogen. Therefore, the actual oxygen content might be slightly lower due to the presence of impurities of sulfur from pTSA (XPS shows sulfur to be less than 1 % for all materials, see Table B.1). For both carbon and oxygen, the only noticeable change in bulk composition occurs on heating the materials up to 300 °C, with a 20 % increase for carbon and a corresponding 20 % decrease for oxygen. Following this, the materials remain fairly stable with regards to carbon and oxygen. Additionally, there is no noticeable difference between the different materials at the same temperature, implying that the alginic acid : chitosan ratio is not having an effect on the degradation process with regards to carbon and oxygen.

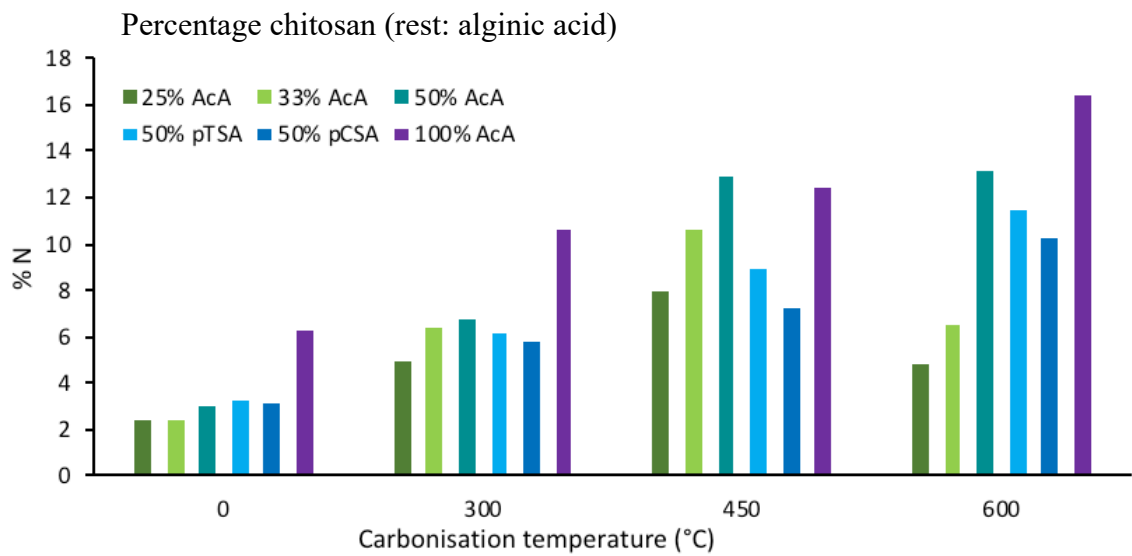


Figure 5.11: Showing the nitrogen content in the range of *N*-Starbon materials.

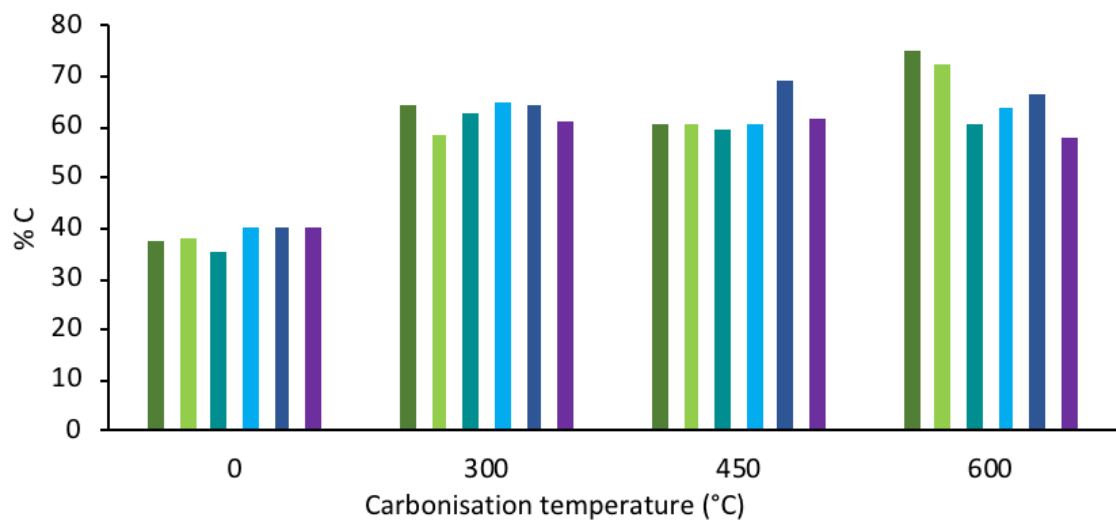


Figure 5.12: Showing the carbon content in the range of *N*-Starbon materials.

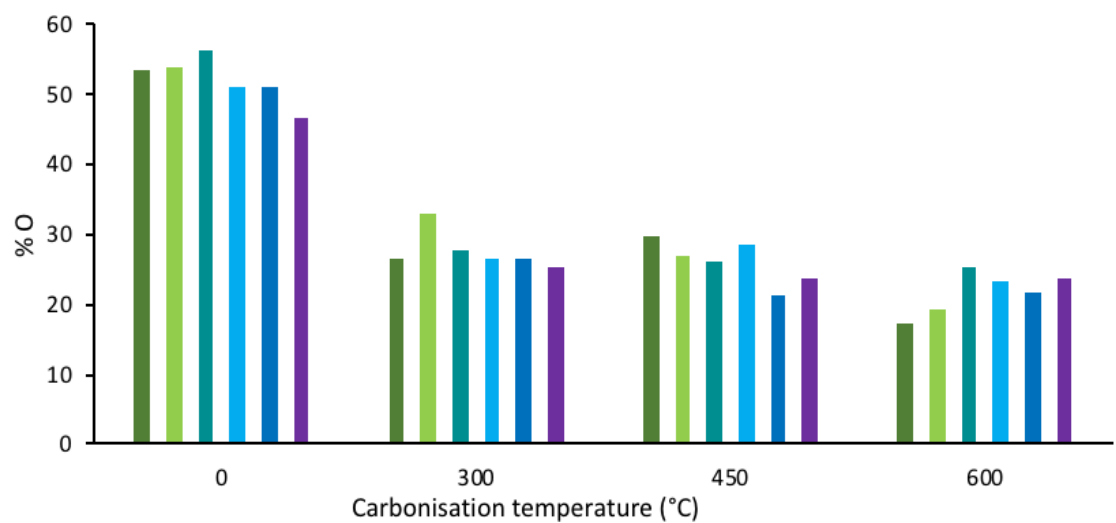


Figure 5.13: Showing the assumed oxygen content in the range of *N*-Starbon materials.

## 5.5 Thermogravimetric analysis

TGA was performed on *N*-Starbon 2:1 to determine the various reactions taking place within the material as it is carbonised from room temperature to 600 °C at a heating rate of 10 °C per minute. For precision, differential thermogravimetry (DTG) was used to analyse the data. The DTG plot is shown in Figure 5.13. Chitosan alone was also analysed for comparison. There are two instances at which mass loss occurs within *N*-Starbon. The first is at ~100 °C, mainly due to dehydration. The similar chitosan peak is shifted to a higher temperature. This behaviour has been observed before, where a higher chitosan content results in water requiring higher temperatures to be released.<sup>146</sup> For *N*-Starbon the second peak is broad, appearing to be caused by overlap of two peaks (215 °C and 240 °C).<sup>147</sup> This is, therefore, where *N*-Starbon begins to thermally decompose. Chitosan, however, mainly decomposes at a higher temperature (>270 °C),<sup>146, 148</sup>

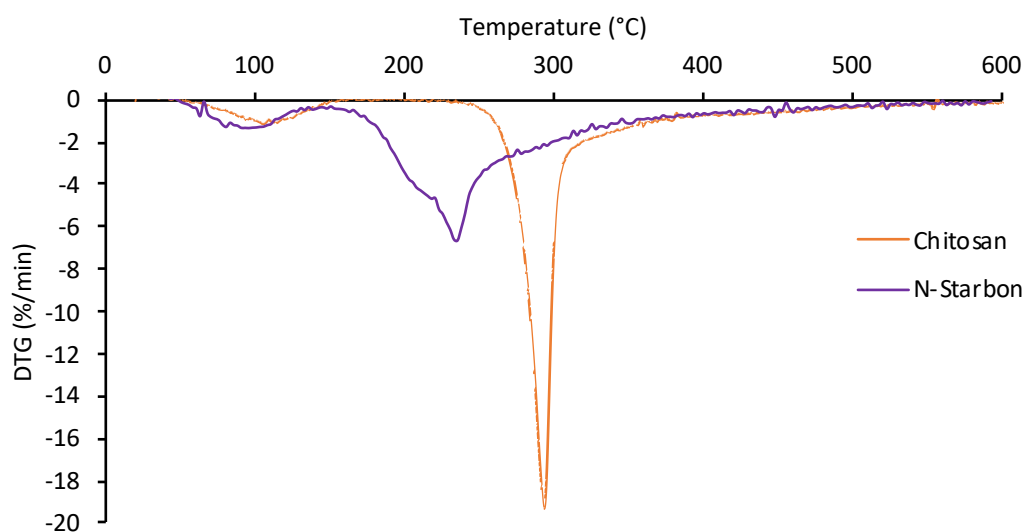


Figure 5.14: Showing the DTG plot for chitosan and *N*-Starbon 2:1 as they are carbonised from room temperature to 600 °C at 10 °C min<sup>-1</sup>.

## 5.6 Infrared spectroscopy

### 5.6.1 Gas-phase DRIFT spectroscopy

During TGA, any gaseous compounds produced upon carbonisation were simultaneously analysed by Diffuse Reflectance Infrared Fourier Transform (DRIFT) spectroscopy. The 3D graphs of IR spectra against time are shown in Figures 5.15 and 5.16. The spectra corresponding to the mass losses discussed in the previous section, and therefore the main points of gas evolution were selected for analysis of their 2D spectra. These were extracted and plotted (Figures 6.16 and 6.17).

At 100 °C, the peaks at  $>3000\text{ cm}^{-1}$  represent dehydration through O - H stretching from loss of H<sub>2</sub>O, which gives another peak at around  $1500\text{ cm}^{-1}$  for H-O-H scissoring. Both spectra show peaks at  $2350\text{ cm}^{-1}$ , caused by asymmetric O - C - O stretching from loss of CO<sub>2</sub>. At 100 °C, CO<sub>2</sub> is in low concentration as it is only due to desorption from the surface. At 240 °C, decomposition takes place and the concentration is much higher, giving an additional peak for CO<sub>2</sub> at  $\sim 670\text{ cm}^{-1}$  (O = C = O bending). The peaks at  $\sim 1720\text{ cm}^{-1}$  are probably due to C = O stretching, which in this case can be attributed to carboxylate groups of carboxylic acid produced.<sup>148, 149</sup>

The main difference between chitosan and *N*-Starbon is ammonia ( $\sim 960\text{ cm}^{-1}$ ). For *N*-Starbon, little is seen to be given off at low temperatures, but nothing at high temperatures. Chitosan continues to give off ammonia as it is heated, even up to 600 °C. This may be an indication that the nitrogen-containing functional groups (amines) have reacted to form more stable compounds, preventing them from being degraded. Given the functionality of alginic acid however, it is unlikely that this is taking place. Alternatively, degradation might indeed be causing loss of ammonia, but this might be trapped within the pore structure of the material, which along with the high temperature, could provide it with the time and right conditions to react and be contained within the material. This falls in line the fact that some ammonia is seen at low temperature as this might be surface nitrogen (not within pores) which cannot be trapped. Furthermore, this agrees with elemental analysis which give higher values for nitrogen content in the bulk than XPS does on the surface.<sup>148, 149</sup>

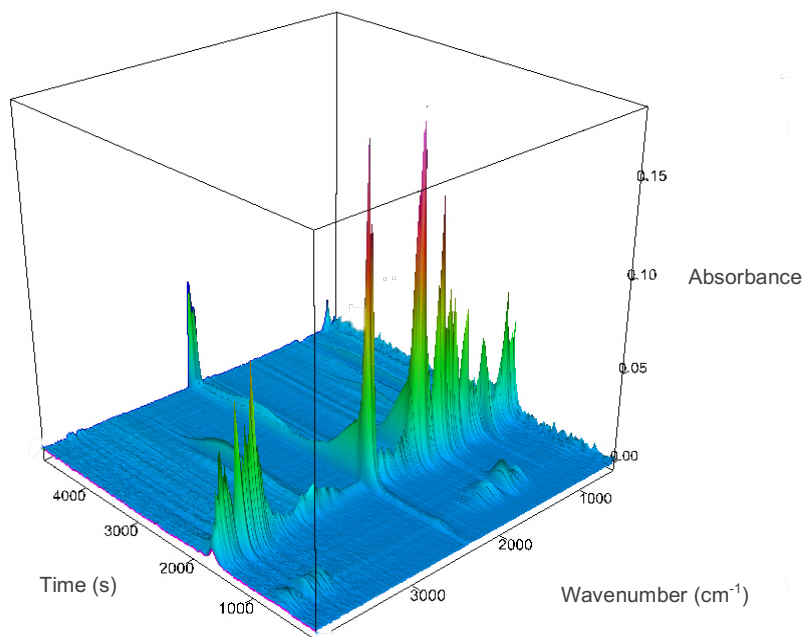


Figure 5.15: Showing the gas-phase 3D DRIFT spectrum recorded during the thermal decomposition of chitosan up to 800 °C at 10 °C min<sup>-1</sup>.

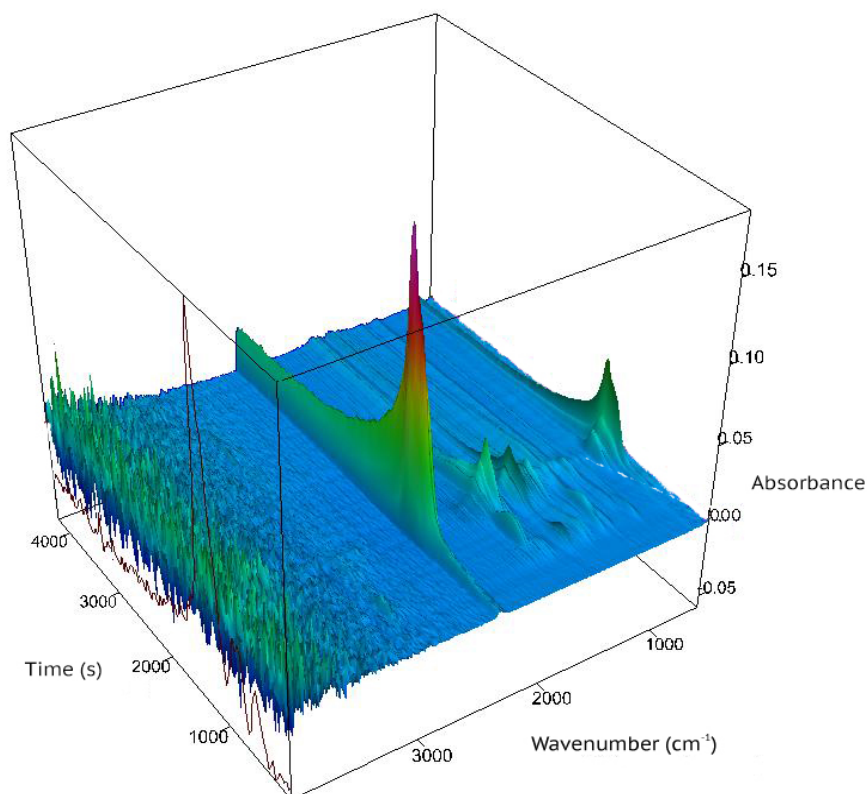


Figure 5.16: Showing the gas-phase 3D DRIFT spectrum recorded during the thermal decomposition of *N*-Starbon 2:1 up to 600 °C at 10 °C min<sup>-1</sup>.

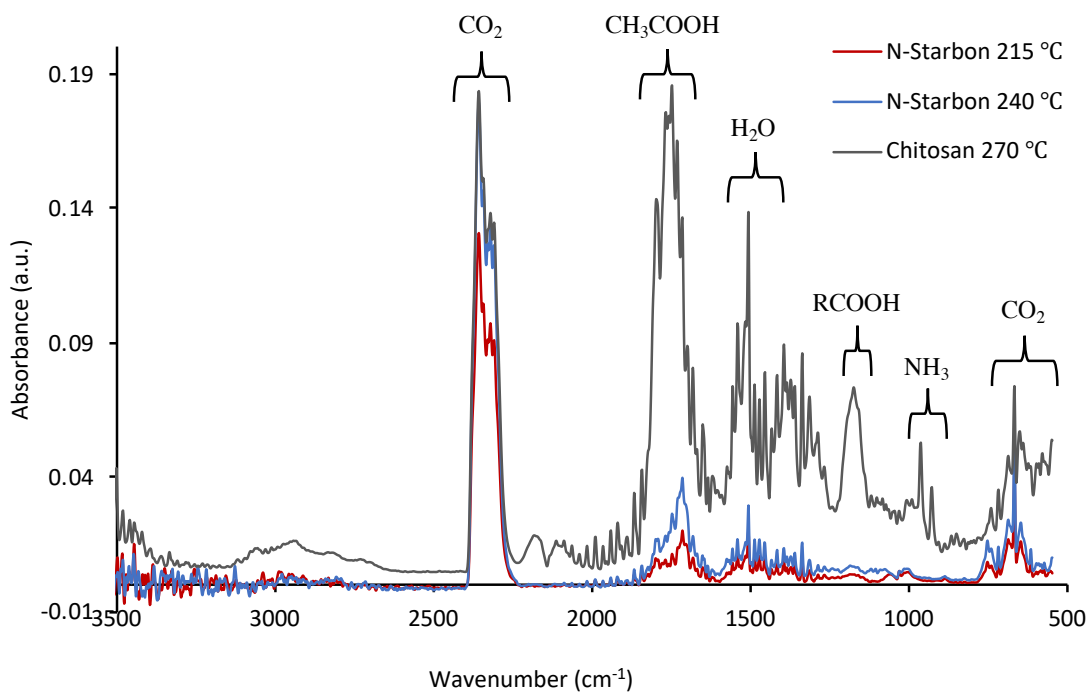


Figure 5.17: Showing the gas-phase DRIFT spectra at the major decomposition temperatures for chitosan and *N*-Starbon.

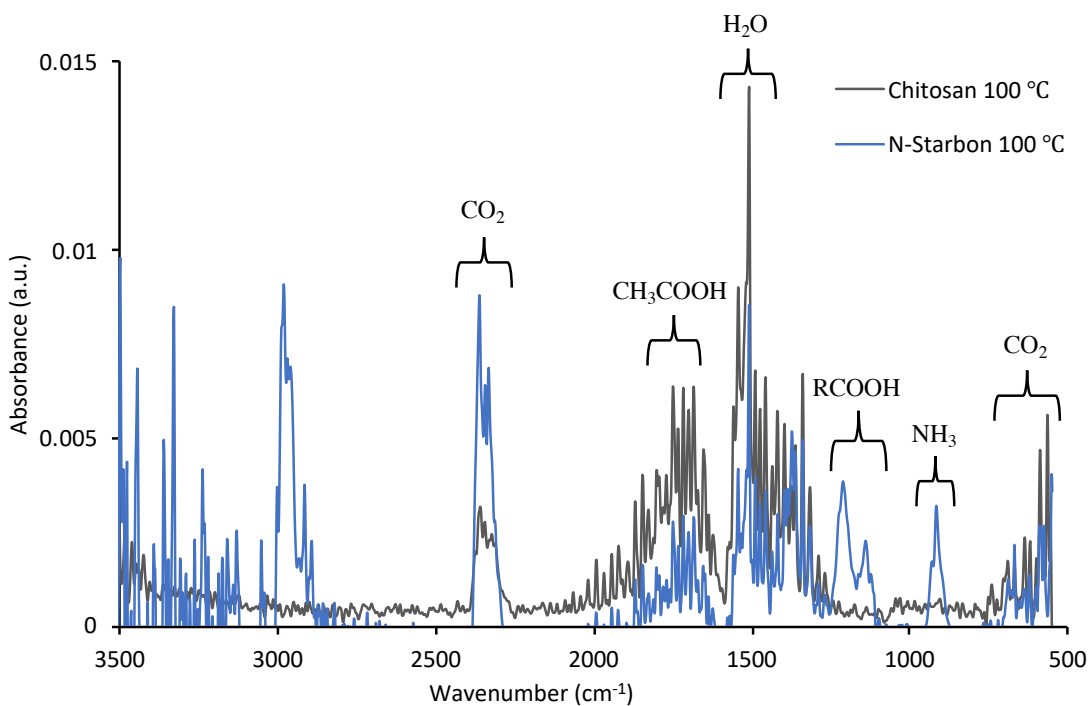


Figure 5.18: Showing the gas-phase DRIFT spectra at 100 °C for chitosan and *N*-Starbon.

## 5.6.2 ATR - FTIR

Attenuated Total Reflection - Fourier Transform Infrared spectroscopy was performed to analyse the chemical functionalities present in *N*-Starbon materials. Prior to the interpretation of *N*-Starbon IR spectra, the IR spectra of the starting materials needed to be obtained, shown in Figure 6.18. Both spectra show peaks for alkyl chains; C - H stretching ( $\sim 2930\text{ cm}^{-1}$ ) and alcohol groups; O - H stretching ( $\sim 3365\text{ cm}^{-1}$ ) and C - O stretching ( $\sim 1030\text{ cm}^{-1}$ ). There are two main differences between the materials' chemical structures however. Chitosan contains an amine group; N - H stretching, asymmetric ( $3354\text{ cm}^{-1}$ ) and symmetric ( $3288\text{ cm}^{-1}$ ), N - H bending ( $1650\text{ cm}^{-1}$ ), and C - N stretching ( $1026\text{ cm}^{-1}$ ) which alginic acid does not contain. Alginic acid, on the other hand contains a carboxylic acid group, giving a sharp peak for C = O stretching ( $1723\text{ cm}^{-1}$ ), which is not shown in the chitosan spectrum.<sup>149</sup>

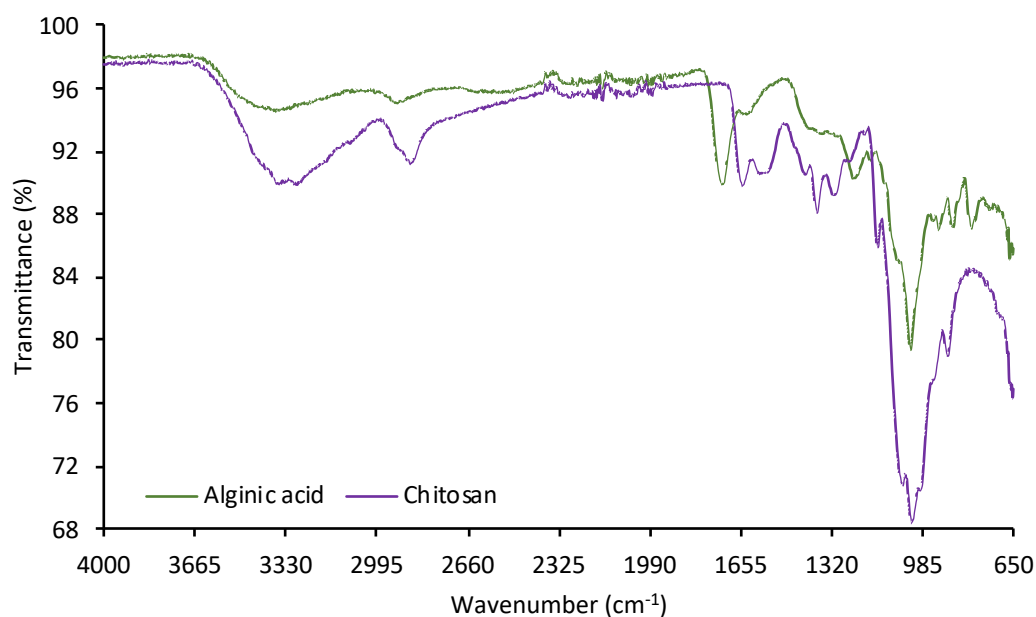


Figure 5.19: Showing the IR spectra of the *N*-Starbon starting materials: alginic acid and chitosan.

Before carbonisation, the white expanded aerogel *N*-Starbon materials contain both alginic acid and chitosan and therefore give a mixture of the peaks from both spectra in Figure 5.20. The spectra for the pre-carbonisation *N*-Starbons 3:1 and 2:1 are shown in Figure 5.21. The spectra are essentially identical. The mixture of both compounds has caused overlap of several similar peaks, making it difficult to interpret them accurately. Even though there is a larger proportion of chitosan in the 2:1 material, the nitrogen content was still found to be similar, likely because the difference in nitrogen content is not significant enough, which explains why there are no differences in the spectra of the two materials.

The identified peaks are the following; the broad O – H stretching peak, overlapped with N – H stretching peaks ( $3100 - 3400 \text{ cm}^{-1}$ ), C – H stretching ( $\sim 2910 \text{ cm}^{-1}$ ), C = O stretching ( $1730 \text{ cm}^{-1}$ ) and N – H bending ( $1620 \text{ cm}^{-1}$ ), C – O stretching, overlapped with C – N stretching ( $1030 - 1070 \text{ cm}^{-1}$ ).<sup>149</sup>

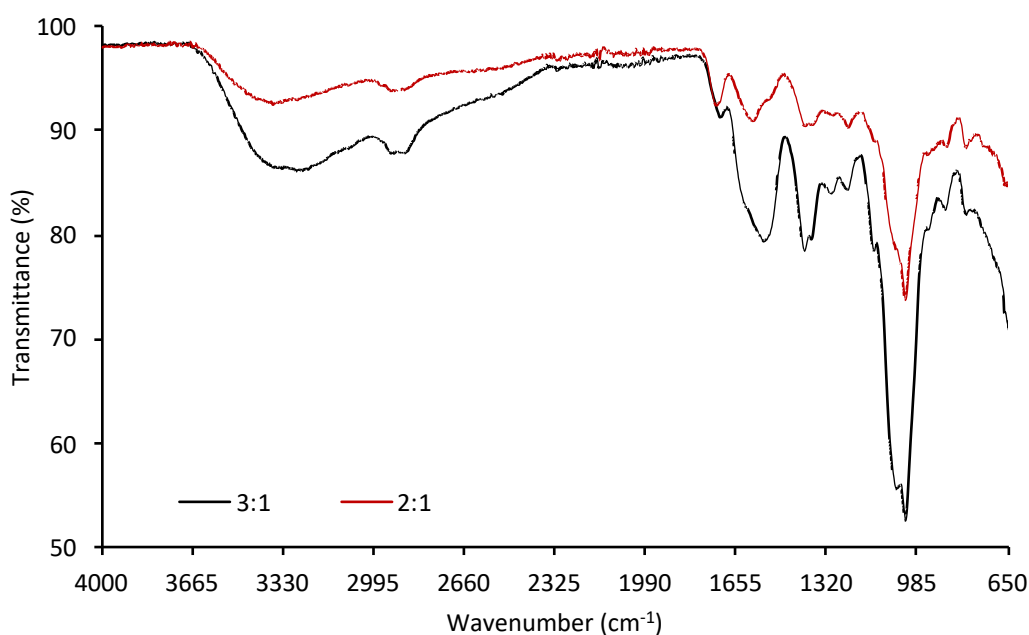


Figure 5.20: Showing the IR spectra of the *N*-Starbon materials pre-carbonisation with different ratios of alginic acid : chitosan (3:1, 2:1).

As the carbonised materials are black in colour, it is not possible to obtain clear IR spectra of the materials via ATR. Having said this however, certain peaks are still visible (Figure 6.20). The materials carbonised to 300 °C show some peaks, but these decrease in intensity as the carbonisation temperature increases.

The broad peak between 3650  $\text{cm}^{-1}$  and 3100  $\text{cm}^{-1}$  is now likely only caused by N – H stretching, as gas-phase DRIFT showed a relatively large amount of water lost at around 100 °C. Thus, it is expected that all the materials described here have few to no remaining hydroxyl groups. Carboxylic acid groups have also reduced to ketones or aldehydes.

Next, the carbonyl peak at around 1710  $\text{cm}^{-1}$  is only visible up to 300 °C. Above this temperature, it appears that any carbonyl functionality is either lost or is no longer detectable. It may also be that the carbonyls are reduced to ethers ( $\sim 1240 \text{ cm}^{-1}$ ). These ether peaks overlap with C – N stretching. There appears to be no change on carbonisation indicating that one or both of these functionalities is thermally stable. Finally, there are strong peaks at around 1600  $\text{cm}^{-1}$  that may either be caused by N – H bending or C = C stretching.<sup>149</sup> These similarly remain present on carbonisation.

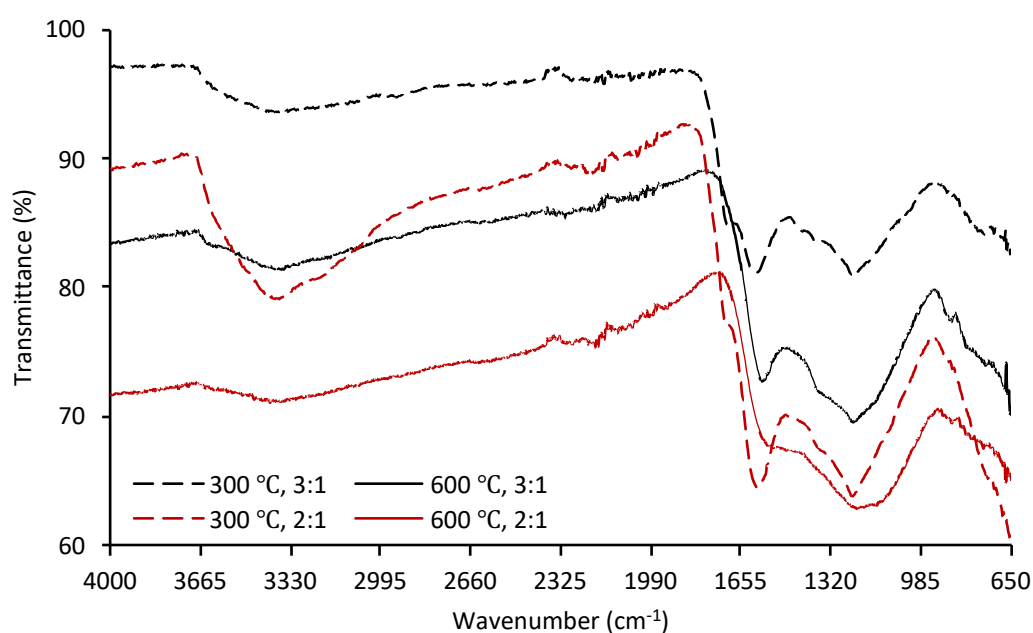


Figure 5.21: Showing the IR spectra of the *N*-Starbons (alginic acid : chitosan; 3:1 and 2:1 carbonised to 300 °C and 600 °C).

### 5.6.3 DRIFT spectroscopy

Diffuse Reflectance Infrared Fourier Transform (DRIFT) spectroscopy was performed on three *N*-Starbon materials; all composed of 2:1 alginic acid : chitosan to obtain a clearer spectrum than what was obtained from ATR - FTIR spectroscopy. The nitrile peak from ATR - FTIR analysis was not clear enough to confirm the presence of nitriles. This is because the energy throughput in ATR is almost zero, and therefore ATR cannot be used to detect peaks in this region. By DRIFT however (Figure 5.22), the peaks are clearly visible. Further confirmation that the peaks do in fact belong to nitrile groups can be given by a peak shift in the presence of a Lewis acid.<sup>150-162</sup> The Lewis acid used here was  $\text{In}^{3+}$  from indium(III) chloride.

The materials analysed were those carbonised to 300 °C, 450 °C and 600 °C, before and after indium adsorption (Figure 6.21). Most of the peaks are consistent with those obtained from ATR-FTIR, with the exception of the stronger peak at 2220  $\text{cm}^{-1}$ . This peak is characteristic of nitriles and is caused by the  $\text{C} \equiv \text{N}$  stretch.<sup>149</sup> At 300 °C, the nitrile peaks are visible but are rather weak as the nitrogen content is still relatively low at 6.4%. At 450 °C the peaks are more pronounced as the nitrogen content reaches 10.6%. Furthermore, at this higher temperature, more of the nitrogen may have converted to nitrile functionality. The peaks are even weaker at 600 °C as the materials are darker, causing transmittance to be too low to give a clear spectrum. Having said that, the nitrile peaks are unquestionably still present. In each case, following indium(III) adsorption, the nitrile peaks shifted to higher frequencies potentially due to shifts in electron density away from the antibonding orbital of the CN triple bond to the metal.<sup>151</sup> The nitrile peaks and their respective shifts are listed in Table 6.1.

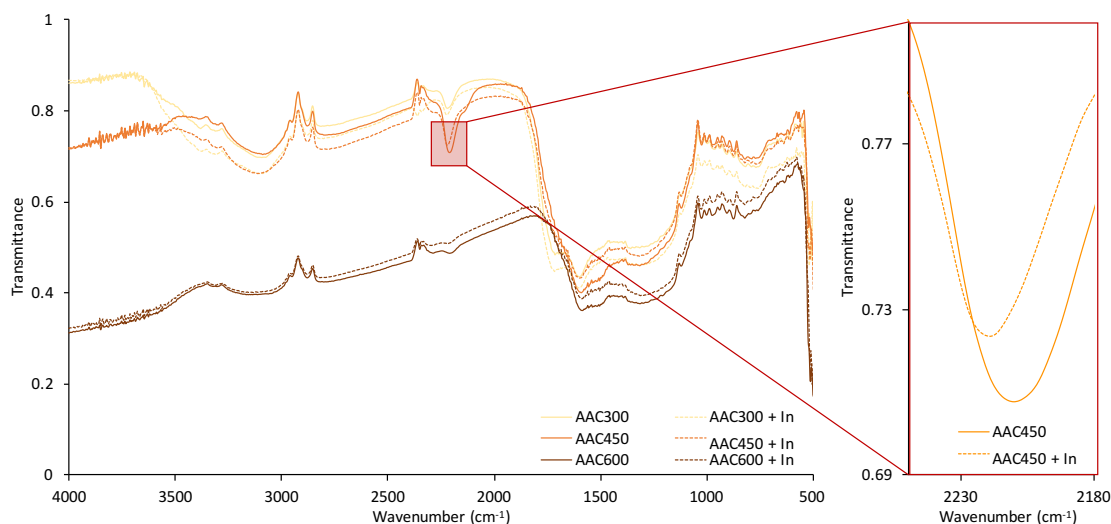


Figure 5.22: Showing the DRIFT spectrum for *N*-Starbon (alginate acid : chitosan; 2:1) materials carbonised to 300 °C, 450 °C and 600 °C with and without indium adsorbed to the surface.

Table 5.1: Showing the nitrile peaks ( $\text{cm}^{-1}$ ) along with their peak shifts ( $\text{cm}^{-1}$ ) caused by the presence of indium on the surface of the *N*-Starbon (alginate acid : chitosan; 2:1) materials carbonised to 300 °C, 450 °C and 600 °C.

Carbonisation temperature (°C)	300	450	600
<i>N</i> -Starbon	2220	2210	2210
<i>N</i> -Starbon + $\text{In}^{3+}$	2224	2220	2218
Peak shift	+4	+10	+8

## 5.7 X-ray Photoelectron Spectroscopy

XPS was used to characterise *N*-Starbons by determining the surface content of nitrogen and whether any differences lie between the surface and the bulk of the material. XPS was also used to identify the functional groups present in the materials, particularly with respect to nitrogen and the differences between the forms of nitrogen pre- and post-carbonisation and how they transform throughout the process. C1s regions were also analysed. Comparisons were made between materials of different alginic acid : chitosan ratios; 3:1 (Figures 6.22 and 6.23) and 2:1 (Figures 6.24 and 6.25). A summary of N1s peaks and their relative concentrations are shown in Tables 6.2 and 6.3, respectively.

C1s spectra show strong peaks for carbon bonded to hydroxyl groups at 285.9 – 286.5 eV in uncarbonised materials. Similar peaks at higher carbonisation temperatures likely result from carbon in imines and nitriles. Overlapping these peaks, at slightly lower binding energies (~285 eV), are carbons alpha to the carboxylic groups. Carboxylic groups themselves gives peaks at 289.2 – 289.4 eV and amide groups give peaks at ~288 eV. Un-functionalised carbon (284.5 eV) is seen only in carbonised materials and its content increases with temperature as materials become more graphitic.<sup>163</sup> The N1s spectra show 5 major peaks: imines or pyridinic-N (398.2 - 398.9 eV), amines (399.3-399.6 eV), nitriles and amides (400.2-400.5), protonated amines or imines (401.4 - 401.8 eV) and oxidised nitrogen (403.3 - 403.9 eV).<sup>55, 163-167</sup> The only two peaks present in the uncarbonised materials are amines (>60%) and protonated amines, as is expected as amines are the only nitrogen-containing functional group in chitosan. Irrelevant of the chitosan content, the amine content is around double the protonated amine content. Protonated amines likely formed with H<sup>+</sup> from either the acetic acid or the carboxylic groups on alginic acid. All the carbonised materials contain imines, protonated imines, nitriles and oxidised nitrogen. Oxidised nitriles are considerably low (<10%) in each case. Nitriles and amides appear to be highest in the 300 °C materials, however concentrations appear random and there is no clear trend indicating any reaction patterns in the materials as they are carbonised. The major change in concentrations is between the pre-carbonisation materials and 300 °C, indicating that the materials are mainly reacting below 300 °C. Process variations may have caused slight differences in the materials. By 600 °C however, the relative concentrations of nitrogen appear similar, indicating that by this point, the materials may be fairly stable.

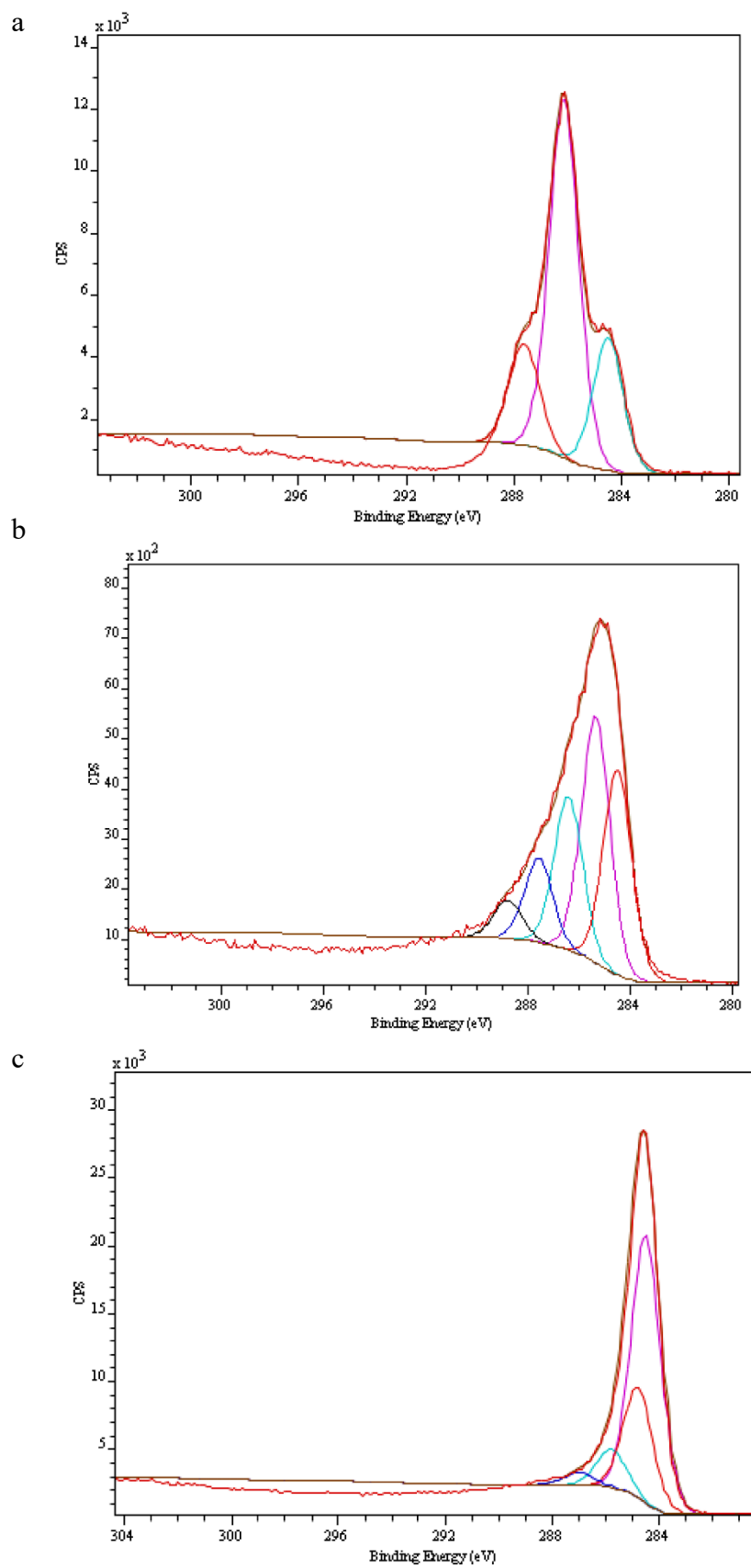


Figure 5.23: C1s region of the XPS spectra of 3:1 *N*-Starbons carbonised as follows: a) pre-carbonisation, b) 300 °C and c) 600 °C.

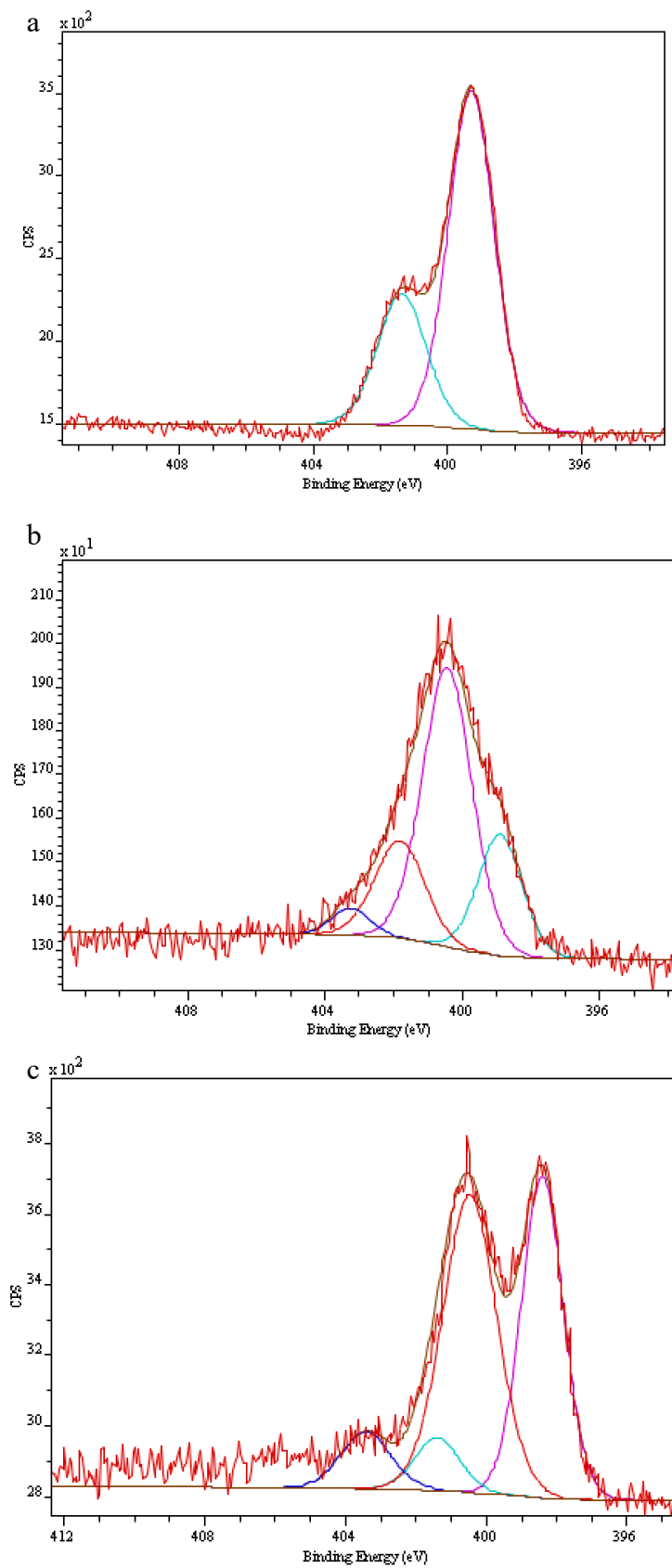


Figure 5.24: N1s region of the XPS spectra of 3:1 *N*-Starbon carbonised as follows: a) pre-carbonisation, b) 300 °C and c) 600 °C.

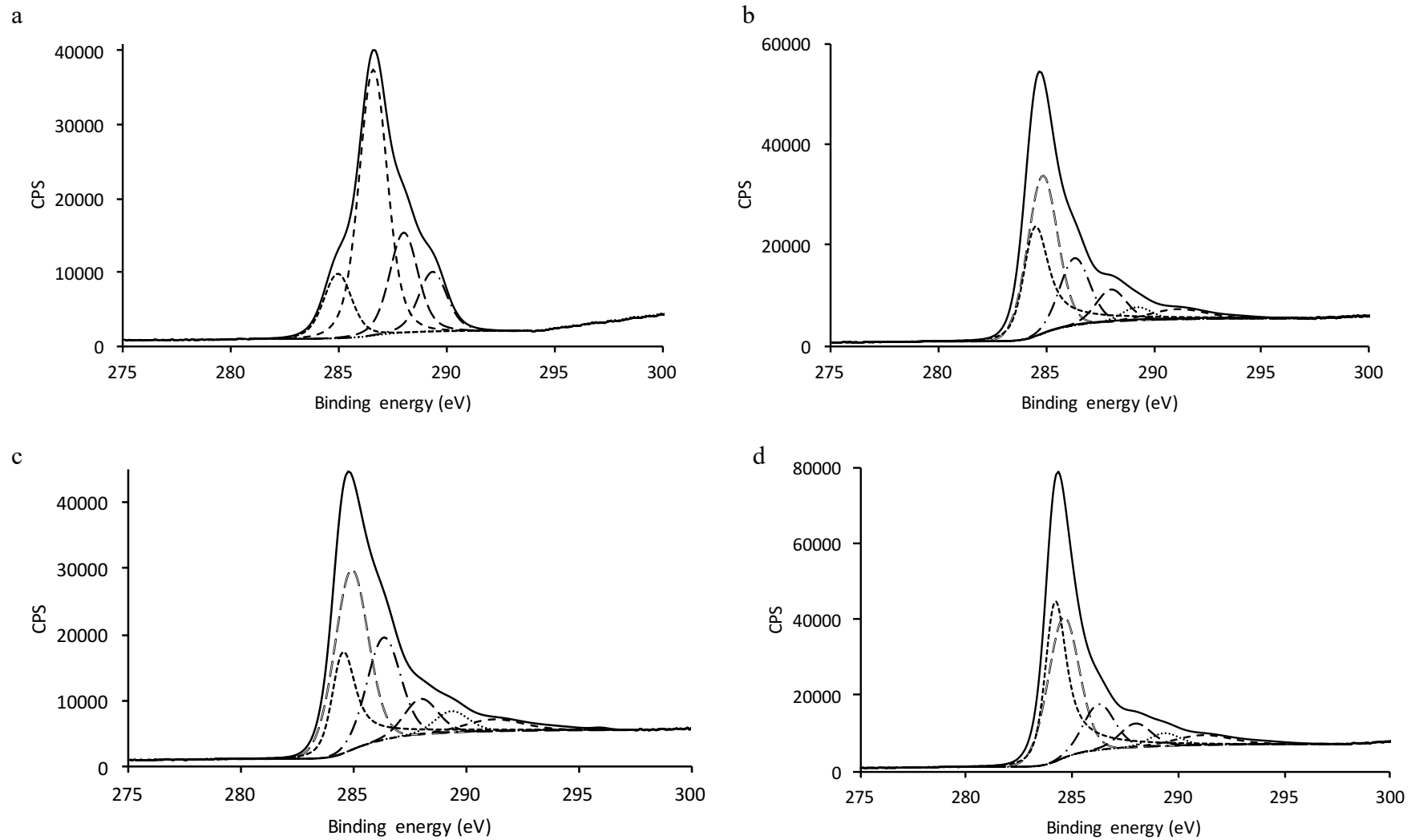


Figure 5.25: C1s region of the XPS spectra for 2:1 *N*-Starbon carbonised as follows: a) pre-carbonisation, b) 300 °C, c) 450 °C and d) 600 °C.

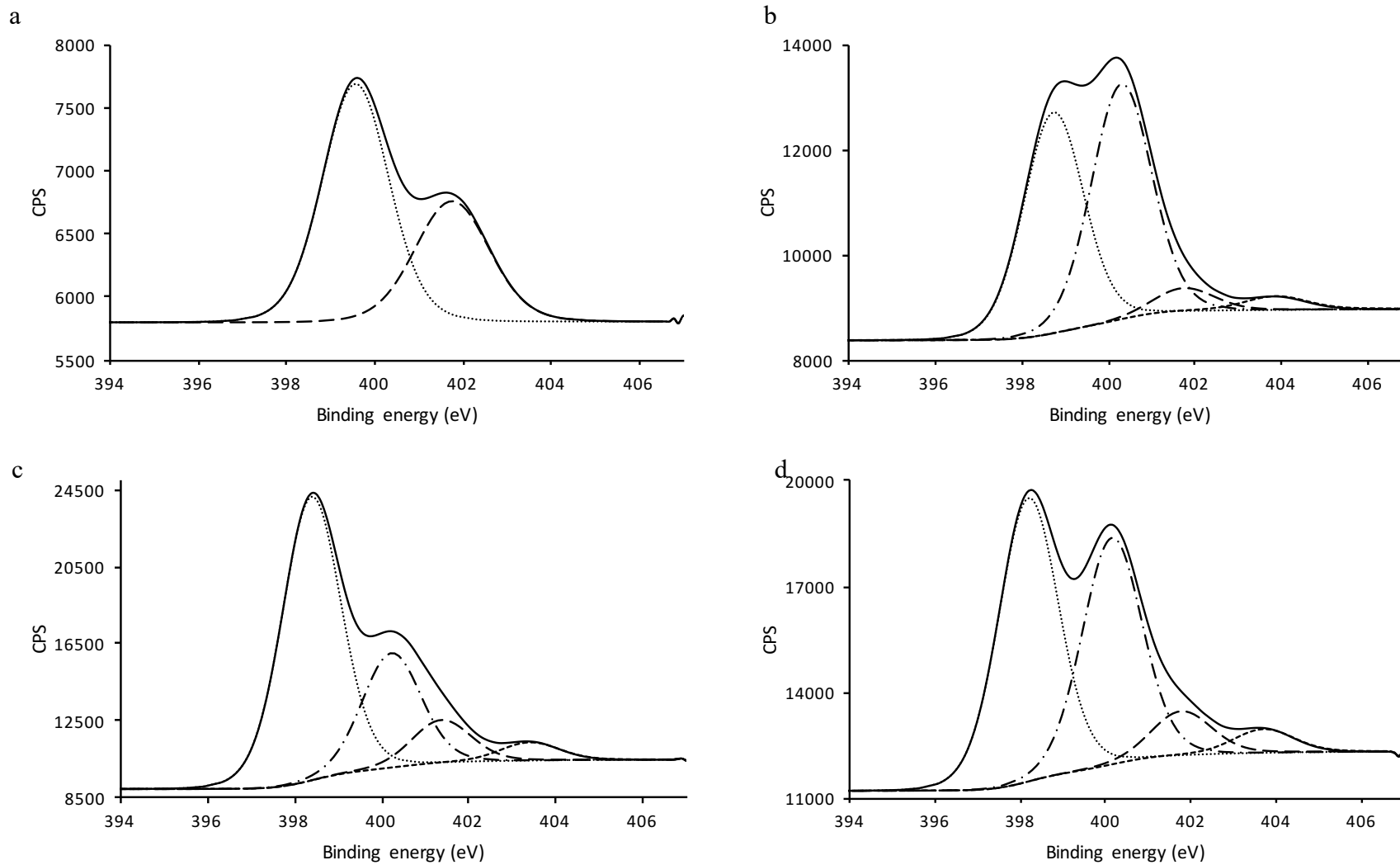


Figure 5.26: N1s region of the XPS spectra for 2:1 *N*-Starbon carbonised as follows: a) pre-carbonisation, b) 300 °C, c) 450 °C and d) 600 °C.

Table 5.2: A summary of the N1s peaks obtained by XPS of *N*-Starbons 3:1 and 2:1.

Material	Temperature (°C)	Imines, pyridines	Amines	Nitriles, amides	Protonated amines/imines	Oxidised N (eg. -N-OH)
<b>3:1</b>	<b>0</b>	-	399.31	-	401.37	-
	<b>300</b>	398.91	-	400.44	401.83	403.26
	<b>600</b>	398.41	-	400.47	401.39	403.43
<b>2:1</b>	<b>0</b>	-	399.57	-	401.75	-
	<b>300</b>	398.72	-	400.29	401.72	403.85
	<b>450</b>	398.37	-	400.21	401.35	403.39
	<b>600</b>	398.19	-	400.15	401.78	403.71

Table 5.3: A summary of the relative concentrations (%) of nitrogen present in each functional group according to XPS data.

Material	Temperature (°C)	Imines, pyridines	Amines	Nitriles, amides	Protonated amines/imines	Oxidised N (eg. -N-OH)
<b>3:1</b>	<b>0</b>	-	70.8	-	29.2	-
	<b>300</b>	21.2	-	55.4	19.4	4.0
	<b>600</b>	38.8	-	46.3	6.8	8.1
<b>2:1</b>	<b>0</b>	-	63.7	-	36.3	-
	<b>300</b>	44.9	-	47.8	4.7	2.6
	<b>450</b>	61.8	-	25.0	9.3	3.9
	<b>600</b>	49.1	-	39.3	7.5	4.0

## Chapter 6

# Capacitance



## 6.1 Introduction

The energy sector is currently facing turbulent times as the world is slowly coming to realise that the switch to more sustainable energy sources and energy materials is a must. If this alone is not enough, population growth, technological advances, economic growth and the human desire for efficiency are simultaneously causing a large growth in the demand for energy. The major countries responsible for this growth are developing countries like China and India.<sup>168, 169</sup>

Energy materials are materials used in energy conversion and storage; namely batteries, capacitors and fuel cells. They require good electrochemical properties; properties that have been studied in depth over the years due to the increase in energy demand. Porosity is a highly sought-after property in energy materials as it increases surface area drastically as well as allowing for ion-transport throughout the pore channels. Another way to improve a material's electrochemical properties is doping with electronegative atoms such as nitrogen. Other required electrochemical properties include thermal and chemical stability. *N*-Starbons display all of the above-mentioned properties and therefore, it makes sense to assume that they may perform well as energy storage materials. Moreover, since it has been shown that the *N*-Starbons contain a portion of their nitrogen in the form of nitriles, they have the added benefit of the high  $C\equiv N$  dielectric constant, which should further improve the material's electrochemical properties.<sup>170, 171</sup>

A capacitor is a device capable of capacitance ( $C$ ); *i.e.* charge storage. Capacitance is measured in farads. One farad is when a potential difference of one volt occurs as the material is charged with one coulomb. The term supercapacitor was coined for systems capable of capacitance of numerous farads per gram. This was achieved initially with  $RuO_2$  films and carbon double-layer capacitors.<sup>172</sup> Supercapacitors are also termed electrochemical capacitors and can be split into two categories. The first are those that work using an electrochemical double-layer (EDL), where charge is accumulated and stored on the electrode's surface. The second are pseudocapacitors, where it is through continuous Faradaic reactions that energy is stored.<sup>173</sup>

Carbon materials are often chosen for EDL capacitor electrodes. Microporous polysaccharide-derived materials have been synthesised at low temperature (180 – 200

°C) showing good capacitance with nitrogen contents of around 5%.<sup>174</sup> However, it is mesoporous materials with high surface areas and pore volumes that are ideal for electrodes in supercapacitors due to improved lifetime and stability, and their ability to adsorb species into their pores and interact with them. Mesopores allow for improved mass transport which may otherwise be inhibited by micropores. Their large surface areas provide several sites for such interactions while their high pore volumes allow for repetitive expansion and relaxation during the uptake and release of these species.<sup>173</sup>

Batteries are another potential application of *N*-materials. Nakano *et al.* showed that having three terminal nitrile groups on poly(oxetane) solid polymer electrolyte film gave a higher conductance than that with one terminal nitrile group due to improved solvation of lithium ions.<sup>175</sup> Similarly, Zhao *et al.* prepared solid-state electrolyte materials by polymerising cyanoethyl polyvinyl alcohol polyacrylonitrile-based electro-spun fibre membranes filled with solid succinonitrile. Apart from a high ionic conductance and high lithium ion transference number, these materials exhibit good flexibility and mechanical strength, making them particularly useful for flexible lithium ion batteries, as well as other electrochemical applications such as lithium / sulfur batteries and supercapacitors.<sup>176</sup> Cathodes for lithium / sulfur batteries were studied by Liu *et al.* who made microporous graphene-like oxygenated carbon nitride materials, reaching nitrogen contents of 20.5% through a one-step pyrolysis from urea and glucose. The material provided a long cycle-life with a high energy density.<sup>177</sup>

Nitrogen-containing materials with enhanced electrical properties have shown potential in green power generation applications too. Fuel cells work through redox reactions that convert chemical energy into electricity. At the anode, a fuel is oxidised while at the cathode, an oxygen reduction reaction (ORR) takes place.<sup>178</sup> ORR requires a catalyst, usually noble metals such as platinum, but these have become critical and need to be recycled or replaced altogether by another material or method. Carbon materials with optimised pore structures are being developed for this purpose too. They may also be used in the form of a composite or doped with heteroatoms.<sup>139</sup> Biomass-derived carbon materials are an attractive possibility for their abundance, low cost and renewability.

Nitrogen-doped carbon (NC) from chitosan has previously been made and subsequently doped with platinum for successful ORR.<sup>179</sup> Chitosan has also been cross-linked using sulfosuccinic acid and glutaraldehyde to improve proton conductivity and methanol

permeability, making the materials promising as polyelectrolytes in direct methanol fuel cells.<sup>180</sup> Other examples demonstrated the possibility of synthesising metal-free NCs with electro-catalytic activity, such as chitosan/graphene composites. The catalytic activity is brought about by the C – N bond. Its polarisation activates the adjacent carbon by lowering the ORR energy barrier.<sup>181</sup> Carbohydrate derivatives: glucose, D-glucosamine and *N*-acetyl-D-glucosamine, and phenolic compounds: phloroglucinol and cyanuric acid are other sustainable precursors that were used to make micro-mesoporous *N*-materials.<sup>182</sup> Ferrero *et al.* made use of mesoporous carbons from citrate salts of zinc and calcium doped with melamine as a source of nitrogen. The resulting nitrogen content was 9%. Compared to commercial Pt/C catalysts, the stability of these materials was higher and their selectivity against methanol electro-oxidation was also superior. Pyridinic-N and quaternary-N were found to be responsible for the material's catalytic activity.<sup>183</sup>

In this work, the capacitance of *N*-Starbons (50% chitosan) was tested and compared to regular Starbons as well as other similar materials described in the literature, such as those discussed above. Capacitance of regular Starbon materials has already been tested previously by Garcia *et al.* The work showed that Starbons alone did show good capacitance under some conditions but did not act as capacitors when undergoing cyclic voltammetry at high scan rates (100 mV s<sup>-1</sup>) because of their poor conductivity. To mitigate this problem, graphene was successfully introduced at 20 wt% by ball milling, achieving a capacitance of 175 F g<sup>-1</sup>.<sup>52</sup> Conductivity in carbons increases with material carbonisation temperature, and this is why graphene was able to improve the conductivity of Starbon in this study.<sup>184</sup> High temperature preparations of graphene however reduce the sustainability of the material preparation process. This study will therefore show whether the role of graphene can be replicated by nitrogen-doped Starbons. The materials to be tested will therefore be high temperature Starbons and *N*-Starbons (600 °C and 800 °C).

### 6.1.1 Electrochemical testing

There are three main tests that are generally used to check the viability of a material for electrodes in supercapacitors; galvanostatic charge/discharge (GCD), cyclic voltammetry (CV) and electrochemical impedance spectroscopy (EIS). In this project, EIS was excluded on the basis that it gives data calculated on the most similar circuit to the material, and not on the material itself. Therefore, the information obtained could be misleading. In fact, several recent publications have also excluded this type of analysis.<sup>174, 177, 185-187</sup>

GCD is based on the chronopotentiometry technique, where a controlled current is applied, simultaneously measuring the resultant potential over time. During the experiment, a constant current is applied for a set amount of time, or until the system's maximum potential is reached. Following this, the system is allowed to self-discharge and once it is fully discharged, the cycle is repeated. The measured voltage is plotted as a function of time, ideally generating a triangular shape for supercapacitors. The reciprocal of the slope ( $dV/dt$ ) of the charge / discharge cycle can then be used to calculate capacitance ( $C$ ) as shown;

$$C = \frac{I}{m(dV/dt)}$$

where  $I$  is the current applied to the system and  $m$  is the mass of the active electrode.<sup>185</sup> Throughout the cycling, a good capacitor should retain its capacitance, giving constant charging and therefore showing good cycle-life.

CV is a quantitative technique that involves applying a triangular potential on the working electrode so that the voltage is increased to a set maximum ( $E_2$ ) and then decreased back to a set minimum ( $E_1$ ) repeatedly. Throughout the experiment, current is measured to give rapid information about any electrochemical reactions or other processes that may take place in a system. The experiment relies solely on diffusion of material to the electrode. The results are displayed as a graph of current against voltage and the capacitance ( $C$ ) from this plot can be found by;

$$C = \frac{S_{area}}{2mv\Delta V} \quad (S_{area} = \oint I\Delta V)$$

where  $S_{area}$  is the loop area of the CV curve,  $m$  is the active electrode mass,  $\nu$  is the scan rate,  $\Delta V$  is the potential window and  $I$  is the resultant current.<sup>188</sup> As the potential is increased, oxidation of species may be induced, resulting in a peak current. If the reaction is electrochemically reversible, a negative peak current will also be observed as the species is reduced back to its original state, and/or other reduced state. Irreversible reactions will not give this negative current peak on reducing the potential back to  $E_1$ . The magnitude of the cathodic and anodic peak currents for a reversible reaction is the same, deviation in peak currents implies an irreversible reaction.<sup>189, 190</sup>

## 6.2 Results

### 6.2.1 Galvanostatic charge-discharge

To calculate capacitance from galvanostatic charge/discharge plots, the equation described in the previous section (and shown below) is used.

$$C = \frac{I}{m(dV/dt)}$$

Using the above equation, it is necessary to know the gradients of the GCD plots. Before discussing any of the plots in detail however, the shape of the plots must be considered, as in most cases, the gradients are not straight lines (Figure 6.1). This means that the gradient values are not obvious, making any data subjective and the resultant calculations unreliable (Table 6.1). This is known to occur due to faradaic processes occurring on the surface.<sup>190</sup> It is possible to improve the measurements by introducing (to the system) a known variable capacitor of similar capacitance to that being measured. This forces linearity on analysis.<sup>191</sup> However for simplicity, this was avoided as these studies are only preliminary ones, aiming to determine the potential of the materials as sustainable supercapacitors.

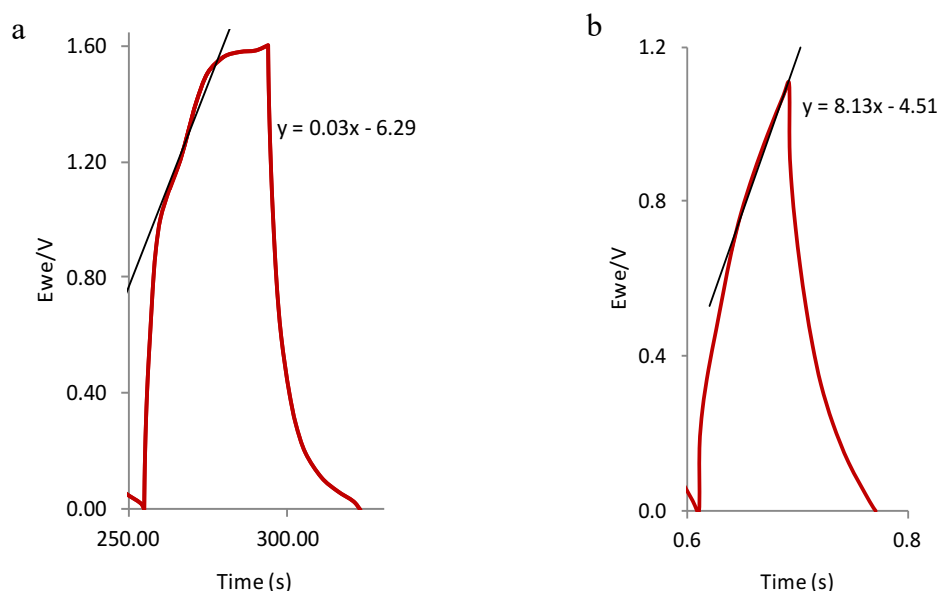


Figure 6.1: Examples of how a gradient can be taken from GCD plots of *N*-Starbons (600 °C) coated on carbon cloth analysed at a) 2 mA and b) 10 mA.

The active mass of the electrode is another essential value for these calculations. Each material was tested in its monolith form and also as a powder pasted onto carbon cloth using PVDF as a binder. With regards to the latter, the cloth is weighed before coating and the whole of the coated surface is immersed in electrolyte solution, thus the exact active mass of material is known. On the other hand, with regards to the monolith, although the mass of the whole sample can always be easily measured, the active mass is not precisely known. The monolith is attached at its top end by a crocodile clip and immersed in electrolyte solution at its bottom end. Two definite errors here are that: (i) it is impossible to immerse precisely half of the weight into the electrolyte solution, and (ii) following this, solution may be pulled up into the pores of the top half of the material by capillary action. This means that the active mass is unknown. For the sake of these calculations, the active mass has been taken to be around half the monolith's weight, but this error must be kept in mind when comparing the data in this chapter to literature data. Literature is unclear in how the active mass is usually calculated for these experiments.

The GCD plots are shown in Figures 6.2 and 6.3 for *N*-Starbon materials carbonised to 600 °C and 800 °C, respectively. At both 600 °C and 800 °C, the monolith gave more ideal plots compared to the coated carbon cloths, indicating that the carbon cloth or the polymer binder may somehow be hindering the experiment. Alternatively, carbonisation of the *N*-Starbon in powder form vs in monolith form may affect the final product. At this stage, the definite reason for this is unclear. Additionally, the 800 °C materials gave better shapes than the 600 °C materials. This is likely due to the higher stability reached at higher temperatures, thus less faradaic processes occur on the surface of 800 °C *N*-Starbons. Additionally, the higher temperature materials are known to be more conductive.<sup>184</sup> These observations are reflected well in the values obtained for capacitance, summarised in Table 6.1. For both the coated carbon cloth and the monolith, *N*-Starbons carbonised to 800 °C performed significantly better than those carbonised to 600 °C, with the monolith performing better than the coated carbon cloth. In all cases however, the materials did not succeed to give a stable capacitance as the applied current was varied, indicating that the materials are less viable at higher currents. This may be due to hindrance in mass transport throughout the materials, either by PVDF pore-blocking in coated carbon cloths, or by the small pore diameters in low quality monoliths.

Previously, monoliths were prepared from starch using the freeze-drying method.<sup>52</sup> This indicated that the gel formed from alginic acid and chitosan must therefore be less strong, potentially due the heterogeneity of the material and also the lower gelling ability of chitosan. Before the freeze-drying method was adopted for drying Starbons, supercritical CO<sub>2</sub> drying was employed.<sup>21</sup> This was tested with *N*-Starbons, in the hope of forming a stronger monolith. In fact, the monolith did hold its shape, and the material shrunk less on drying indicating that the material may be holding its larger pores on drying. The GCD plots for the scCO<sub>2</sub> dried monolith are shown in Figure 6.4(1). Finally, the freeze-drying method was attempted for 800 °C monoliths several times as it may be a more efficient method for drying Starbons. Unfortunately, in all cases, the drying process gave a very fragile and flaky monolith that could not hold its shape on being transferred from the freeze-drying equipment to the furnace. Therefore, no progress could be made towards a more efficient monolith preparation procedure.

To improve stability, an alteration to carbonisation process was made to include an additional final hold at 800 °C for two hours (whereas previously, cooling would begin the moment the temperature reached 800 °C, immediately after the ramping up stage). This ensures that the entire material is fully carbonised, which is especially important in the monolith form as the outer surface temperature may be different to the bulk temperature of the material. The GCD plots for the stabilised monolith are shown in Figure 6.4(2).

In comparison to the vacuum-oven drying, both scCO<sub>2</sub> dried monoliths performed better. This was shown both by the shape of their GCD plots; which give straight charging and discharging lines, as well as in their stability at higher applied currents; showing a lower percentage change between each current step. Additionally, the added two hours of heating at 800 °C showed a significant improvement in the capacitance of the material, making it the most successful material overall.

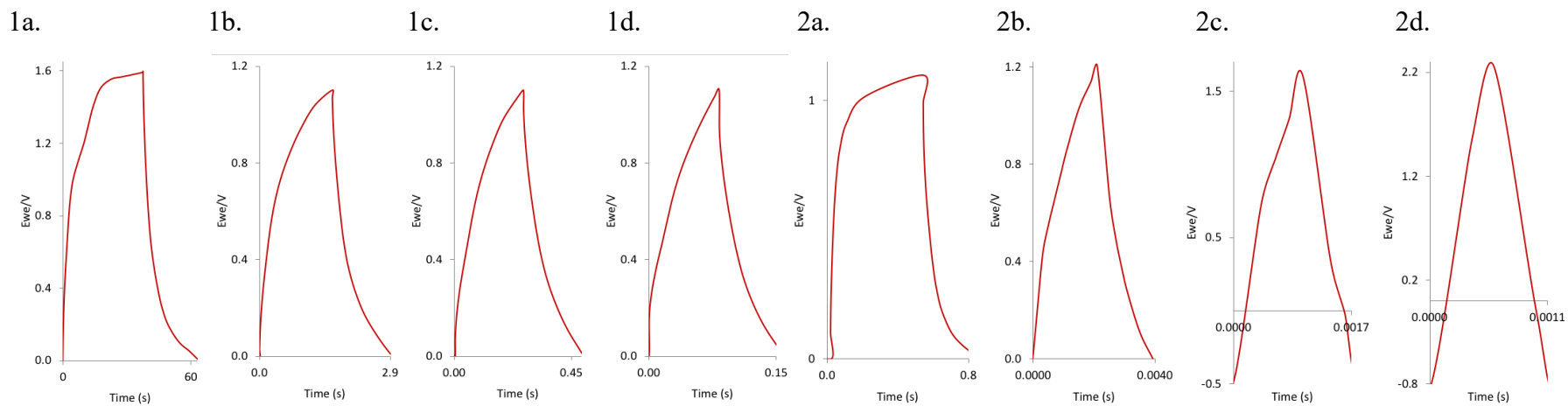


Figure 6.2: Galvanostatic charge/discharge of an *N*-Starbon (600 °C) 1) coated carbon cloth and 2) monolith at a) 2 mA, b) 10 mA, c) 25 mA and d) 50 mA.

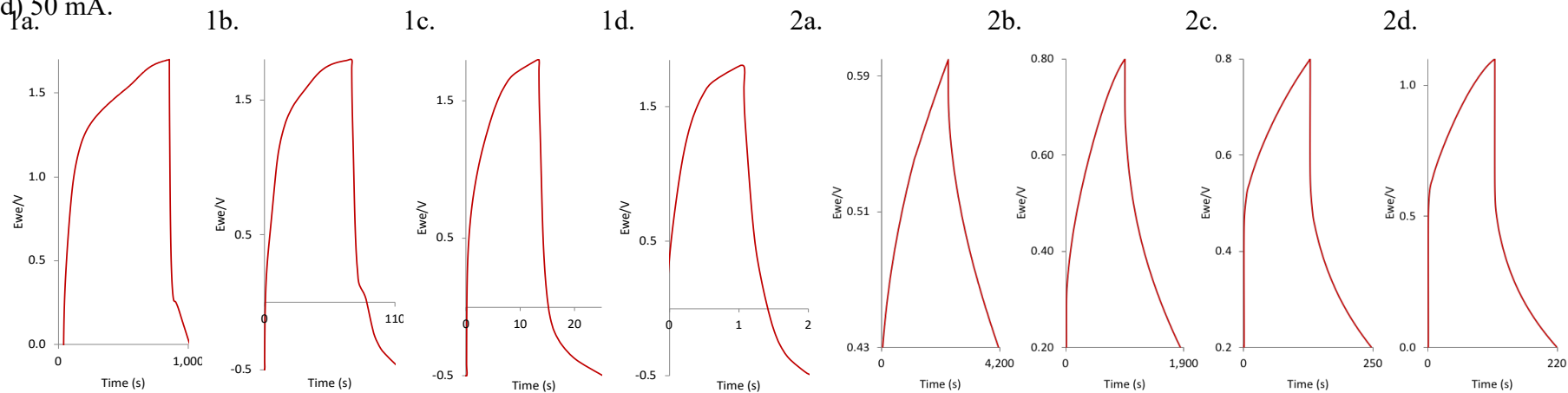


Figure 6.3: Galvanostatic charge/discharge of an *N*-Starbon (800 °C) 1) coated carbon cloth and 2) monolith at a) 2 mA, b) 10 mA, c) 25 mA and d) 50 mA.

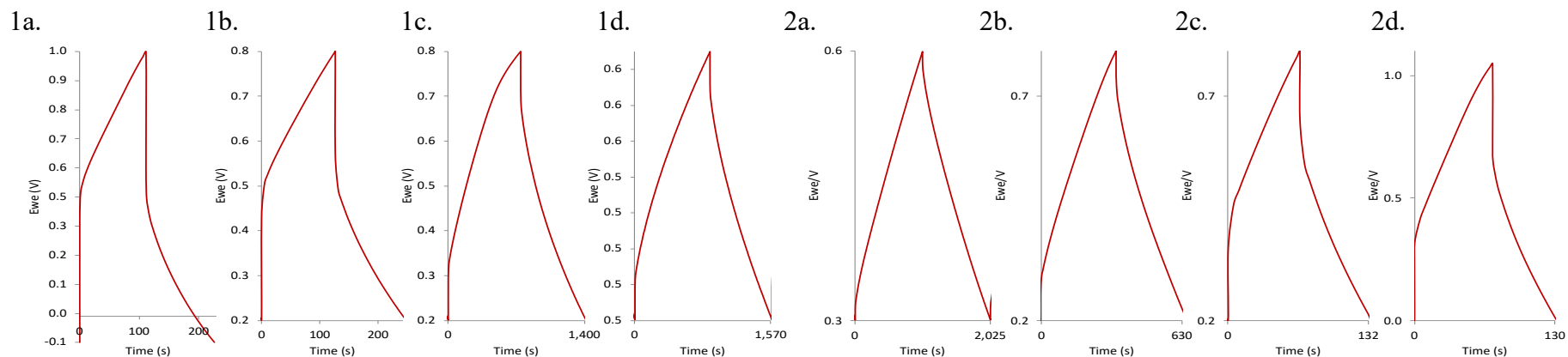


Figure 6.4: Galvanostatic charge/discharge of an *N*-Starbon (ScCO<sub>2</sub> dried, 800 °C) monolith having undergone 1) standard carbonisation and 2) carbonisation with a prolonged (2 h) hold at 800 °C, a) 2 mA, b) 10 mA, c) 25 mA and d) 50 mA.

Table 6.1: The capacitance (F g<sup>-1</sup>) measurements calculated from galvanostatic charge/discharge plots where materials were dried by either freeze-drying, vacuum oven drying or scCO<sub>2</sub> drying.

Material form		Coated carbon cloth		Monolith			
		Freeze-drying		Vacuum oven		scCO <sub>2</sub>	
Drying method							
Carbonisation Temp (°C)		600	800	600	800	800	800 (+ 2 h)
Applied current (mA)	2	35.5	139	0.0374	222	100	152
	10	11.3	124	0.000167	133	63	133
	25	5.44	109	0.000111	72	54	96
	50	3.08	34	0.0000595	71	54	99

Apart from measuring capacitance, GCD plots are used to measure the stability of a material's capacitance over a number of cycles. Initially, a blank carbon cloth sample was tested (Figure 6.5). As would be expected, the blank shows repeatability indicating that there will not be a negative impact on stability of any of the *N*-Starbons from the carbon cloth itself. The blank carbon cloth also shows no capacitance, meaning that all capacitance observed when coated, is completely a result of the *N*-Starbons themselves.

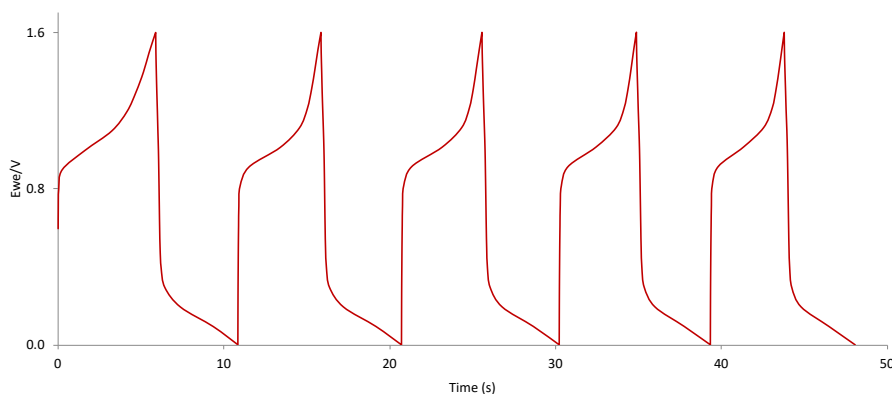


Figure 6.5: Galvanostatic charge/discharge of a blank 2x1 cm section of carbon cloth at 2 mA over 5 cycles.

All *N*-Starbon samples were also tested over five cycles and showed the same reproducibility, indicating some level of stability. The first five charge/discharge cycles of the best performing material (N800 monolith: scCO<sub>2</sub> dried + 2 h temperature hold at 800 °C) are plotted in Figure 6.6, which already show promising stability. The monolith was additionally tested over 320 cycles. The capacitance was calculated every 10 cycles and is plotted in Figure 6.7. The maximum negative fluctuation in capacitance is less than 3%, thus the exceptional stability of this *N*-Starbon monolith is clear. Although literature often shows exponentially more cycles than what is displayed here, this is past the scope of this work, which aims to show the potential of *N*-Starbons in this field.

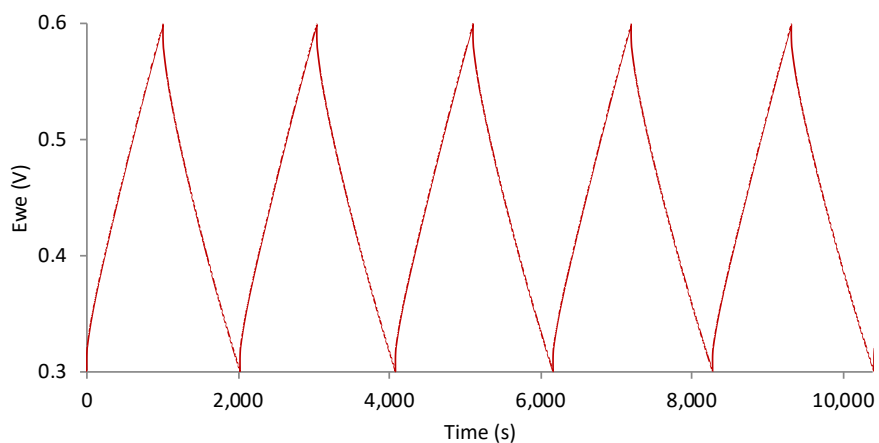


Figure 6.6: Galvanostatic charge/discharge of an *N*-Starbon (ScCO<sub>2</sub> dried, 800 °C + 2 h hold) monolith at 2 mA over 5 cycles.

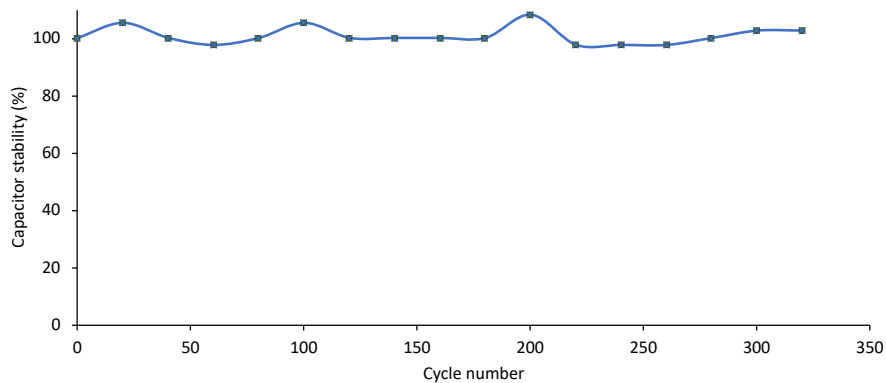


Figure 6.7: Capacitance stability of an *N*-Starbon (ScCO<sub>2</sub> dried, 800 °C + 2 h hold) monolith at 25 mA over 320 cycles, as measured by galvanostatic charge/discharge.

## 6.2.2 Cyclic voltammetry

*N*-Starbons were also analysed by cyclic voltammetry. As before, the plots are shown (Figures 6.8 – 6.11) as well as the calculated capacitance values (Table 6.2), determined using the following equation, as previously explained;

$$C = \frac{S_{area}}{2mv\Delta V}$$

As with the GCD calculations, active masses of the *N*-Starbon monoliths and the blank carbon cloth (used as a blank sample for coated samples) were assumed to be half the mass of the whole sample. The blank carbon cloth sample gave a negligible capacitance, ensuring that it is not contributing to the capacitance results obtained for any of the *N*-Starbons. Unless otherwise stated, the materials tested were composed of 1:1 alginate acid : chitosan.

An initial indication of capacitance can be taken from the shape of CV plots. The ideal shape of these plots is a rectangle.<sup>192</sup> As with GCD, CV was first performed on 600 °C *N*-Starbons; both in the monolith form and coated on carbon cloth (Figure 6.8). The plots, being far from a rectangular shape, clearly do not show behaviour of an ideal capacitor. This is also reflected in the low capacitance values calculated from the curves. The non-ideal behaviour seen here is likely due the surfaces still being electrochemically active, as any oxidation or reduction reaction will cause peaks in the curve, shifting it away from the ideal rectangular shape.

Thus, more favourable results may be obtained with materials carbonised to a higher temperature (800 °C) as their surface is more reduced and therefore more stable (Figure 6.9). The monolith, although slightly improved, again performed poorly here. To rectify this, scCO<sub>2</sub> drying and additional pTSA doping post drying were attempted to improve the pore structure. As shown in Figure 6.10a and the calculated capacitance values however, no improvement was seen in either case. To further reduce and stabilise the material's surface, an additional two-hour hold at 800 °C was added to the carbonisation process (Figure 6.10b). The plot now begins to resemble a rectangle, indicating that the material is acting as a capacitor. A capacitance of 80 F g<sup>-1</sup> was obtained for this sample, which is not far from a publishable value, as shown by similar materials described in

the literature as listed in Table 6.3.<sup>52, 186, 187, 193-196</sup> This shows the great potential of these materials in this field.

In the case of the N800 coated carbon cloth, the result was even more promising, achieving a close to ideally shaped cyclic voltammogram and an increased capacitance of  $103 \text{ F g}^{-1}$ .  $\text{ScCO}_2$  drying is a gentler method of drying than freeze-drying, so it is unlikely that the drying process is improving the pore quality in the powders. The reason for the poorer performance may therefore imply that there is reduced conductivity in the monolith compared to when a powder is pasted on carbon cloth. To ensure that the nitrogen in this *N*-Starbon (50% chitosan, 7.9% N) is indeed a major contributor to the capacitance achieved, the material was compared to similar materials with less nitrogen content. These included regular Starbons; S800 (0% N), A800 (0.2% N) and P800 (0.8% N), and *N*-Starbon with half the chitosan content (25% chitosan, 2.8% N). The CV plots for these materials coated onto carbon cloth are shown in Figure 6.11 and the capacitance results have been included in Table 6.2 for comparison. P800 and A800 gave slightly better capacitance compared to S800, potentially due to a combination of their nitrogen content and higher pore volume, which may allow for better ease of mass transport throughout the material. This trend is again observed in all alginic acid containing materials with different proportions of chitosan. On going from A800 with 0% chitosan, to *N*-Starbons with 25% and 50% chitosan, capacitance is significantly increased. It is likely that the increase in capacitance is so significant due to a proportion of the nitrogen being present as nitriles, which have a high dielectric constant, but it is impossible to know for certain at this stage.

Overall, irrespective of carbonisation temperature, the CV results clearly show that the monoliths give poorer capacitance when compared to the coated carbon cloths. This further confirms that it may be the formation of the monolith itself that is detrimental to pore quality. When comparing the capacitance values for the monolith calculated from GCD and CV, there is a large discrepancy of  $72 \text{ F g}^{-1}$ , making the results unreliable. With regards to the coated carbon cloth however, this discrepancy, although still present, is significantly reduced to  $36 \text{ F g}^{-1}$ , exactly half. Given the lack of linearity in the GCD plots, it is likely that adjustments to the experimental procedure will further reduce the errors.<sup>191</sup> Furthermore, with the powdered material, the addition of PVDF or other polymer may allow for applications such as in flexible batteries or capacitors.<sup>176</sup>

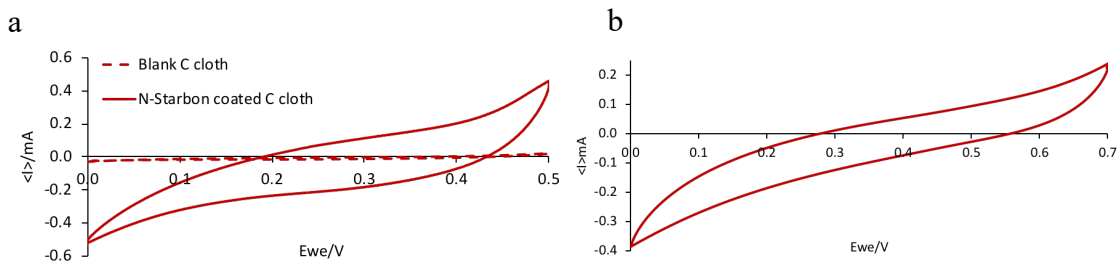


Figure 6.8: The cyclic voltammogram of an *N*-Starbon (600 °C) a) coated carbon cloth and b) monolith.

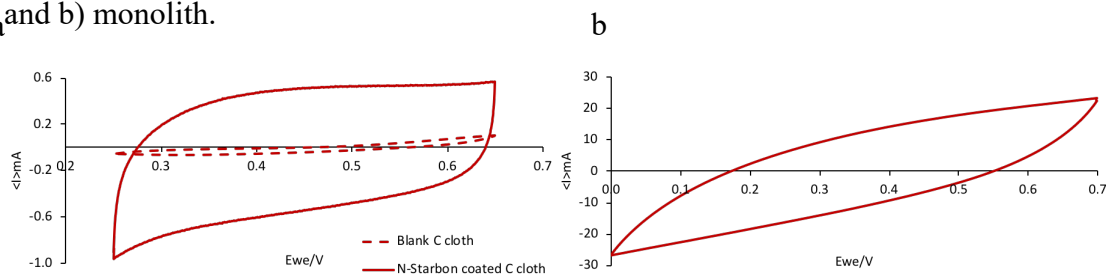


Figure 6.9: The cyclic voltammogram of an *N*-Starbon (800 °C) a) coated carbon cloth and b) monolith.

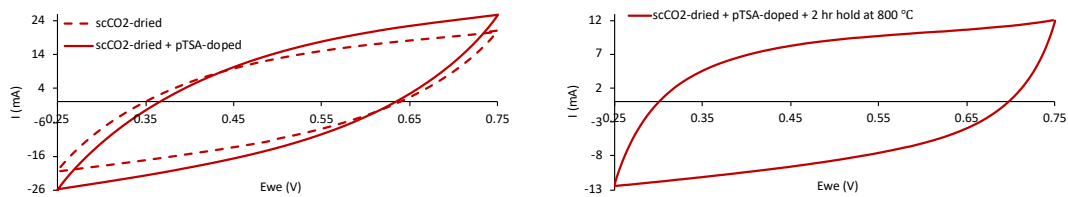


Figure 6.10: The cyclic voltammograms of scCO<sub>2</sub> dried *N*-Starbon (800 °C) monoliths prepared a) normally, with post-drying pTSA doping and b) post-drying pTSA doping at 2 h hold at 800 °C.

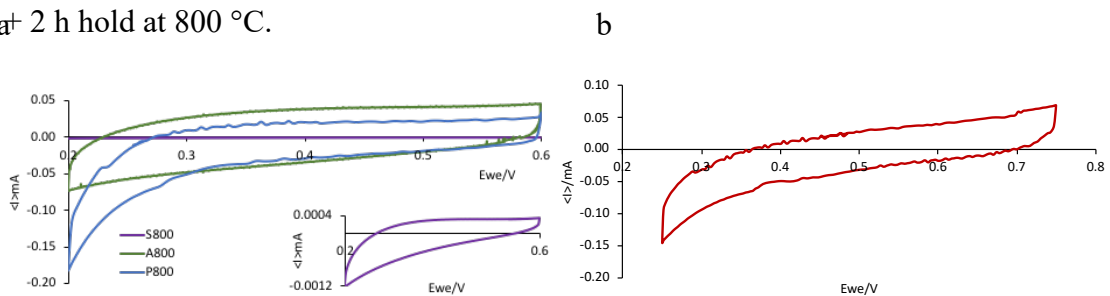


Figure 6.11: The cyclic voltammograms of carbon cloths coated with various materials carbonised to 800 °C: a) regular Starbons and b) *N*-Starbon containing 25% chitosan.

Table 6.2: The capacitance measurements calculated from CV plots. †

<b>Sample</b>	<b>Capacitance (F g<sup>-1</sup>)</b>
Blank carbon cloth	< 1
Starbon 800 coated carbon cloth	0.04
Algibon 800 coated carbon cloth	5.47
Pecbon 800 coated carbon cloth	4.72
<i>N</i> -Starbon 600 °C coated carbon cloth	27.5
<i>N</i> -Starbon 600 °C monolith	0.189
<i>N</i> -Starbon 800 °C coated carbon cloth (25% chitosan)	11.9
<i>N</i> -Starbon 800 °C coated carbon cloth	103
<i>N</i> -Starbon 800 °C monolith (vacuum oven dried)	27.7
<i>N</i> -Starbon 800 °C monolith (scCO <sub>2</sub> )	21.1
<i>N</i> -Starbon 800 °C monolith (scCO <sub>2</sub> + acid doping)	19.7
<i>N</i> -Starbon 800 °C monolith (scCO <sub>2</sub> + acid doping + temperature hold)	79.9

† Unless stated otherwise, all *N*-Starbons used for electrochemistry were made from a 1:1 mixture of chitosan and alginic acid.

As in GCD tests, the stability of the most superior samples was tested by CV too. The samples chosen were the 800 °C N-Starbon, both as a monolith and as a powder coated on carbon cloth. This was done by performing CV at increasing quantities of current to determine their usability under these conditions. The CV plots are shown in Figures 6.12 and 6.13 for the monolith and coated carbon cloth, respectively. Unfortunately, at higher currents, the monolith deviates away from its more ideal shape and thus fails to perform as a capacitor. This indicates that the material is poorly conductive; a common occurrence amongst materials with smaller pore channels, which results in high resistance within the material.<sup>52</sup> N800 powder coated onto carbon cloth does not suffer the same resistance that occurs in the monolith, making it a stable capacitor even at a current of up to 50 mA (Figure 6.13).

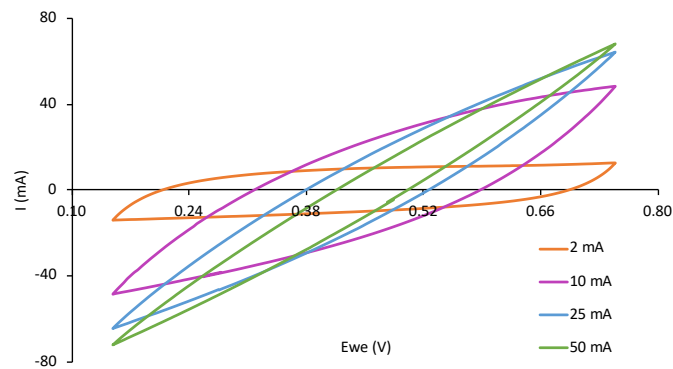


Figure 6.12: CV of N-Starbon 800 °C monolith at 2 mA, 10 mA, 25 mA and 50 mA.

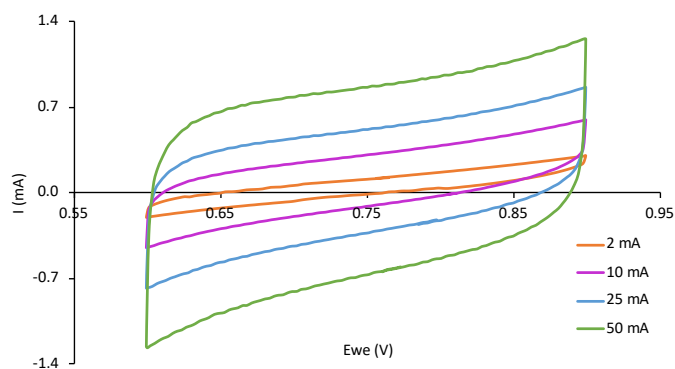


Figure 6.13: CV of N-Starbon 800 °C coated carbon cloth at 2 mA, 10 mA, 25 mA and 50 mA.

Finally, to determine how well *N*-Starbons have performed in these electrochemistry experiments, a handful of similar materials from the literature were chosen as examples for comparison (Table 6.3). All results listed are from electrochemical experiments carried out in a 1 mol dm<sup>-3</sup> H<sub>2</sub>SO<sub>4</sub> electrolyte solution, the same conditions used for this work. The *N*-Starbon promisingly falls within the range of capacitance values in the table, without any modification or optimisation, confirming its ability to compete with the materials that are being researched today.

Table 6.3: A comparison of the capacitance of *N*-Starbons to other porous carbons in the literature.

<b>Sample</b>	<b>Capacitance (F g<sup>-1</sup>)</b>
Carbon Nanotube/Polyacrylonitrile Blends	100 <sup>193</sup>
<b><i>N</i>-Starbon (this work)</b>	<b>103</b>
Micro/mesoporous carbon nanosheets	140 <sup>194</sup>
Starbon800 with 20% graphite	175 <sup>52</sup>
Melamine-based carbon	205 <sup>195</sup>
3D porous reduced graphene oxide film	206 <sup>186</sup>
CO <sub>2</sub> -activated porous graphene	279 <sup>187</sup>
N-doped porous graphene/carbon	405 <sup>196</sup>

# Chapter 7

# CO<sub>2</sub> Capture

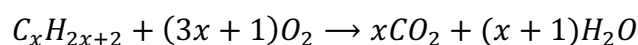


## 7.1 Introduction

“The industrial revolution yielded an unprecedented combination of cheap and abundant energy and cheap and abundant raw materials. The result was an explosion in human productivity.” ... “Consumerism sees the consumption of ever more products and services as a positive thing. It encourages people to treat themselves, spoil themselves, and even kill themselves slowly by overconsumption.” – Yuval Noah Harari, *Sapiens*

The jump in technology caused by the industrial revolution allowed our species to create an enormous abundance of products for every use imaginable to the human mind, including even products with no use whatsoever. Apart from the consequences associated with the exploitation of natural resources, this surge in production caused a parallel surge in greenhouse gas (GHG) emissions into the atmosphere.<sup>197</sup>

This surge in GHG emissions led to an increase in atmospheric temperatures, via the greenhouse effect, resulting in increased occurrences of heat waves, floods, droughts and other dangers to our existence. We have become experts in measuring these changes but current trends for GHG production show that we are still amateurs at diminishing emissions at a sufficiently effective rate.<sup>4</sup> Capturing the gases and storing them for alternative applications is not ideal but may currently be a more realistic approach. The main GHGs causing global warming are methane, chlorofluorocarbons (CFCs), nitrous oxide, and most significantly, carbon dioxide.<sup>4</sup> Carbon dioxide is produced from the combustion of fossil fuels by the following general hydrocarbon oxidation reaction:



CO<sub>2</sub> is subsequently released into the atmosphere where it absorbs and re-emits infrared radiation which would otherwise continue upwards into space. For the above reasons, carbon dioxide capture and storage (CCS) is a hot research topic today.<sup>198</sup>

There are different methods employed for CO<sub>2</sub> adsorption / desorption / material regeneration; (i) pressure-swing adsorption (PSA); where pressure is repeatedly increased and decreased, (ii) temperature-swing adsorption (TSA); where temperature is repeatedly increasing and decreased, or (iii) a hybrid of the two: pressure and

temperature swing adsorption (PTSA). Vacuum-swing adsorption (VSA) and electric-swing adsorption (ESA) are less common techniques.<sup>199</sup>

As described in previous chapters, porous materials are highly capable of adsorption, or capture, of substances out of liquid solutions. This chapter will address their capability in adsorbing compounds in the gas phase. The importance of this capability is relevant not only in CCS for waste air treatment but also in the purification of hydrogen, natural gas (for helium production) and bio-methane as well as personal protection devices. Separation processes also use these materials, such as in air separation for obtaining oxygen for medical or other purposes, and also propane / propylene mixture separation for producing polypropylene. Moreover, the storage capability is vital for hydrogen in fuel cell cars and methane as an energy carrier.<sup>198, 200</sup>

Typically, liquid amines can be used for CO<sub>2</sub> capture however solids are often easier to handle and simpler to re-use.<sup>201</sup> This challenge has been taken up by several groups using a range of different amine supports.<sup>202-204</sup> One example is by Plaza *et al.*, where the alkylamines were immobilised onto a commercially available carbon; activated carbon.<sup>141</sup> Although this was successful, it was found that the alkylamines significantly reduced the microporosity of the material, negatively impacting its adsorption capacity.

The main groups of porous materials that have been studied include zeolites<sup>205-207</sup>, activated carbons<sup>208-210</sup> and metal-organic frameworks (MOFs).<sup>211</sup> Carbons are widely available and cheap, making them desirable as adsorbents. Due to their high temperature preparation, they are thermally stable and often hydrophobic meaning that their adsorption is less hindered by water vapour compared to other more polar materials.<sup>212</sup> As will be seen later on in this section, they are unfortunately limited to high pressure and low temperature applications. Therefore, further research is required to overcome these challenges, such as by increasing the surface area enough to compensate for the lower adsorption capacity at higher temperatures. Unlike carbons, zeolites' adsorption capacity is greatly hindered by moisture due to their hydrophilicity. This means that they require high temperatures for regeneration. This polarity means that selective adsorption is capable based on electrostatic properties, so CO<sub>2</sub> adsorption is preferential over H<sub>2</sub>, N<sub>2</sub>, and CH<sub>4</sub>.<sup>213</sup> However, this selectivity is lost on heating, making them unusable at high temperature, similar to carbons. The main advantages of MOFs are their exceedingly high surface area and their easily controllable structure. The latter

allows for their structures to be modelled precisely, meaning that adsorption can be easily understood and predicted. The main drawbacks of using MOFs are their high cost, particularly on regeneration, and their instability in the presence of water vapour; two qualities that are inherently overcome in carbon materials.<sup>211</sup>

As discussed in Chapter 1, Starbon materials, having several desirable properties for CO<sub>2</sub> adsorption, have been tested by Dura *et al.*<sup>51</sup> In this study, it was found that having a proportion of mesoporosity along with microporosity was highly beneficial because it allowed movement of CO<sub>2</sub> towards the micropores, making them more accessible and therefore increasing the effective surface area of adsorption. Other literature has shown that nitrogen-doping too can improve CO<sub>2</sub> adsorption through strong interactions with the basic nitrogen functionalities.<sup>214, 215</sup> Thus, it follows that *N*-Starbons, possessing high surface areas, some balance of micro- and mesoporosity, as well as high nitrogen contents, should be suitable for CO<sub>2</sub> adsorption.

## 7.2 Results

As described in section 7.1, carbon dioxide adsorption is useful in several different scenarios, each having their own specific requirements, or conditions under which adsorption must occur. Experiments have therefore been conducted both at atmospheric pressure (Figures 7.1 – 7.3) and at 10 bar. The calculated mmol CO<sub>2</sub> adsorbed per gram of porous material under atmospheric pressure and at 10 bar are tabulated in Tables 7.1 and 7.2, respectively. Experiments were first done at atmospheric pressure, which immediately showed an improvement on going from low temperature materials (Figure 7.1) to high temperature materials (Figure 7.2). This was consistent with both the literature and theory, as the higher surface areas in high temperature materials greatly improve adsorption capacity.<sup>51</sup> For this reason, under high pressure, low temperature materials were excluded and instead, a wider range of high temperature materials were tested. All *N*-Starbons used in this chapter are the 1:1 alginic acid : chitosan materials characterised in Chapter 5, and will be referred to as, for example, N600: *N*-Starbon carbonised to 600 °C. Comparisons were also made with chitosan-based materials, which will similarly be referred to as, for example, C600.

## 7.2.1 Adsorption at atmosphere pressure

The experiments at atmospheric pressure were performed using an STA and involved 5 cycles of CO<sub>2</sub> adsorption and desorption by repeatedly flowing 100% CO<sub>2</sub> followed by 100% N<sub>2</sub>. In Figures 7.1 - 7.3, the increase in heat flow indicates that an exothermic reaction is taking place. This corresponds to the CO<sub>2</sub> adsorption onto the Starbon surface and is followed by the endothermic desorption by flow of nitrogen, causing a decrease in the heat flow. In all cases it is clear that CO<sub>2</sub> adsorption is completely reversible, and both adsorption and desorption are fast.

As mentioned, it is clear that the materials carbonised to higher temperatures are superior. Apart from the surface area influence however, Dura *et al.* added that, although generally it is microporosity that is considered to be the most important variable, a degree of mesoporosity improves adsorption. This is because mesoporosity makes an additional volume of micropores accessible, thus increasing the capacity of the materials.<sup>51</sup> In Chapters 2 and 5 (Starbon and N-Starbon Characterisation), Figures 2.2, 2.3, 5.2 and 5.3 showed that materials carbonised to 300 °C contain a large degree of mesoporosity and little to no microporosity. It is therefore understandable that without the high surface area that micropores provide, the materials performed poorly.

Having said this, the C300 has a lower surface area, pore volume and mesoporosity than both A300 or N300 but still shows improved performance, with A300 performing the poorest. Since the textural properties are unfavourable in this case, the positively contributing factor must be the increasing nitrogen content on going from A300 (0%) to N300 (6%) to C300 (11%). Dura *et al.* also determined that although for all materials, physisorption is the major adsorption mechanism, in low temperature materials, some chemisorption also takes place. This was attributed to the oxygen still present on the materials' surface.<sup>51</sup> Nitrogen-content may similarly allow for additional chemisorption of CO<sub>2</sub> onto the surface of these materials through the basicity of the nitrogen in whatever form it may be present as.<sup>214</sup>

The results show similar patterns at higher temperatures, but potentially for different reasons. Again, a decrease in pore volume is present on going from A to N to C materials. The increase in CO<sub>2</sub> adsorption is once more observed with C600, however here, the increase likely corresponds to: (i) the increase in microporosity, or available

microporosity and (ii) the higher nitrogen-content. Both the surface areas and micropore volumes for these high temperature materials are significantly higher than those of low temperature materials, which follows well with the increase in mmol of CO<sub>2</sub> adsorbed per gram of material.

A preparation temperature of 800 °C proved to be most advantageous for CO<sub>2</sub> adsorption using Starbons.<sup>51</sup> The nitrogen present in high temperature materials however is more likely to be graphitic nitrogen. A molecular study on the effect of this kind of nitrogen on CO<sub>2</sub> adsorption has been done by Kumar *et al.* Although their materials, similar to the *N*-Starbons, likely contained other functional groups, these proved too complex to model and thus for simplicity, it was assumed that only graphitic-*N* was present in the materials. With this assumption, nitrogen was theoretically found to only marginally, if at all, affect the CO<sub>2</sub> adsorption of the carbon materials.<sup>214</sup> It is thus most probable that other nitrogen-containing functional groups are giving the higher CO<sub>2</sub> adsorption seen experimentally. Additionally, nitrogen content does not appear to increase significantly, or at all, with temperatures higher than 600 °C. For these two reasons, it is not expected that a C800 material will perform any better than C600.

Activated carbon (AC), a common carbon material known to show fair levels of CO<sub>2</sub> adsorption, was tested for comparison (Figure 7.3). AC is known to contain a large degree of microporosity. However, the nitrogen adsorption / desorption porosimetry instrument is unable to accurately measure microporosity as it requires a much longer degas time and a stronger vacuum pump compared to mesoporosity analysis. Thus, the pore data shown is likely to be heavily understated and is only an indication of AC's real properties. It is therefore likely that AC has the highest surface area of the materials tested. Given this however, it performed poorly compared to the rest of the materials prepared at high temperature, further giving evidence for the need for mesoporosity and / or nitrogen, which are both lacking in AC.

Overall, the results at atmospheric pressure clearly further confirm the theory put forward by Dura *et al.*: mesoporosity has indeed shown to be effective.<sup>51</sup> Moreover, the nitrogen content in both *N*-Starbons and chitosan-based mesoporous materials has further increased the ability of the materials to adsorb CO<sub>2</sub>, giving rise to higher adsorption capacities.

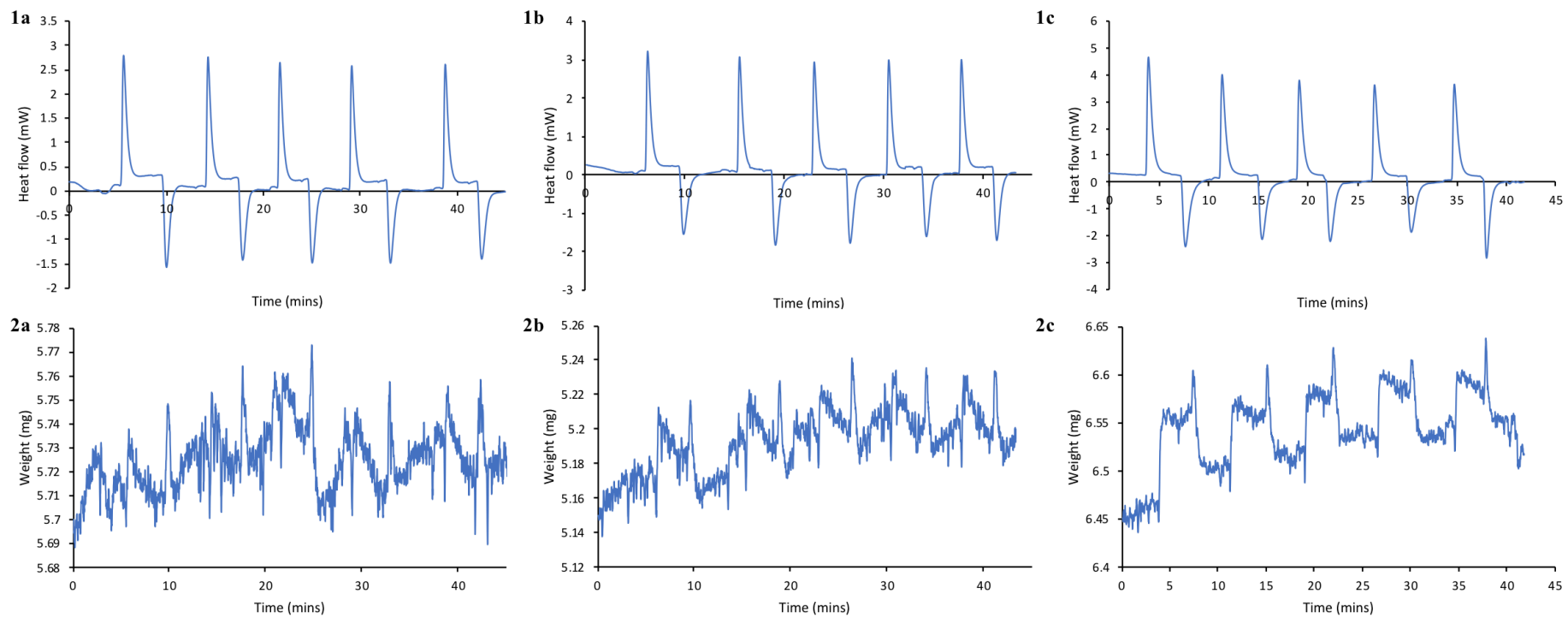


Figure 7.1: The 1) heat flow data and 2) weight change over time for A300 (a), N300 (b) and C300 (c) for 5 cycles of CO<sub>2</sub> adsorption and desorption.

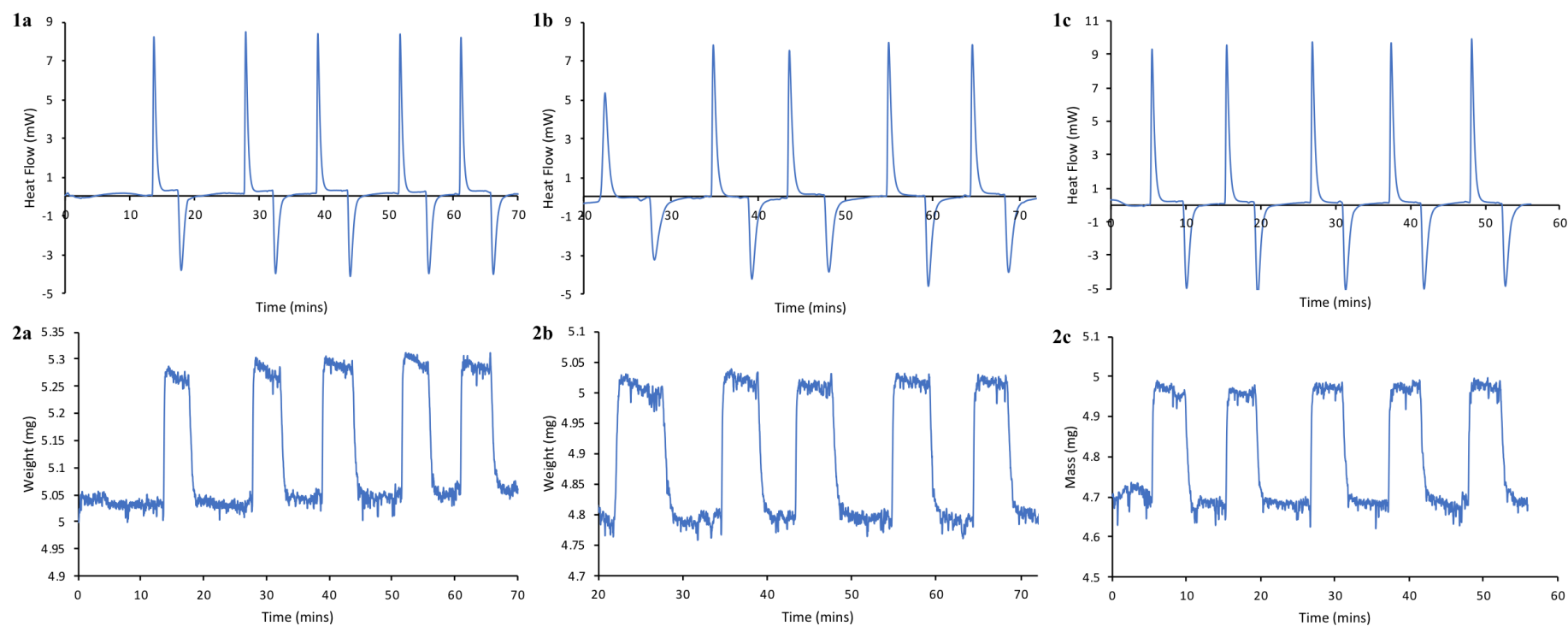


Figure 7.2: The 1) heat flow data and 2) weight change over time for A800 (a), N800 (b) and C600 (c) for 5 cycles of CO<sub>2</sub> adsorption and desorption.

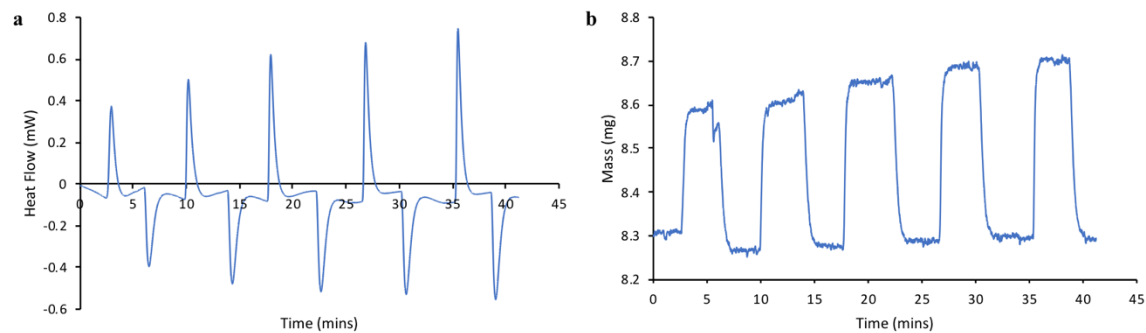


Figure 7.3: The a) heat flow data and b) weight change over time for activated carbon for 5 cycles of CO<sub>2</sub> adsorption and desorption.

Table 7.1: Calculated CO<sub>2</sub> adsorption data for a range of Starbons and activated carbon at atmospheric pressure, including their pore properties and nitrogen content.

<b>Material</b>	<b>BET surface area (m<sup>2</sup> g<sup>-1</sup>)</b>	<b>Total pore volume (m<sup>3</sup> g<sup>-1</sup>)</b>	<b>Microporosity (%)</b>	<b>N-content (%)</b>	<b>CO<sub>2</sub> adsorbed (mmol g<sup>-1</sup>)</b>	<b>Error (%)</b>
<b>A300</b>	174	0.64	2.1	0.00	0.095	23
<b>A800</b>	610	0.67	26	0.216	1.2	3.4
<b>C300</b>	67.9	0.19	11	10.7	0.23	30
<b>C600</b>	710	0.46	58	16.4	1.4	2.7
<b>N300</b>	138	0.57	2.9	6.12	0.14	14
<b>N800</b>	621	0.61	35	7.95	1.2	5.5
<b>AC</b>	526	0.32	76	0.160	1.0	12

## 7.2.2 Adsorption at high pressure

Starbons have also been shown to adsorb more CO<sub>2</sub> at higher pressures as high pressure improves CO<sub>2</sub> uptake into micropores.<sup>216, 217</sup> Higher pressure lowers the activation energy of adsorption in activated carbons and forms stronger adsorbate-adsorbent interactions. This essentially means that a high pressure can force CO<sub>2</sub> molecules into smaller spaces, which would otherwise require a higher activation energy. Due to the small size of the pores, the CO<sub>2</sub> molecules are more surrounded by the material's surface and therefore bound more strongly. Conversely at low pressure, the activation energy for CO<sub>2</sub> to enter these sites is too high and therefore they will only form interactions with pores of a larger diameter. Larger diameters imply a flatter surface and hence less points of contact with CO<sub>2</sub>. This also means that there is room for more CO<sub>2</sub> molecules in one pore, which means that there is more repulsion to overcome between the adsorbed CO<sub>2</sub> molecules; this further increases the activation energy required for adsorption.

The results for CO<sub>2</sub> adsorption at 10 bar are shown in Table 7.2. As expected, A800 and N800 both performed better than their 600 °C counterparts, showing the same trend as under atmosphere pressure. In the case of chitosan-based materials, as previously discussed, a decrease in *N*-content, increase in graphitic-*N* and higher microporosity resulted in C800 performing poorly compared to C600. The increase in pressure allowed for AC to exhibit an improved performance, however once again, a lower capacity than most of the other materials was observed. The top performing materials were C600, N600 and N800, presumably due their well-balanced mesoporosity, microporosity, surface area and *N*-content, with N800 showing the highest capacity at 2.36 mmol g<sup>-1</sup>.

The potential of *N*-Starbon, and additionally chitosan-based materials in the field of CO<sub>2</sub> adsorption has been clearly demonstrated here. Under both atmospheric pressure and high pressure, the materials performed significantly better than their Starbon counterparts, and also activated carbon. In future, improving the pore stability of chitosan at higher carbonisation temperatures may allow it to surpass *N*-Starbon in its CO<sub>2</sub> adsorption capacity.

Table 7.2: Calculated CO<sub>2</sub> adsorption data for a range of Starbons and activated carbon at 10 bar, including their pore properties and nitrogen content.

<b>Material</b>	<b>BET surface area (m<sup>2</sup> g<sup>-1</sup>)</b>	<b>Total pore volume (m<sup>3</sup> g<sup>-1</sup>)</b>	<b>Microporosity (%)</b>	<b>N-content (%)</b>	<b>CO<sub>2</sub> adsorbed (mmol g<sup>-1</sup>)</b>	<b>Error (%)</b>
<b>A600</b>	520	0.83	17	0	1.38	7.26
<b>A800</b>	610	0.67	26	0.216	1.59	5.51
<b>C600</b>	710	0.46	58	16.4	1.92	3.83
<b>C800</b>	341	0.20	65	9.60	1.44	5.34
<b>N600</b>	509	0.57	31	11.5	2.21	7.74
<b>N800</b>	621	0.61	35	7.95	2.36	2.94
<b>AC</b>	526	0.32	76	0.160	1.48	15.1

## Chapter 8

# Conclusions & Further Work



## 8.1 Starbons

All Starbon, Algibon and Pecbon materials were successfully prepared to a standard sufficient for application testing in Chapters 3 and 4. Pecbons were prepared for the first time from in-house extracted orange-peel waste. Potential improvements that can be made to the Pecbon manufacturing process in the future are described.

### 8.1.1 Pecbon development

A suitable method to produce mesoporous materials from pectin was previously developed on a 0.5 g scale (mass of starting material). The materials showed similar, if not superior, pore properties compared to Starbons and Algibons. Furthermore, the Pecbon manufacturing procedure is simpler and more sustainable compared to Starbons and Algibons; avoiding both the heating step during gelation and also pTSA addition before carbonisation.

Previously, Pecbon production was carried out using pectin bought from Sigma-Aldrich. This work was followed up in this study by using OPEC produced pectin. In the future, it can be optimised further to reduce certain unnecessarily repeated steps in order to make the process more efficient: The final steps of pectin extraction from orange peel involve washing with hot ethanol, filtering and freeze-drying. These steps are similar to the expansion and freeze-drying processes of Pecbon production. The method can therefore be altered to combine both procedures. The third wash can instead be done in hot TBA, filtered and re-dissolved in TBA / water (25 wt%) for direct gelation. This can then be allowed to stand for 24 hours proper to freeze-drying to allow for retrogradation. The resulting powder can subsequently be carbonised.

Additionally, attempts could be made to scale-up Pecbon production. Currently, only 0.5 g pectin can be gelated in one batch. Since both Starbons and Algibons have been produced in much larger amounts than this, it should be possible to do the same with Pecbons. Previous work on this has been unsuccessful, however the reason for this has not yet been understood.

## 8.2 WEEE recycling

Two types of E-waste were selected for metal recovery; the PCB and LCD. All of the gold found in a PCB leachate solution was successfully extracted with high selectivity, using A800 as the adsorbent. The gold was subsequently completely desorbed by cyclic voltammetry.

However, attempts to recover indium from LCD waste were unsuccessful. Further tests involved pre-prepared solutions of (i) indium alone and (ii) a mixture of indium and tin. These solutions mimicked the concentrations of ITO used on LCD screens. Complete adsorption and desorption of indium was simple and straight forward when indium was alone. P450 showed an adsorption capacity of  $114 \text{ mg g}^{-1}$  and high reusability without any need for regeneration. When indium was mixed with tin however, selective adsorption of indium was not possible with any of the materials. Having said this, S300 was successful in selectively adsorbing 100% of the tin in solution and none of the indium. S300 also showed exceptional reusability.

### 8.2.1 Indium recovery

Since tin was selectively extracted out of the mixture of indium and tin with the S300, it is unclear as to why this was not possible from the LCD leachate solution. The experiments were unsuccessful in both aqua regia at its natural pH, as well as when the pH was adjusted to 3.7 (to imitate the standard mixtures prepared). This therefore implies that it is not the acid content of aqua regia that is hindering adsorption, but some other factor. A possible explanation is that the Starbons are being preferentially overloaded with other metals, leaving no sites for the adsorption of tin. The other metals present in high concentration in the LCD waste solution are iron, zinc and copper. Further work may possibly determine whether any of these metals were removed from solution. If this is found to be the case, cleaning of the LCD screen combined with more selective leaching may ensure that only indium and tin are present in the final solution. This would allow tin to be selectively adsorbed and the indium precipitated out.

## 8.2.2 Starbon supported gold for catalysis

Gold from real WEEE was efficiently adsorbed onto the surface of the A800. Although recovery was successful, an alternative next step here could be to test possible applications for Au/A800. Gold, as supported nanoparticles on carbon, has shown to perform exceptionally well as a heterogeneous catalyst. Literature states that it is possible to replace catalysts such as the unstable and environmentally hazardous mercuric chloride in hydrochlorination reactions by supporting gold on activated carbon.<sup>218-220</sup> Currently, the commercial synthesis of this catalyst currently involves producing the activated carbon itself, adding chloroauric acid and impregnating the gold *via* sol-immobilisation techniques.<sup>219</sup> Using Algibons made from algae, a renewable resource, and gold obtained from e-waste, would significantly reduce the environmental impact of the catalyst and move towards a more circular system.

## 8.3 Separation of MAAs

This novel work showed a simple and sustainable method using Starbon materials to isolate usujirene, a potentially high-value molecule for sunscreen formulations, from a mixture of MAAs. S450 was found to be the most ideal Starbon for this purpose due to its geometry, which paralleled that of usujirene better than any other adsorbent, including activated carbon. Exceedingly high reusability was shown, with no decrease in activity throughout any experiments. The final usujirene product was acquired with a high purity not previously described in the literature. Such promising results should inevitably be scaled up in the future. The production of Starbons themselves has already been scaled-up and a simple solid-phase extraction system should prove simple on a larger scale once all the parameters are determined.

## 8.4 *N*-Starbon characterisation

Alginic acid and chitosan were mixed together to form the first nitrogen-doped Starbon material. Full characterisation showed that the materials contained significant quantities of up to 12% nitrogen. High pore quality, comparable to those of regular Algibons was achieved. The materials were additionally found to contain nitrile groups, which is not a common functionality amongst N-doped carbons. The reactivity of nitriles makes the material highly versatile, allowing it to be further functionalised for a wider range of applications than regular carbon or N-doped carbons.

### 8.4.1 Proteins as precursors

The mesoporous structure in Starbon materials is due to the ability of the starting materials to form helices with a mesopore diameter in their gel forms. Future work could therefore investigate whether it is possible to branch out from the use of polysaccharides as starting materials and attempt to produce N-containing mesoporous materials using the proteins that are also present in shellfish waste. Proteins have a much higher nitrogen content than chitin as well as having a vastly different chemical structure. As with chitosan, this could potentially lead to another new series of mesoporous materials having different properties.

## 8.5 Capacitance

Cyclic voltammetry of N800 powder coated onto carbon cloth showed that the material exhibits typical capacitor behaviour provided by its mesoporous framework and high nitrogen-content. This behaviour was stable even at a high applied current. Although capacitance from galvanostatic charge-discharge was immeasurable due to the material's characteristic unfavourable plot, the curve does show some capacitor behaviour. The capacitance calculated by CV is comparable to those in the literature, meaning that there is potential for *N*-Starbon's electrochemical properties to be studied further, for example by electrochemical impedance spectroscopy (IES) or GCD with an optimised experimental set-up.

Preparing N800 as a monolith proved challenging and although significant improvements were made to the material's properties, CV still showed non-ideal behaviour. The material showed poor conductivity at high currents, indicating that microporosity was high, hindering transport within the bulk of the material. Further work could include even more optimisation on the material, potentially through slower carbonisation to prevent pores from collapsing. It would be highly favourable to be able to obtain a good monolith because this avoids the use of polymer binders that are required when using N800 in its powder form.

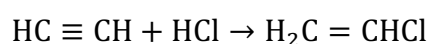
## 8.6 CO<sub>2</sub> capture

CO<sub>2</sub> adsorption was tested at atmospheric pressure and at an elevated pressure of 10 bar. The results clearly showed that in both cases, all materials containing nitrogen (*N*-Starbons and chitosan) performed better than those that did not contain nitrogen (Algibons and AC). In general, materials carbonised to higher temperatures (up to 800 °C) performed best, likely due to the higher surface area achieved at this temperature. N800 was found to be the best material, possibly due to it containing the right balance of microporosity, mesoporosity, a high surface area and reasonable nitrogen content. The results obtained in this work, unfortunately, did not match those achieved by Dura *et al.* using Algibons. It is unclear whether this is due to differences in the experimental set-up or differences in the quality of the Algibons, which were prepared by slightly different methods. It is thus impossible to compare *N*-Starbons to the published work.

Given the promising results so far, work can be done to further improve the quality of the chitosan-based materials. A first attempt may be to use pTSA as a pre-carbonisation acid dopant instead of acetic acid, which was shown to cause the *N*-Starbon mesopores to collapse. Furthermore, experimental conditions were not optimal when preparing the material. The pressure of the freeze-dryer was not optimal, and carbonisation was carried out several months after drying, allowing the material to potentially adsorb water from the air during this time. Thus, if all of these issues are rectified, a highly efficient and sustainable adsorbent for CO<sub>2</sub> may be prepared.

## 8.7 Acetylene hydrochlorination

Polyvinyl chloride (PVC) is the third most widely used polymer.<sup>221</sup> It is strong, cheap, transparent and highly resistant to degradation, making it applicable in a vast range of applications, such as in pipes, cable insulation, water-resistant clothing, healthcare devices and packaging.<sup>221</sup> PVC is made through the polymerisation reaction of the vinyl chloride monomer, or VCM. VCM itself is produced by acetylene hydrochlorination;



Industrially, the catalyst used for this reaction is mercury chloride on carbon.<sup>222</sup> Mercury chloride is however unstable at the reaction temperature and a proportion of the catalyst is thus lost during the reaction, giving it a short life-span. Apart from the waste aspect of losing a catalyst in a reaction, this drawback is exponentially worse due to the mercury being highly toxic, and thus heavily polluting the environment.<sup>220, 222-225</sup>

Most recently, research has therefore focused on metal-free catalysts.<sup>226-228</sup> Prof. Ying Li's research group developed mesoporous *N*-doped carbons using wheat flour as both the carbon and nitrogen source, and silica as a templating agent.<sup>228</sup> After carbonisation to 850 °C, the materials exhibited a surface area of 672 m<sup>2</sup> g<sup>-1</sup>, pore volume of 0.86 cm<sup>3</sup> g<sup>-1</sup> and *N*-content of 1.6%. The activity of the catalysts was attributed to nitrogen present as quaternary nitrogen, although other research groups have attributed catalytic activity to other *N*-containing functionalities; including both pyridinic-*N* and pyrrolic-*N*.<sup>228</sup>

The similarity between the wheat flour materials developed by Prof. Li and *N*-Starbon materials implied that there was a good chance that *N*-Starbon would also perform well as a catalyst in acetylene hydrochlorination. Thus, *N*-Starbons (N300, N450 and N600) were tested by Prof. Li's group at the Zhejiang University of Technology. The catalytic activity of *N*-Starbons increased with increasing carbonisation temperature, implying that high temperature carbonisation favours the formation of the catalytically active functional groups. Initial conversions were exceedingly high, significantly higher than both activated carbon and the wheat-flour carbon. However, this initial activity quickly dropped off, suggesting that the catalyst is not stable. Thus, there is great opportunity for this work to be continued by attempting the same reaction with a more stable *N*-Starbon catalyst, perhaps carbonised to 800+ °C.

## Chapter 9

# Experimental



## 9.1 Materials and chemicals

Starbons were produced using starch (food starch for industrial application, Univar), alginic acid (100%, Qingdao Jiaonan Bright Moon Seaweed Industrial Co., Ltd.), oranges (various varieties of sweet oranges purchased from local supermarkets), chitosan (low molecular weight, Aldrich), *tert*-butanol (>99%, Fluorochem Ltd.), *p*-toluenesulfonic acid monohydrate (98.5%, Sigma Aldrich), glacial acetic acid (analytical reagent grade, Fisher Scientific), ethanol (absolute, VWR Chemicals) and acetone (ACS grade, VWR).

*p*-Cymenesulfonic acid was prepared using *p*-Cymene (99%, Aldrich), sulfuric acid (fuming 20%, Sigma-Aldrich) and ~ 37% hydrochloric acid (analytical reagent grade, Fisher Scientific).

Indium adsorption and desorption studies were performed using a stock indium solution prepared using indium (III) chloride hydrate (~ 39% indium, Aldrich). pH adjustment was done by ~ 37% hydrochloric acid (analytical reagent grade, Fisher Scientific), 70% nitric acid (analytical reagent grade, Fisher Scientific), 0.1 M sodium hydroxide (volumetric solution, Fisher Scientific) and 1 M sodium hydroxide (volumetric solution, Fisher Scientific) addition. Activated carbon (powder, particle size 75% ≤ 40 μm) was obtained from Fluka. Tin adsorption studies were performed using a stock solution prepared from tin (IV) chloride pentahydrate (98%, Sigma-Aldrich).

Aqua regia for WEEE dissolution was prepared as a 3:1 mixture of ~ 37% hydrochloric acid (analytical reagent grade, Fisher Scientific) and 70% nitric acid (analytical reagent grade, Fisher Scientific). Neutralisation of aqua regia solution was performed by addition of sodium hydroxide pellets (analytical reagent grade, Fisher Scientific).

Sample preparation for ICP-MS was done by diluting samples in 1% nitric acid prepared by diluting a 70% nitric acid solution (≥ 99.999% trace metal basis, Aldrich) or in 1% hydrochloric acid prepared by diluting ~ 37% hydrochloric acid (for trace analysis, fuming, Fluka Analytical).

Before each use, the pH meter was calibrated using the following pH buffers purchased from Fisher Scientific; Buffer Solution pH 4 (phthalate), pH 7 (phosphate) and pH 9.2 (borate).

Potassium bromide (99+%, for spectroscopy, IR grade, ACROS Organics) was used for DRIFT.

Dulse and Nori seaweeds were provided by Unilever. Solvents used for extraction were methanol ( $\geq 99.9\%$ , Sigma-Aldrich) and ethanol (absolute, VWR Chemicals). Methanol ( $\geq 99.9\%$ , Sigma-Aldrich) was used as the liquid phase for HPLC, and formic acid ( $\geq 96\%$ , Sigma-Aldrich).

Slurries for carbon cloth (Spectracarb 2050A – 1550, FuelCellsEtc) coating were prepared using N,N-dimethylacetamide (anhydrous, 99.8%, Sigma-Aldrich) and poly(vinylidene fluoride) (average Mw 534,000, powder, Aldrich).

For electrochemical testing, sulfuric acid ( $> 95\%$ , Fisher Scientific) was used to prepare the electrolyte solution. The reference electrode was a custom-made Ag/AgCl electrode and the counter electrode used was platinum mesh.

## 9.2 Starbon<sup>®</sup> production

The general process is made up of 3 steps; expansion, drying and pyrolysis.<sup>21</sup> Although all three starting materials are put through these 3 main steps, slight modifications in the procedure have been made due the differences in their structures. Several Starbons, Algibons and Pecbons have been prepared per the procedures explained in this section.

### 9.2.1 Starch

Starbons were prepared by first gelating 40 g starch with 280 mL water. The mixture was microwaved in a CEM MARS 6 Microwave. The mixture was heated to 140 °C over 10 minutes with continuous stirring and kept at 140 °C for a further 10 minutes. Once removed from the microwave, the gel was allowed to cool for 24 hours at 5 °C for retrogradation to take place. Following this, 120 g *tert*-butanol as well as 0.4 g *p*-toluenesulfonic acid dissolved in a minimum amount of 20 wt% solution of TBA / water were added. The solution was stirred for an hour and then freeze-dried in a VirTis SP Scientific sentry 2.0 freeze-drier for 24 hours.<sup>28</sup> The resulting powder was placed in a Barnstead Thermolyne 6000 Furnace and carbonised according to the procedure in

Table 9.1, stopping at the desired carbonisation temperatures; 300, 450, 600 and 800 °C.

Table 9.1: Showing the furnace carbonisation steps.

Ramp temperature (°C)	Ramp rate (°C min <sup>-1</sup> )	Hold time (min)
<b>RT - 100</b>	5	60
<b>100 - 210</b>	0.3	60
<b>210 - 400</b>	0.3	-
<b>400 - 600</b>	1	-
<b>600 - 800</b>	3	-

### 9.2.2 Alginic acid

To produce Algibons, 200 g of alginic acid were gelled in 2 L of water at 90 °C for 180 mins. The resulting gel was placed in a refrigerator at 5 °C for 24 h for retrogradation. Following this, the gel was centrifuged at 3500 rpm for 10 mins using a Thermo Scientific Hereus Megafuge 40R Centrifuge, and the water layer was decanted. TBA (220 g) was added to the gel, as well as 2 g pTSA dissolved in a minimum amount of a 20 wt% TBA / water solution. The solution was stirred for 1 h, separated into 25 g portions in 100 mL flasks and freeze-dried for 24 h. The powder was carbonised to 300 °C, 450 °C, 600 °C and 800 °C as in Table 9.1.

### 9.2.3 Pectin

Previously prepared Pecbons used pectin purchased from Sigma Aldrich. However, there was an ongoing project at the Green Chemistry Centre of Excellence where the OPEC group (Orange Peel Exploitation Company) was extracting pectin from orange peel. It was ideal therefore to use this same extracted pectin to create Pecbons. Orange peel (4 g) and water (70 mL) were added to a microwave vessel along with a stirrer bar. The vessel was placed in a CEM MARS 6 Microwave and heated to 120 °C over 7.5 minutes, held at that temperature for a further 7.5 minutes and then allowed to cool back

down to room temperature. Once the vessels had cooled down, they were removed from the microwave and their contents vacuum filtered through a Buchner funnel. The filtrate was combined with double its volume in ethanol, stirred for 15 minutes and allowed to stand overnight. The ethanol / water solutions were poured into centrifuge flasks and centrifuged for 20 mins at 3500 rpm. The liquid phase was discarded while the solid phase was washed by dissolving in ethanol and stirring for 10 mins. The solution was then centrifuged as before. The washing step was repeated twice, after which the washed pectin was vacuum filtered and freeze-dried.

To make mesoporous pectin, extracted pectin was directly gelled in a 25 wt% TBA / water, eliminating the TBA addition step. This was done in 0.5 g portions of pectin in vials containing 5 mL of solution. Dissolution of the pectin was facilitated by 2 hours of sonication at 35 °C, after which the vials were stirred and placed in a refrigerator at 5 °C for 24 hours. The resulting gels were transferred to separate 50 mL round-bottomed flasks and freeze-dried for 24 hours. The dried expanded porous pectin was sifted using a 1 mm sieve and carbonised in 2 g portions to 300 °C, 450 °C, 600 °C and 800 °C per the heating rates listed in Table 9.1.

#### 9.2.4 Alginate acid / Chitosan hybrid (*N*-Starbon)

Several methods were attempted to determine the best method for *N*-Starbon production. To ensure that alginate acid forms its usual gel structure, alginate acid was gelatinised separately from chitosan. Initial attempts were made with a 1:3 chitosan : alginate acid mixture. Alginate acid (3 g) was dissolved in 30 mL distilled water, heated up to 90 °C and stirred for 180 mins. In a separate flask, 1 g chitosan was dissolved in 46 mL water and 4 mL 5 mol dm<sup>-3</sup> acetic acid, with continuous stirring at 65 °C. Once the alginate acid gel formation was complete, the chitosan gel was added dropwise, keeping both gels at 65 °C with vigorous stirring. Following dispersion, the gel mixture was stirred again with a stronger overhead stirrer in an attempt to improve homogeneity. The gel was kept in a refrigerator at 5 °C for 24 h.

The gel was split into two. To the first half, 20 wt% TBA was added, mixed and freeze-dried for 24 h. With the second half, solvent exchange was performed. The first wash was done by addition of ethanol (the same volume as the gel), followed by mixing for

3 h and centrifugation at 3500 rpm for 20 mins. The resulting liquid phase was decanted, and the gel was washed again, twice with ethanol and three times with acetone. The final gel was dried in a vacuum oven at 40 °C for 12 h. Both processes were repeated using various amounts of water and acid in the gel formation stage.

To improve homogeneity, the above procedure was later modified such that the starting powders (chitosan and alginic acid) were mixed first with subsequent combined gelation. The volume of water required in this case was 50 mL, along with 10 drops of 5 M acetic acid. The dried expanded porous alginic acid / chitosan samples carbonised to 300 °C, 450 °C and 600 °C per the heating rates listed in Table 9.1.

As the highest quality uncarbonised material was obtained through combined gelation, TBA addition and freeze-drying, this was repeated with increased amounts of chitosan for increased nitrogen contents, to give mixtures of 2:1 and 1:1 alginic acid : chitosan. These were again carbonised to 300 °C, 450 °C and 600 °C.

Acetic acid may not have the required properties to hold the materials' pore structures on carbonisation, therefore the 1:1 materials (4 g) were repeated again with 80 mL of water using pTSA (0.2 g) instead of acetic acid. Following gelation, 20 g TBA was added, the gel was cooled, freeze-dried and carbonised to 300 °C, 450 °C and 600 °C.

A bio-based form of pTSA is pCSA. p-CSA was prepared by sulfonating p-cymene (5 mL) with fuming sulfuric acid (20 %). The two were mixed together for 4 hours in a round-bottomed flask at room temperature. Subsequently 6 mL of distilled water were added to the mixture and it was cooled to 5 °C in a refrigerator overnight. The resulting purple solid was filtered, placed in a petri dish and warmed. Hydrochloric acid was added dropwise until the solid dissolved. Once completely dissolved, the solution was left to cool slowly, allowing the white pCSA crystals to form. The crystals were filtered and dried between two pieces of filter paper. The final yield of pCSA was 0.9 g.<sup>229</sup>

The pCSA was then used in place of pTSA to keep the *N*-Starbons completely bio-based. A 4 g batch of 1:1 (alginic acid : chitosan) *N*-Starbon was prepared with 80 mL of water and 0.2 g pCSA. Following gelation, 20 g TBA was added, the gel was cooled, freeze-dried and carbonised to 300 °C, 450 °C and 600 °C.

## 9.3 Starbon & *N*-Starbon characterisation

### 9.3.1 Porosimetry

Porosimetry of all starbons was performed using a Micrometric ASAP 2020 Surface Area and Porosity Analyzer. In each case, a 100 mg sample was analysed. Before performing porosimetry, all carbonised samples were degassed for 6 hours at 140 °C under nitrogen. Uncarbonised materials were degassed for 6 hours at 40 °C to avoid altering their chemical structures. Surface areas were calculated by means of the Brunauer–Emmett–Teller theory. Mesopore volumes and pore size distributions were calculated using the Barrett-Joyner-Halenda theory, and micropore volumes were calculated using the t-plot method. Total pore volumes were taken to be the summation of the micro- and mesopore volumes.

### 9.3.2 Scanning electron microscopy

Scanning electron microscopy was performed with the help of Meg Stark, on samples A300, A800 and P300 to compare their surface structures. Sample preparation involved fixing adhesive tape onto the sample holder and placing a small amount of the sample for a thin layer to stick to the holder. This was then coated with gold-palladium using a Polaron Sputter Coater. Finally, the sample holder was placed inside the JEOL JSM-6490LV SEM.

### 9.3.3 Elemental analysis

Elemental analysis was performed to determine the percentage content of carbon, hydrogen and most importantly, nitrogen in the *N*-Starbon materials and compare these values to those of regular Starbons. This was done with an Exeter Analytical CE-440 elemental analyser, used in conjunction with a Sartorius S2 analytical balance.

### 9.3.4 Thermogravimetric analysis

Thermogravimetric analysis was performed on expanded starch, alginic acid and pectin using a NETZSCH STA 409 where the change in mass over time was analysed

throughout the carbonisation process. The temperatures and ramp rates were as shown in Table 10.1 and the analysis was performed under nitrogen.

### 9.3.5 Thermogravimetric analysis – Diffuse reflectance infrared spectroscopy in Fourier transform mode

TGA – DRIFT was performed using a NETZSCH STA 409 and Bruker Equinox 55. A sample of *N*-Starbon 2:1 was heated at 10 °C min<sup>-1</sup> up to 600 °C under nitrogen. Any gaseous materials produced in the carbonisation process was analysed by DRIFT.

### 9.3.6 X-ray Photoelectron Spectroscopy

X-ray photoelectron spectroscopy was performed on *N*-Starbons 3:1 at the Department of Chemical and Biomolecular Engineering at the National University of Singapore. Samples were prepared by adhering a few milligrams onto a circular metal sample holder using adhesive tape. The samples were then submitted and run by the XPS service team on a Kratos AXIS Ultra<sup>DLD</sup>. XPS analysis of *N*-Starbons 2:1 was performed by Dr David Morgan at the Cardiff Catalysis Institute at Cardiff University.

### 9.3.7 Attenuated Total Reflection - Fourier Transform Infrared Spectroscopy

Attenuated total reflection – Fourier transform infrared spectroscopy was used to perform solid IR spectroscopy on alginic acid, chitosan and various *N*-Starbons using a Perkin Elmer FTIR/FTNIR Spectrum 400 Spectrophotometer.

### 9.3.8 Diffuse Reflectance Infrared Fourier Transform

Diffuse Reflectance Infrared Fourier Transform analysis was performed using a Bruker Equinox 55 on *N*-Starbons and *N*-Starbons containing adsorbed indium(III) in order to compare their nitrile peak positions and shifts. A blank spectrum was performed with ground potassium bromide powder. Analysis was performed using 2% sample combined and ground in potassium bromide, heated to 110 °C under vacuum in an environmental chamber.

## 9.4 Metal solution qualitative and quantitative analysis

### 9.4.1 Inductively Coupled Plasma – Mass Spectrometry

When testing for indium, samples were diluted to 1:100 in 1% nitric acid, or 1% hydrochloric acid for both indium and tin combined and sent to Dr. Lorna Eades at the University of Edinburgh for ICP-MS. When testing for a range of metals in aqua regia, samples were diluted 1:50 with distilled water and sent to Yara Analytical Services, where a rapid scan of 42 elements was performed by ICP-MS.

## 9.5 Real e-waste metal leaching & adsorption

### 9.5.1 Waste from an industrial waste stream

When testing the acidic solution of real electronic waste obtained from Benito Roggio Ambiental SA, 10 mL leaching solution was mixed with 10 mg adsorbent using a stirrer bar for 24 h at room temperature. The solutions were then centrifuged to remove the Starbons. Final metal concentrations were tested by ICP-MS. The Starbons were dried overnight in an oven at 40 °C to remove any remaining solution so that they can subsequently be analysed and characterised.

### 9.5.2 Waste from a laptop

A laptop was taken apart manually to obtain the PCB and LCD. The two parts were cut up into 3 cm x 3 cm squares using a pair of scissors and put into separate flasks. Aqua regia was added to each flask with a ratio of 1:7 glass (g) / liquid (mL). Leaching took place over 4 days, collecting samples from each at 0.5, 1, 2, 24, 48, 72 and 96 h for ICP-MS to determine the effect of time on leaching.

Next, the ability of Starbons to adsorb metals from the leached solution was tested. Leached solution (5 mL) was pipetted into a glass vial along with 20 mg adsorbent and a magnetic stirrer bar. The solution was stirred at 300 rpm and heated to 35 °C for 24 h. This was done using 12 different adsorbents; A000, A300, A450, A600, A800, S300, S450, S600, S800, P300, P450 and P600. To avoid centrifuging aqua regia, the mixtures were allowed to settle for 1 hour before pipetting out samples for ICP-MS.

To test for metal desorption, A800 and P800 was repeated as above with a new PCB leachate at a 40 mg Starbon scale for 2.5 h. Following adsorption, the Starbons were removed from the leachate solutions by centrifugation, washed with water for 15 mins, centrifuged again and dried in an oven at 100 °C. All solutions before and after adsorption were sent for ICP-MS analysis to ensure metal adsorption occurred as above. Both Starbons were sent for XPS analysis to further confirm ICP-MS results. Next, metal desorption was tested by cyclic voltammetry and chronoamperometry by coating carbon cloth sections with metal-Starbon samples so as to form an electrode off of which the metals can be desorbed. Three 1.5 x 3 cm pieces of carbon cloth were cut out. One was kept as a blank. With the other two cloths, a section (back and front) was covered in Teflon tape so as to be used for connection to the circuit. The remaining area was coated in Starbon slurry. To prepare the slurry, Starbons (25 mg) were mixed with 6.25 mg PVDF and 0.625 mL dimethyl acetamide and stirred overnight. Sides were coated one at a time, drying in an oven at 80 °C for 30 mins between each coating until all (or most) of the paste was used up. Once coated, the samples were placed in a drying oven at 100 °C for 2 hours and then under vacuum at 50 °C for an hour.

The electrolytic cell was a 25 mL three-necked round-bottomed flask containing 13 mL electrolyte solution (either 1 mol dm<sup>-3</sup> H<sub>2</sub>SO<sub>4</sub> or 1 mol dm<sup>-3</sup> HCl), an Ag/AgCl reference electrode, a carbon rod counter electrode and the working electrode (Starbon coated carbon cloth). The experiments were performed using a Bio-Logic Science Instruments SAS SP-150 Potentiostat and analysed using EC-Lab<sup>®</sup> software also by Bio-Logic Science Instruments SAS. Cyclic voltammetry was performed at 50 and 100 mV s<sup>-1</sup> until any changes in the voltammogram stabilised. Following this, chronoamperometry was performed at 2 V for 10 minutes. Finally, cyclic voltammetry was repeated to check for any changes in the samples. Experiments were first performed in H<sub>2</sub>SO<sub>4</sub> as this was believed to be the less likely of the two to be successful.

Once it was assumed that all the metal was removed from the Starbons, the solutions were transferred out of the electrolytic cell and sent for ICP-MS to check whether any metals had desorbed into solution. The cloths were placed in dimethyl acetamide and sonicated for 30 minutes to re-dissolve PVDF and detach the Starbons from the cloths. The mixtures were filtered, the Starbons dried in an oven at 170 °C and sent for XPS and TEM analysis (see section 9.11).

## 9.6 Indium (III) studies

### 9.6.1 Adsorption

A standard solution of  $70 \text{ mg L}^{-1} \text{ In}^{3+}$  was prepared using  $\text{InCl}_3 \cdot x\text{H}_2\text{O}$  in water. The resulting pH of the solution was found using a JENWAY 3505 pH/mV/Temperature Meter. For each experiment, 10 mg Starbon was weighed out in a sample vial.  $\text{In}^{3+}$  solution (5 mL) was pipetted into each vial. The use of stirrer bars was avoided as it was found that Starbons have a tendency to get stuck to the surface and this could affect adsorption. The solutions were instead mixed using a sample shaker. Preliminary experiments found that indium adsorption is unaffected by heating and can reach 100% within 3 h thus all experiments were run at room temperature for 3 h. A preliminary pH study was also conducted by testing adsorption from  $\text{InCl}_3$  solutions at pH values of 1.5, 2.5, 4.5 and 5.5 using HCl and NaOH to adjust the pH. As none of these gave better results than the unadjusted pH 3.7 solution, pH adjustment was avoided. Following adsorption, the solutions were centrifuged, and the resulting liquid analysed by ICP-MS to determine the extent of adsorbed indium onto the Starbons. ICP-MS was also performed on the stock  $\text{InCl}_3$  solutions to confirm the initial concentration each time. Experiments were repeated using activated carbon for comparison.

### 9.6.2 Desorption

Testing desorption first requires initial adsorption of indium. Following this, the indium solution needs to be removed and replaced by the desorption media. Complete removal of the indium solution is imperative as any unadsorbed indium would dissolve in the desorption medium and falsely increase the results. Therefore, to ensure complete removal of indium from solution, amounts below the Starbon's adsorption capacity were used. As maximum adsorption with 10 mg Starbon was found to be  $0.35 \mu\text{g In}^{3+}$ ,  $0.28 \mu\text{g In}^{3+}$  was used instead. Complete adsorption was confirmed by ICP-MS.

Following adsorption, the solutions were centrifuged, and the liquid removed. The desorption solvent (4 mL) was added to the Starbon-containing vial and mixed on a shaker for 24 h at room temperature. Desorption of indium into solution was analysed by ICP-MS as before. Tested desorption media were acetone, water, three different

acidic solutions (pH 1 and 4 prepared using HNO<sub>3</sub> in water and pH 3.7 prepared using HCl in water) and two basic solutions (pH 10 and 14 prepared using NaOH).

### 9.6.3 Re-use

The reusability of the P300 and P800 was investigated by repeatedly adsorbing and desorbing indium(III) from the samples. Adsorption was done using 6 mL of 70 mg L<sup>-1</sup> In<sup>3+</sup> solution in 2 hours and desorption was done with 6 mL of 0.1 mol dm<sup>-3</sup> nitric acid or hydrochloric acid overnight. All steps were performed at room temperature on a sample shaker. In between adsorptions and desorptions, samples were rinsed with 6 mL distilled water. Adsorption followed by desorption was repeated 4 times. Following each stage, solutions were centrifuged and analysed by ICP-MS as above.

## 9.7 Tin (IV) studies

Adsorption of tin(IV) by Starbon materials was tested by preparing a solution of 70 mg L<sup>-1</sup> tin(IV) using tin(IV) chloride pentahydrate. Each adsorption test was performed using 10 mg Starbon and 10 mL tin(IV) solution. The solution was found to have a pH of 2.6. Dilutions for ICP-MS analysis were done in 1% HCl.

## 9.8 Indium (III) vs. Tin (IV) studies

Selective adsorption of indium(III) over tin(IV) by Starbon materials was tested by preparing a solution of 55 mg L<sup>-1</sup> indium(III) using indium(III) chloride hydrate and 5 mg L<sup>-1</sup> tin(IV) using tin(IV) chloride pentahydrate. Each adsorption test was performed using 10 mg Starbon and 8 mL In<sup>3+</sup>/Sn<sup>4+</sup> solution. Dilutions for ICP-MS analysis were performed in 1% HCl.

## 9.9 Starbon-metal characterisation

### 9.9.1 Transmission electron microscopy

TEM was performed with the help of Meg Start on A300 and A800 samples containing adsorbed gold and indium separately. Sample preparation was done by placing a small amount of material in an eppendorf along with some ethanol. The eppendorfs were shaken and a drop of the mixture was pipetted onto a copper gates grid coated with pioloform. The samples were allowed to dry for 20 minutes and then placed in the TEM sample holder, which was inserted into a Philips TECNAI TEM with a Hamamatsu camera. AnalySIS was used as the acquisition program.

### 9.9.2 X-ray photoelectron and auger electron spectroscopy

XPS and AES were performed on gold-containing-Starbons and indium-containing-Starbons by the NEXUS team at Newcastle University. Samples were prepared by sticking a 1 cm x 1 cm piece of adhesive tape onto a microscopy cover slide. The tape was then covered by a thin layer of the Starbon sample and packed in aluminium foil.

### 9.9.3 Simultaneous thermal analysis

Simultaneous thermal analysis (STA) was performed using PL Thermal Sciences STA 625 on a Starbon sample (A300) containing adsorbed indium. The sample (10 mg) was weighed and heated from room temperature to 600 °C.

## 9.10 Separation of MAAs

### 9.10.1 High-Performance Liquid Chromatography

HPLC was performed on an LC-20AD prominence liquid chromatograph using an SPD-M20A prominence diode array detector. A C<sub>18</sub> column was used with a mobile phase of methanol and water (70:30 v/v) with 0.1% formic acid. Each run was 30 minutes with a flow rate of 0.5 mL min<sup>-1</sup>, temperature of 35 °C, an injection volume of 5 µL and detection at 310 nm, 320nm, 330 nm and 360 nm. The gradient used was that provided by Unilever: 1:99 hold for 10 min; to 20:80 over 5 min; to 99:1 over 5 min; hold for 3 min; to 1:99 over 2 min; hold for 5 min.

### 9.10.2 Repeated solvent wash extraction

The extraction method developed by Unilever was used for both Dulse and Nori seaweeds so that the extracts of the two can be compared. Seaweed (1 g) was rehydrated with 5 mL water in the fridge overnight. Methanol (17 mL) was added and the mixture was sonicated for 5 minutes in an ice bath. This was then centrifuged at 3,500 rpm for 10 minutes. The supernatant was removed and retained in the fridge. Another 17 mL 50% methanol was added to the seaweed and the extraction was repeated until a total of 3 extractions were performed. The supernatants from each repeat were pooled. The methanol was removed from the extract by rotary evaporation at 45 °C.

To further clean-up the crude extract, the material was re-constituted in 90% ethanol, left at -20 °C overnight and centrifuged. The supernatant was retained and the floridoside precipitate discarded. The ethanol was removed by rotary evaporation at 45 °C.

### 9.10.3 Soxhlet extraction

The set up for Soxhlet extraction is shown in Figure 9.1. The extraction was performed using both ethanol and methanol with Dulse seaweed and using only methanol with Nori seaweed. The volume of solvent used in each case was 300 mL and the mass of seaweed used was 30 g. Soxhlet extractions were run at the solvents' respective boiling points long enough for the solvent to syphon 5 times (circa 4 hours). The remaining seaweed was discarded, and the solvent evaporated off by rotary evaporation to obtain the crude extract.

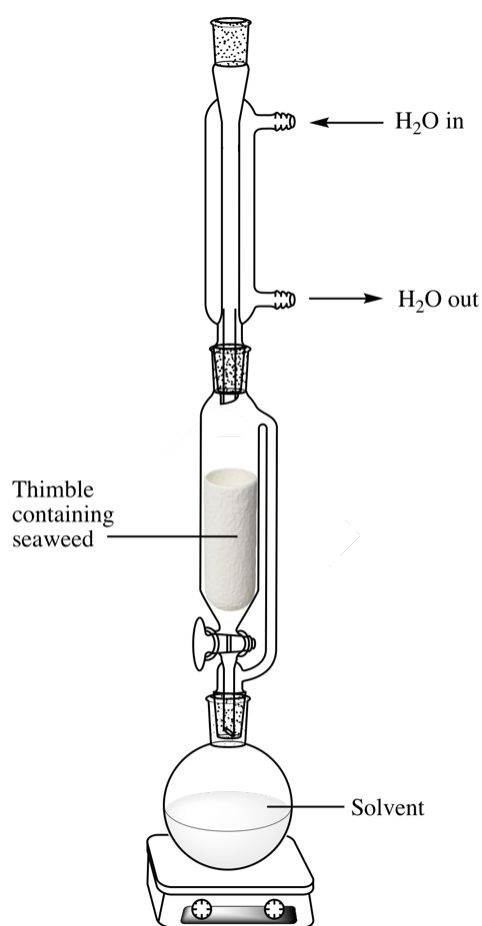


Figure 9.1: Soxhlet extraction set-up

#### 9.10.4 Counter-current chromatography simulation

CCC was simulated using 6 representative solvent mixtures (Table 9.2) that span a range of polarities. For each mixture, a total of 5 mL was prepared and 100 mg of Dulce extract (obtained by methanol Soxhlet extraction) was dissolved.

Table 9.2: The solvent mixtures selected for simulating CCC of MAAs from Dulce extract.

No	Heptane	EtOAc	MeOH	Butanol	Water
1	-	-	-	1	1
9	1	6	1	-	6
13	2	5	2	-	5
17	1	1	1	-	1
21	5	2	5	-	2
28	1	-	1	-	0

#### 9.10.5 Automated Starbon screening

Experiments were performed on an Anatune MultiPurpose Sampler using Gerstel Maestro software. ITSP cartridges containing 18 mg S300, S450, S800, A300, A450 and A800 were purchased. Adsorption was done by passing 300  $\mu$ L of a solution prepared by dissolving 1 g of extract in 20 mL water. This was followed by a rinse with 2.5 mL water to ensure that any unadsorbed material was washed out. Desorption was done with 300  $\mu$ L methanol and was followed by a 2.5 mL rinse with methanol. Following this, the cartridges were rinsed with another 2.5 mL water to condition them for the next adsorption. Before every change in solvent, the syringe and needle were rinsed with 2.5 mL of the subsequent solvent. The adsorption steps, desorption steps and washes were repeated to obtain a total of 4 runs for each Starbon material.

### 9.10.6 Scale-up

Adsorption and desorption were repeated at a larger scale in 4 repeats with 1 g S450 and 15 mL Nori extract solution provided by Unilever.

### 9.10.7 Flow simulation

To simulate a flow-type set-up (as opposed to batch processing) and test it on a 1 g scale, the aqueous solution collected after adsorption through S450 from the scale-up experiment was passed through the same Starbon repeatedly to obtain a total of 6 runs through the Starbon. Following each adsorption, the Starbon was rinsed with 5 mL water and material was desorbed with 15 mL methanol. For this experiment, the fourth repeat from the scale-up experiment was used to best simulate what would be obtained in a real industrial process when the Starbon would have been repeatedly used.

### 9.10.8 Further purification

The usujirene collected during desorption in the scale-up phase may be further purified by re-running the desorption solution through the Starbon again. To do this, the methanol was removed by rotary evaporation and the sample re-dissolved in 15 mL water. This was passed through the same 1 g of S450, which was then washed with 5 mL water. The material adsorbed onto S450 was then desorbed using 15 mL methanol. For this experiment, the second repeat from scale-up phase was used since the third and fourth repeats were taken for further characterisation.

## 9.11 Electrode preparations

To test *N*-Starbon's electrochemical properties, it had to be made into a material that is capable of acting as an electrode. The material can either be mixed into a slurry and pasted on carbon cloth, or, if possible, the material can be formed into a monolith and used directly. Both methods were tested and are described here.

### 9.11.1 Carbon cloth coating

In a vial, 40 mg *N*-Starbon (1:1, alginic acid : chitosan made with pTSA and carbonised to 600 °C and 800 °C) was weighed. To this, 1 mL diacetamide and 10 mg PVDF were added. The mixture was stirred at room temperature overnight.

Carbon cloth was cut into a rectangle of 2 x 1 cm. The top half (1 x 1 cm) was covered in Teflon tape to ensure that it remained clean for attachment to the crocodile clips during electrochemical experiments. On the remaining half, slurry was pipetted until the whole surface was covered. The carbon cloth was then placed in an oven at 70 °C overnight and then placed in a vacuum oven at 50 °C for 2 hours.

### 9.11.2 Monolith preparation

Before this work, monoliths have only been made through former Starbon production methods. The first attempt was made using starch through microwave gelation, solvent exchange with ethanol followed by supercritical CO<sub>2</sub> extraction to remove the ethanol, and finally carbonisation.<sup>21</sup> Later, a successful attempt was achieved with alginic acid through solvent exchange with ethanol and then with acetone, followed by vacuum oven drying and carbonisation. As the materials to be made into monoliths were alginic acid / chitosan hybrid Starbons, a modified version of the latter alginic acid method was attempted first. The method utilising supercritical CO<sub>2</sub> for drying was also attempted to ensure that the quality of the two materials was the same.

An 8 g mixture of 1:1 alginic acid and chitosan was weighed out and mixed carefully. To this, 100 mL of water containing 0.3 g pTSA was added. The mixture was stirred at 90 °C for 3 hours. The gel was split into two, half was poured into three 10 mL syringes. To the second half, 12.5 g TBA was added, mixed and poured into five 10 mL syringes.

All 8 syringes were refrigerated for 4 days. The syringes were then sliced open with a spatula at the bottom end and the gels were pushed out of the top end with the plunger. The TBA-containing samples did not hold their shape and could therefore not be used to make monoliths. The remaining gels held their shape and so were placed in a beaker for solvent exchange, with 100 mL ethanol for 48 hours, replacing the ethanol 3 times. This was followed by 48 hours in 100 mL acetone, again replacing the acetone 3 times. To the final acetone addition, 0.8 g pTSA was added.

The now firmer gel was placed in a vacuum oven for 1 hour at 40 °C. Afterwards, the dried monolith was placed in Pyrex glass tube surrounded by sand. The tube was then placed in a metal heating block (also filled with sand) on a heating mantle. This was slowly heated under vacuum up to 210 °C at 0.5 °C min<sup>-1</sup>. Once cooled, the monolith was transferred to a quartz flask and heated in a vacuum furnace, first up to 210 °C at 5 °C min<sup>-1</sup> and then up to 600 °C at the regular Starbon heating rates listed in Table 9.1. The changes in the appearance of the monolith throughout the process are shown in Figure 9.2. This was repeated with a carbonisation temperature of 800 °C.

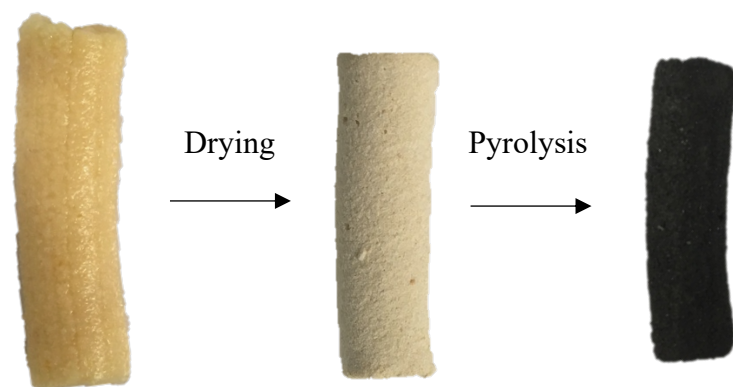


Figure 9.2: The appearance of the *N*-Starbon throughout monolith formation.

Monolith gel drying was also performed by supercritical CO<sub>2</sub>. This was done using a supercritical fluid extractor (SFE-500) provided by Thar technologies at 150 bar and 40 °C with a flow rate of 30 g min<sup>-1</sup>, using ethanol as a co-solvent at 1.5 g min<sup>-1</sup> for 40 minutes, then 0.75 g min<sup>-1</sup> for the next 90 minutes and then no ethanol for the remaining 120 minutes. Depressurisation was done slowly overnight at 0.15 bar min<sup>-1</sup>.

## 9.12 Electrochemical testing

Each of electrochemical experiments were tested on blank carbon cloth (2 cm x 1 cm), the carbon cloth (2 cm x 1 cm) half coated with the *N*-Starbon, and the *N*-Starbon monolith. All experiments were performed on a Bio-Logic Science Instruments SAS SP-150 Potentiostat and analysed using EC-Lab<sup>®</sup> software also by Bio-Logic Science Instruments SAS.

For each experiment, a 25 mL three-necked round-bottomed flask was used as the electrochemical cell, filled with 13 mL of 1 mol dm<sup>-3</sup> H<sub>2</sub>SO<sub>4</sub> solution. The three-electrode set-up was employed. The counter electrode (CE) used was a Pt mesh, which was chosen to have a high surface area so as to be as similar as possible to the working electrode. The reference electrode was an Ag/AgCl electrode. Each was placed in contact with the electrolyte solution through separate necks of the round-bottomed flask. It was ensured that they were as far apart as possible, and that none of the electrodes came into contact with each other. It was also important to ensure that the platinum mesh was not positioned beneath any of the other components since any evolved gas bubbles may rise to the other electrodes and block their surfaces, hindering their function. Each electrode was connected to the appropriate wire using crocodile clips. When coated carbon cloth was used as the working electrode, the coated half was immersed into the electrolyte solution. This was imitated when using the blank carbon cloth. When the monolith was being tested, half the monolith was immersed in solution. The set-up is shown in Figure 9.3.

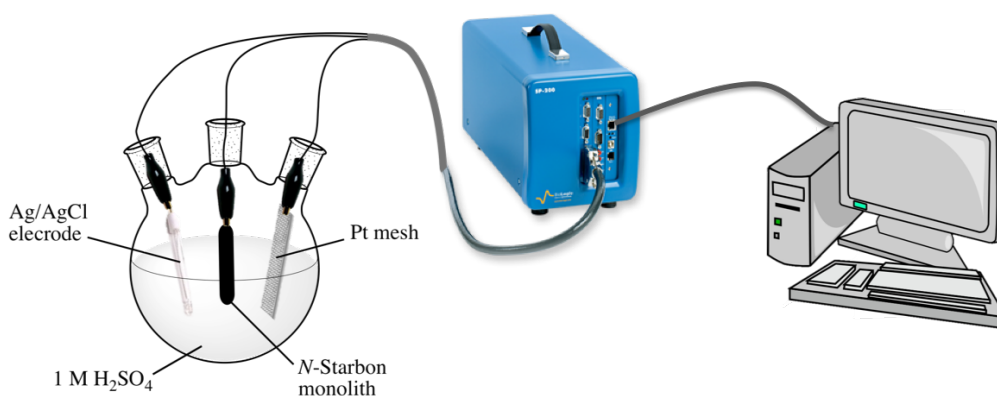


Figure 9.3: Showing the set-up used for electrochemical experiments.

### 9.12.1 Galvanostatic charge/discharge

Galvanic charge/discharge was performed using the chronopotentiometry technique. The parameters used for carbon cloth samples and monolith samples are listed in Tables 9.3 and 9.4, respectively.

Table 9.3: The parameters entered into the EC-Lab® software for galvanostatic charge/discharge experiments of carbon cloth samples.

Parameter	User input	
	Charge	Discharge
<b>Apply <math>I_s</math></b>	2, 10, 25, 50 mA	-2, -10, -25, -50 mA
<b>Limits: <math>E_{we} &gt; E_M</math></b>	1.6 V	0 V
<b>E range</b>	-10 V; 10 V	-10 V; 10 V
<b>I range</b>	10, 100 mA	10, 100 mA
<b>Bandwidth</b>	7 (fast)	7 (fast)

Table 9.4: The parameters entered into the EC-Lab® software for galvanostatic charge/discharge experiments of monoliths samples.

Parameter	User input	
	Charge	Discharge
<b>Apply <math>I_s</math></b>	2, 10, 25, 50 mA	-2, -10, -25, -50 mA
<b>Limits: <math>E_{we} &gt; E_M</math></b>	1.1 V	-0.1 V
<b>E range</b>	-10 V; 10 V	-10 V; 10 V
<b>I range</b>	10, 100 mA	10, 100 mA
<b>Bandwidth</b>	7 (fast)	7 (fast)

## 9.12.2 Cyclic voltammetry

For CV, the parameters used for carbon cloth samples and monolith samples are listed in Tables 9.5 and 9.6, respectively.

Table 9.5: The parameters entered into the EC-Lab® software for cyclic voltammetry of carbon cloth samples.

<b>Parameter</b>	<b>User input</b>
<b>Set <math>E_{we}</math> to <math>E_i</math></b>	0 V vs. Ref
<b>Scan <math>E_{we}</math> with <math>dE/dt</math> to vertex potential <math>E_1</math></b>	2 mV/s 0.5 V vs. Ref
<b>Reverse scan to vertex <math>E_2</math></b>	0 V vs. Ref
<b>E range</b>	-10 V; 10 V
<b>I range</b>	Auto
<b>Bandwidth</b>	5 (medium)

Table 9.6: The parameters entered into the EC-Lab® software for cyclic voltammetry of monolith samples.

<b>Parameter</b>	<b>User input</b>
<b>Set <math>E_{we}</math> to <math>E_i</math></b>	0 V vs. Ref
<b>Scan <math>E_{we}</math> with <math>dE/dt</math> to vertex potential <math>E_1</math></b>	2 mV/s 0.7 V vs. Ref
<b>Reverse scan to vertex <math>E_2</math></b>	0 V vs. Ref
<b>E range</b>	-10 V; 10 V
<b>I range</b>	Auto
<b>Bandwidth</b>	5 (medium)

## 9.13 CO<sub>2</sub> capture

### 9.13.1 Atmospheric pressure

CO<sub>2</sub> adsorption was tested at atmospheric pressure at 35 °C using a PL Thermal Sciences STA 625. Before adsorption, samples (5 – 10 mg) were loaded onto the instrument and heated to 120 °C at 10 °C min<sup>-1</sup> and kept at that temperature for an hour to remove any water from the surface of the materials. The mass loss during this time was recorded and subtracted from the original mass. CO<sub>2</sub> was then passed to the sample, measuring both heat flow and mass change with time. Once the heat flow returned to 0 W, indicating the CO<sub>2</sub> adsorption reaction was complete, CO<sub>2</sub> flow was stopped and N<sub>2</sub> flow was started to remove the CO<sub>2</sub>. N<sub>2</sub> flow was continued until the heat flow again returned the 0 W and the process was repeated to obtain a total of 5 CO<sub>2</sub> / N<sub>2</sub> cycles. The change in mass could then be found from the weight plot and an average calculated from the 5 cycles. The mass was then converted to moles of CO<sub>2</sub> adsorbed per gram of adsorbent material.

### 9.13.2 Elevated pressure

CO<sub>2</sub> adsorption of Starbons, *N*-Starbons and activated carbon was also tested at a pressure of 10 bar. This was done in a sealed pressure vessel connected to a pressure gauge at room temperature. A known mass of each material was added to a sealed vial, with a syringe inserted through the cap for gas transfer. The vials were placed into the pressure vessel, the vessel sealed, and CO<sub>2</sub> was flowed into the chamber until a pressure of 10 bar was attained. The sealed vessel was left to stand for 30 mins for adsorption to take place. Once the 30 minutes were up, the vessel was opened, and the vials reweighed. The new masses of the vials were measured and the difference in masses was taken to be the adsorbed CO<sub>2</sub>. Since CO<sub>2</sub> is heavier than air, to account for the CO<sub>2</sub> in the vial that is not adsorbed, an empty vial was also weighed, and the mass difference subtracted from all samples.

# Appendix A

## HPLC data



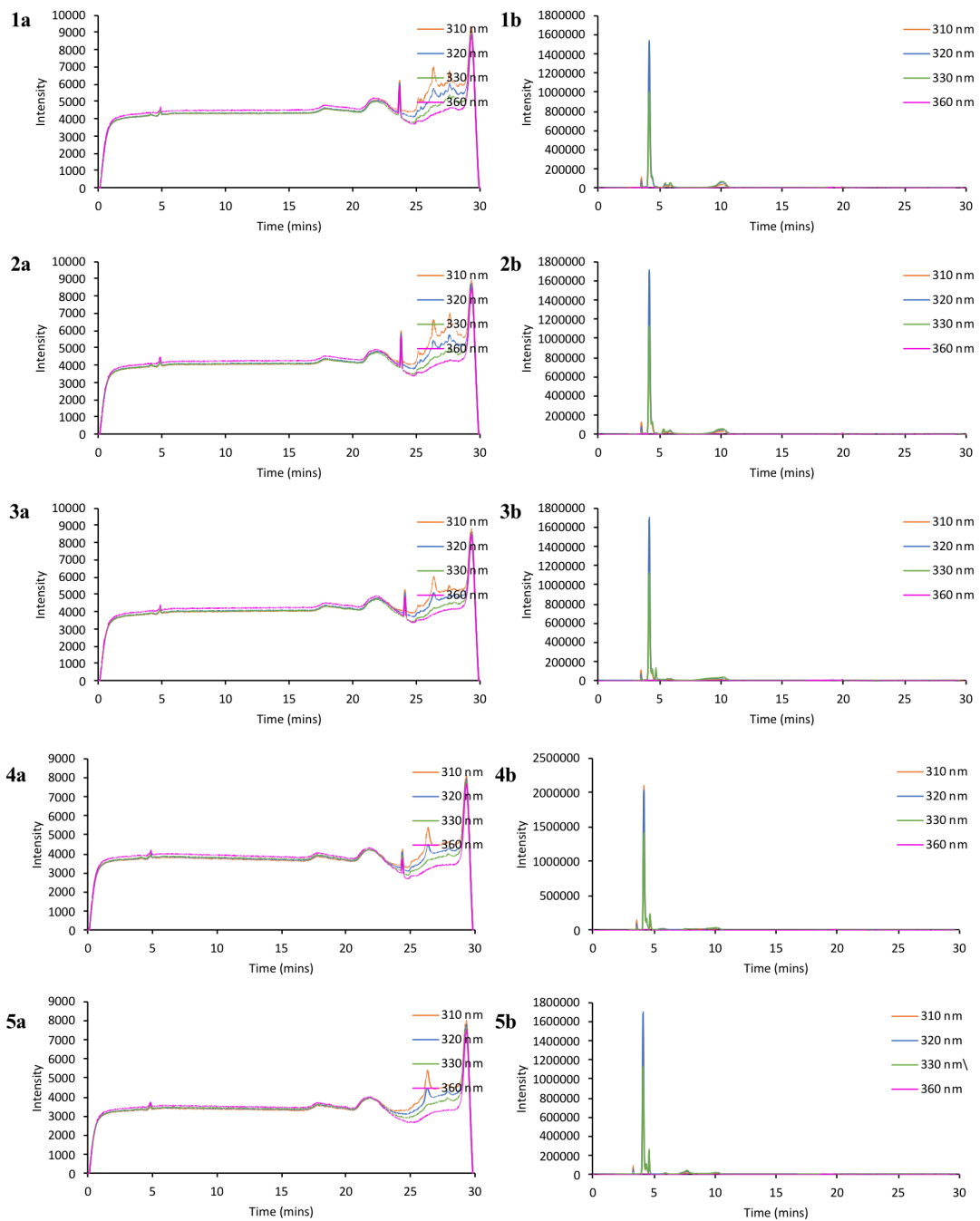


Figure A.1: HPLC chromatogram for the Dulse extract in solvent systems 1) 9, 2) 13, 3) 17, 4) 21 and 5) 28 as described in Table 10.10, a) upper (less polar) phase and b) lower (more polar) phase.

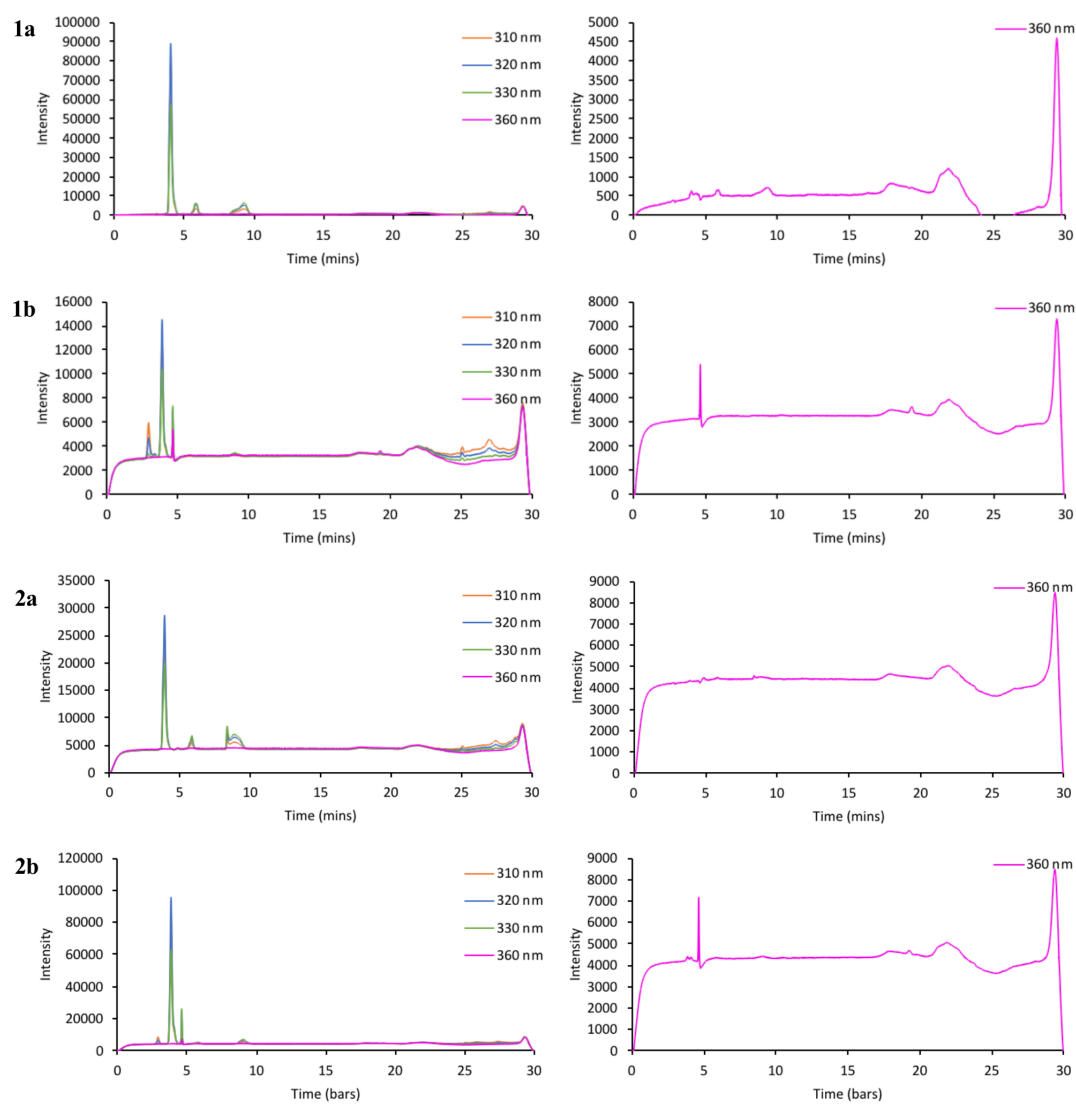


Figure A.2: HPLC chromatograms of the fourth repeat of Starbon screening for isolation of usujirene from Dulse extracts using 1) S300 and 2) S800, showing a) adsorption in water and b) desorption in methanol at 310 nm, 320 nm, 330 nm and 360 nm on the left, and zoomed in at 360 nm on the right.

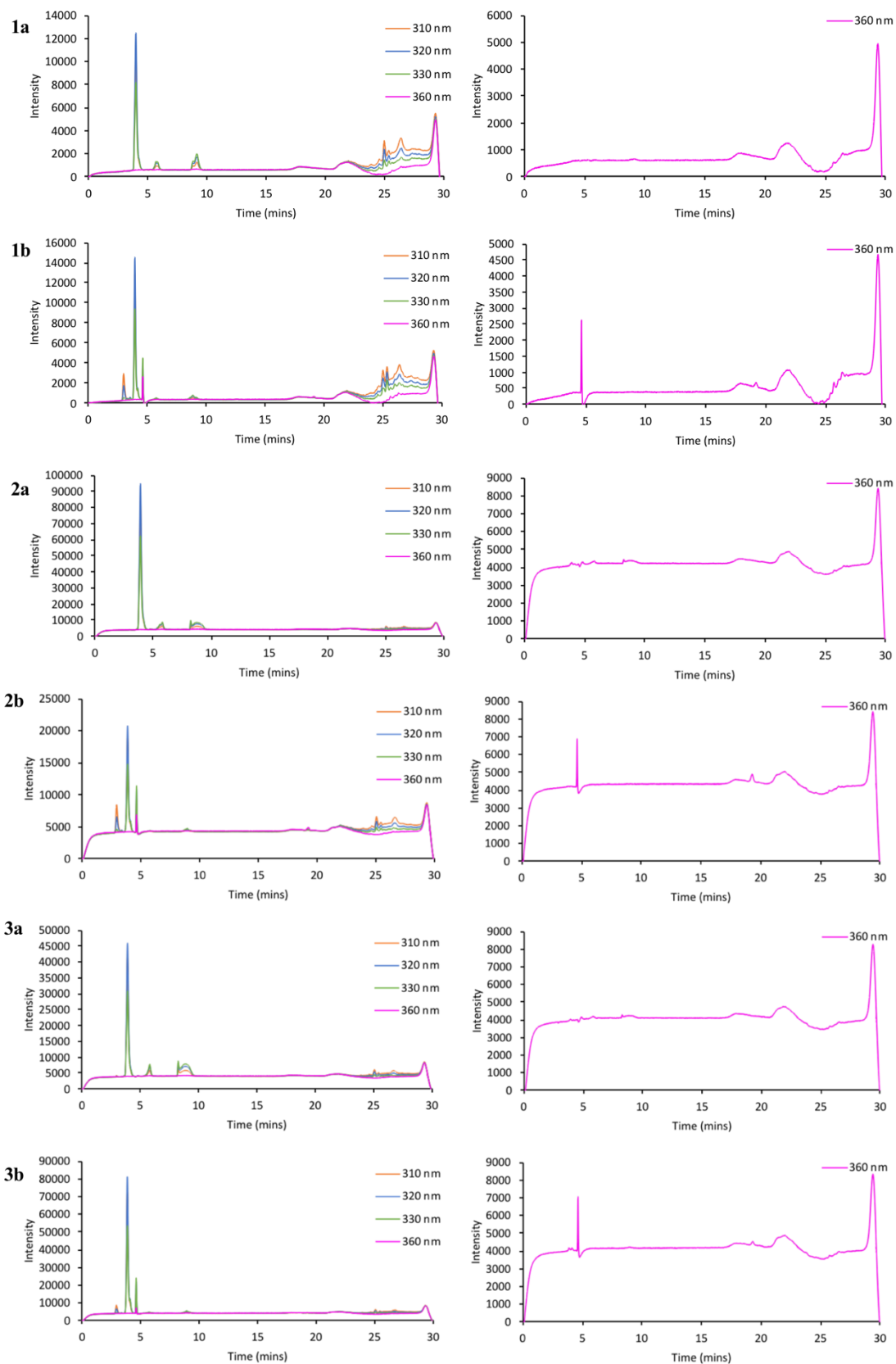


Figure A.3: HPLC chromatograms of the fourth repeat of Starbon screening for isolation of usujirene from Dulse extracts using 1) A300, 2) A450 and 3) A800, showing a) adsorption in water and b) desorption in methanol at 310 nm, 320 nm, 330 nm and 360 nm on the left, and zoomed in at 360 nm on the right.

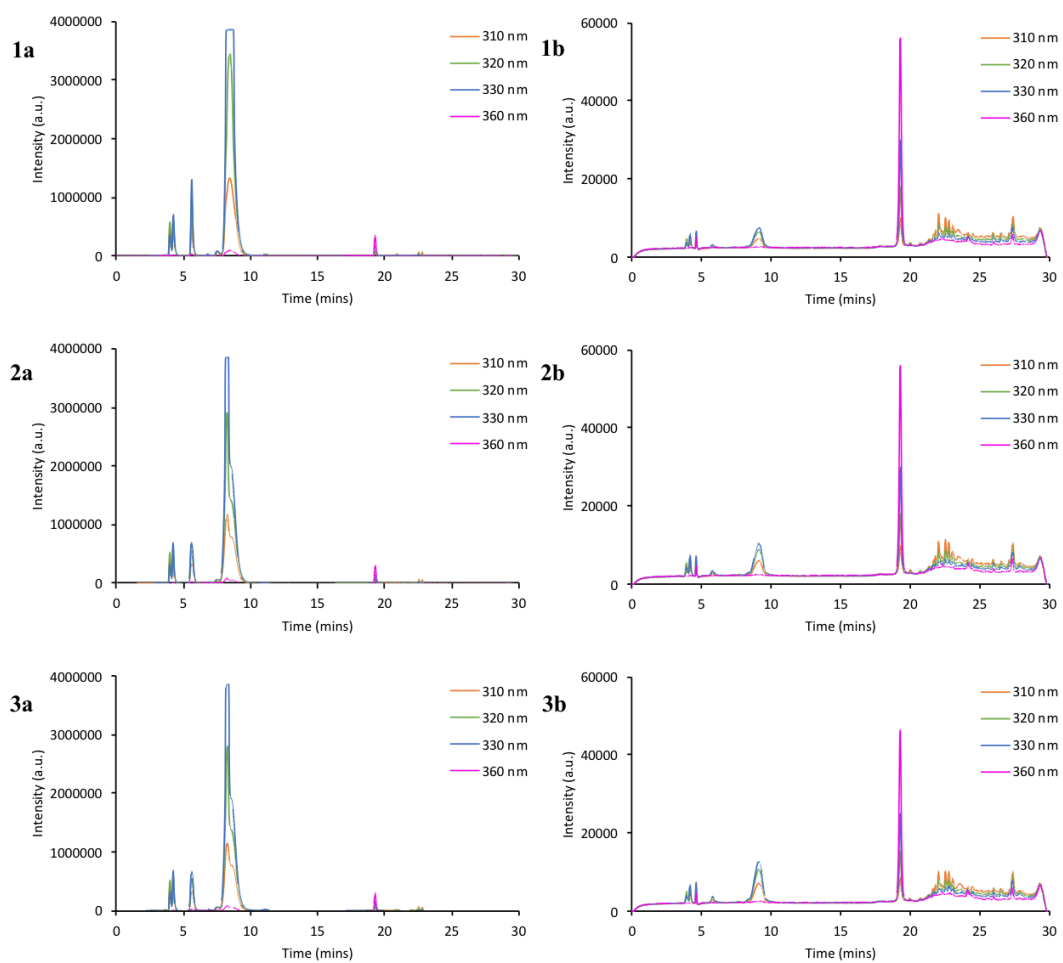


Figure A.4: HPLC chromatograms of first three repeats (1, 2, 3) for purification of usujirene from Nori extract using S450, showing a) adsorption in water and b) desorption in methanol at 310 nm, 320 nm, 330 nm and 360 nm.

# Appendix B

## Material Characterisation



Table B.1: Elemental analysis determined by XPS of *N*-Starbons (alginic acid : chitosan; 2:1) prepared at different carbonisation temperatures.

<b>Temperature (°C)</b>	<b>C</b>	<b>Ca</b>	<b>N</b>	<b>Na</b>	<b>O</b>	<b>S</b>
<b>0</b>	57.2	0.3	1.5	0.7	40.3	0.0
<b>300</b>	77.5	0.5	4.9	1.0	16.0	0.1
<b>450</b>	67.6	1.9	11.6	4.0	14.3	0.6
<b>600</b>	81.4	0.6	6.8	2.4	8.5	0.2



# Abbreviations

<b>°C</b>	Degrees Celsius
<b>µg</b>	Microgram
<b>µm</b>	Micrometre
<b>%</b>	Percent
<b>at%</b>	Atomic percent
<b>wt%</b>	Weight percent
<b>AC</b>	Alternating current
<b>AES</b>	Auger electron spectroscopy
<b>ATR</b>	Attenuated total reflection
<b>BET</b>	Brunauer–Emmett–Teller
<b>BJH</b>	Barrett-Joyner-Halenda
<b>C</b>	Capacitance
<b>CCS</b>	CO <sub>2</sub> capture and storage
<b>CE</b>	Counter electrode
<b>CFC</b>	Chlorofluorocarbon
<b>cm</b>	Centimetres
<b>COD</b>	Chemical oxygen demand
<b>CRT</b>	Cathode ray tube

<b>CV</b>	Cyclic voltammetry
<b>CVD</b>	Chemical vapour deposition
<b>DEHPA</b>	di-2-ethylhexylphosphoric acid
<b>DRIFT</b>	Diffuse reflectance infrared spectroscopy in Fourier transform mode
<b>DTG</b>	Differential thermogravimetry
<b>ECS</b>	Expanded corn starch
<b>EDL</b>	Electrochemical double-layer
<b>EIS</b>	Electrochemical impedance spectroscopy
<b>E<sub>B</sub></b>	Binding energy
<b>E<sub>K</sub></b>	Kinetic energy
<b>ESA</b>	Electric-swing adsorption
<b>Et<sub>4</sub>TDS</b>	tetraalkylthiuramdisulphides
<b>eV</b>	Electron volts
<b>FD</b>	Freeze-drying
<b>FTIR</b>	Fourier transform infrared spectroscopy
<b>g</b>	Grams
<b>G</b>	Gibbs free energy
<b>GCCE</b>	Green Chemistry Centre of Excellence
<b>GHG</b>	Greenhouse gas
<b>GHSV</b>	Gas hourly space velocity
<b>Hz</b>	Hertz

<b>h</b>	Hour
<b>ICP-MS</b>	Inductively coupled plasma – mass spectrometry
<b>IR</b>	Infrared
<b>ITO</b>	Indium tin oxide
<b>IUPAC</b>	International Union of Pure and Applied Chemistry
<b>K</b>	Kelvin
<b>kg</b>	Kilograms
<b>L</b>	Litres
<b>LCA</b>	Life cycle assessment
<b>LCD</b>	Liquid crystal display
<b>m</b>	Metres
<b>MCM</b>	Mobil Composition of Matter
<b>Me<sub>2</sub>dazdt</b>	N,N' dimethyl-perhydrodiazepine-2,3-dithione
<b>mg</b>	Milligram
<b>min</b>	Minute
<b>mL</b>	Millilitre
<b>MOF</b>	Metal-organic framework
<b>MPa</b>	Mega Pascals
<b>mV</b>	Millivolts
<b>N-materials</b>	Nitrogen-containing materials
<b>N-Starbons</b>	Nitrogen-containing Starbons

<b>NC</b>	Nitrogen-doped carbon
<b>N-MC-W</b>	Wheat flour-based mesoporous carbon prepared at 850 °C
<b>nm</b>	Nanometre
<b>OPEC</b>	Orange peel exploitation company
<b>ORR</b>	Oxygen reduction reaction
<b>Pa</b>	Pascals
<b>PCB</b>	Printed circuit board
<b>pCSA</b>	<i>para</i> -Cymenesulfonic acid
<b>PEIS</b>	Potential-electrochemical impedance spectroscopy
<b>ppb</b>	Parts per billion
<b>PSA</b>	Pressure-swing adsorption
<b>pTSA</b>	<i>para</i> -Toluenesulfonic acid
<b>PTSA</b>	Pressure and temperature swing adsorption
<b>PVC</b>	Polyvinylchloride
<b>PVDF</b>	Polyvinylidifluoride
<b>RE</b>	Reference electrode
<b>REE</b>	Rare earth elements
<b>rpm</b>	Revolutions per minute
<b>RT</b>	Room temperature
<b>S</b>	Entropy
<b>SBA</b>	Santa Barbara Amorphous

<b>scCO<sub>2</sub></b>	Supercritical CO <sub>2</sub>
<b>SEM</b>	Scanning electron microscopy
<b>SFE</b>	Supercritical fluid extraction
<b>STA</b>	Simultaneous thermal analysis
<b><i>t</i></b>	Time
<b>T</b>	Temperature
<b>TBA</b>	<i>tert</i> -Butanol
<b>TBP</b>	Tributyl phosphate
<b>TEM</b>	Transmission electron microscopy
<b>TGA</b>	Thermogravimetric analysis
<b>TSA</b>	Temperature-swing adsorption
<b>V</b>	Volts
<b>VCM</b>	Vinyl chloride monomer
<b>VSA</b>	Vacuum-swing adsorption
<b>W</b>	Watts
<b>WE</b>	Working electrode
<b>WEEE</b>	Waste electrical and electronic equipment
<b>XPS</b>	X-ray photoelectron spectroscopy
<b><math>Z_i</math></b>	Imaginary impedance
<b><math>Z_r</math></b>	Real impedance



# Bibliography



1. D. W. Pearce and R. K. Turner, *Economics of Natural Resources and the Environment*, Johns Hopkins University Press, 1990.
2. M. Bertau, H. Offermanns, L. Plass, F. Schmidt and H. J. Wernicke, *Methanol: The Basic Chemical and Energy Feedstock of the Future: Asinger's Vision Today*, Springer Berlin Heidelberg, 2014.
3. M. Lieder and A. Rashid, *Journal of Cleaner Production*, 2016, **115**, 36-51.
4. IPCC, *Global Warming of 1.5 °C*, 2018.
5. J. H. Clark, *Green Chemistry*, 1999, **1**, 1-8.
6. J. H. Clark, *Green Chemistry*, 2006, **8**, 17-21.
7. P. T. Anastas and J. C. Warner, *Green Chemistry: Theory and Practice*, Oxford University Press, 2000.
8. M. Thommes, K. Kaneko, V. Neimark Alexander, P. Olivier James, F. Rodriguez-Reinoso, J. Rouquerol and S. W. Sing Kenneth, *Journal*, 2015, **87**, 1051.
9. F. Schüth and W. Schmidt, *Advanced Materials*, 2002, **14**, 629-638.
10. I. N. Savina, G. C. Ingavle, A. B. Cundy and S. V. Mikhalovsky, *Scientific Reports*, 2016, **6**, 21154.
11. S.-W. Woo, K. Dokko, H. Nakano and K. Kanamura, *Journal of Materials Chemistry*, 2008, **18**, 1674-1680.
12. R. J. White, V. Budarin, R. Luque, J. H. Clark and D. J. Macquarrie, *Chemical Society Reviews*, 2009, **38**, 3401-3418.
13. C. T. Kresge, M. E. Leonowicz, W. J. Roth, J. C. Vartuli and J. S. Beck, *Nature*, 1992, **359**, 710-712.
14. U. Ciesla and F. Schüth, *Microporous and Mesoporous Materials*, 1999, **27**, 131-149.
15. C. Liang, Z. Li and S. Dai, *Angewandte Chemie International Edition*, 2008, **47**, 3696-3717.
16. H. M. Montenegro, *Journal of the American Oil Chemists' Society*, 1985, **62**, 259-261.
17. H. Marsh and F. R. Reinoso, *Activated Carbon*, Elsevier Science, 2006.
18. A. H. Lu and F. Schüth, *Advanced Materials*, 2006, **18**, 1793-1805.
19. C. Liang and S. Dai, *Journal of the American Chemical Society*, 2006, **128**, 5316-5317.
20. 2009.

21. A. Munoz Garcia, A. J. Hunt, V. L. Budarin, H. L. Parker, P. S. Shuttleworth, G. J. Ellis and J. H. Clark, *Green Chemistry*, 2015, **17**, 2146-2149.
22. V. Budarin, J. H. Clark, R. Luque and R. White, *Material Matters*, 2009, **4.1**, 19.
23. V. Budarin, J. H. Clark, J. J. E. Hardy, R. Luque, K. Milkowski, S. J. Tavener and A. J. Wilson, *Angewandte Chemie International Edition*, 2006, **45**, 3782-3786.
24. A. Poli, G. Anselmo, G. Fiorentino, B. Nicolaus, G. Tommonaro and P. Di Donato, in *Biotechnology of Biopolymers*, ed. P. M. Elnashar, Intech, 2011, ch. 2, pp. 33-56.
25. T. N. Zvyagintseva, N. M. Shevchenko, I. B. Popivnich, V. V. Isakov, A. S. Scobun, E. V. Sundukova and L. A. Elyakova, *Carbohydrate Research*, 1999, **322**, 32-39.
26. P. S. Shuttleworth, V. Budarin, R. J. White, V. M. Gun'ko, R. Luque and J. H. Clark, *Chemistry - A European Journal*, 2013, **19**, 9351-9357.
27. R. J. White, C. Antonio, V. L. Budarin, E. Bergström, J. Thomas-Oates and J. H. Clark, *Advanced Functional Materials*, 2010, **20**, 1834-1841.
28. A. Borisova, M. De Bruyn, V. L. Budarin, P. S. Shuttleworth, J. R. Dodson, M. L. Segatto and J. H. Clark, *Macromol Rapid Commun*, 2015, **36**, 774-779.
29. S. Doi, J. H. Clark, D. J. Macquarrie and K. Milkowski, *Chemical Communications*, 2002, 2632-2633.
30. K. Milkowski, J. H. Clark and S. Doi, *Green Chemistry*, 2004, **6**, 189-190.
31. M. J. Gronnow, R. Luque, D. J. Macquarrie and J. H. Clark, *Green Chemistry*, 2005, **7**, 552-557.
32. V. L. Budarin, J. H. Clark, R. Luque, D. J. Macquarrie and R. J. White, *Green Chemistry*, 2008, **10**, 382-387.
33. R. J. White, V. L. Budarin, J. W. B. Moir and J. H. Clark, *International Journal of Molecular Sciences*, 2011, **12**.
34. V. Budarin, J. H. Clark, F. E. I. Deswarte, J. J. E. Hardy, A. J. Hunt and F. M. Kerton, *Chemical Communications*, 2005, 2903-2905.
35. V. L. Budarin, J. H. Clark, R. Luque and D. J. Macquarrie, *Chemical Communications*, 2007, 634-636.
36. V. L. Budarin, J. H. Clark, R. Luque, D. J. Macquarrie, A. Koutinas and C. Webb, *Green Chemistry*, 2007, **9**, 992-995.
37. V. Budarin, R. Luque, D. J. Macquarrie and J. H. Clark, *Chemistry – A European Journal*, 2007, **13**, 6914-6919.

38. J. H. Clark, V. Budarin, T. Dugmore, R. Luque, D. J. Macquarrie and V. Strelko, *Catalysis Communications*, 2008, **9**, 1709-1714.
39. R. Luque, V. Budarin, J. H. Clark and D. J. Macquarrie, *Applied Catalysis B: Environmental*, 2008, **82**, 157-162.
40. R. Luque, V. Budarin, J. H. Clark and D. J. Macquarrie, *Green Chemistry*, 2009, **11**, 459-461.
41. R. Luque, V. Budarin, J. H. Clark, P. Shuttleworth and R. J. White, *Catalysis Communications*, 2011, **12**, 1471-1476.
42. R. Luque, J. H. Clark, K. Yoshida and P. L. Gai, *Chemical Communications*, 2009, 5305-5307.
43. R. Luque and J. H. Clark, *Catalysis Communications*, 2010, **11**, 928-931.
44. K. S. W. Sing, D. H. Everett, R. A. W. Haul, L. Moscou, R. A. Pierotti, J. Rouqu  rol and T. Siemieniewska, *Journal*.
45. F. Rouquerol, J. Rouquerol and K. Sing, in *Adsorption by Powders and Porous Solids*, Academic Press, London, 1999, pp. 1-26.
46. H. L. Parker, A. J. Hunt, V. L. Budarin, P. S. Shuttleworth, K. L. Miller and J. H. Clark, *RSC Advances*, 2012, **2**, 8992-8997.
47. H. L. Parker, V. L. Budarin, J. H. Clark and A. J. Hunt, *ACS Sustainable Chemistry & Engineering*, 2013, **1**, 1311-1318.
48. M. A. Tony, H. L. Parker and J. H. Clark, *Journal of Environmental Science and Health, Part A*, 2016, **51**, 974-979.
49. M. A. Tony, H. L. Parker and J. H. Clark, *Water and Environment Journal*, 2018, **0**.
50. V. G. Zuin, V. L. Budarin, M. De bruyn, P. S. Shuttleworth, A. J. Hunt, C. Pluciennik, A. Borisova, J. Dodson, H. L. Parker and J. H. Clark, *Faraday Discussions*, 2017, **202**, 451-464.
51. G. Dur  , L. Budarin Vitaliy, A. Castro-Osma Jos  , S. Shuttleworth Peter, C. Z. Quek Sophie, H. Clark James and M. North, *Angewandte Chemie International Edition*, 2016, **55**, 9173-9177.
52. A. M. Garcia, V. L. Budarin, Y. Zhou, M. De bruyn, A. J. Hunt, L. Lari, V. K. Lazarov, H. J. Salavagione, E. Morales, G. J. Ellis, J. H. Clark and P. S. Shuttleworth, *Journal of Materials Chemistry A*, 2018, **6**, 1119-1127.
53. R. J. White, V. L. Budarin and J. H. Clark, *Chemistry – A European Journal*, 2010, **16**, 1326-1335.
54. M. Kruk and M. Jaroniec, *Chemistry of Materials*, 2001, **13**, 3169-3183.

55. M. Barber, J. A. Connor, M. F. Guest, I. H. Hillier, M. Schwarz and M. Stacey, *Journal of the Chemical Society, Faraday Transactions 2: Molecular and Chemical Physics*, 1973, **69**, 551-558.
56. A. S. Matharu, in *Element Recovery and Sustainability*, The Royal Society of Chemistry, 2013, pp. 207-219.
57. *Report on Critical Raw Materials for the EU*, 2014.
58. A. J. Hunt, A. S. Matharu, A. H. King and J. H. Clark, *Green Chemistry*, 2015, **17**, 1949-1950.
59. *Communication from the Commission to the European Parliament, The Council, The European Economic and Social Committee and The Committee of the Regions on the 2017 list of Critical Raw Materials for the EU*, Brussels, 2017.
60. J. H. Clark, in *Green and Sustainable Medicinal Chemistry: Methods, Tools and Strategies for the 21st Century Pharmaceutical Industry*, The Royal Society of Chemistry, 2016, pp. 1-11.
61. U. Jadhav and H. Hocheng, *Scientific Reports*, 2015, **5**, 14574.
62. J. Cui and L. Zhang, *Journal of Hazardous Materials*, 2008, **158**, 228-256.
63. A. Serpe, F. Artizzu, D. Espa, A. Rigoldi, L. Mercuri Maria and P. Deplano, *Green Processing and Synthesis*, 2014, **3**, 141.
64. A. Alzate, M. E. López and C. Serna, *Waste Management*, 2016, **57**, 113-120.
65. L. A. Diaz, T. E. Lister, J. A. Parkman and G. G. Clark, *Journal of Cleaner Production*, 2016, **125**, 236-244.
66. D. Pilone and G. H. Kelsall, 2003.
67. A. Serpe, A. Rigoldi, C. Marras, F. Artizzu, M. Laura Mercuri and P. Deplano, *Green Chemistry*, 2015, **17**, 2208-2216.
68. Y. He and Z. Xu, *RSC Advances*, 2015, **5**, 8957-8964.
69. J. Emsley, *Nature's building blocks : everything you need to know about the elements*, Oxford University Press, Oxford ; New York, New edn., 2011.
70. A. Birich, S. Raslan Mohamed and B. Friedrich, *Journal of Sustainable Metallurgy*, 2018, **4**, 265-275.
71. T. Graedel, J. Allwood, J. Birat, B. Reck, S. Sibley, G. Sonnemann, M. Buchert and C. Hagelüken, *A Report of the Working Group on the Global Metal Flows to the International Resource Panel, United Nations Environment Programme*, 2011.

72. Á. Imre-Lucaci, M. Nagy, F. Imre-Lucaci and S. Fogarasi, *Chemical Engineering Journal*, 2017, **309**, 655-662.
73. A. Işıldar, J. van de Vossenbergh, E. R. Rene, E. D. van Hullebusch and P. N. L. Lens, *Waste Management*, 2016, **57**, 149-157.
74. J. E. Madrigal-Arias, R. Argumedo-Delira, A. Alarcón, M. R. Mendoza-López, O. García-Barradas, J. S. Cruz-Sánchez, R. Ferrera-Cerrato and M. Jiménez-Fernández, *Brazilian Journal of Microbiology*, 2015, **46**, 707-713.
75. A. Sheel and D. Pant, *Bioresource Technology*, 2018, **247**, 1189-1192.
76. E. Lahtinen, L. Kivijärvi, R. Tatikonda, A. Väisänen, K. Rissanen and M. Haukka, *ACS Omega*, 2017, **2**, 7299-7304.
77. M. P. Casaletto, A. Longo, A. Martorana, A. Prestianni and A. M. Venezia, *Surface and Interface Analysis*, 2006, **38**, 215-218.
78. E. D. Park and J. S. Lee, *Journal of Catalysis*, 1999, **186**, 1-11.
79. A. P. O'Mullane, S. J. Ippolito, Y. M. Sabri, V. Bansal and S. K. Bhargava, *Langmuir*, 2009, **25**, 3845-3852.
80. R. Díaz, I. Díez-Pérez, P. Gorostiza, F. Sanz and J. R. Morante, *Journal of the Brazilian Chemical Society*, 2003, **14**, 523-529.
81. T. Hezard, K. Fajerweg, D. Evrard, V. Collière, P. Behra and P. Gros, *Journal of Electroanalytical Chemistry*, 2012, **664**, 46-52.
82. T. L. Barr, *The Journal of Physical Chemistry*, 1978, **82**, 1801-1810.
83. J. E. Castle, *Surface and Interface Analysis*, 1984, **6**, 302-302.
84. O. González-García, C. Ariño, J. M. Díaz-Cruz and M. Esteban, *Electroanalysis*, 2007, **19**, 429-435.
85. N. Moussaif, C. Pagnouille, J. Riga and R. Jérôme, *Polymer*, 2000, **41**, 3391-3394.
86. Y. He, E. Ma and Z. Xu, *Journal of Hazardous Materials*, 2014, **268**, 185-190.
87. J. R. Wullert and T. J. Nelson, *Electronic Information Display Technologies*, World Scientific Publishing Co., Inc., 1997.
88. G. Dodbiba, H. Nagai, L. P. Wang, K. Okaya and T. Fujita, *Waste Management*, 2012, **32**, 1937-1944.
89. H. S. Hong, H. Jung and S.-J. Hong, *Research on Chemical Intermediates*, 2010, **36**, 761-766.
90. S. Virolainen, D. Ibane and E. Paatero, *Hydrometallurgy*, 2011, **107**, 56-61.
91. K. Ryoshi, Y. Hattori and H. Kobayashi, *JP2008137825*, 2008.

92. M. J. C. Calagui, D. B. Senoro, C.-C. Kan, J. W. L. Salvacion, C. M. Futralan and M.-W. Wan, *Journal of Hazardous Materials*, 2014, **277**, 120-126.
93. X. Chun-hua, L. Bi-wen and W. Yong-jiang, *Journal of Wuhan University of Technology-Mater. Sci. Ed.*, 2002, **17**, 47-50.
94. H. Li, J. Liu, X. Gao, C. Liu, L. Guo, S. Zhang, X. Liu and C. Liu, *Hydrometallurgy*, 2012, **121–124**, 60-67.
95. J. Li, S. Gao, H. Duan and L. Liu, *Waste Management*, 2009, **29**, 2033-2039.
96. X. Wang, X. Lu and S. Zhang, *Journal of Hazardous Materials*, 2013, **244–245**, 342-347.
97. M. Souada, C. Louage, J.-Y. Doisy, L. Meunier, A. Benderrag, B. Ouddane, S. Bellayer, N. Nuns, M. Traisnel and U. Maschke, *Ultrasonics Sonochemistry*, 2018, **40**, 929-936.
98. K. Zhang, B. Li, Y. Wu, W. Wang, R. Li, Y.-N. Zhang and T. Zuo, *Waste Management*, 2017, **64**, 236-243.
99. T. Shimofusa, H. Abe, Y. Kikuchi and W. Hasegava, *JP2000128531*, 2000.
100. J. Felix, H. Tunell, B. Letcher, S. Mangold, J. Yang, T. Retegan, A. Grammatikas, T. Rydberg and H. Ljungkvist, 2012.
101. T. Sato, *Journal of Inorganic and Nuclear Chemistry*, 1975, **37**, 1485-1488.
102. T. Sato and K. Sato, *Hydrometallurgy*, 1992, **30**, 367-383.
103. W.-S. Chou, Y.-H. Shen, S.-J. Yang, T.-C. Hsiao and L.-F. Huang, *Environmental Progress & Sustainable Energy*, 2016, **35**, 758-763.
104. B. B. Adhikari, M. Gurung, H. Kawakita and K. Ohto, *Journal of Inclusion Phenomena and Macrocyclic Chemistry*, 2011, **71**, 479-487.
105. G. M. Escandar, A. C. Olivieri, M. Gonzalez-Sierra, A. A. Frutos and L. F. Sala, *Journal of the Chemical Society, Dalton Transactions*, 1995, 799-804.
106. Y. Yuan, J. Liu, B. Zhou, S. Yao, H. Li and W. Xu, *Hydrometallurgy*, 2010, **101**, 148-155.
107. T. L. Barr and L. Ying Li, *Journal of Physics and Chemistry of Solids*, 1989, **50**, 657-664.
108. A. W. C. Lin, N. R. Armstrong and T. Kuwana, *Analytical Chemistry*, 1977, **49**, 1228-1235.
109. A. E. Smith, *Analyst*, 1973, **98**, 209-212.
110. D. R. Lide, *Handbook of Chemistry and Physics*, CRC Press, 84 edn., 2004.
111. F. R. de Gruijl, *European Journal of Cancer*, 1999, **35**, 2003-2009.

112. B. K. Armstrong and A. Krickler, *Journal of Photochemistry and Photobiology B: Biology*, 2001, **63**, 8-18.
113. F. R. de Gruijl, H. J. van Kranen and L. H. F. Mullenders, *Journal of Photochemistry and Photobiology B: Biology*, 2001, **63**, 19-27.
114. M. Widel, A. Krzywon, K. Gajda, M. Skonieczna and J. Rzeszowska-Wolny, *Free Radical Biology and Medicine*, 2014, **68**, 278-287.
115. H. van Steeg and K. H. Kraemer, *Molecular Medicine Today*, 1999, **5**, 86-94.
116. M. J. Molina and F. S. Rowland, *Nature*, 1974, **249**, 810.
117. P. J. Crutzen, *Quarterly Journal of the Royal Meteorological Society*, 1970, **96**, 320-325.
118. J. C. Farman, B. G. Gardiner and J. D. Shanklin, *Nature*, 1985, **315**, 207.
119. U. S. D. o. State, The Montreal Protocol on Substances that Deplete the Ozone Layer, (accessed 12<sup>th</sup> December 2018, 2018).
120. T. Henriksen, A. Dahlback, S. H. H. Larsen and J. Moan, *Photochemistry and Photobiology*, 1990, **51**, 579-582.
121. H. Slaper, G. J. M. Velders, J. S. Daniel, F. R. de Gruijl and J. C. van der Leun, *Nature*, 1996, **384**, 256.
122. D. Karentz, F. S. McEuen, M. C. Land and W. C. Dunlap, *Marine Biology*, 1991, **108**, 157-166.
123. H. Nakamura, J. i. Kobayashi and Y. Hirata, *Journal of Chromatography A*, 1982, **250**, 113-118.
124. H. Nakamura, J.-i. Kobayashi and Y. Hirata, *Chemistry Letters*, 1981, **10**, 1413-1414.
125. R. P. Sinha, S. P. Singh and D.-P. Häder, *Journal of Photochemistry and Photobiology B: Biology*, 2007, **89**, 29-35.
126. M. S. Cooke, *British Journal of Dermatology*, 2018, **178**, 1239-1240.
127. J. I. Carreto, M. O. Carignan, G. Daleo and S. G. D. Marco, *Journal of Plankton Research*, 1990, **12**, 909-921.
128. W. M. Bandaranayake, J. E. Bemis and D. J. Bourne, *Comparative Biochemistry and Physiology Part C: Pharmacology, Toxicology and Endocrinology*, 1996, **115**, 281-286.
129. R. P. Sinha, M. Klisch, A. Gröniger and D. P. Häder, *Journal of Photochemistry and Photobiology B: Biology*, 1998, **47**, 83-94.

130. A. Oren and N. Gunde-Cimerman, *FEMS Microbiology Letters*, 2007, **269**, 1-10.
131. Y. Athukorala, S. Trang, C. Kwok and V. Y. Yuan, *Molecules*, 2016, **21**.
132. F. R. Conde, M. O. Carignan, M. Sandra Churio and J. I. Carreto, *Photochemistry and Photobiology*, 2007, **77**, 146-150.
133. Y. Xia and R. Mokaya, *Advanced Materials*, 2004, **16**, 1553-1558.
134. Y. Xia and R. Mokaya, *Chemistry of Materials*, 2005, **17**, 1553-1560.
135. R. J. White, N. Yoshizawa, M. Antonietti and M.-M. Titirici, *Green Chemistry*, 2011, **13**, 2428-2434.
136. M. Terrones, P. M. Ajayan, F. Banhart, X. Blase, D. L. Carroll, J. C. Charlier, R. Czerw, B. Foley, N. Grobert, R. Kamalakaran, P. Kohler-Redlich, M. Rühle, T. Seeger and H. Terrones, *Applied Physics A*, 2002, **74**, 355-361.
137. Yang, Xu, A. Tomita and T. Kyotani, *Chemistry of Materials*, 2005, **17**, 2940-2945.
138. H. J. Burch, J. A. Davies, E. Brown, L. Hao, S. A. Contera, N. Grobert and J. F. Ryan, *Applied Physics Letters*, 2006, **89**, 143110.
139. K. Gong, F. Du, Z. Xia, M. Durstock and L. Dai, *Science*, 2009, **323**, 760.
140. W. Yang, T.-P. Fellingner and M. Antonietti, *Journal of the American Chemical Society*, 2011, **133**, 206-209.
141. M. G. Plaza, C. Pevida, A. Arenillas, F. Rubiera and J. J. Pis, *Fuel*, 2007, **86**, 2204-2212.
142. E. F. Franca, R. D. Lins, L. C. G. Freitas and T. P. Straatsma, *Journal of Chemical Theory and Computation*, 2008, **4**, 2141-2149.
143. Y. Gao, X. Chen, J. Zhang and N. Yan, *ChemPlusChem*, 2015, **80**, 1556-1564.
144. *The State of World Fisheries and Aquaculture*, FAO, Rome, 2014.
145. N. Yan and X. Chen, *Nature*, 2015, **524**, 155-157.
146. D. Kulig, A. Zimoch-Korzycka, A. Jarmoluk and K. Marycz, *Polymers*, 2016, **8**.
147. J. P. Soares, J. E. Santos, G. O. Chierice and E. T. G. Cavalheiro, *Eclética Química*, 2004, **29**, 57-64.
148. I. Corazzari, R. Nisticò, F. Turci, M. G. Faga, F. Franzoso, S. Tabasso and G. Magnacca, *Polymer Degradation and Stability*, 2015, **112**, 1-9.
149. R. M. Silverstein, F. X. Webster and D. Kiemle, *Spectrometric Identification of Organic Compounds, 7th Edition*, Wiley, 2005.

150. I. R. Beattie and T. Gilson, *Journal of the Chemical Society (Resumed)*, 1964, 2292-2295.
151. T. L. Brown and M. Kubota, *Journal of the American Chemical Society*, 1961, **83**, 4175-4177.
152. R. J. H. Clark, J. Lewis, D. J. Machin and R. S. Nyholm, *Journal of the Chemical Society (Resumed)*, 1963, 379-387.
153. H. Knoezinger and H. Krietenbrink, *Journal of the Chemical Society, Faraday Transactions 1: Physical Chemistry in Condensed Phases*, 1975, **71**, 2421-2430.
154. T. Montanari, M. Bevilacqua, C. Resini and G. Busca, *The Journal of Physical Chemistry B*, 2004, **108**, 2120-2127.
155. A. Zecchina, E. Guglielminotti, S. Coluccia and E. Borello, *Journal of the Chemical Society A: Inorganic, Physical, Theoretical*, 1969, 2196-2199.
156. J. Reedijk, A. P. Zuur and W. L. Groeneveld, *Recueil des Travaux Chimiques des Pays-Bas*, 1967, **86**, 1127-1137.
157. T. Szymańska-Buzar, T. Głowiak and I. Czełusniak, *Journal of Organometallic Chemistry*, 1999, **585**, 215-224.
158. I. Salla, T. Montanari, P. Salagre, Y. Cesteros and G. Busca, *Physical Chemistry Chemical Physics*, 2005, **7**, 2526-2533.
159. J. C. Lavalley, *Catalysis Today*, 1996, **27**, 377-401.
160. J. A. Lercher, C. Gründling and G. Eder-Mirth, *Catalysis Today*, 1996, **27**, 353-376.
161. R. E. Clarke and P. C. Ford, *Inorganic Chemistry*, 1970, **9**, 227-235.
162. B. N. Storhoff and H. C. Lewis Jr, *Coordination Chemistry Reviews*, 1977, **23**, 1-29.
163. D. Cagniant, P. Magri, R. Gruber, S. Berlozecki, P. D. Salbut, J. Bimer and G. Nansé, *Journal of Analytical and Applied Pyrolysis*, 2002, **65**, 1-23.
164. I. Bertóti, G. Varsányi, G. Mink, T. Székely, J. Vaivads, T. Millers and J. Grabis, *Surface and Interface Analysis*, 1988, **12**, 527-530.
165. H. Schmiers, J. Friebel, P. Streubel, R. Hesse and R. Köpsel, *Carbon*, 1999, **37**, 1965-1978.
166. L. T. Weng, C. Poleunis, P. Bertrand, V. Carlier, M. Sclavons, P. Franquinet and R. Legras, *Journal of Adhesion Science and Technology*, 1995, **9**, 859-871.
167. R. J. J. Jansen and H. van Bekkum, *Carbon*, 1995, **33**, 1021-1027.
168. I. E. Agency, *Global Energy and CO2 Status Report*, 2018.

169. BP, *BP Energy Outlook*, 2018.
170. I. Treufeld, D. H. Wang, B. A. Kurish, L.-S. Tan and L. Zhu, *Journal of Materials Chemistry A*, 2014, **2**, 20683-20696.
171. L. Li, R. Kikuchi, M.-A. Kakimoto, M. Jikei and A. Takahashi, *High Performance Polymers*, 2005, **17**, 135-147.
172. B. E. Conway, *Electrochemical Supercapacitors: Scientific Fundamentals and Technological Applications*, Springer, US, 1 edn., 1999.
173. W. Li, J. Liu and D. Zhao, *Nature Reviews Materials*, 2016, **1**, 1-17.
174. L. Zhao, L.-Z. Fan, M.-Q. Zhou, H. Guan, S. Qiao, M. Antonietti and M.-M. Titirici, *Advanced Materials*, 2010, **22**, 5202-5206.
175. Y. Nakano and H. Tsutsumi, *Solid State Ionics*, 2014, **262**, 774-777.
176. D. Zhou, Y.-B. He, R. Liu, M. Liu, H. Du, B. Li, Q. Cai, Q.-H. Yang and F. Kang, *Advanced Energy Materials*, 2015, **5**, 1500353-n/a.
177. J. Liu, W. Li, L. Duan, X. Li, L. Ji, Z. Geng, K. Huang, L. Lu, L. Zhou, Z. Liu, W. Chen, L. Liu, S. Feng and Y. Zhang, *Nano Letters*, 2015, **15**, 5137-5142.
178. M. Winter and R. J. Brodd, *Chemical Reviews*, 2004, **104**, 4245-4270.
179. X. Zhao, J. Zhu, L. Liang, C. Li, C. Liu, J. Liao and W. Xing, *Applied Catalysis B: Environmental*, 2014, **154**, 177-182.
180. E. Dashtimoghadam, M. M. Hasani-Sadrabadi and H. Moaddel, *Polymers for Advanced Technologies*, 2010, **21**, 726-734.
181. M. Qiao, C. Tang, G. He, K. Qiu, R. Binions, I. P. Parkin, Q. Zhang, Z. Guo and M. M. Titirici, *Journal of Materials Chemistry A*, 2016, **4**, 12658-12666.
182. N. Brun, S. A. Wohlgemuth, P. Osiceanu and M. M. Titirici, *Green Chemistry*, 2013, **15**, 2514-2524.
183. G. A. Ferrero, A. B. Fuertes, M. Sevilla and M.-M. Titirici, *Carbon*, 2016, **106**, 179-187.
184. Y.-R. Rhim, D. Zhang, D. H. Fairbrother, K. A. Wepasnick, K. J. Livi, R. J. Bodnar and D. C. Nagle, *Carbon*, 2010, **48**, 1012-1024.
185. Y. Zhao, W. Ran, J. He, Y. Huang, Z. Liu, W. Liu, Y. Tang, L. Zhang, D. Gao and F. Gao, *Small*, 2015, **11**, 1310-1319.
186. C. Z. Yuan, L. Zhou and L. R. Hou, *Materials Letters*, 2014, **124**, 253-255.
187. S. Yun, S.-O. Kang, S. Park and H. S. Park, *Nanoscale*, 2014, **6**, 5296-5302.
188. L.-N. Han, X. Wei, Q.-C. Zhu, S.-M. Xu, K.-X. Wang and J.-S. Chen, *Journal of Materials Chemistry A*, 2016, **4**, 16698-16705.

189. C. H. Hamann, A. Hamnett and W. Vielstich, *Electrochemistry*, Wiley-VCH, Weinheim ; New York, 1998.
190. A. C. Fisher, *Electrode dynamics*, Oxford University Press, New York, 1996.
191. D. K. Kampouris, X. Ji, E. P. Randviir and C. E. Banks, *RSC Advances*, 2015, **5**, 12782-12791.
192. Y. Wang, Y. Song and Y. Xia, *Chemical Society Reviews*, 2016, **45**, 5925-5950.
193. F. Béguin, K. Szostak, G. Lota and E. Frackowiak, *Advanced Materials*, 2005, **17**, 2380-2384.
194. A. B. Fuertes and M. Sevilla, *ACS Applied Materials & Interfaces*, 2015, **7**, 4344-4353.
195. D. Hulicova, J. Yamashita, Y. Soneda, H. Hatori and M. Kodama, *Chemistry of Materials*, 2005, **17**, 1241-1247.
196. X. Ning, W. Zhong, S. Li, Y. Wang and W. Yang, *Journal of Materials Chemistry A*, 2014, **2**, 8859-8867.
197. IPCC, *Global Warming of 1.5o<sup>C</sup>*, 2018.
198. M. Bui, C. S. Adjiman, A. Bardow, E. J. Anthony, A. Boston, S. Brown, P. S. Fennell, S. Fuss, A. Galindo, L. A. Hackett, J. P. Hallett, H. J. Herzog, G. Jackson, J. Kemper, S. Krevor, G. C. Maitland, M. Matuszewski, I. S. Metcalfe, C. Petit, G. Puxty, J. Reimer, D. M. Reiner, E. S. Rubin, S. A. Scott, N. Shah, B. Smit, J. P. M. Trusler, P. Webley, J. Wilcox and N. Mac Dowell, *Energy & Environmental Science*, 2018, **11**, 1062-1176.
199. A. A. Olajire, *Energy*, 2010, **35**, 2610-2628.
200. Y.-S. Bae and R. Q. Snurr, *Angewandte Chemie International Edition*, 2011, **50**, 11586-11596.
201. K. Damen, M. v. Troost, A. Faaij and W. Turkenburg, *Progress in Energy and Combustion Science*, 2006, **32**, 215-246.
202. A. Arenillas, K. M. Smith, T. C. Drage and C. E. Snape, *Fuel*, 2005, **84**, 2204-2210.
203. G. P. Knowles, S. W. Delaney and A. L. Chaffee, *Industrial & Engineering Chemistry Research*, 2006, **45**, 2626-2633.
204. F. Zheng, D. N. Tran, B. J. Busche, G. E. Fryxell, R. S. Addleman, T. S. Zemanian and C. L. Aardahl, *Industrial & Engineering Chemistry Research*, 2005, **44**, 3099-3105.
205. P. D. Jadhav, R. V. Chatti, R. B. Biniwale, N. K. Labhsetwar, S. Devotta and S. S. Rayalu, *Energy & Fuels*, 2007, **21**, 3555-3559.

206. A. Zukal, I. Dominguez, J. Mayerová and J. Čejka, *Langmuir*, 2009, **25**, 10314-10321.
207. H. Deng, H. Yi, X. Tang, Q. Yu, P. Ning and L. Yang, *Chemical Engineering Journal*, 2012, **188**, 77-85.
208. R. V. Siriwardane, M.-S. Shen, E. P. Fisher and J. A. Poston, *Energy & Fuels*, 2001, **15**, 279-284.
209. S. Himeno, T. Komatsu and S. Fujita, *Journal of Chemical & Engineering Data*, 2005, **50**, 369-376.
210. P. J. M. Carrott, I. P. P. Cansado and M. M. L. R. Carrott, *Applied Surface Science*, 2006, **252**, 5948-5952.
211. Z. Zhang, Z.-Z. Yao, S. Xiang and B. Chen, *Energy & Environmental Science*, 2014, **7**, 2868-2899.
212. C.-H. a. H. C.-H. a. T. C.-S. Yu, *Aerosol and Air Quality Research*, 2012, **12**, 745-769.
213. H. Yang, Z. Xu, M. Fan, R. Gupta, R. B. Slimane, A. E. Bland and I. Wright, *Journal of Environmental Sciences*, 2008, **20**, 14-27.
214. K. V. Kumar, K. Preuss, L. Lu, Z. X. Guo and M. M. Titirici, *The Journal of Physical Chemistry C*, 2015, **119**, 22310-22321.
215. J. Wei, D. Zhou, Z. Sun, Y. Deng, Y. Xia and D. Zhao, *Advanced Functional Materials*, 2013, **23**, 2322-2328.
216. A. I. Sarker, A. Aroonwilas and A. Veawab, *Energy Procedia*, 2017, **114**, 2450-2459.
217. A. Torres-Knoop, A. Poursaeidesfahani, T. J. H. Vlugt and D. Dubbeldam, *Journal of Chemical Theory and Computation*, 2017, **13**, 3326-3339.
218. X. Liu, M. Conte, D. Elias, L. Lu, D. J. Morgan, S. J. Freakley, P. Johnston, C. J. Kiely and G. J. Hutchings, *Catalysis Science & Technology*, 2016.
219. Y. Ryabenkova, Q. He, P. J. Miedziak, N. F. Dummer, S. H. Taylor, A. F. Carley, D. J. Morgan, N. Dimitratos, D. J. Willock, D. Bethell, D. W. Knight, D. Chadwick, C. J. Kiely and G. J. Hutchings, *Catalysis Today*, 2013, **203**, 139-145.
220. P. Johnston, N. Carthey and G. J. Hutchings, *Journal of the American Chemical Society*, 2015, **137**, 14548-14557.
221. pvc.org, PVC, (accessed 17<sup>th</sup> December 2018, 2018).
222. M. Zhu, Q. Wang, K. Chen, Y. Wang, C. Huang, H. Dai, F. Yu, L. Kang and B. Dai, *ACS Catalysis*, 2015, **5**, 5306-5316.

223. K. Zhou, W. Wang, Z. Zhao, G. Luo, J. T. Miller, M. S. Wong and F. Wei, *ACS Catalysis*, 2014, **4**, 3112-3116.
224. H. S. Shankar and J. B. Agnew, *Industrial & Engineering Chemistry Product Research and Development*, 1980, **19**, 232-237.
225. J. B. Agnew and H. S. Shankar, *Industrial & Engineering Chemistry Product Research and Development*, 1986, **25**, 19-22.
226. C. Zhang, L. Kang, M. Zhu and B. Dai, *RSC Advances*, 2015, **5**, 7461-7468.
227. S. Chao, F. Zou, F. Wan, X. Dong, Y. Wang, Y. Wang, Q. Guan, G. Wang and W. Li, *Scientific Reports*, 2017, **7**, 39789.
228. G. Lan, Y. Wang, Y. Qiu, X. Wang, J. Liang, W. Han, H. Tang, H. Liu, J. Liu and Y. Li, *Chemical Communications*, 2018, **54**, 623-626.
229. J. H. Clark, E. M. Fitzpatrick, D. J. Macquarrie, L. A. Pfaltzgraff and J. Sherwood, *Catalysis Today*, 2012, **190**, 144-149.